

5-2016

Energy transfer and localization in molecular crystals

Mitchell A. Wood
Purdue University

Follow this and additional works at: https://docs.lib.purdue.edu/open_access_dissertations

 Part of the [Condensed Matter Physics Commons](#), [Materials Science and Engineering Commons](#), and the [Physical Chemistry Commons](#)

Recommended Citation

Wood, Mitchell A., "Energy transfer and localization in molecular crystals" (2016). *Open Access Dissertations*. 728.
https://docs.lib.purdue.edu/open_access_dissertations/728

This document has been made available through Purdue e-Pubs, a service of the Purdue University Libraries. Please contact epubs@purdue.edu for additional information.

**PURDUE UNIVERSITY
GRADUATE SCHOOL
Thesis/Dissertation Acceptance**

This is to certify that the thesis/dissertation prepared

By Mitchell A Wood

Entitled

Energy Transfer and Localization in Molecular Crystals

For the degree of Doctor of Philosophy



Is approved by the final examining committee:

Alejandro Strachan

Chair

Edwin Garcia

Eric Kvam

Steven Son

To the best of my knowledge and as understood by the student in the Thesis/Dissertation Agreement, Publication Delay, and Certification Disclaimer (Graduate School Form 32), this thesis/dissertation adheres to the provisions of Purdue University's "Policy of Integrity in Research" and the use of copyright material.

Approved by Major Professor(s): Alejandro Strachan

Approved by: David Bhar

Head of the Departmental Graduate Program

4/18/2016

Date

ENERGY TRANSFER AND LOCALIZATION
IN MOLECULAR CRYSTALS

A Dissertation
Submitted to the Faculty
of
Purdue University
by
Mitchell A. Wood

In Partial Fulfillment of the
Requirements for the Degree
of
Doctor of Philosophy

May 2016
Purdue University
West Lafayette, Indiana

To the giants on whose shoulders I stood.

ACKNOWLEDGMENTS

It is with my deepest sincerity that I want to thank my advisor, Alejandro Strachan, for his guidance and positive influence over my personal and professional development throughout the last five years. For the expertise that he shared and his persistent push for me to be the best researcher possible, I am forever grateful. Although I may have lost more than my fair share of those petty research bets against him, I appreciate that he strove to instill a pride in commanding my knowledge of a particular topic. To my committee members, Steve Son, Edwin Garcia and Eric Kvam, thank you for your guidance and allowing me to leveraging your expertise into my work, it is greatly appreciated. A list of names of collaborators and friends who helped me along the doesn't do justice for my appreciation, but a sincere thank you to Marc Cawkwell, Ed Kober, Dave Moore, Diego Dalvit, Anders Niklasson, Edwin Antillion, Chris Fancher, Andrew Kustas, Heather Meredith, Sam Reeve, Ben Haley, Nicolas Onofrio and Jairo Diaz Amaya. The funding support from the Office of Naval Research through grant number N00014-11-1-0466 has enabled this work and the Rosen Center for Advanced Computing and Network for Computational Nanotechnology has been an invaluable resource for my graduate work and I am thankful for their technical support. I also owe a special thank you to Kevin Chaput and Mathew Cherukara, who have played a significant role in shaping how I think and approach my research, through our numerous discussions and arguments I have gained an engineers perspective that I would otherwise be severely lacking. Kara, thank you for giving me balance in my life when I need it the most, thank you. To my family, I am immensely appreciative that you have always supported me and helped me pursue what has truly become a passion of mine.

TABLE OF CONTENTS

	Page
LIST OF TABLES	vi
LIST OF FIGURES	vii
ABSTRACT	xii
CHAPTER 1. INTRODUCTION	1
CHAPTER 2. COMPUTATIONAL METHODS	5
2.1 Introduction	5
2.2 Atomistic Simulation Tools	8
2.2.1 Reactive Molecular Dynamics	10
2.2.2 General Analysis Techniques	13
CHAPTER 3. CHEMICAL RESPONSE TO ENERGY INPUT	23
3.1 Introduction	23
3.2 Advances in Reaction Rate Theory	26
3.3 Non-equilibrium Chemistry Through Vibrational Coupling	30
3.3.1 Simulation Details	31
3.3.2 Results and Discussion	37
3.3.3 Conclusions	51
3.4 Role of Non-equilibrium Chemistry for Shock Initiation	53
3.4.1 Simulation Details	58
3.4.2 Results and Discussion	61
3.4.3 Conclusions	72
CHAPTER 4. THERMAL RESPONSE TO ACOUSTIC ENERGY INPUT	75
4.1 Introduction	75
4.2 Acoustic Coupling To Heterogeneous Media	77
4.2.1 Results and Discussion	81
4.2.2 Conclusions	88
CHAPTER 5. ELECTROMAGNETIC RESPONSE TO ENERGY INPUT	92
5.1 Introduction	92
5.2 Non-Linear Light-Matter Interactions	93
5.2.1 Simulation Details	96
5.2.2 Results and Discussion	101
5.2.3 Conclusions	106

	Page
CHAPTER 6. SUMMARY	110
LIST OF REFERENCES	115
APPENDICES	133
Appendix A: Code Description	133
Appendix B: Published Work	138
VITA	182

LIST OF TABLES

Table	Page
3.1 Distance cutoffs used to identify bonds for molecule recognition, length in Angstroms	60

LIST OF FIGURES

Figure	Page
2.1 Example local property calculation on a shock compressed sample of RDX. The entire sample moves toward a fixed piston. This velocity must be subtracted from each grid volume (shown in blue) before a temperature can be calculated.	15
2.2 Example local temperature calculation on a shock compressed sample of RDX after grid velocities have been subtracted. Local temperatures show hot spots around the collapsed pore.	16
2.3 Example spectral analysis on a sample HMX crystal at 300K and 1atm pressure using the ReaxFF force field. Vertical offset of the power spectrum of each element is done only for clarity.	19
2.4 Resultant vibrational density of states for a continuous sine wave versus one that has been stitched from multiple smaller segments.	21
3.1 Adapted schematic from Zewail J. Phys. Chem. A 2000 , 104, 5660-5694 highlighting the relevant timescales for chemical dynamics. The reaction timescale is placed such that a statistical reaction is expected, but these reaction times are variable based on the temperature, pressure and material of interest.	25
3.2 Adapted schematics from Bunker and Hase J. Chem. Phys. 1973 , 59 (9), 4621-4632 showing possible phase space trajectories (at constant energy) for different A) statistical or B)-D) non-statistical interpretations. . . .	27
3.3 Calculated power spectrum per molecule from MD at 300 K and 1 atm for (A) nitromethane, (B) HMX, and (C) PETN using Equation 2.6. The vertical offset is for visual clarity. Panels (D)-(F) contain the predicted infrared spectrum of the respective vertically aligned material, with colored arrows indicating the frequency of vibrational insults used in this study. Atom colors correspond to carbon (gray), hydrogen (white), oxygen (red), and nitrogen (blue).	33
3.4 Typical simulation of HMX decomposition due to a constant heating of the system via a Nose-Hoover thermostat at a rate of 50 K/ps. Chemical species information in (A) and dynamic vibrational density of states in (B) share a common axis which is the temperature of the system. . . .	36

Figure	Page
3.5 Example temperature versus time curves for all insults tested in NM. Each has a heating rate recorded near 50K/ps at the time of one-third decomposed	38
3.6 Relative kinetic energy content for each subset of vibrations for an electric field coupled to the CH Stretch vibration in A) NM B) HMX and C) PETN. The series in brown for each panel is the frequency range that contains the insult. A value of one for the normalized kinetic energy content is that of equipartition.	40
3.7 Two temperature plots of target mode temperature versus bulk temperature during an electric field insult as calculated in Equation 2.7. Each data point is 1 ps apart. Panels (A)(C) are the CH stretch modes in each material, respectively, (D)(F) the NO stretch mode, and (G)(I) are low-frequency intramolecular modes that are unique to each molecules geometry. Color matched arrows indicate the first chemical reaction for each insult, and the equilibrium reactions are indicated in black. The nonequilibrium distribution of energy among vibrations is clearly seen as data points lying above the solid black equipartition line ($T_{mode} = T_{bulk}$). . .	42
3.8 Observed reaction rates under equilibrium conditions for (A) NM, (C) HMX, and (E) PETN. Each data series is heated at a constant rate using a Nose-Hoover thermostat. Using the procedure outlined here, activation energies obtained from fitting Equation 3.2 are plotted against the reaction progress for (B) NM, (D) HMX, and (F) PETN, respectively.	44
3.9 Nitromethane reaction rates obtained from simulations of electric field induced decomposition for the intramolecular modes at (A) $651cm^{-1}$ and (C) $1913cm^{-1}$; see the body of the text in this section for mode assignments. The fits to Equation 3.2 yield the activation energies plotted in panels (B) for the mode at $651cm^{-1}$ and (D) for the mode at $1913cm^{-1}$	47
3.10 PETN reaction rates obtained from simulations of electric field induced decomposition for the intramolecular modes at (A) $1266cm^{-1}$ and (C) $799cm^{-1}$. The fits to Equation 3.2 yield the activation energies plotted in panels (B) for the mode at $1266cm^{-1}$ and (D) the mode at $799cm^{-1}$. Both target modes show clear insult strength dependence as seen by lower activation energies at high insult strengths and early reaction progress.	48
3.11 Observed bulk temperature at a fixed one-third decomposition for (A) NM, (B) HMX, and (C) PETN, where each point is averaged over ten independent simulations at the same insult strength. Equilibrium decomposition is denoted by the direct heating data series in orange diamonds in all panels.	50

Figure	Page
3.12 Populations of RDX over time at different densities calculated using the ReaxFF bond orders a) and b) RDX populations calculated using atomic distances. Each system is heated to 1500K in the NVE ensemble. . . .	60
3.13 Maps of T_{CoM} and T_{Vib} , as well as molecular populations for RDX, intermediates and products at key stages in the shock to deflagration transition. t_0 corresponds to $t = 17.3ps$ after impact with the piston.	63
3.14 Area percent of material above a preset ignition temperature of 1700K for all pore sizes studied. Note the quenching of voids smaller than 40 nm. Raw simulation time is used here rather than the shifted reference as used in Figure 3.13	65
3.15 Profiles of T_{CoM} and T_{Vib} (left axis), and molecular populations of RDX, intermediates and products (right axes) at key stages in the shock to deflagration transition. Time is measured from void collapse (17.3 ps after impact)	66
3.16 Example time snapshots of the intermediate and product molecules formed after the collapse of a 40nm void in RDX. The narrow reaction front that forms includes molecules from the entire reaction path of RDX decomposition.	67
3.17 T_{CoM} and T_{Vib} of RDX molecules at the time of their decomposition, and those of intermediates and products at the time of their formation: (a) 20 nm void; (b) 40 nm void.	69
3.18 Initial and final states of the (a) dynamic hot spot formed following pore collapse, (b) crescent shaped thermal hot spot initially at 2000 K, (c) cylindrically shaped hot spot heated to 2000 K, and (d) cylindrical hot spot with an inner disc heated to 2000 K and the outer ring heated to 1000K.	70
3.19 Chemistry evolution following shock and thermal initiation. Insets show an expanded view of events within the first 10 ps.	71
4.1 Example snapshots of the simulation cell as the PBX is formed. A) Initial structures with HMX to the left and Teflon to the right. B) While the surface HMX is heated to 900K it vaporizes and forms an amorphous layer as the two systems are pressed together. C) Final structure with the Teflon layer removed and D) with all components shown, scale bar is 1nm. . .	80
4.2 Stress-strain curves of tensile loading for the PBX with an A) Roughened or B) Planar Interface, arrows indicate when the snapshots shown in C) and D) are taken, respectively. Qualitatively, the interface properties did not affect the overall mechanical failure.	82

Figure	Page
4.3 Observed heating rates of PBX structures subjected to a longitudinal polarized acoustic wave; the rate is normalized by the period of the oscillation to bias against increased energy deposition rates at high frequencies. The pair of plots shown in A) and C) correspond to the planar interface case while panels B) and D) are the observed heating rates, broken down by region in the sample, for the roughened interface. The the low frequency regime is shown in C) and D).	84
4.4 At a fixed overall temperature of 400K and driving frequency of 375GHz, the local temperatures vary based on which component is coupled to the acoustic insult. The diffuse (roughened) and sharp (planar) interfaces result in different widths of the localized energy, this is largely due to differences in thermal conductivity through these interfaces.	85
4.5 Observed heating rates of PBX structures subjected to a transverse polarized acoustic wave, this rate is normalized by the period of the oscillation to bias against increased energy deposition rates at high frequencies. The pair of plots shown in A) and C) correspond to the planar interface case while panels B) and D) are the observed heating rates, broken down by region in the sample, for the roughened interface. A close of up of the low frequency regime is shown in C) and D).	87
4.6 Stress-strain histories for PBX structures with a planar interface under shear polarized waves of various frequencies. The A), C) and E) panels show the density of points at each stress and strain value throughout the entire simulated time. The color axis in the right panels represents the overall temperature of the simulation cell. The frequencies shown here correspond to insults that are A),B) below the structural resonance, C),D) in close proximity to resonance and E),F) at frequencies much higher than resonance.	89
4.7 Stress-strain histories for PBX structures with a roughened interface under shear polarized wave of various frequencies. The A), C) and E) panels show the density of points at each stress and strain value throughout the entire simulated time. The color axis in the right panels represents the overall temperature of the simulation cell. The frequencies shown here correspond to insults that are A),B) below the structural resonance, C),D) in close proximity to resonance and E),F) at frequencies much higher than resonance.	90

Figure	Page
5.1 A), C) Representative orthoscopic views of the [100] crystallographic direction for PETN and ammonium nitrate. Panels B), D) show the [010] direction in either material, which exemplifies the unique molecule arrangement in either direction. E) Perspective view of the simulation domain showing how the free surface is created in MD, perpendicular to this free surface is the propagation direction of both applied and emitted fields. This simulation setup enables realistic absorption and emission polarizations within MD. Atom colors correspond to carbon (grey), hydrogen (white), oxygen (red) and nitrogen (blue).	98
5.2 A) Two example Gaussian electric field pulses with different carrier frequencies applied in PETN. Absorption is measured as the difference between the total energy after and before the pulse is applied. B) Absorbance (normalized by the peak value for each polarization), as a function of the input carrier frequency and input polarization, for PETN (red) and AN IV (blue). The unique molecule geometry in each direction leads to polarization-dependent absorbance.	99
5.3 ReaxFF calculated power spectrum for A) PETN and B) AN at 50 K and 1 atm of pressure. These spectra aid in analyzing the radiated electric field signals shown in the Results section. The sum of all element contributions normalized by total kinetic energy yields the vibrational density of states.	100
5.4 Emission signals from PETN along the [100] (x direction) for electric field pulses applied in the A) [100] and B) [010] directions. Complementary emission signals, with pulses along the [010] (y direction) for the C) [100] and D) [010] applied field directions in PETN. Where the emission signals are aligned with the pulse polarization, Rayleigh scattering dominates the observed emission. Perpendicular directions do show emission at unique frequencies different from the applied pulse, confirming the frequency conversion due to internal scattering.	102
5.5 Emission signals from AN along the [100] (x direction) for electric field pulses applied in the A) [100] and B) [010] directions. Complementary emission signals with pulses along the [010] (y direction) for the C) [100] and D) [010] applied field directions in AN. Third harmonic emission is clearly seen for parallel emission directions to the applied field and is much weaker in orthogonal directions.	103
5.6 Average emission signals for all output polarizations for impulses applied in the [100] direction for A) PETN and D) AN, along with field pulses in the orthogonal, [010] direction in panels B) and E). Total emission signals for all absorption and exit polarizations for C) PETN and F) AN.	105

ABSTRACT

Wood, Mitchell A. PhD, Purdue University, May 2016. Energy Transfer and Localization in Molecular Crystals. Major Professor: Alejandro Strachan.

With the aim of developing new technologies for the detection and defeat of energetic materials, this collection of work was focused on using simulations to characterize materials at extremes of temperature, pressure and radiation. Each branch of the work here is collected by which material response is potentially used as the detectable signal.

Where the chemical response is of interest, this work will explore the possibility of non-statistical chemical reactions in condensed-phase energetic materials via reactive molecular dynamics (MD) simulations. We characterize the response of three unique high energy density molecular crystals to different means of energy input: electric fields of various frequencies ($100 - 4000\text{cm}^{-1}$) and strengths, and direct heating at various rates. It was found that non-equilibrium states can be created for short timescales when the energy input targets specific vibrations through the electric fields, and that equilibration eventually occurs even when the insults remain present. Interestingly, for strong fields these relaxation timescales are comparable to those of the initial chemical decomposition of the molecules. On similar timescales, we have studied the relaxation process of shock compressed molecules. Details of how energy localization, either from these vibrational or mechanical insults, affects the preferred uni- or multi-molecular reactions are discussed. These results provide insight into non-equilibrium or coherent initiation of chemistry in the condensed phase that would be of interest in fields ranging from catalysis to explosives.

Without initiating reactions, the thermal response of a material subject to a mechanical stimulus can be used to inform on the chemical characteristics. Here MD

simulations are performed to study how energy from an acoustic wave is localized in a composite material of a polymer and molecular crystal. Insight is provided on how the interface between these two materials will affect which component absorbs and localizes this insult energy. Furthermore these results provide an explanation to anomalous experimental results that subject similar composites to acoustic insults.

In parallel efforts for the detection and defeat of explosives, we study the scattering of electromagnetic waves in anisotropic energetic materials. Nonlinear light-matter interactions in molecular crystals result in frequency-conversion and polarization changes. Applied electromagnetic fields of moderate intensity can induce these nonlinear effects without triggering chemical decomposition, offering a mechanism for non-ionizing identification of explosives. We use molecular dynamics simulations to compute such two-dimensional THz spectra for planar slabs made of PETN and ammonium nitrate. We discuss third-harmonic generation and polarization-conversion processes in such materials. These observed far-field spectral features of the reflected or transmitted light may serve as an alternative tool for stand-off explosive detection.

CHAPTER 1. INTRODUCTION

This initial introduction will serve as a backdrop, or perspective, on the work collected here, the technical merit will be supplied in the introduction and discussions in each of the research chapters in the body of this text. It seems necessary to provide the themes of this research up front because this collection of work will span seemingly disparate applications with only the material system as the common feature. Rather than telling the story strictly chronologically, an attempt is made to reorder and present the work in a way that best fits the theme of the title. Parallel with these scientific themes, this work is enabled by significant advances in high performance computing in recent years and it is worth discussing the results show here in this context as well.

In general, this thesis is concerned with the process of energy absorption by chemically reactive materials, and the governing relaxation processes that bring the system back to equilibrium. This is then a study of the transient excited states that a material exhibits as it interacts with its external environment; the aim here is to assess the changes in material properties as a function of which excited states are realized. [1, 2] This topic has an enormous number of known and potential areas of application as scientists and engineers push the boundaries of what sort of environments a material can withstand. Those who study any sort of high rate phenomena, such as shock physics, photonics, electronics, *etc.*, need to be concerned with the excited state properties of the given material. For example, in the same way that a martensite phase behaves much differently than the equilibrium phase of the metal, these transient excited states of a material offer a unique perspective to study materials. A fundamental understanding of the topic of energy transfer is applicable in all of physics and chemistry, and to date significant progress has been made experimentally,

theoretically and computationally. [3, 4] One of the common themes throughout the work collected here has to do with the critical timescales for the absorption of energy from the environment and subsequent relaxation processes, and how it will affect the response of the material. Interestingly, the decay times of these non-equilibrium states are both material specific and sensitive to the absorbing degrees of freedom. [5] This provides an even larger test bed to study these non-equilibrium states. Many of the unique observations that will be shown are enabled by the ability of simulation tools to compress or dilate relevant timescales which would prove to be experimentally challenging (or impossible) given current technologies. [6, 7]

By using computer simulations, a greater degree of control over the external stimuli can be achieved(not to mention superb reproducibility), which simplifies the analysis of the true nature of the physics at play. This external stimulus can be thermal, mechanical, or electromagnetic just to name a few energy input types. Depending on the means of energy input to the material, usually only a small number of degrees of freedom are capable of coupling to the external stimulus. While the stimulus is present, the coupled modes will carry more than the equipartition of energy that is observed in equilibrium; these are denoted as non-equilibrium states of the system. To predict how a given material would respond to an external stimulus, the first, and most logical, way to proceed is to consider a perturbation that modifies the normal equilibrium behavior. Statistical mechanics provides the mathematical framework for such a prediction, but is restricted to measurements made in equilibrium for an ensemble of particles. This measurement, made assuming the system is close to equilibrium, is a good assumption for state processes that only care about the final (or difference between initial and final) states of the system. [8] However, if the measured quantity is determined by the path which the system follows from initial and final state, the prediction becomes increasingly complex.

For the topic outlined above, the choice of material to study is equally as important as the computational methods that enable this work. Ideally, the material of interest has a rich variety of mechanical, thermal and chemical behavior that can be

elucidated by multiple energy input types. In addition, the transient non-equilibrium states need to survive long enough that they can be studied relative to the material response that is of interest. Again, the theme of relative timescales emerges here in material selection as well. [1] The emphasis on a variety of chemical responses narrows the search significantly toward organic materials that are multi-element in nature. Molecular solvents, however, are largely uninteresting when it comes to their thermal and mechanical properties. Therefore, molecular crystals are then an ideal choice that exhibits each of the aforementioned material responses. Further detail on this material selection will be highlighted as it applies to the energy input and response pair in the latter chapters of this work. Energetic materials are a special class of molecular crystals that have had their thermo-mechanical properties well characterized over the past few decades. [9] These well characterized energetic materials will be the primary focus of this work, but now are being looked at in a new perspective, which aims to contrast the well known equilibrium behavior with that of the non-equilibrium or excited state dynamics.

The work collected here is organized into chapters by subset of the overall material response of interest, with the goal of determining its' sensitivity to the means of energy input to the system. In each of these chapters, how a material selectively absorbs energy from the external stimuli, and the rapid processes by which that energy is redistributed throughout the system, is discussed. How the observed response differs from the equilibrium dynamics will accompany each of the presented data sets for each external stimuli. The remainder of this work is organized as follows. Chapter 2 is devoted to the computational methods that underpin all of the work displayed here; the focus will be on the advantages as well as the assumptions made with the simulation methods used here. Accompanying the discussion of simulation methods is a background for the common analysis techniques used to extract meaningful observations from the wealth of available simulation data. Subsequently, Chapter 3 will collect a pair of research topics that study the chemical response of energetic materials subject to either an electromagnetic or mechanical energy input. Additional

background and literature review on the topics of reaction kinetics, vibrational energy relaxation and the shock to detonation transition are given in Chapter 3. The research collected in Chapter 4 focuses on the localization of mechanical energy as thermal hot spots in a composite material and includes a review of the relevant literature. Next, Chapter 5 covers the electromagnetic response of an energetic material subject to intense light pulses in the THz range. The discussion and literature review in this chapter will be focused on the potential applications of this work to the standoff detection of explosives. Finally, concluding remarks about this work and its potential future applications is discussed in Chapter 6.

CHAPTER 2. COMPUTATIONAL METHODS

It is interesting to think about the characteristics of a scientist through time. A few hundred years ago, it was common to be proficient in both experimental and theoretical techniques of discovery. Onward, an ever increasing need for specialization has made scientists experts of either experimental or theoretical technique, that is until recently. The advent of computers and fast parallel algorithms has brought on a new mode of research that has a flavor of both the experimental and theoretical efforts. Consider now the vast number of possible experiments that can be preformed where no other piece of equipment is accurate enough or where equations can be solved faster and more precisely than any human can offer. What could you design and test for this virtual lab? Given the enormous possibilities, scientists are more often making use of virtual experiments to bolster existing experimental and theoretical efforts. Even more interesting is the number of new fields of scientific study that have spawned from this technology, not to mention the simultaneous economic impact. This chapter will, of course, not be able to cover all of these aspects of computational work. Rather, the focus will be on the usage and impact in material science, which has been a pillar of computational experiments for many decades.

2.1 Introduction

One of the key insights into the field of computational material science has to be the acknowledgment of the wide variety of modeling and simulation tools available to this one particular field of study. One way to argue how useful computation has become in the engineering world is to display the vast number of available and supported software for virtual experiments across nearly all length and time scales. Highlights of this toolkit include new material discovery using ab initio electronic

structure codes [10] as well as product design and validation for well established engineering problems [11–13].

One of the long standing problems, however, is an efficient and intuitive way to link multiple computational tools together. This is what is known as multi-scale modeling and it has become commonplace in the engineering research landscape. There are practical limitations on the uses of multi-scale modeling, largely due to the lack of transferability of the method between specific applications. For example, a finite element model(FEM), which normally computes material properties at the micro- to millimeter scales, could benefit from detailed atomistic simulations at areas of large deformation in the structure. [14] But, when these fine scale simulations are launched and how the information is communicated to modify the FEM is a significant challenge. This and other multi-scale modeling efforts often boil down to a problem of work balancing between each of the tools used. Making proper use of true multi-scale modeling has been a focus of this nation’s government in order to ensure competitiveness at the global scale when it comes to innovation. [15, 16] This is because integrating modeling and simulation into the engineering design loop has the promise to shorten the times between concept and commercial impact. Furthermore, the resources expended per experiment is far lower with these computational tools, which cuts out plenty of wasted trial-and-error loops. Modeling and simulation tools are finding impact beyond what has direct economic impact as well. In publishing of research, there has been a push by high impact journals to field and print multi-disciplinary work, which now means two or more experiment, theory and computational contributions are sought after. [17] This, of course, is not too surprising: if there is already an external validation on the work, it decreases the workload of the peer reviewers. Although it is not common practice currently, there is hope that published computational research will be supplemented with a level of detail that the exact same results can be produced by the readers. The obvious advantage is the transparency of reporting results, thereby accelerating further research efforts. [18–20] This transferability of results is unlike any other mode of research.

To augment this style of reporting, some institutions are actually providing the necessary computational resources for free as part of a cloud computing effort. [21,22] The availability (and justified use of taxpayer dollars) of such a cloud computing service begs the obvious question of why can't this work be carried out using commercially available computers? This, however, is a question regarding the scale of research computing versus what is common to a personal laptop machine. The ever evolving buzzword that has been alluded to thus far is High Performance Computing (HPC). A breakdown of the essential components of HPC would yield three major themes; theory/methods, algorithms and hardware. This triplet is highly interdependent, and which problems are available for researchers to explore will be controlled by the hardware and algorithms of that era. As a prime example, Section 3.4 will cover a problem that was revisited after ten years of hardware and algorithm development, with the availability to reveal new physics of energetic materials and detonation. Efforts into improving hardware have been advancing at a much faster pace than the other two and, as such, have dictated what research is performed at the extreme scales of computing. Although not an exhaustive list, these improvements include: higher transistor densities, multi-threaded central processing units (CPUs), and the fast processing but communication limited graphics processing units (GPUs). For the emerging needs of computationalists, and bragging rights of owning the most powerful computer, universities and national labs across the world have been building massive computing centers that incorporate these hardware developments. [23] Model and simulation forms that take advantage of parallel computation are commonplace on these supercomputers; molecular dynamics(MD) is one such example. In order to forcibly focus the remainder of this section, a sole discussion MD and its' impact in materials science will be undertaken. The reader is directed to the following references if they are looking for more information on electronic structure [24–27] meso-scale modeling [14, 28–30] or device level modeling [13, 31]. All of these tools have their foothold in materials science but address vastly different length and time scales that will be discussed further.

2.2 Atomistic Simulation Tools

Many of the macroscopic properties of materials that are familiar to all can be understood as extrapolations of interatomic interactions at the nanoscale. Given the symmetry and types of bonds in a crystal, much of the mechanical, electrical and thermal information of a material can be inferred. Therefore, it should not come as a surprise that significant effort has been made to develop simulation tools that concern themselves with the dynamics of atoms. When the collection of atoms are treated using classical mechanics, meaning they strictly obey Newton's equations of motion, these simulations are known as molecular dynamics (MD). To study the motion of atoms, these codes will solve $F = ma$ for all atoms in the system. Each force can be calculated as the gradient of some potential energy, i.e. $-\nabla U = m\ddot{x}(t)$, and the model forms of this potential energy surface, also known as the interatomic potential(IAP), are the leading approximations in MD. To obtain the positions and velocities of atoms at a later time, this equation is integrated in time by taking small time steps to alternate when the positions or velocities are updated. There are several approaches to integrate the equations of motion [32,33] but the most common is the Verlet algorithm, which is used here. In order for these simulations to accurately integrate the equations of motion (think of a Riemann sum), very small time steps must be taken which are on the order of femtoseconds. This inevitably limits the amount of time that the atomistic dynamics can be studied: nanosecond length simulations are common, but in rare cases micro- and mili- second MD runs are possible [34]. However, the extremely high spatial (Angstrom) and temporal (femtosecond) resolution make MD ideal for the study of materials in extreme conditions. Furthermore, MD has benefited greatly from the HPC push due to its impressive parallel computing efficiency. This efficiency is because each force calculation can be spatially decomposed based on which atoms form a short ranged neighborhood, allowing for each processor to manage a different location in the MD simulation. To the end user of a MD code, this means

as the computer scales so can the size of the simulation domain. This is rarely the case with other computational tools without special programming tricks. [35]

There are a number of impressive uses of MD to date, and these have not been restricted to just materials science. For any system that can be treated classically, it is the ideal tool to gain mechanistic insight at the atomic scale. Examples of high impact MD work outside of materials science include detailed information about the conformation dynamics [36] and enzymatic activity of proteins in solution [37], the structure of nucleic acids [38] and self-assembly of molecules on surfaces [39]. In many of these cases, MD work is used to motivate future experimental work which exemplifies the usefulness of such a computational tool. Other aspects of MD research are the background developments to allow for more accurate simulations. In large part, these advancements have used one key approximation, that the interatomic potential made more realistic, thus can capture more detailed physics. For example, consider an interatomic potential that describes a simple molecule like benzene. As an initial guess, one can assume each bond that forms the molecule has a harmonic potential with the stiffness and equilibrium distance tuned individually. There are a number of widely used IAP that use this formalism [40–42] and some software that can automatically generate these harmonic potentials for arbitrary molecules [43]. Calculation of these harmonic bonds are relatively inexpensive; Chapter 4.2 covers one such potential used for a polymer/molecular crystal composite material. These IAP have a glaring weakness, which is that the bonds that are defined as the initial state of the simulation can never break, because the harmonic energy term diverges at large separation distances. Therefore, any IAP of this type is severely limited in what chemical properties can be studied. A majority of the work collected here will be concerned with the effects arising from anharmonic potential energy surfaces as well as chemical reactions in the condensed phase. As such, a detailed discussion of these ‘*chemistry enabled*’ IAP and a perspective on their development and future directions will be the focus of the next section.

2.2.1 Reactive Molecular Dynamics

Rather than predetermining the bonded atoms, these reactive IAP (commonly called force fields) need to be able to dynamically recognize atoms that should be bonded to one another. This could be achieved simply by setting a cut off distance beyond which atoms cannot bond, but another requirement of the potential energy function is that the energy is a smooth function, meaning its derivative (force) is not discontinuous. A discontinuous force curve would cause unphysical dynamics of atoms and would ruin the credibility of the simulation. Therefore, using an IAP that captures both the details of the reactants, products and the transition states between is key for the stability of the simulation. Although reactive MD is typically thought of for organic chemistry, the same effect in metals is achieved by formulating the potential energy in such a way that includes environment or density dependent terms. Examples of these metallic IAP include the Embedded Atom Method [44, 45], electron Force Field [46] and Gaussian Approximation Potentials [47–49]. Some of these metallic IAP actually include angle dependent potential energies which makes them more akin to the molecular reactive potentials than the simple pair-wise potentials like Lenard-Jones or Morse potentials. Returning to organic systems, much of the early work using reactive IAP surrounded chemical reactions that occurred at MD timescale, namely propellants and explosives. Advancements in accelerated MD has allowed for the study of ‘slow’ chemical reactions, but none of these techniques are employed in this work. The reader is directed to the works of Voter, Chen, Germann and others for these methods of accelerated MD. [50] Physically, the hybridization of molecular orbitals and increased overlap of electrons from bonded atoms results in stronger bonds. [51, 52] For computational convenience, it is easier to calculate an order parameter of the bond rather than the details of the electronic states. These are known, unsurprisingly, as bond orders (BO), and differs for each atom pair. Therefore, energies and forces in MD can be dependent on these BO, which permits adding more physical rules on when a bond order should increase or decrease. For exam-

ple, rules about covalency and which atom pairs form double or triple bonds can be built into the calculation of the BO. [53, 54] The set of rules for how bond orders are calculated and the training geometries from ab initio calculations for a set of element types is what is called a parameterization. Somewhat of an art form, creating a parameterization is a difficult balance between how many training structures are supplied, how to weight the relative importance of each structure and of course the challenges that arise from a many-dimensional optimization problem. Early parameterizations contained few elements, in order to restrict the number of reaction paths need to train against. Several attempts have been made to automate this process but the most reliable parameterizations were generated by a handful of expert users. The use of partial bond orders to construct IAP capable of describing chemical reactions was pioneered by Tersoff [55]. Thereafter, more and more researchers have been attracted to BO potentials due to the predictive power that a flexible chemical environment affords. Now, since bonds do not need to be predetermined, the user only needs to supply the initial positions of the atoms to begin a simulation. Some of the early applications of these potentials were on detonation in model systems with simple and, importantly, fast chemistry [56–59]. Tersoff style potentials have been developed for a number of semiconducting materials and remain widely in use today by researchers. [60, 61] Following the enormous push of research into graphene and other carbon nanostructures, some reactive IAP have focused their parameterizations to accurately predict mechanical and thermal properties of these systems [41, 62].

Fitting back into the aforementioned interplay between hardware and simulation capability, the use of reactive IAP necessitates a much larger allocation of memory per atom than a normal MD simulation and, as such, these potentials were scarcely used until hardware limitations were lifted. [63–66] These memory restrictions stem from the need to calculate and store bond orders for every atom pair that depend on local configurations of nearby atoms. A new and very recent chapter in this coupled growth of simulation capability is anchored by the ability to employ GPUs running in tandem to CPUs. [67, 68] Certain aspects unique to reactive IAP can be ported to

the faster computing GPUs, which in turn opens up new physics that can be explored at longer timescales.

The most versatile reactive IAP, in terms of the usage and available parameterizations, has been ReaxFF, which was proposed by Goddard and van Duin in 2001. [53] With the exception of the work in Chapter 4.2 (which is not interested in chemical reactions), the entirety of the work collected here uses the ReaxFF IAP. In addition to being a flexible bond order potential, ReaxFF builds off work done by Rappe and Goddard that allows for charges on atoms to move with respect to the chemical environment. [69, 70] Although the charge is localized on the atoms' nucleus, which is an obvious approximation, the ReaxFF force field is polarizable given the inclusion of this charge equilibration scheme. Researchers have been employing ReaxFF in applications ranging from hydrocarbon combustion [71], catalysis [72, 73], biological processes [74], batteries [75], zeolites [76], energetic materials [77, 78] and nanoelectronics [79, 80] to name a few. While the number of ReaxFF parameterizations grows, each is not completely transferable. This means that the same element basis cannot accurately describe all the materials (or molecules) that can be formed. For example, a force field containing carbon, hydrogen, nitrogen and oxygen that best suits propellants and explosives may be terrible at describing the structure of proteins with the same constituents. For that reason, ReaxFF force fields are divided into branches based on their intended purpose. A listing of these is available via the web. Lastly, ReaxFF has shown to be amenable to the extreme scales of computation with a very high parallel efficiency within the LAMMPS molecular dynamics package. [35, 81] Although ReaxFF is a more cumbersome IAP than other many body potentials, its efficient parallel computation allows for simulation sizes of many millions of atoms for nanosecond time periods.

Despite the tremendous progress in the last 20 years and the science that has been enabled, reactive IAP are not without limitations. For example, electronic processes such as metallization or dielectric breakdown cannot be captured directly. In addition, as mentioned before, the force fields can provide inaccurate results for con-

ditions away from those used during training. Identifying the bounds on this are up to the researcher, not the parameterization developer. Spurious predictions can arise from excessively high temperature and pressure states of the material which can induce drastic changes in bonding characteristics. Electronic properties can completely change at high pressures; therefore, it is reasonable to assume that a force field that is parameterized for ground state electronic behavior will not capture, for example, the insulator to metallic transition in silica [82, 83]. Some researchers have tried to include electronic excitations in MD by having multiple force fields (for each excited state) calculated per timestep and their forces are recombined given some occupancy probability. [84–88] These approaches are not widely used due to their recent invention and the excessive training needed for each of the excited state potential energy surfaces. While not always critical under detonating conditions in typical molecular energetics, electronic transitions and excited states are critical in many planetary or geological applications, where electronic structure calculations are the only simulation option [82, 83, 89, 90]. Therefore, a careful balance must be struck between the types of simulations that fit the size and time restrictions to MD and the extreme conditions that may cause spurious results for the given parameterization.

2.2.2 General Analysis Techniques

While MD simulations provide an unprecedented length and time resolution for materials characterization, this wealth of data is overwhelming (and useless) without analysis tools to reduce the data into meaningful quantitative measurements. It is most common to reduce the raw output of positions, velocities and forces of each atom into thermodynamic quantities of interest such as the enthalpy, temperature and pressure, respectively. [91] For large simulations of dynamic phenomena, it is possible that the local response of the material will vary throughout the sample. An easy example to picture is a polycrystalline metal: the grain boundaries are chemically similar to the rest of the material, but their thermal and mechanical response will be much different than the bulk crystalline regions. These property impulses are

localized in space and time, but there are plenty of material responses that are delocalized in space and are periodic in time. Details of how to extract relevant local and spectroscopic properties from MD will be given using an example simulation of shock compression, which will be discussed in Section 3.4. Outlines for best practices and potential pitfalls will be given here and pseudo-codes for each method are attached as appendices.

When a MD simulation runs, it is much more computationally efficient to only calculate interatomic distances and forces for atoms that are known to be nearby versus checking every atoms' relative position. In the same sense, to process a large amount of spatially decomposed data the first step is to define grid volumes and assign atoms into them. Care must be taken to define grid volumes that are small enough to resolve small changes in local properties but include enough atoms that the property being calculated is well-converged. Usually, a few hundred atoms per grid volume is sufficient when calculating local densities, pressures or temperatures. Figure 2.1 shows a typical simulation cell used for a shock compression study; overlaid in the top left is an example grid that would be present throughout the cell.

To launch a shock wave, all of the atoms are given an additional velocity toward an infinitely massive piston (fixed in space), which is modeled here as a momentum mirror. From the conservation of momentum, atoms that come in contact with the wall will have the sign of their momentum reversed and thus the sample will begin to compress. As the material compresses, the sample has an inhomogeneous velocity distribution belonging to the center of mass translation of the cell as a whole. This velocity should not be considered in the temperature calculation and should be subtracted from each grid volume. For each grid volume this is simply defined as the mass weighted atomic velocities (v_i) of all atoms in the bin (N_g); this is given in Equation 2.1. Subtracting these translational motions from each grid volume makes the simulation cell at rest with respect to the traveling shock front.

$$v_g^{cm} = \frac{1}{\sum_j^{N_g} m_j} \sum_i^{N_g} m_i v_i \quad (2.1)$$

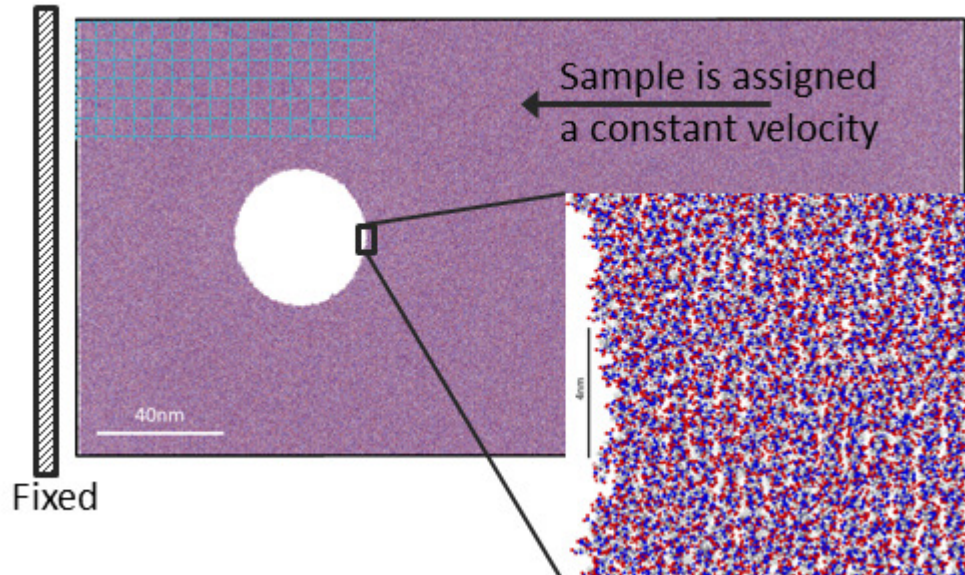


Figure 2.1. Example local property calculation on a shock compressed sample of RDX. The entire sample moves toward a fixed piston. This velocity must be subtracted from each grid volume (shown in blue) before a temperature can be calculated.

Following classical statistical mechanics, the temperature for the atoms inside any grid volume is given by equation 2.2. Each atomic velocity, v_i , is corrected by the grid velocity in which it resides, v_g^{cm} , and the summation runs again over all atoms in the grid cell. The prefactor in equation 2.2 comes from the equality of classical kinetic energy and equipartition of energy among $3N_g$ degrees of freedom.

$$T_g = \frac{2}{3N_g k_b} \sum_i^{N_g} m_i |v_i - v_g^{cm}|^2 \quad (2.2)$$

The resulting grid temperatures are shown in Figure 2.2 where now the uncompressed region shows no increase in temperature above the intended $300K$ even though it is moving at $2 \frac{km}{s}$ to the left.

In molecules it is common to distinguish where kinetic energy is localized between the translational and vibrational degrees of freedom. In other words, one would like to distinguish between the temperature associated with collisions between molecules and the temperature which would give rise to a unimolecular reaction. The

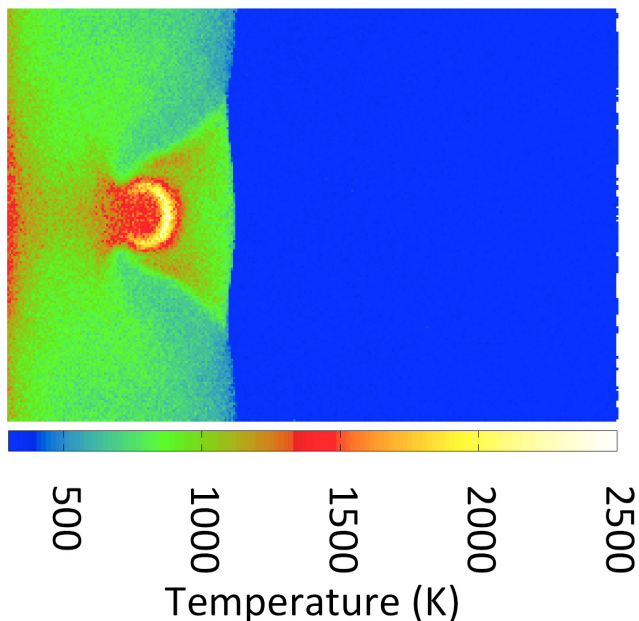


Figure 2.2. Example local temperature calculation on a shock compressed sample of RDX after grid velocities have been subtracted. Local temperatures show hot spots around the collapsed pore.

main challenge is identifying which atoms form a molecule in a way that is computationally efficient and robust with respect to the random fluctuations inherent to MD. Surprisingly, there are a large number of ways to uniquely define a molecule, and in large part has to do with the minimum interaction between atoms that constitutes a bond. One could argue, though rarely the case employed, that van der Waals interactions constitute a weak bond, thereby forming very large molecules. Several methods have been used in the literature that range from solely distance-based criterion [78], distances plus kinetic energy differences [92], bond orders [93] and molecular orbital overlap [94]. Regardless of the method used to identify bonds, a molecule can be quickly identified by its composition once all atoms in the bond network have been separated into unique clusters. This clustering method can be done by using a minimum spanning tree algorithm [95] that will search for unique atom atoms that are identified as bonded to any other atom in the growing cluster. A cluster is identified

as a molecule when no more unique atoms can be added to it. The drawback to this method is that no information on the molecule's conformation is retained. Because of this limitation, isomers of the same molecule would be recognized as the same, which, depending on the simulation needs, could prove problematic. Returning to the example simulation cell shown in Figure 2.1, the center of mass velocity of each identified molecule has to first be corrected by the motion of the grid volume it exists in.

$$v_K^{cm} = \frac{1}{M_K} \sum_{k \in K} m_k (v_k - v_g^{cm}) \quad (2.3)$$

This is given in Equation 2.3, where $M_K = \sum_{k \in K} m_k$ is the mass of molecule K made up of atoms k. Therefore, the center of mass temperature of each molecule is given by:

$$T_{cm} = \frac{2M_k}{3k_b} |v_K^{cm}|^2 \quad (2.4)$$

There is a complication in this analysis that arises when two adjacent grid volumes are moving at vastly different velocities. One can imagine that some molecules at the boundaries of these cells do not lie completely in one cell; then, the question arises which v_g^{cm} is used? For the shock work in Chapter 3.4, a weighted average of nearby cells of v_g^{cm} is used to correct for these artifacts, but in general the number of molecules affected by this is very small relative to the entire simulation. This center of mass temperature only encompasses three of the $3N_{mol}$ degrees of freedom available in the molecule, the remaining belonging to the intramolecular vibrations. To isolate the vibrational temperature, each atomic velocity is transformed into the reference frame of the molecule it belongs to by subtracting the corresponding center of mass velocity v_K^{cm} of the molecule.

$$T_{vib} = \frac{2}{3k_b(N_{mol} - 1)} \sum_{k \in K} m_k |v_k - v_K^{cm}|^2 \quad (2.5)$$

Equation 2.5 describes the vibrational temperature of each molecule K which is an indicator of the likelihood of a unimolecular reaction. In later sections, details of how chemical reactions evolve differently when $T_{cm} \neq T_{vib}$ will be discussed. It will be shown how these non-equilibrium reactions play a key role during shock compression. For small molecules ($N_{mol} < 5$), the number of vibrational degrees of freedom does not significantly outweigh the center of mass modes and, thus, the overall temperature is closer to an equal average of T_{cm} and T_{vib} . Conversely, the parent molecules shown in Figure 2.1 have sixty of the available sixty-three modes wrapped up in the vibrational components. Therefore, in some applications it is advantageous to further subdivide the T_{vib} into the kinetic energy per vibration, but this requires a change in analysis technique. Rather than using a single time snapshot one could look at the time series of velocities to understand what characteristic frequencies dominate the seemingly random noise. This can be achieved using a discrete Fourier Transform [96] of the individual atomic velocity trajectories; the resultant Fourier coefficients are proportional to the kinetic energy density. Collecting each of the Fourier coefficients, and normalizing by the overall kinetic energy, the result is known as the vibrational density of states, $P(\omega)$, as is given in Equation 2.6. Performing a Fourier transform on a discrete set of data versus a continuous function does involve certain approximations, which limit the frequency range and resolution. The inverse of the sampling rate, Δt , determines the uppermost frequency that can be identified and the number of discrete points n will limit the $\Delta\omega$ between points in $P(\omega)$.

$$P(\omega) = \frac{\tau}{Nk_bT} \sum_{j=1}^{3N} m_j \left(\sum_{n=0}^{N-1} v_j(n\Delta t) e^{-i2\pi\omega n\Delta t} \right)^2 \quad (2.6)$$

In order to capture all of the intramolecular vibrations, Δt should be larger than three femtoseconds and the length of the trajectory should be greater than twenty picoseconds for a well resolved density of states. These trajectory files do become exceedingly large quickly with this small of a sampling interval, so caution is needed when performing this sort of analysis. The outer sum in Equation 2.6 runs over all atoms in the system (after which the Fourier coefficients are averaged) which

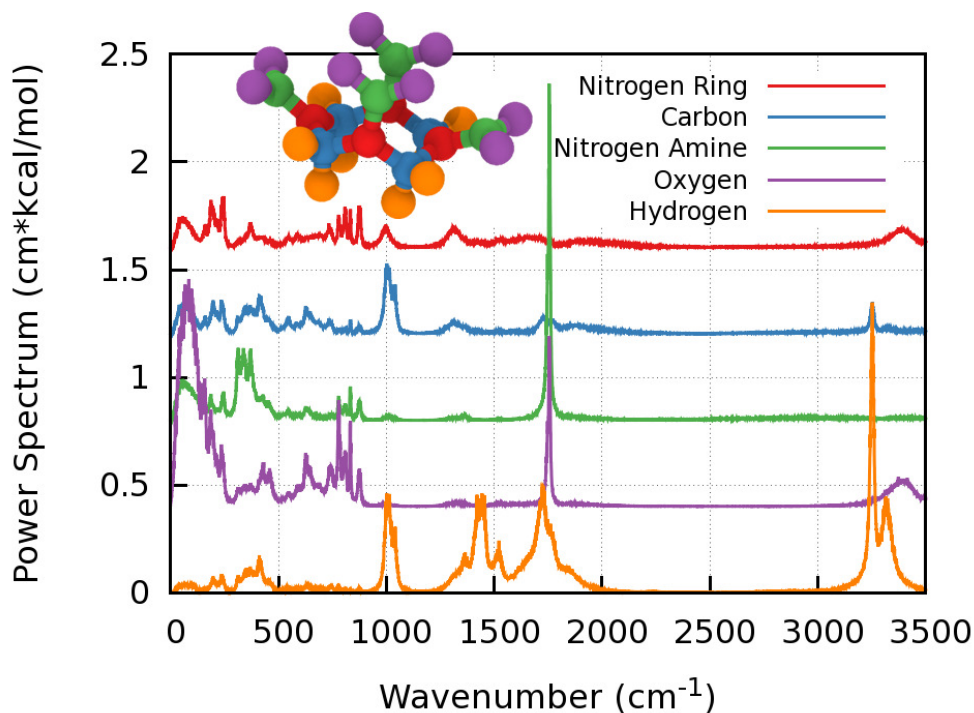


Figure 2.3. Example spectral analysis on a sample HMX crystal at 300K and 1atm pressure using the ReaxFF force field. Vertical offset of the power spectrum of each element is done only for clarity.

affords the possibility for the user to look the vibrational density of states (VDOS) for each element at a time. What this buys is the ability to assign peaks in $P(\omega)$ to experimentally known vibrations (Raman or IR) of the material based on which element types are contributing. In Figure 2.3, Equation 2.6 is applied to a HMX crystal, which is an energetic material similar to what is shown in Figure 2.1. Here, the overall power spectrum (un-normalized VDOS) is broken down by element type, which is more informative for interpreting what vibrational properties the force field predicts.

In the example shown in Figure 2.3, a simulation of many tens of picoseconds was needed, but studying dynamical changes in the VDOS that occur in smaller timescales would not be possible. To do so, one can imagine that a long velocity trajectory could be assembled by collecting an ensemble of smaller length trajectories.

Now, the advantage is that the time window that the spectrum represents is smaller, but there has not been a sacrifice on the frequency resolution. This method has been coined internally as ‘stitching’ a trajectory together, and the advantages are enormous when analyzing the effects of frequency localized insults as in Section 3.3. Certain artifacts arise in the resultant VDOS, since the trajectory has been stitched. These are exemplified by Figure 2.4. In this Figure, a simple sine wave with frequency set to 2000cm^{-1} is Fourier transformed (in blue) while the series in red has a random phase applied every 1ps . This random phase is the same effect as merging independent trajectories from multiple MD simulations. In effect, the peak positions are the same between these two trajectories, but the stitched trajectory has a noticeable width to it, while the unperturbed sine wave Fourier transforms into a delta function. As will be shown in later chapters, this artificial width to the vibrational peaks is inconsequential when a small integration window is used to analyze the temperature of each mode. However, this trick preserves the frequency resolution of a long continuous run while enabling users to dynamically study changes that result from chemical reactions.

An interesting result of calculating the power spectrum at small time intervals is the capability to assign a temperature to a specific group of vibrations. Consider a material in equilibrium at a temperature of T_0 : this implies that each vibration, or any subset of vibrations from ω_1 to ω_2 , is also at the same temperature. Now consider that there is a dynamic condition that makes the temperature of each of those vibrations different, but still the overall temperature is T_0 . One can assign the temperature to each group of vibrations by comparing the dynamic spectra to that of the equilibrium conditions on discrete frequency windows ω_1 to ω_2 , given in Equation 2.7.

$$T^{mode}(\omega_1, \omega_2) = T_0 \frac{\int_{\omega_1}^{\omega_2} P_{Dynamic}(\omega) d\omega}{\int_{\omega_1}^{\omega_2} P_{Equilibrium}(\omega) d\omega} \quad (2.7)$$

If the frequency ranges are chosen carefully, the inherent broadening from stitching trajectories (e.g. Figure 2.4) will not affect the calculated mode temperature. In Chapter 3.3, where energy is selectively input into intramolecular modes, this

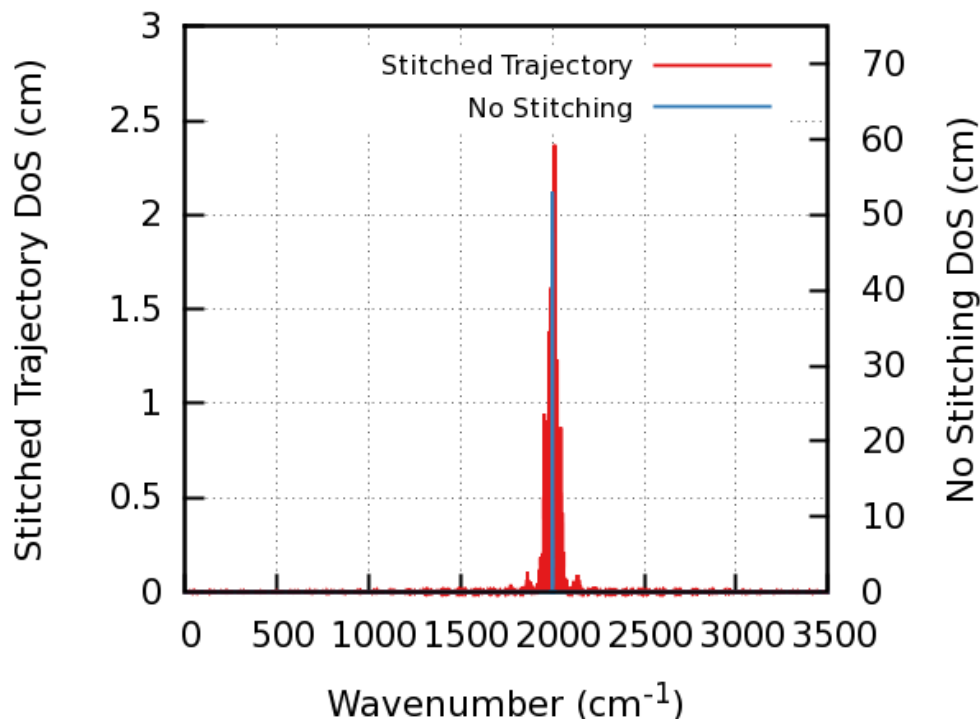


Figure 2.4. Resultant vibrational density of states for a continuous sine wave versus one that has been stitched from multiple smaller segments.

rapid calculation of the power spectrum will provide important information about the strength of the energy localization as well as the rates of dissipation into other vibrations.

Experimentally, the vibrational density of states is not directly accessible; rather, vibrations that are either Raman or IR active can be detected. It is important to know which vibrations are IR active because these will strongly absorb and emit light. From MD, one can calculate the IR response of a material by tracking the dipole moments of each atom. The obvious approximation here is that there is no charge distribution that is polarized to form a dipole moment when point charges are used. However, the coupled motion of these point charges gives rise to an IR moment that is easily calculated. More specifically, the autocorrelation function of each dipole derivative gives the time series of the IR signal. and the Fourier transform yields the

frequency space IR signal. [97] Equation 2.8 shows the details of this calculation. The inner sum is the autocorrelation function, and the outer is discrete Fourier transform, which uses the same nomenclature as Equation 2.6 where $\dot{M} = \sum_{j=1}^N q_j(i)v_j(i)$ with $q_j(i)$ and $v_j(i)$ representing the charge and velocity of atom j at sampling frame i .

$$I(\omega) = \frac{2\pi\omega}{3\hbar cn} (1 - e^{\frac{\hbar\omega}{k_b T}}) \sum_{n=0}^{N-1} e^{-i2\pi\omega n \Delta t} \left[\sum_{i=1}^{i-n} \frac{\dot{M}(i)\dot{M}(i+n)}{i-n} \right] \quad (2.8)$$

Most of the computation time for this IR calculation is spent on the autocorrelation function rather than the Fourier transform (only performed once); thus, is much faster than Equation 2.6. The same considerations for the sampling rate from the VDOS calculation should be considered here and, to obtain the best resolution, the limits of the autocorrelation should be set to $n = \frac{i}{2}$. In doing so, the auto-correlation function is calculated up to the first half of the trajectory, looking at correlations into the later half. Additional details of how these calculations are performed and how to optimize the run times will be supplied as an appendix to this document.

CHAPTER 3. CHEMICAL RESPONSE TO ENERGY INPUT

After a single introductory chemistry course it is easy to understand how the thermodynamic conditions (i.e. temperature, pressure, chemical potential) will affect the rate of a known chemical reaction. The underlying assumption that makes these predictions intuitive is one that is common to any statistical rate theory, namely that the reactants and products are always in thermodynamic equilibrium. Now this is a very good approximation for many scenarios because the timescales associated with a reaction are far longer than those that bring the system to equilibrium. In this chapter, a great deal of time will be spent exploring the outliers to this approximation, where thermal equilibrium is no longer guaranteed. First, an overview of statistical and non-statistical reaction rate theories will be put forth followed by two example cases where this idea of non-equilibrium chemistry has a strong foothold. By the end of this chapter, the hope is that the reader understands how common non-equilibrium chemistry is and its potential applications for external control of reactivity.

3.1 Introduction

Despite decades of progress, there is still a significant knowledge gap between chemical reaction rates that are derived from classical statistical mechanics and those from quantum mechanical treatments. These manifestations are often given the name non-statistical reactions and stem from the observation that energy in different forms has different efficacies in promoting a reaction. [98] Understanding and predicting which molecule geometries or which types of reactions will deviate from statistical reaction rates is considered as the ultimate goal here. Beyond the pure academic achievement of such a theory, progress in this area of research would provide a set of rules of how to externally control when reactions occur. More importantly, under-

standing how to best prepare a molecule for reaction could mean a lower energy cost for the same resultant reaction. This, in turn, has the potential for revolutionizing the way catalysts are designed, how energy or memory is stored, and for the work here, how threats from energetic materials can be safely detected. This effect goes by many names in the literature, such as state-selective or bond-selective chemistry [99–103], or non-equilibrium and non-statistical reactions [78, 104–107].

Clear examples of non-statistical chemistry range from chemisorbed methane [102] or water [108] on transition metal surfaces to many vibration-specific excitations of deuterated small molecules [101] that result in unsuspected decomposition rate changes. Recently, Viada *et al.* identified atmospheric photo-dissociation as another example where non-statistical reactions are the norm rather than the exception to the rule [109]. Additionally, low activation energy isomerization reactions have been repeatedly shown to behave non-statistically; these were heavily studied theoretically by Bunker and Hase [110–112] and computationally by Patra. [113]

In this chapter, the discussion will be tilted toward the language used in classical descriptions of molecules and reactions. Therefore, one can identify at any given time a single state (conformation, position, momenta etc.) of the molecule rather than a superposition of any number of allowed states. This gives way to a description of a phase space that has a recognizable division between reactant and products, with a select few points reserved for the transition states between them. A classical description also negates any tunneling to a reactant state, which would yield a reaction rate orders of magnitude faster than a classical trajectory. In addition, it also allows for a more straightforward approach to vibrational energy relaxation (VER), in which excitations are extinguished by energy exchange via molecular collisions or anharmonic scattering (vibrational overlap). Many of the examples of non-statistical reactions come from competing VER and reactions timescales, primarily where the former lags the latter. These competing timescales for VER and reaction are laid out in Figure 3.1 in an adaptation of results by Zewail and coworkers. [1] Below the arrow of time in this figure are the timescales of typical material responses for reference;

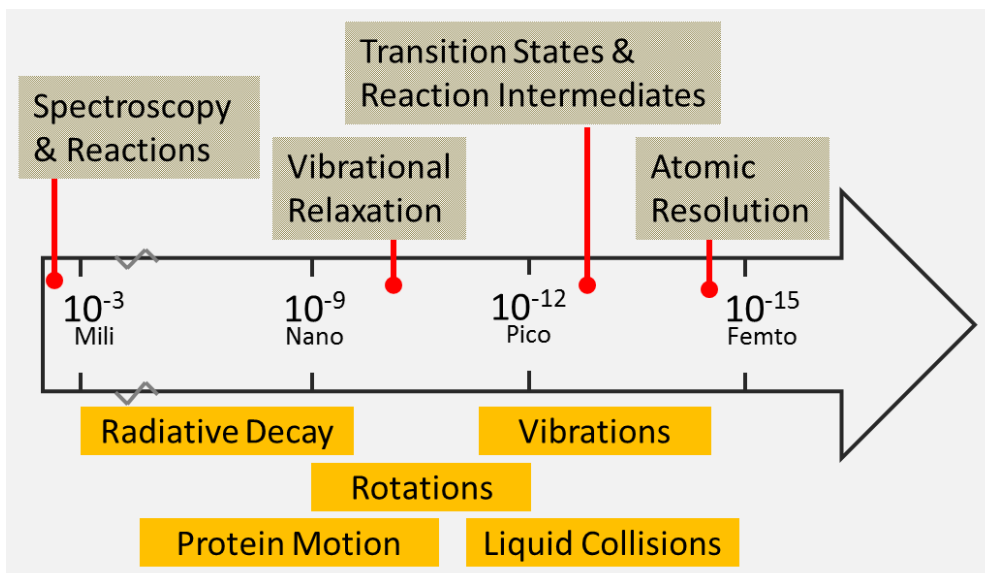


Figure 3.1. Adapted schematic from Zewail J. Phys. Chem. A **2000**, 104, 5660-5694 highlighting the relevant timescales for chemical dynamics. The reaction timescale is placed such that a statistical reaction is expected, but these reaction times are variable based on the temperature, pressure and material of interest.

note that individual vibrations occur much faster than the VER process that couples intramolecular modes together. In this figure, the reaction timescale is placed far to the right in the millisecond regime, but this of course is variable based on the material and thermodynamic conditions studied.

By comparison, the VER timescale is many orders of magnitude less than the reaction, therefore making the details of the relaxation process irrelevant to the reaction rate because the system has enough time to equilibrate and can be considered statistically. However, if the VER times are dilated (gas phase approximation) or the reactions occur much faster, now the possibility of a non-statistical reaction is increased. All the work collected in this thesis involves physical processes that fall close to the vibrational relaxation times shown in Figure 3.1

In the next section, a more detailed historical overview of the developing reaction rate theories is presented. This will provide the model descriptions for the subsequent

sections. The rate theories that are outlined here are mathematically built up and tested on systems with few degrees of freedom, which is no surprise. Unfortunately, the goal is to understand the deviations in the statistical rate laws for comparatively large systems, which makes this work unique to previous efforts. It is the opinion of the author that the simulation methods used here have great potential to shed new light on this very old problem.

3.2 Advances in Reaction Rate Theory

In a statistical reaction, like one that is depicted in Figure 3.1, to calculate the rate, one is only concerned with the number of states of the reactant that yield a product molecule. If you consider that all available states of the molecule at a fixed energy are equally probable (ergodic trajectory in phase space) then the population should decrease exponentially with time, as in Equation 3.1, when the energy is greater than the transition state energy. [114, 115] Where $D(E)$ is the number of number of states leading to a reaction and $\rho(E)$ is the density of states at energy E and $\alpha(t)$ is the population of the reactant.

$$\alpha(t) = \alpha(0)e^{\frac{-D(E)}{2\pi\hbar\rho(E)}} \quad (3.1)$$

This equation was borne out of the celebrated RRK and RRKM statistical theories which added a few key assumptions to transition state theory that explain the behavior of gas phase unimolecular reactions. [116–118] The basic principles of the RRKM (statistical) rate law are that collisions between molecules can produce an activated complex that is a saddle point between two energy minima, which correspond to the products and reactants. Furthermore, it is assumed that a single internal degree of freedom (vibration) is responsible for the reaction. While these statistical rate theories have provided a baseline prediction for experimental results, there have been several cases where non-RRKM behavior is the rule rather than the exception. For example, the work of Bunker and Hase [110, 111], in a tour de force, outlined several classes of reactions that would deviate from an accurate statistical reaction. In general, Bunker

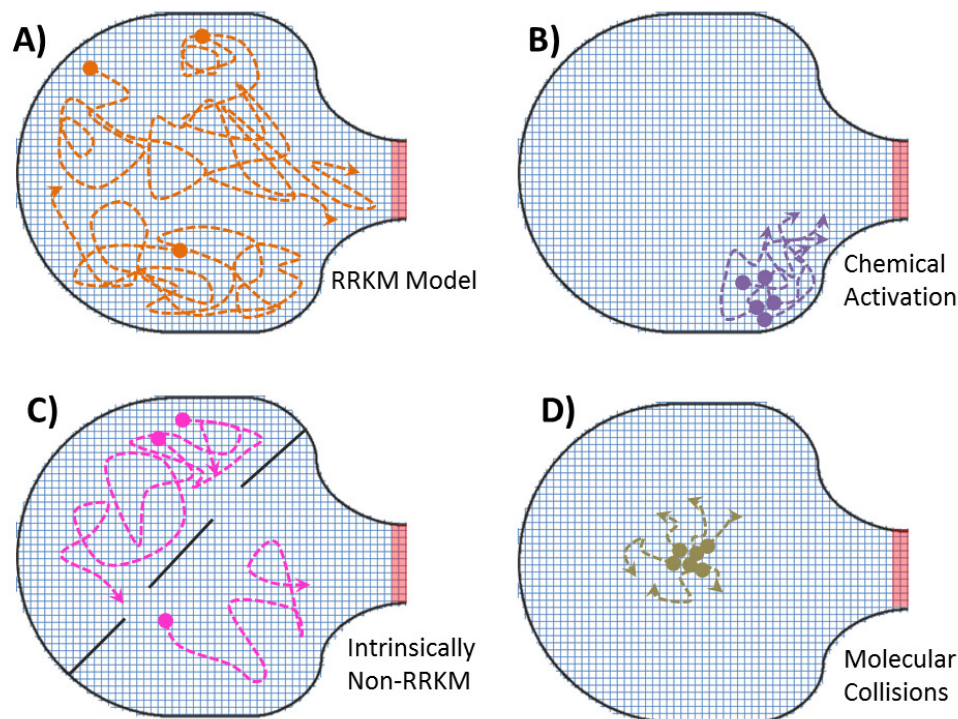


Figure 3.2. Adapted schematics from Bunker and Hase J. Chem. Phys. **1973**, 59 (9), 4621-4632 showing possible phase space trajectories (at constant energy) for different A) statistical or B)-D) non-statistical interpretations.

and Hase showed that different means of reaching an activated complex would affect the reaction. These are schematically collected in Figure 3.2 as paths through phase space at the activation energy. In these schematics, the ray traces of various colors represent a molecule traversing different states (grid volumes) at the same energy, but only the states in red are the transition states lead to a prompt reaction. If the system evolves for a long period of time before a reaction occurs the RRKM model (shown in Figure 3.2 A) is a good representation. If the system is promoted to this transition state energy through a strong, orientation specific collision (panel D) or where another atom attacks a portion of the molecule (panel B), the lifetime distribution (first time derivative of Equation 3.1) will be non-exponential. Lastly, Figure 3.2 (C) represents a type of reaction that has a bottleneck in the phase space. A common

example of this scenario is a necessary conformation change prior to a reaction; these cases are denoted as intrinsically non-RRKM behaving. Several realistic examples of these schematics have been studied. A short list includes ozone [119], dipeptides [120], methyl isonitrile [110, 111], stilbene [121] and water [108].

If ergodicity is not guaranteed, which is true for small molecules that display a mixed chaotic and regular phase space exploration, the lifetime distribution will also violate statistical treatment. These mixed trajectories are a focus of many scientists studying nonlinear resonances, periodic orbits, KAM tori and ‘sticky’ Hamiltonians. [122–124] Many of these mixed trajectories have direct corollaries in quantum mechanics (i.e. entanglement and coherent states) and are thought to hold the key to a classical-quantum reaction rate bridge. [122] Although these subjects are worth mentioning here, no attempt has been made in this work to analyze the results through these lenses. Returning to the purely classical treatment of phase space, the mixed regular and chaotic trajectories tie in the subject of VER which, approximately, is the timescale that determines when one of these trajectories can be considered as chaotic rather than regular. The restricted flow of energy among vibrations means only some of the available phase volume is accessed. The challenge is identifying, *a priori*, which bonds or vibrations are key players in the overall reaction. Polanyi suggested a few pair of limiting cases where atom-diatom reactions could be accelerated based on where energy is localized. First, if a reaction has a reactant-like or relatively early barrier, energy localized on translational degrees of freedom is more effective in overcoming the barrier than vibrational energy. Second, an intramolecular vibrational excitation becomes more effective than translational energy if the reaction has a product-like or late barrier. [125] A more elegant approach, the Sudden Vector Projection (SVP) considers all degrees of freedom in both the forward and reverse reaction and weights which most strongly contribute to the reaction coordinate. [98] Guo *et al.* used the SVP approach to confirm the rules of thumb that Polanyi suggested, but also showed that even very simple gas phase reactions have multiple degrees of freedom (DoF) that contribute strongly. This method is akin to a normal

mode analysis [126] coupled to a minimum energy pathway identification, like nudged elastic band [127] or nebterpolation [128]. For example, the $Cl + CH_4 \rightarrow HCl + CH_3$ reaction in the forward direction shows no single dominant vibration driving the reaction but the two-body, high frequency C-H modes contributing most strongly. The reverse reaction however, shows near complete dependence on the excitation of the H-Cl stretch vibration. In the absence of any VER, the SVP predicts the optimal modes to be targeted for external control of the reaction, albeit the method has only been applied in relatively low DoF systems. For reactions occurring in solids, this method has obvious shortcomings due to the number of DoF, but is still useful in logically guiding which vibrations should be considered as important to the reaction.

As outlined in Chapter 2.2, this work will take a more general approach to identifying which vibrations are key to the overall reaction. Somewhere between Polanyi’s rules and the SVP method, the techniques here are sensitive enough to highlight when any DoF has more (or less) than its share of energy with respect to equipartition. Coupling these observations of where energy is localized to the overall reaction behavior, one can determine which DoF are important to the reaction, even without predetermining the transition state or minimum energy path in phase space. Depending on how energy is inputted into the system, this may mean looking at translational DoF versus all vibrations or looking at the differences in energy distributed among individual vibrations. While it is understood that there are a number of different causes to non-statistical reactions, most of these predictions are made for systems in the microcanonical ensemble, which is rarely ever achievable in a laboratory experiment. An outstanding question to many of these reference texts used above is this: can the overall kinetics of a reaction be affected by these non-statistical constructions? This involves sampling an ensemble of reaction events rather than identifying the lifetimes of isolated molecules. Most importantly, the work collected here will attempt to simultaneously predict the overall changes in reaction behavior with respect to statistical or non-statistical means of excitation to temperatures (now working in the canonical ensemble) that initiate decomposition. The first example

will be a set of simulations that use a vibration specific insult in order to induce reactions in a molecular solid. The results here go beyond showing that non-statistical reactions can be realized in solids where extremely strong VER tend to negate these effects. Second, large shock compression studies of a molecular solid are undertaken which prepare the material for decomposition with an unequal distribution of energy between translational and vibrational DoF. Here it will be shown that the ignition and growth behaviors of explosives depends on the chemistry under non-equilibrium conditions. The simulations, for both cases of means of energy input, better align with the experimental capability to observe the same effects and show great potential to expand upon the current understanding of the role of non-RRKM reactions.

3.3 Non-equilibrium Chemistry Through Vibrational Coupling

This study is enabled by the development of reactive interatomic potentials that provide a realistic description of complex chemical reactions in a computationally efficient way, enabling large-scale reactive simulations in condensed matter. [53, 71, 129] In order to best highlight the possible effects of a non-statistical reaction, a trio of molecular crystals was chosen; nitromethane (NM), octahydro-1,3,5,7-tetranitro-1,3,5,7-tetrazocine (HMX), and pentaerythritol tetranitrate (PETN), under a range of mode-specific energy insults, quantify the non-statistical degree of their decomposition. To a first approximation, the solvation shell or crystal environment surrounding a reacting molecule in a condensed phase system can be taken as an inert medium, resulting in only small modifications on the observed kinetics from the gas phase. However, in the molecular crystals studied here, the local environment is not inert, and local reaction kinetics will certainly be affected by nearby endothermic or exothermic processes. Therefore, one must expect a nontrivial interplay between chemical activation from a thermal bath versus the local environment that leads to reactions in the condensed phase. Furthermore, short VER time scales and strong intermolecular interactions in molecular crystals tend to negate non-statistical chemistry. [5, 7, 130] Thus, the main goal of this paper is to establish whether nonequilib-

rium states (unequal energy distribution among vibrations) can be constructed via frequency-localized insults for long enough time scales to affect chemistry. Following the discussion in Section 2.2, reactive molecular dynamics are employed, and a constant excitation to a subset of intramolecular modes is applied using external electric fields with frequency matched to a specific vibration. Reactions resulting from such insults are compared to those that maintain equilibrium conditions through constant coupling to a thermal bath. These results, supported by experimental work, [131,132] show that nonequilibrium states can be created with these mode specific insults; for strong electric fields, these time scales are comparable to those of the initial chemical decomposition of the molecules. [100,104] In all cases, the appropriate choice of target vibration and insult strength can result in initial reactions under conditions where the temperature of the target modes exceeds that of the bulk, sometimes up to hundreds of degrees Kelvin. Differences drawn between the three materials, which are considered as model materials given the contrasting VER and reaction time scales, aid in the understanding of (non)statistical reaction behavior, in particular for condensed-phase systems, and in the capability of externally controlled reactions.

3.3.1 Simulation Details

In order to study the decomposition and reaction of various energetic materials, the reactive force field ReaxFF is used, which has also been successfully used to study the shock [78,133–135] and thermal [136–139] decomposition of such materials. [54] The force field used here merges the training set from the combustion branch [140] with the nitramines force field [134] and has been parametrized against unimolecular as well as multi-molecular reactions that occur in the condensed phase. [53] All simulations in this chapter were performed using the LAMMPS code. [35] Self-consistent partial atomic charges are updated at every time step (0.1 fs) using a conjugate gradient method with a tolerance of 1×10^{-6} , which has been shown to properly describe chemical reactions at extreme conditions. [129]

To more effectively study the differences in reaction behavior as a function of insult type, three molecular high-energy density (HE) materials with different characteristics were chosen for this study. The simplest of the three is NM (CH_3NO_2), which has been widely studied for its combustion, detonation, and vibrational properties using both experimental and computational approaches. The initial structure is a perfect crystal with 3D periodic boundary conditions obtained by replicating the orthorhombic crystal structure four times along a, four along b, and four along c, resulting in 256 molecules. The secondary explosive HMX (cyclic $(CH_2-NNO_2)_4$) is a nitramine that exhibits an alternating carbon-nitrogen ring. Starting from the α -crystal structure, the unit cell is replicated $2 \times 1 \times 4$ to obtain a simulation cell with 64 molecules. Lastly, PETN ($C-(CH_2-ONO_2)_4$) was also studied, which has different molecular geometry and chemistry than both NM and HMX but a similar initial reaction mechanism as HMX. Both the nitroester (PETN) and nitramine (HMX) initially decompose through the unimolecular NO_2 loss through $N-O$ or $N-N$ scission, respectively. PETN has a tetragonal crystal structure that is replicated $4 \times 4 \times 4$ times, resulting in 128 molecules in the simulation cell.

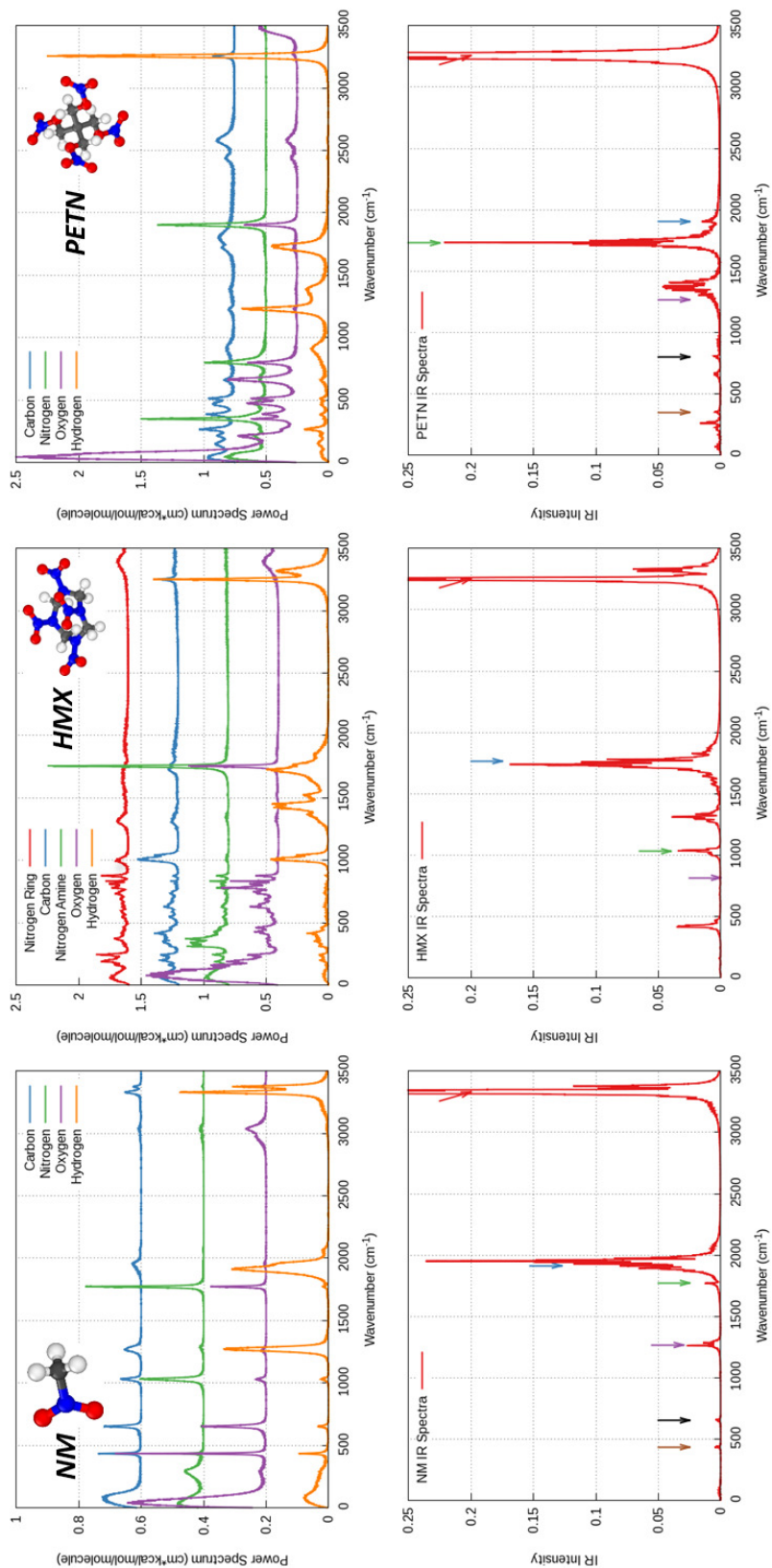


Figure 3.3. Calculated power spectrum per molecule from MD at 300 K and 1 atm for (A) nitromethane, (B) HMX, and (C) PETN using Equation 2.6. The vertical offset is for visual clarity. Panels (D)-(F) contain the predicted infrared spectrum of the respective vertically aligned material, with colored arrows indicating the frequency of vibrational modes used in this study. Atom colors correspond to carbon (gray), hydrogen (white), oxygen (red), and nitrogen (blue).

Differences in the molecular structures of the three materials lead to different vibrational properties and inter- and intramolecular energy relaxation characteristics. This can be seen in the top panels of Figure 3.3, where the vibrational power spectrum of the three systems is computed. [97] The infrared (IR) intensities [96] are shown in the bottom panels, and these will be used to discuss the coupling of the vibrations to the electric field insults.

In order to characterize the decomposition of the materials of interest under various conditions, a constant insult is applied throughout the simulation as either a sinusoidal electric field at various frequencies or a constant heating rate with a Nose-Hoover thermostat. This continuous input of energy is in contrast to previous work which used a pulsed insult [129], and enables the study of the reacting systems in the presence of the insult. Also, since these systems are heated at known rates, traditional kinetics analysis techniques can be applied to the reacting system to extract activation energies and attempt frequencies; [141, 142] this will be further discussed in Section 3.3. Electric field strengths in the range 0.01–1 V/nm were used, which result in heating rates of the order 0.1 – 100 K/ps, sufficient to decompose the material on MD time scales. Several field frequencies were applied as described below to localize energy into various modes. For each insult type and strength, ten statistically independent simulations were performed after a thermalization at 300 K for 20 ps. Each simulation had velocities initially assigned from a randomly seeded Maxwell-Boltzmann distribution, which decouples the trajectories from one another by the time the insult is applied. Since the Nose-Hoover thermostat scales all atomic velocities by the same number, the initial equipartition of energy per mode is held even when the system is constantly heated with this thermostat. A set of frequencies were selected for the electric field insults for each material based on vibrational properties; these are indicated by arrows in the lower panels of Figure 3.3. For each driving frequency chosen, ten different field strengths were applied (and ten repetitions of each) in order to properly address the effect of insult strength on the relaxation times and resultant chemistry.

Identification of vibrational modes can be performed using the per element power spectra, shown in Figure 3.3, in conjunction with experimentally reported spectra. From these results and Appalakondaiah *et al.* [143] the NM target modes were assigned as follows: 3330cm^{-1} (CH stretch), 1913cm^{-1} (CH_2 angle bend + CH_3 deform), 1772cm^{-1} (NO stretch), 1266cm^{-1} (NCH deform + CN stretch), 651cm^{-1} (CN stretch + NO_2 angle bend), and 433cm^{-1} (NO_2 rock). Similarly, following Pravica *et al.* [144] for HMX: 3254cm^{-1} (CH stretch), 1765cm^{-1} (NO stretch), 1030cm^{-1} (NN stretch + CH_2 rock), and 814cm^{-1} (Ring twist + NO_2 angle bend). Lastly for PETN, following Gupta *et al.*: [145] 3258cm^{-1} (CH stretch), 1903cm^{-1} (NO stretch), 1728cm^{-1} (CH_2 angle bend), 1266cm^{-1} (CH_2 wag + CO stretch + C_5 deform), 799cm^{-1} ($O-NO_2$ umbrella), 348cm^{-1} ($O-NO_2$ rock + C_5 deform). Note that, while ReaxFF is not parametrized to reproduce the entire vibrational spectra of energetic materials, it provides a reasonable description as compared with the ab initio predictions (see refs [143–145]); this is because ReaxFF is parametrized to describe bond breaking, angle, and torsion bending curves. The largest discrepancies in vibrational frequencies are associated with high-frequency bond stretch modes such as the $N-O$ and $C-H$ modes that are common to all three materials. As was discussed in Section 2.2, the exact peak positions do not affect the main results shown here.

A simulation of such complexity necessarily involves approximations: the most significant ones are those associated with the description of atomic interactions using the ReaxFF force field, and the second is the use of classical mechanics (as opposed to quantum) to describe ionic dynamics. The implications of these approximations in the results shown here are addressed in Section 3.3.

One of the main goals here is to understand whether nonequilibrium states, i.e., when the energy is not equally distributed among the various inter- and intramolecular modes as dictated by equilibrium statistical mechanics, can exist for long enough to affect chemical reactions in the condensed phase. Using the methods outlined in Section 2.2 for Equation 2.6, a trajectory window of 1 ps and velocity sampling rate of 4.7 fs give a resolvable frequency window of $33\text{--}3500\text{cm}^{-1}$, within which all three

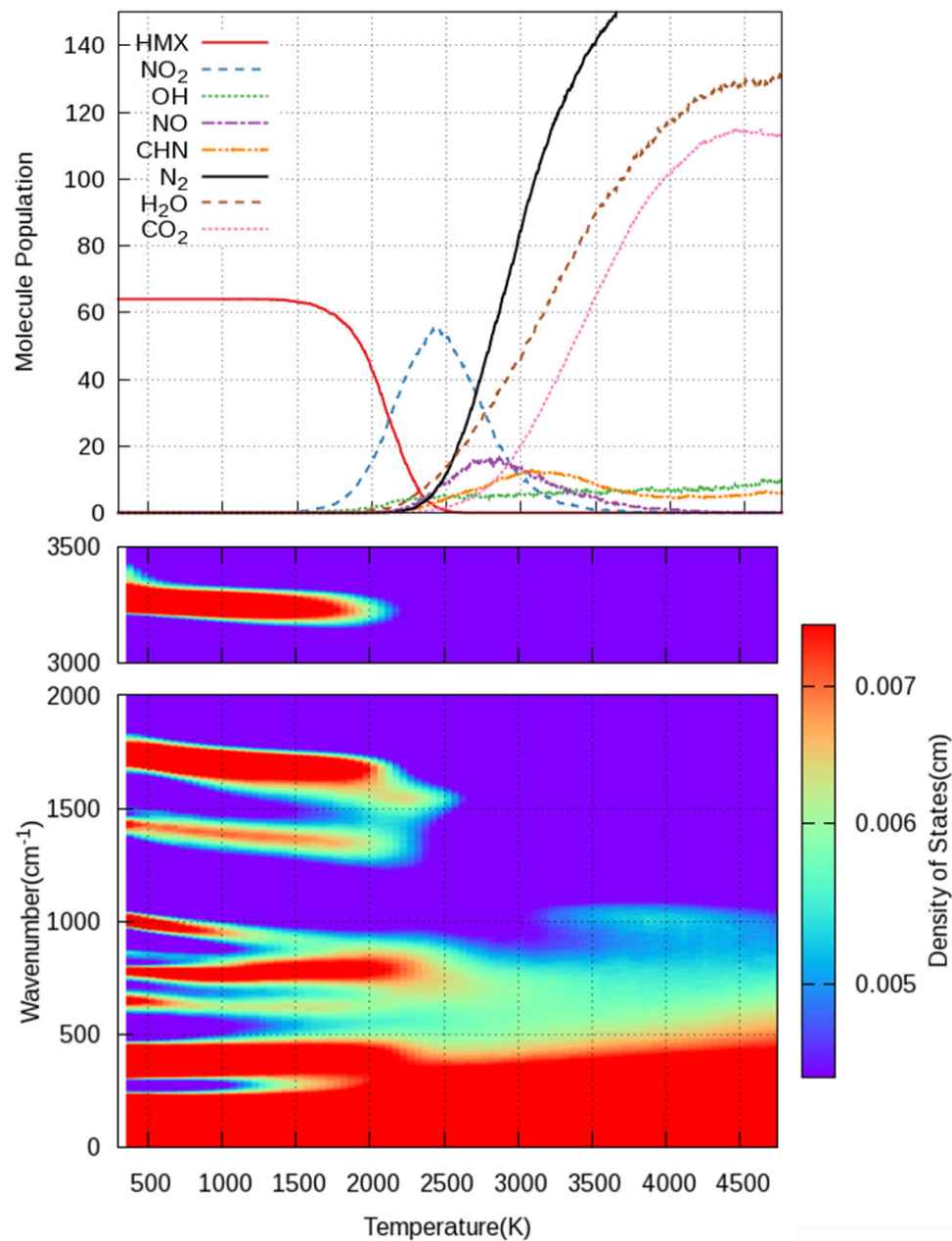


Figure 3.4. Typical simulation of HMX decomposition due to a constant heating of the system via a Nose-Hoover thermostat at a rate of 50 K/ps. Chemical species information in (A) and dynamic vibrational density of states in (B) share a common axis which is the temperature of the system.

test materials have their full vibrational spectrum. Figure 3.4 illustrates a typical simulation of thermal decomposition of HMX for a heating rate of 50 K/ps. Figure 3.4 (A) shows the population of HMX, key intermediate, and final product molecules as a function of temperature, and panel (B) shows the evolution of the vibrational DoS with temperature. ReaxFF bond orders were used to identify chemical bonds, and this connectivity information is subsequently analyzed with a cluster expansion algorithm to identify molecules. Figures 3.4 (A) and (B) show that significant red-shifts and broadening of the HMX peaks occur before decomposition begins. At temperatures over 1500 K, peaks in the density of states begin disappearing, indicating chemical reactions. The original *NO* stretch peaks (near 1765cm^{-1}) in HMX persist longer than other high-frequency modes; this is due to the large number of *NO* and *NO*₂ moieties at early stages of the decomposition. The large number of small and very mobile molecules explains the strong signal at low frequencies coming from intermolecular collisions. Altogether, the increased time resolution on the vibrational spectra and molecule recognition allows for greater insight into the decomposition and, as will be shown, how these processes can be altered by the means of energy input.

3.3.2 Results and Discussion

Where a thermostat is used to control the temperature of the material, the heating rate is well defined and constant throughout the simulation. This, however, is not as simple when an electric field is used to couple to intramolecular vibrations. This is best exemplified by Figure 3.5. In this figure, the temperature evolution is shown for each vibrational insult frequency studied in NM, all of which have an overall heating rate (neglecting the exothermic reaction spike above 2250K) close to 50K/ps. What is clear for all of the vibrational insults is that the heating rate is variable with time; this is due to a strong resonance coupling at low temperatures and a loss of this efficient absorption as modes broaden and shift at higher temperatures.

To study a range of heating rates across all materials, the electric field amplitude was adjusted, resulting in a different range of power densities. The power density is

computed as $\rho = \frac{\epsilon\epsilon_0}{2V} E^2 \omega$, where E is the amplitude of the field, ω is the frequency, V is the volume of the simulation cell and ϵ is the dielectric constant of the material. For HMX and PETN, this range of insult strengths were 0.1604 to 16.04 $\mu W/nm^3$, while NM coupled less readily to the electric field and required insult strengths in the range of 1.604 to 40.1 $\mu W/nm^3$ to give the similar heating rates.

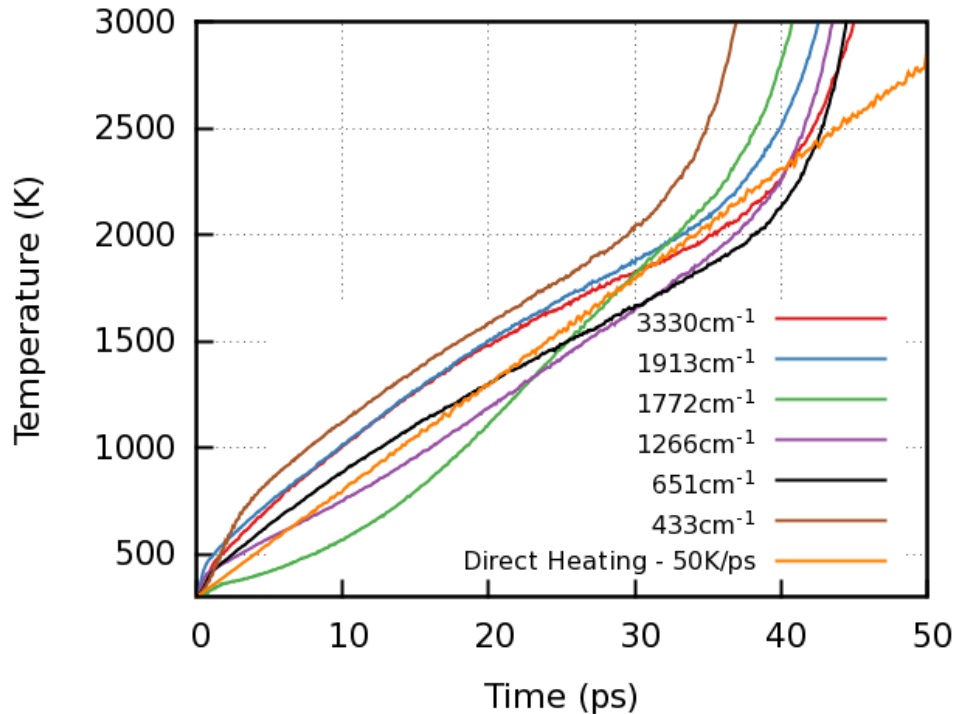


Figure 3.5. Example temperature versus time curves for all insults tested in NM. Each has a heating rate recorded near 50K/ps at the time of one-third decomposed

Using the method outlined in Section 2.2, the power spectrum can be broken down into unique segments for the purpose of identifying where energy is localized when one of these electromagnetic insults is present. To illustrate this, Figure 3.6 shows the kinetic energy content of each set of modes relative to that of an equipartition of energy, which on these plots is a value of unity on the vertical axis. In all panels of this figure, the CH symmetric stretch vibration is targeted with the external stimulus, which is why the highest frequency range shows a large spike above unity

before VER returns it to equilibrium. Even though the insult is present throughout the time shown in these plots, each material returns to an equipartition of energy in due time. Interestingly, there are some subsets of modes that are starved of their share of an equipartition of energy. This effect is schematically represented in Figure 3.2 B).

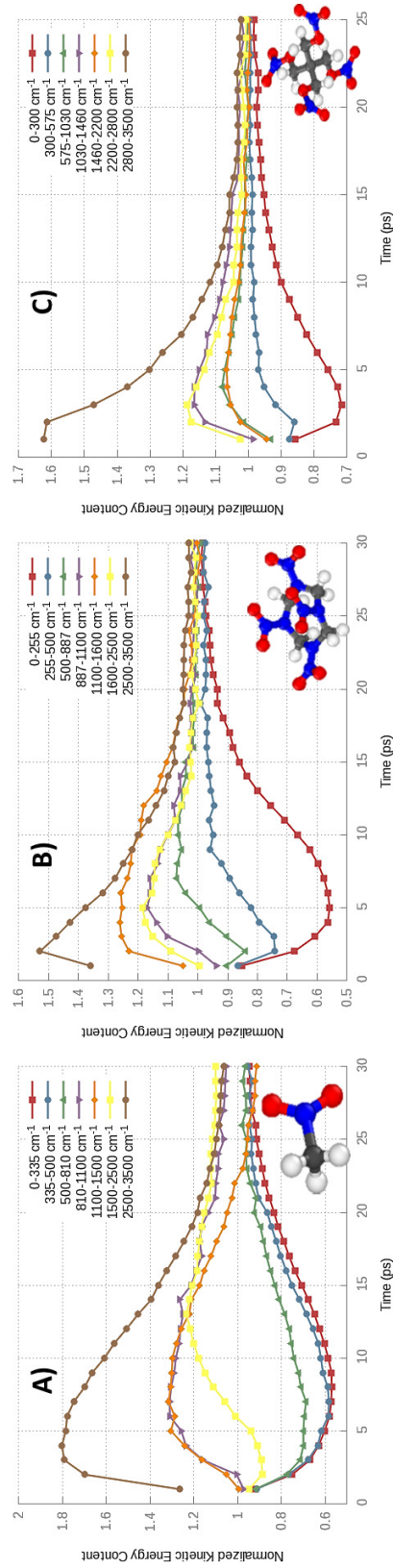


Figure 3.6. Relative kinetic energy content for each subset of vibrations for an electric field coupled to the CH Stretch vibration in A) NM B) HMX and C) PETN. The series in brown for each panel is the frequency range that contains the insult. A value of one for the normalized kinetic energy content is that of equipartition.

To simplify the analysis, only the frequency range containing the target mode will be plotted; its temperature is assigned simply by comparison to the thermal vibrational spectra, which is used to normalize the non-equilibrium spectra (per Equation 2.7). Figure 3.7 shows the temperature associated with modes within frequency regions, including the target mode versus bulk temperature (obtained from the overall kinetic energy in the simulation cell) of each material for a few target frequencies tested. The solid diagonal solid lines with slope one indicate equilibrium, i.e., the selected modes exhibiting the same temperature as the overall system; in other words, the solid lines indicate equipartition of energy. It is observed that, in all cases, the frequency range containing the excited mode exhibits more than its share of the kinetic energy; i.e., those modes are hotter than the rest. As expected, higher energy input rates lead to increased nonequilibrium. Interestingly, even though the insult is maintained throughout the simulations, the systems eventually achieve equilibrium. Each point on these plots is 1 ps apart, which gives a measure of the relaxation process in both time and temperature. This relaxation occurs because anharmonicities in the potential energy surface (PES) are sampled more predominantly as temperature increases (see peak broadening in Figure 3.4), leading to faster energy transfer between modes and weaker coupling with the external electric field. The arrows matching the plot lines in color in Figure 3.7 mark the average times at which the first molecule is observed to decompose, while the solid black arrows indicate the first decomposition in the directly heated samples for comparable heating rates.

Interestingly, often the time scales for equilibration are comparable to those associated with the initial chemistry; for some target modes in HMX and PETN, decomposition occurs when the target modes are several hundreds of degrees Kelvin higher than the bulk temperature at which the material begins to decompose. The vibrationally tuned insults are labeled by the energy density of the electric field. More details about this calculation and additional two temperature plots can be found in the Supporting Information of Wood *et al.* [105]. The results in Figure 3.7 point to several possible scenarios regarding the possibility of nonstatistical decomposition. In

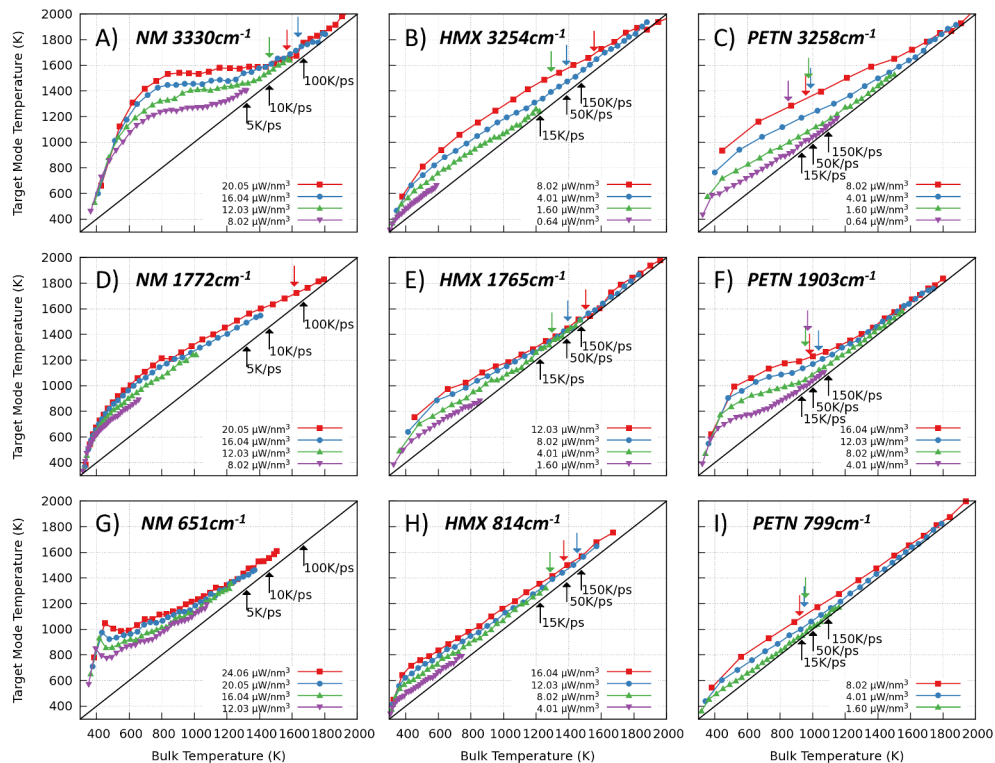


Figure 3.7. Two temperature plots of target mode temperature versus bulk temperature during an electric field insult as calculated in Equation 2.7. Each data point is 1 ps apart. Panels (A)(C) are the CH stretch modes in each material, respectively, (D)(F) the NO stretch mode, and (G)(I) are low-frequency intramolecular modes that are unique to each molecules geometry. Color matched arrows indicate the first chemical reaction for each insult, and the equilibrium reactions are indicated in black. The nonequilibrium distribution of energy among vibrations is clearly seen as data points lying above the solid black equipartition line ($T_{mode} = T_{bulk}$).

the case of NM, while a significant degree of nonequilibrium is achieved in samples excited with the electric fields, the chemical reactions occur after equilibration has occurred. Actually it appears that the targeted insults may delay the reactions as compared to thermal excitation (color arrows indicate higher temperatures than the black ones). PETN also exhibits a significant degree of nonequilibrium, and, contrary to NM, reactions occur at these elevated mode temperatures. Quite significantly, reactions in PETN under targeted insults occur at lower bulk temperatures than those in thermally excited samples. HMX exhibits the least degree of nonequilibrium, and except in the case of fields targeting CH vibrations, the reactions occur under essentially equilibrium conditions. Even in the high frequency excitation case, reactions occur at temperatures comparable to the thermal cases indicating that the localized energy input does not significantly affect chemistry. The next set of results and corresponding discussion quantifies the effect of insult type and strength on chemistry.

To quantify the kinetics associated with the insult-dependent reactions discussed previously, the decomposition rate as a function of temperature for all insult types and strengths was studied. A first-order, thermally activated process would lead, within the harmonic approximation, to an exponential decomposition rate of the form

$$\dot{n}(t) = \frac{\dot{\alpha}(t)}{\alpha(t)} = \nu e^{-\Delta G/kT} \quad (3.2)$$

where the dot denotes time derivative; $\alpha(t)$ is the population of the parent molecules remaining at time t ; ΔG is the activation energy for decomposition; T is temperature; and k is Boltzmanns constant. The prefactor ν can be thought of as an attempt frequency; more accurately, within transition state theory, it is the ratio of the $3N$ vibrational frequencies of the reagents divided by the $3N - 1$ positive vibrational frequencies at the transition state. [114,146,147] The reactive MD simulations provide direct access to the quantities α and $\dot{\alpha}$ in Equation 3.2 (see left panels in Figure 3.8 and, thus, enable a direct comparison of the effect of insult type and chemistry on kinetics.

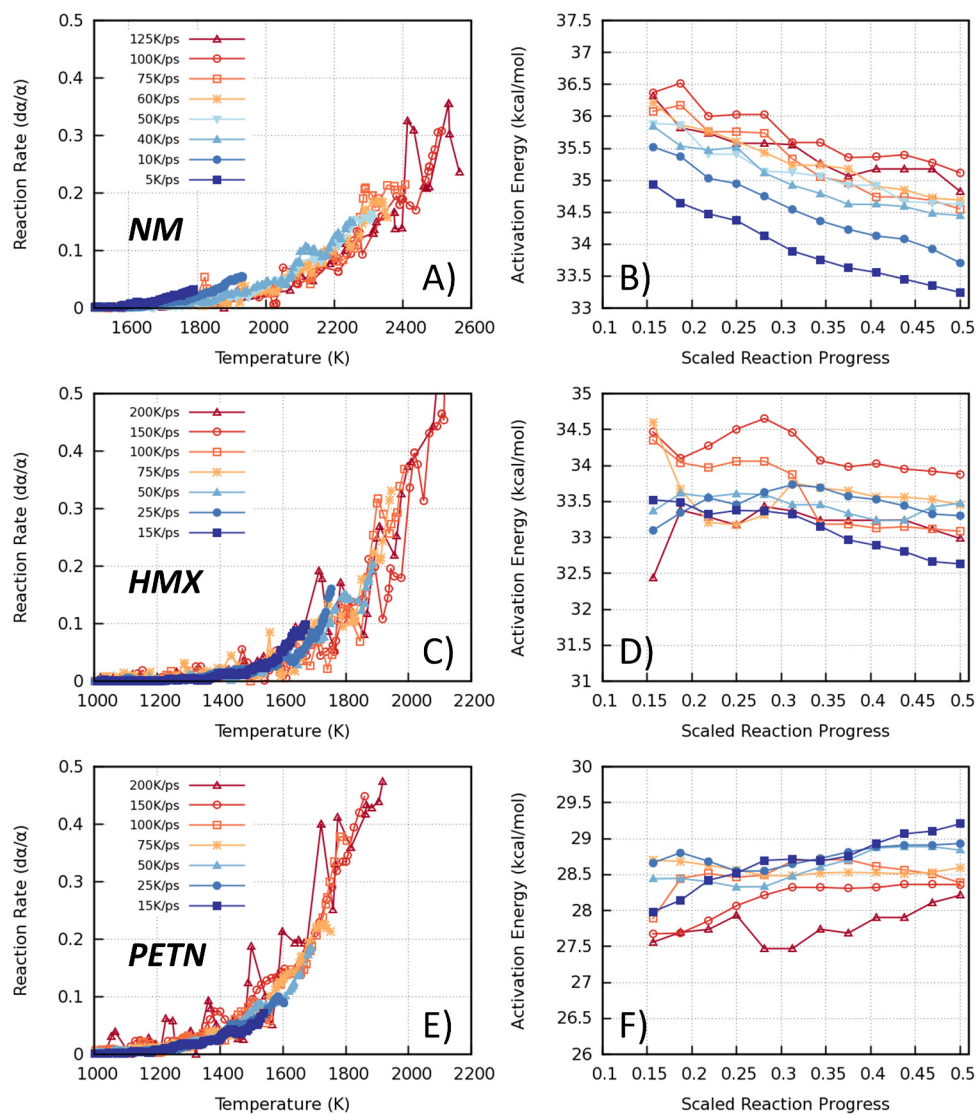


Figure 3.8. Observed reaction rates under equilibrium conditions for (A) NM, (C) HMX, and (E) PETN. Each data series is heated at a constant rate using a Nose-Hoover thermostat. Using the procedure outlined here, activation energies obtained from fitting Equation 3.2 are plotted against the reaction progress for (B) NM, (D) HMX, and (F) PETN, respectively.

To isolate the role of insult type and strength on the activation barrier, and to minimize correlations with the frequency prefactor a two-step process is adopted to fit Equation 3.2 to the MD data. First, a fit is made of Equation 3.2 to the collection of all thermal insult strengths for each material, NM, PETN, and HMX. The resulting frequency prefactor is taken as a constant for all other fitting procedures within the same material. For this global fitting procedure of the thermally induced decomposition, the reaction rate is fitted up to a value of $\dot{\alpha}(t)/\alpha(t=0) = 0.5$, i.e., the initial decomposition of one-half of the starting material. This is an important choice for condensed-phase reactions, where the evolving molecular environment can affect chemical reactions. After this global two-parameter fit, which forces ν into a constant, the activation energy is, thus, the only free fit parameter, and it is used to compare the kinetics across insult types and strengths. In addition, the fitting of the reaction rate is carried out up to different amounts of reaction progress (i.e., $\dot{\alpha}(t)/\alpha(t=0)$), which provides information regarding changes in Equation 3.2 as the evolving environment of intermediate and final products can affect the decomposition of the remaining parent molecules.

Left panels in Figure 3.8 show decomposition rates as a function of temperature for thermal excitation for various heating rates (high to low in red to blue), and the right panels show the extracted activation energies for the various heating rates as a function of the maximum reaction progress used in the exponential fits. In all these cases involving energy input with a thermostat, the effect of heating rate and reaction progress on activation energy is relatively weak. This is an important validation of the approach to extract kinetics parameters from reactive MD simulations. Still, within these weak dependencies some interesting trends can be observed. Both for HMX and NM a slight increase in activation energy is observed with increasing heating rate; this can be expected, as faster heating might lead to overshooting of the transition state, this is a consequence of using the canonical versus micro-canonical ensemble for calculating rate constants. Interestingly, PETN exhibits the reverse trend: the activation energy decreases slightly for faster heating rates. In addition, HMX and

PETN show little to no effect of heating rate (about 1 kcal/mol in activation energy) on reaction progress, which is consistent with a unimolecular reaction. [148–151]

Figure 3.9 shows the observed reaction rates versus temperature, and resulting activation energies as a function of extent of reaction, for various insult strengths for two selected electric field frequencies coupled to vibrations in NM. The resulting activation energies and their dependence on insult strength and extent of reaction are similar to those for the thermal decomposition in Figure 3.8. This is consistent with the observation from Figure 3.7 that chemistry in NM occurs after equilibration between the various degrees of freedom is achieved. Decomposition rates and activation barriers for HMX are omitted here, because the data show no new trends relative to the NM and PETN data. As with NM, no significant differences in the activation energies between frequency-targeted insults and thermal excitation was found. This is also consistent with the results, shown in Figure 3.8, that show HMX to have the weakest degree of nonequilibrium kinetic energy distributions between vibrational modes out of the three materials.

Turning now to the reaction kinetics for PETN, Figure 3.10 shows decomposition rates and the resulting activation energies for two field frequencies and a range of insult strengths. The results show striking differences from the prior cases. For both frequencies, stronger insults (faster heating rates) result in reduced effective activation energies; this can be confirmed from the left panels, which clearly show faster decomposition for stronger insults (red). For both target modes shown in Figure 3.10, the energy input rate not only leads to the opposite trend in activation energy with respect to NM and HMX, but also its effect is more dramatic. This is consistent with the results shown in Figure 3.8, where reactions are seen earlier in the frequency-targeted insults in PETN and suppressed in NM. Furthermore, the data shown in Figure 3.9(A) and (C) show that the observed reaction rate is particularly low for early decomposition due to the strongest fields. Both frequencies show low activation energy for the early decomposition at high insult strengths that relax back to a value close to the thermal insults for higher decomposition degrees.

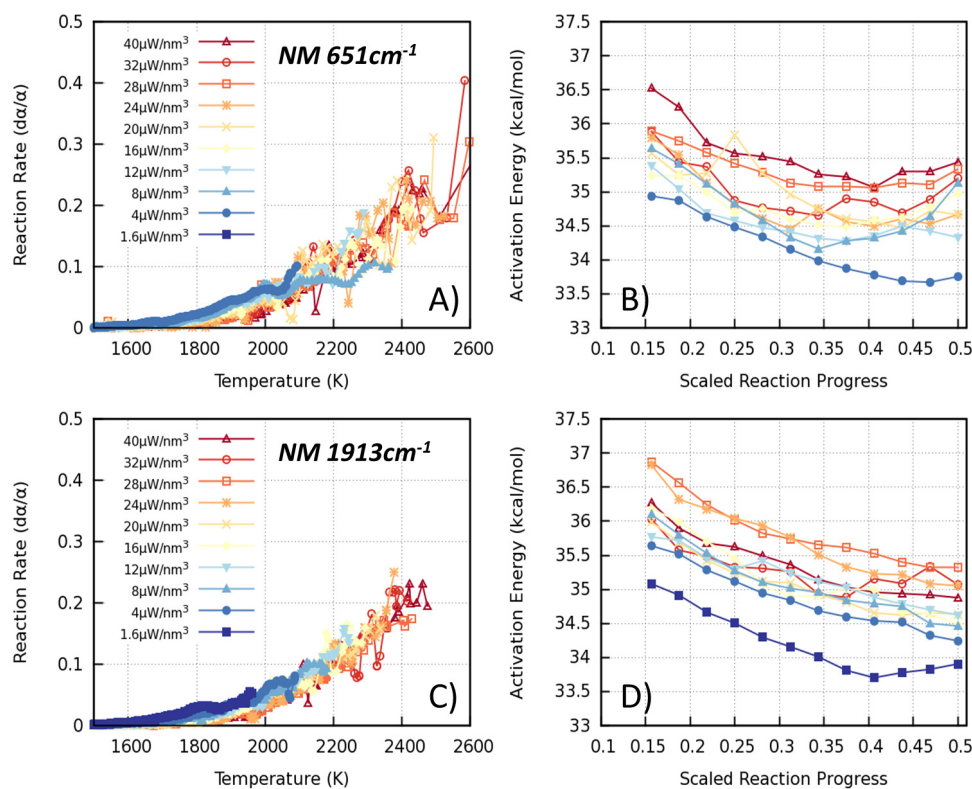


Figure 3.9. Nitromethane reaction rates obtained from simulations of electric field induced decomposition for the intramolecular modes at (A) 651cm^{-1} and (C) 1913cm^{-1} ; see the body of the text in this section for mode assignments. The fits to Equation 3.2 yield the activation energies plotted in panels (B) for the mode at 651cm^{-1} and (D) for the mode at 1913cm^{-1} .

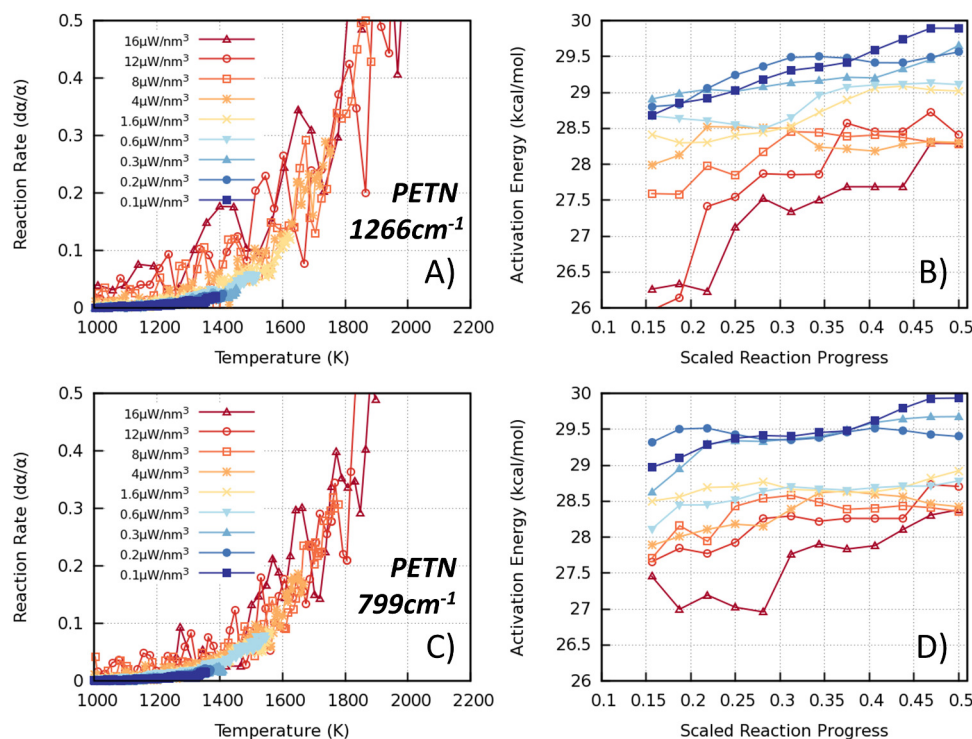


Figure 3.10. PETN reaction rates obtained from simulations of electric field induced decomposition for the intramolecular modes at (A) 1266cm^{-1} and (C) 799cm^{-1} . The fits to Equation 3.2 yield the activation energies plotted in panels (B) for the mode at 1266cm^{-1} and (D) the mode at 799cm^{-1} . Both target modes show clear insult strength dependence as seen by lower activation energies at high insult strengths and early reaction progress.

To provide a complementary picture of whether inputting energy of specific frequencies accelerates or hinders the initial chemistry, the temperature at which one-third of the original molecules have decomposed is studied. This is clearly a heating rate dependent quantity; thus, Figure 3.11 shows the temperature corresponding to one-third of the original molecules having decomposed as a function of heating rate for the various insult types. The simulations of electric field induced decomposition result in time-dependent heating rates due to modulations of coupling strength between the fields and the starting material (see Figure 3.5). The reported heating rate in Figure 3.11 is simply the linear approximation up to one-third decomposed: $(T_{\frac{1}{3}} - T_0)/\Delta t$. The simulations exhibit very interesting trends of initial chemistry on molecular structure and insult. PETN was shown to exhibit nonstatistical decomposition for some electric field frequencies, and it was found that for many of those cases 1/3 decomposition is achieved at lower temperatures than when heating with a thermostat (orange line). This is consistent with the reduced activation barrier shown in Figure 3.10.

Regarding the data in Figure 3.11, for NM, several vibrationally tuned energy inputs result in an apparent delay of initial reactions as compared to thermally excited cases and, consequently, require higher temperatures (and energy input) to reach one-third decomposition. HMX lies somewhere between these two cases; except for the 814cm^{-1} field excitation that slows down reactions, the temperatures corresponding to one-third decomposition are rather insensitive to insult type. In NM and HMX, the temperatures at one-third decomposed are close to the onset of exothermic chemistry, which means any delay in the initial reactions will lead to a large temperature difference in Figure 3.11. This is exemplified in Figure 3.5, where insults applied to NM with heating rates close to 50 K/ps result in one-third decomposition temperatures of 2200-2300K, which neighbors a significant increase in heating rate. This late increase in heating rate has contributions from exothermic chemistry as well as additional coupling of the electric field with product molecules.

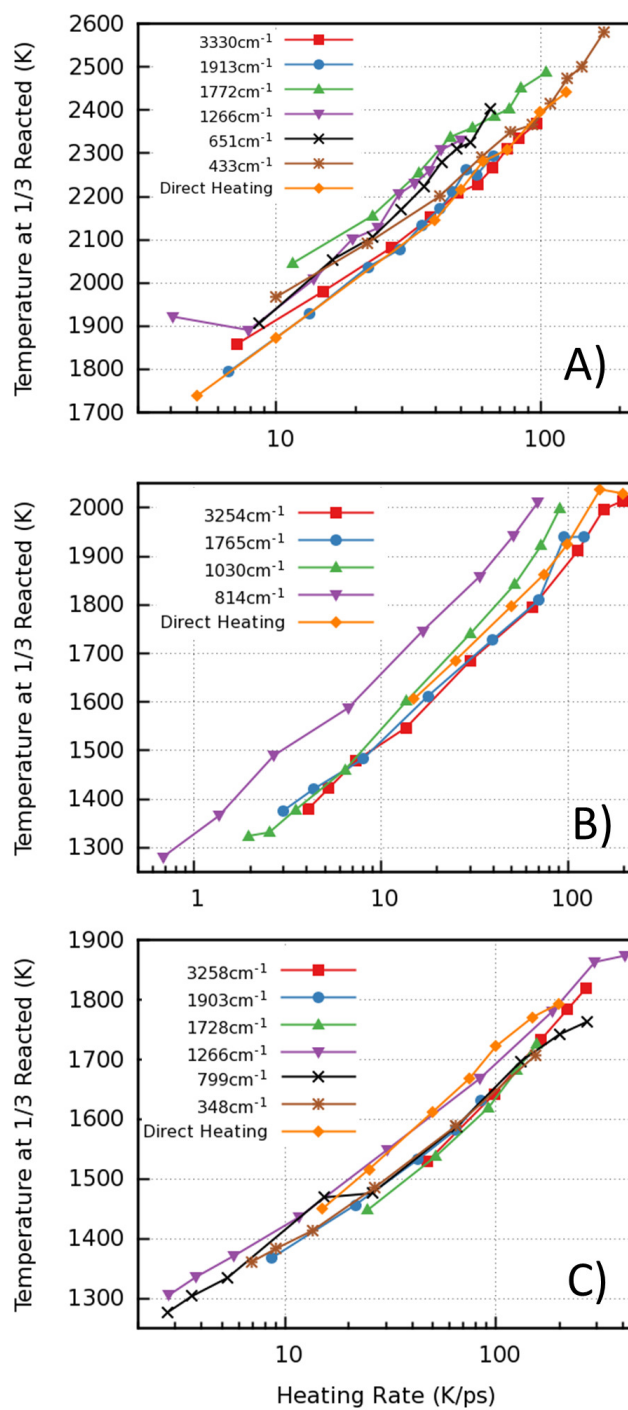


Figure 3.11. Observed bulk temperature at a fixed one-third decomposition for (A) NM, (B) HMX, and (C) PETN, where each point is averaged over ten independent simulations at the same insult strength. Equilibrium decomposition is denoted by the direct heating data series in orange diamonds in all panels.

3.3.3 Conclusions

Understanding energy localization, transfer, and relaxation in condensed-phase materials and their effect on chemical reactions is a key step toward coherent control of chemistry, with the potential to impact fields like catalysis, atmospheric chemistry, and energetic materials. For the energetic materials studied here, the interplay of vibrational energy relaxation and chemistry plays a significant role in the formation of a self-sustained deflagration wave. [78] More generally, coherent initiation of high-energy density materials could lead to safer formulations and remote detection or neutralization of explosives.

Our simulations demonstrate that frequency-localized insults can affect the decomposition of certain HE materials with respect to thermal equilibrium reactions. More importantly, these effects can be explained based on the vibrational spectra and decomposition mechanism of the material. The sample sizes, however, prohibit a detailed phase trajectory mapping (a la Figure 3.2) that might provide direct information about these nonequilibrium states (nonergodic trajectories) and explain the origin of the change in activation barrier. Future work along these lines could provide a more quantitative understanding of how insult character and strength affect the exploration of phase space and match them with the various categories for non-RRKM behavior proposed by Bunker and Hase. [110,111]

It is worth discussing at this point the two fundamental approximations made in these simulations and their impact on the results. First, the use of ReaxFF (or of any other method, including electronic structure ones) leads to an approximate description of the interactions between atoms. This affects the time scales for relaxation and equilibration processes and also kinetics and energetics associated with chemical reactions. ReaxFF has been extensively used to model energetic materials, [77, 134, 152, 153] and it is known to capture key aspects of the decomposition mechanisms of these materials and the overall reaction time scales. Its activation energies are in reasonable agreement with available experiments [148, 150, 154, 155]

and electronic structure-based calculations. [146, 149, 151] The use of a model or approximate PES underlies all trajectory mapping or direct studies of non-RRKM chemical reactions; [115, 156, 157] the simulation method here is no different. More importantly, the main results in the current paper are drawn from differences in the response of the same model to various insults; in a way, these results could be thought of as representing model materials as opposed to actual NM, PETN, and HMX. These model materials provide varying characteristics of preferred reaction path (uni- and multimolecular) as well as VER and reaction time scales. A second fundamental approximation in this work is the use of classical (rather than quantum) mechanics to describe ions. Classical mechanics lacks energy quantification that affects how high-frequency modes (those where the quantum of energy $\hbar\omega$ is comparable to or larger than kT) exchange energy with an electromagnetic field and their relative distribution of energy. Rather, the classical description allows for a continuous absorption of energy from the electric field, and at low temperatures every mode shares $kT/2$ of the total energy. Similarly, the classical description allows for anharmonic exchange of energy between modes continuously rather than in a quantized fashion. Despite these differences, both in quantum and classical mechanics, a field couples to modes with an associated electric dipole matching in frequency and equilibration occurs via anharmonicities in the PES. Thus, the classical description is able to describe energy localization and its equilibration as well as the general trends of relaxation time scales with temperature, which are key to the present study.

In this work, molecular dynamics was used to study the effect of frequency localized energy input on the excitation and decomposition of three energetic materials. NM, PETN, and HMX were chosen since they exhibit different vibrational spectra and decomposition mechanisms. Interestingly, these materials chemically react in time scales comparable with the intramolecular relaxation times. Despite the similarity of overlapping critical time scales the effect of energy input on chemistry showed disparate results. HMX exhibited the smallest degree of thermal nonequilibrium which was attributed to the higher density of intermediate frequency modes that

help energy equilibration. Consequently, the insult type and strength had a negligible effect on chemistry. For nitromethane, whose decomposition is governed by multi-molecular reactions, the frequency-localized insults do not affect its decomposition kinetics even though a significant thermal nonequilibrium is achieved. PETN, on the other hand, decomposes unimolecularly via the formation of NO_2 , and frequency-localized insults lead to nonstatistical decomposition with an observed reduction in activation energy. This work provides new insight into the possibility of coherent control of chemical reactions in energetic materials and in other fields.

3.4 Role of Non-equilibrium Chemistry for Shock Initiation

The coupled chemical and structural response of materials subjected to dynamical mechanical loads has long been an area of intense activity, and resulted in important contributions to materials science, [158] chemistry, [159] and astrophysics. [160] This shock wave travels at enormous speed in a solid, at the length scale of a single molecule, the temperature and pressure will increase by hundreds of Kelvin and tens of GPa in just a few picoseconds. Although this transition between thermodynamic states occurs rapidly, there are outstanding questions as to the role of the non-equilibrium states that a material experiences during shock compression. The passage of the shockwave triggers a material response that aims at minimizing the free energy of the system, either by relaxing the uniaxial stress via plastic deformation or through a change in thermodynamic state (phase transformations). In these cases, the material response weakens the shock as the relaxation reduces the compressive stress along the shock direction. However, some materials respond in strikingly different fashion. Explosives use the energy in the shockwave to disrupt chemical bonds and trigger a series of reactions that lead to low-energy gaseous products. The exothermic and volume-expanding reaction enhances the shockwave and can turn it into a detonation. Under such conditions, the shock front propagation speed reaches a steady state value known as the detonation velocity, which depends on the kinetics

(reaction rate) and thermodynamics (volume expansion and exothermicity) of the chemical wave and is, therefore, material specific.

Several fundamental mechanisms could contribute to the conversion of the initial mechanical energy into chemical reaction, ranging from direct mechanical disruption of bonds to thermal activation following the transfer of energy from lattice phonons to molecular vibrations (up-pumping). [77, 94, 161] In addition, within some of the pressure and temperature ranges of interest, the formation of plasma and metallized states is plausible, further complicating the definition of chemical mechanisms. [162] Given the extremely short time scales (pico to nanoseconds), spatial scales down to the submicron regime, and extreme conditions of temperature and pressure associated with these processes, it has proven to be experimentally challenging to unravel the different contributions to the overall process of initiation. [3, 163, 164]

Modeling a full detonation in realistic materials remains beyond the scales of MD simulations, but the development of reactive interatomic potentials over the last two decades enabled the study of the initial chemical reactions [77, 78] and even the transition from shock to a deflagration wave, an important first step in the description of detonation. [133] On the other hand, coarse grain models with the capability of describing chemical reactions are capable of capturing detonation in relatively simple explosives and providing insight into the coupling between chemistry and shock propagation. [165, 166] Different aspects of this shock to detonation transition have been studied in great detail using MD, with most efforts focused on either resolving the physics at the shock front or well within the chemical front of molecular energetics. This section focuses on the shock response of energetic molecular crystals and the phenomena related to the formation of a sustained chemical wave. And, in hand with the increase in compute power, the complexity of the atomistic models increased and current reactive force fields are capable of describing non-trivial aspects of the chemistry of HE materials.

The stark difference in shock strength required for detonation for single crystal high explosives versus powder formulations [9] shows the importance of defects and

microstructure in the initiation of the chemical wave that leads to detonation. The formation of hot spots (spatial localization of energy) and the interplay between the leading shock and chemical front has been intensely studied by both experimental and computational techniques due to the rich physics of thermal and mechanical processes, which are not well understood in the condensed phase. Homogeneous reaction waves have been observed to nucleate immediately following the elastic shock for strongly driven simple chemistry (so called AB) systems [167] and these models have also been used to study the role of defects on initiation. A defect helps localize the mechanical energy in the shock into high-temperature hot spots that speed up reactions that would otherwise occur much further behind the shock front [168]. Complex microstructures, including voids and multiple-phase systems, have been studied by adding in some amount of desensitizing agent (i.e. inert material) [169,170] Holian and collaborators [171] studied pore collapse in a Lennard-Jones solid to understand the mechanisms of energy localization. The authors found that, for shock strengths above a critical value, the hot spot temperature resulting from pore collapse increases with defect size, but this trend saturates for larger pores due to the mechanical work needed to close these large pores; this slows down the ejected molecules responsible for the initial temperature rise. The density of hot spots in addition to their individual strength, is believed to be important in the transition to detonation. More recent work using the AB chemistry model has incorporated multiple voids into a sample in order to study the detonation wave that forms cooperatively across multiple hot spots [66].

The development of the reactive force field ReaxFF in the early 2000s [53] enabled the first MD simulation of shock loading of a realistic HE material [77]. ReaxFF was shown to have the ability to describe the complex chemistry of explosives, including uni-molecular and multi-molecular pathways for various HE materials. These early simulations, while very small by today's standards, revealed surprisingly fast initial chemical reactions, right after the passage of the shock. These results and subsequent ones are, at least partially, in conflict with the up-pumping model, which

requires the energy deposited by the shock into long-wavelength, low-frequency vibrational modes to be transferred to high-frequency bond vibrations, which can then trigger chemical reactions. Assessing the accuracy of reactive force fields to describe fast chemical reactions under extreme conditions remains challenging due to the lack of experimental data with the required resolution. The first MD shock simulations of the decomposition of an HE material [77] were performed soon after the development of ReaxFF for hydrocarbons. [71]

Since then, a suite of work has been focused on the condensed phase reactions of these energetic materials. A nice collection of condensed phase reactivity was collected by Zhang *et al.* for the pair of materials HMX and RDX [172]. As has been the approach of many other researchers, the shock compressed state was not assessed directly, but rather reactions at a number of compression ratios and temperatures that comply with the Hugoniot relations [168] were taken as the initial state of the simulation.

Reactive MD simulations were also used to extract kinetics parameters (those needed for the overall rate equation) for the condensed phase chemistry of TNT [136], RDX [172], HMX [173] and NM [137]. These reaction rate predictions are surprisingly accurate, given only a subset of possible reactions are parameterized against, when compared with *ab initio* or experimental decomposition. A key contribution of these simulations is their ability to isolate the contributions of competing reaction paths. Long *et al.* [173] showed a very detailed kinetics analysis of over nine thousand different reaction paths for HMX at various densities, which allowed for an accurate prediction of the entire reaction zone in detonating HMX.

Very recently, it has become possible to simulate realistic HE materials with scales sufficient to study the interaction of shocks with defects and their effect on chemical initiation. Shi and Brenner used a nitro-cubane (NC) specific reactive potential that accurately captured the shock response of a heterogeneous material of NC and a polymeric binder [57]. They showed how the reflected shock wave at the interface between the two materials localizes mechanical work that initiates chemistry in a

small area. Follow-ups to this work use a similar interface geometry but with various energetic materials (RDX, PETN and Si-PETN), each with a hydroxyl-terminated polybutadiene polymer [174, 175]. These publications studied areas of localized reactivity at interfaces where the shock wave is reflected back onto the compressed material and shear-induced hot spots at angled interface.

Here, the focus is on hot spots originating from the shock-induced collapse of voids within the secondary energetic material RDX. Such defects are presumed to be the dominant initiation sites in this class of materials, and most initiation models include some ad hoc representation of their physical response. [176–178] Continuum models have been used to analyze the hot spot initiation process, but these necessarily make assumptions regarding reaction kinetics, local equilibration and materials properties that are not well-known under the conditions of interest [161, 179–186] Additionally, continuum simulations are limited in their resolution by the underlying computational mesh (with cell dimensions typically ranging from a micro to 10 nm) and, in the case of nanoscale hot spots, by the validity of continuum descriptions when properties change significantly over few nanometers. MD simulations provide, naturally, atomic resolution. The pertinent question is, then, whether they can access a sufficiently large spatial and temporal regime for analysis. As shown below, the MD simulations here capture, for the first time, the transition to deflagration following the formation of a hot spot in a realistic material with subdetonation conditions, and with no other approximation than those inherent in the interatomic potential used. It was found that multistep chemical reactions, including the formation of exothermic products, occur in time scales shorter than previously thought and contribute to the development of a deflagration wave characterized by an extremely thin chemical reaction front. Similar to the methods of the vibrational hot spots in the previous section, the reaction details from hot spots that are dynamically formed are compared to those that best resemble equilibrium conditions. It was found that the non-equilibrium reactions resulting from shock compression result in a completely different ignition behavior than ‘statistical’ hot spots.

3.4.1 Simulation Details

In order to characterize the role of pores on the initiation of energetic materials, simulations of supported shock loading of a series of RDX samples with pores of various sizes ranging from 10 to 40 nm in diameter were explored. The initial structures for the simulations consist of a perfect crystal of α -RDX with the exception of a single cylindrical pore of variable size. Figure 2.1 shows the initial structure of the largest system studied, with a pore 40 nm in diameter and obtained by replicating an α -RDX unit cell (8 molecules) 84 times along the \mathbf{x} [100] direction, 3 along the \mathbf{y} (the axial direction of the pore), and 204 times along the \mathbf{z} (the shock direction, [001] crystal direction). The total length of the largest simulation along the shock direction is 243.1 nm and its width is 120.6 nm, where the cylindrical pore of 40 nm in diameter is centered 60 nm from the impact surface. The structure was relaxed via energy minimization and equilibrated at 300 K under isobaric, isothermal conditions for 5 ps followed by isochoric, isothermal conditions for 10 ps. Similarly, samples are built with 20 and 10 nm pore diameters with linear dimensions along \mathbf{x} and \mathbf{z} scaled by the pore diameter. That is, the sample with the 20 nm pore was created by replicating the unit cell $42 \times 3 \times 102$ times, while the 10 nm pore was created by unit cell replications of $21 \times 3 \times 51$ times. In these smaller samples, the pores are centered at 30 and 15 nm from the sample edge, respectively.

All simulations were performed using the LAMMPS package [35] with atomic interactions described by the ReaxFF force field. [53] The parametrization used [129] has been trained to describe numerous unimolecular and multimolecular reactions. Specifically, the force field used here merges the nitramines force field from ref [134] with the combustion branch of ReaxFF [71] using training data that captures numerous unimolecular and multimolecular reactions for RDX. Self-consistent partial atomic charges are updated [69] at every time step (0.1 fs) using a conjugate gradient method with a tolerance of 1×10^{-6} , which has been shown to properly describe chemical reactions at extreme conditions. [129] ReaxFFs accuracy to describe mechano-chemistry

in nitramines, including combustion of RDX, has been established in several prior publications [77, 134, 187, 188], as well as shock induced chemistry in the energetic nitroester, PETN. [133, 189, 190] While baseline tests indicate the appropriateness of ReaxFF for the problem at hand, uncertainties in the description of atomic interactions are inescapable for such complex systems. As discussed below, comparison of the evolution of the dynamically formed hot spot with an artificial one show that the main conclusions of the paper are robust with respect to such uncertainties.

To establish a supported shock wave, all atoms are assigned at time zero an additional velocity over their thermal ones toward an infinitely massive piston, modeled here as a momentum mirror. The shock is then modeled using constant energy MD (NVE ensemble). A particle velocity of 2 km/s (leading to a pressure of approximately 11 GPa) was chosen because it leads to insignificant chemistry in a defect-free sample (at least on the sub μ s time scales of accessible to MD), and the effects of pore collapse can be isolated. For the chosen particle velocity, the shock front is sharp (about 4 nm thickness) and the material is plastically overdriven, [191] i.e. plastic deformation occurs immediately following the shock front.

The local averaging of relevant quantities such as temperature, composition and density are carried out using the procedure from Section 2.2. In order to save on computational cost, a simplified approach was undertaken to identify molecular species that are in contrast to the vibrational insults from the previous section. Here, several millions of atoms are tracked simultaneously, which is very memory consumptive; storing ReaxFF calculated bond orders for each atom adds to this problem. Since local properties are already necessary for the planned analysis, bonds were identified using distances between atoms rather than bond orders (which would have been more accurate). To ensure that this was not a poor approximation, three test simulations were carried out at different densities of RDX. Each allowed for the material to decompose at a fixed 1500K, and the resultant molecular species were calculated with either a distance or bond order criterion. The results are shown in Figure 3.12 and the associated distance cutoffs shown in Table 3.1. The discrepancy is not too severe,

though the distance-based criterion does come with significantly more noise in the populations it reports.

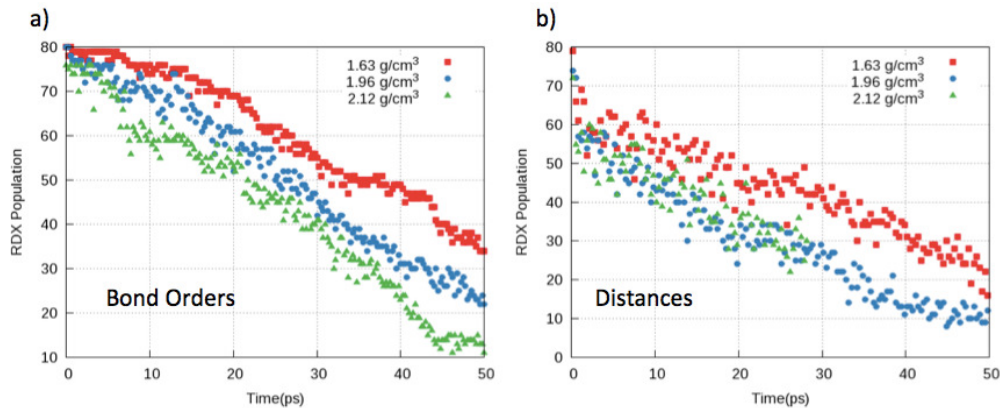


Figure 3.12. Populations of RDX over time at different densities calculated using the ReaxFF bond orders a) and b) RDX populations calculated using atomic distances. Each system is heated to 1500K in the NVE ensemble.

Table 3.1.

Distance cutoffs used to identify bonds for molecule recognition, length in Angstroms

<i>Elements</i> — <i>H</i> — <i>N</i> — <i>O</i> — <i>C</i>	
<i>H</i> — 1.51 — 1.65 — 1.65 — 1.65 — 1.25	
<i>N</i> — 1.65 — 1.70 — 1.70 — 1.40 — 1.74	
<i>O</i> — 1.65 — 1.40 — 1.37 — 1.60 — 1.65	
<i>C</i> — 1.25 — 1.74 — 1.74 — 1.65 — 1.75	

Much like the vibrational insults shown previously, the resulting reactions need to be compared to an equilibrium, which in this case is a controlled introduction of a hot spot into an otherwise static simulation. To simulate purely thermal hot spots equivalent to those formed under pore collapse, several hot spots were created that match the dynamical one in thermodynamic conditions, and with similar shapes and

sizes using a thermostat only in select regions of the sample. These hot spots are created within a simulation cell that is preheated to 500 K and precompressed to 11 GPa. These conditions are chosen to match the bulk conditions of the shocked, unreacted, and defect free regions of the crystal. Temperatures in the hot spot are ramped from 500 to 2000K in 2.0ps (same as the shock rise time), and then subsequently held at 2000 K for 2.0 ps, while keeping the rest of the sample at 500K. Afterward, the thermostats are removed, and the evolution of chemistry is followed under NVE conditions. Several different geometries and sizes of these artificially formed thermal hot spots were studied, as discussed in the next section.

3.4.2 Results and Discussion

The interaction of the shockwave with the cylindrical pores of different sizes results in similar processes and leads to the formation of hot spots in all cases. Local temperature maps of T_{CoM} and T_{Vib} at various times (Figure 3.13) provide insight into the void collapse process and subsequent chemistry. Time will be measured from the point when the ejecta impact the downstream surface of the void (t_0 in the second row of Figure 3.13). As the shock hits the upstream section of the void, a rarefaction wave is created, while the ejecta expands freely into the vacuum and undergoes slight cooling. The material entering the pore near the periphery heats up due to friction; see temperature maps at $t = t_0 - 1$ ps. The impact of ejected material against the far wall of the pore leads to a significant spike in the local temperatures, giving rise to a crescent-shaped hot spot; see temperature maps at t_0 in Figure 3.13. Note that the initial hot spot is far away from local equilibrium, with molecular center of mass DoF (which couple strongly with the translational energy in the shock) exhibiting a significantly higher temperature than the intramolecular DoF. This impact generates a forward directed shock that starts out stronger than the initial, planar shock though its strength diminishes with time because of its divergent flow. The collision also generates a backward-directed shock wave that recompresses and heats the material that has flowed into the void; see times 5 and 12 ps in Figure 3.13. The hot

spots for all pore sizes are characterized by significantly higher temperatures than the homogeneously shocked material, and give rise to accelerated chemical reactions.

Locally, the initial temperature is somewhat independent of pore size (around 1500K), but the volume of high temperature material increases with void size. Figure 3.14 shows the time evolution of the spatial extent of the dynamically formed hot spots for different pore sizes by tracking the amount of material in the simulation cell above 1700 K. This choice of cutoff temperature is, of course, arbitrary, but motivated by the timescales relevant to MD, and this temperature effectively captures the area of reacting material. In all cases studied, there is an initial sudden rise in the hot spot area due to the collision of the ejected material with the downstream wall of the pore. The overall behavior described thus far is fairly consistent with current understanding of hot spot formation from continuum modeling and experiments. [133, 180, 182–186, 192] An important distinction is the initial temperature spike and local nonequilibrium state at short times, which continuum models suppress through limited resolution, artificial viscosity and equilibrated equations of state. Following pore collapse, thermal conduction away from the hot spot and the initial endothermic reactions quench the hot spots for the smaller pores with 10 and 20 nm diameters, as shown in Figure 3.14. The remarkable result of the simulations is that the 40 nm pore results in a rapid, self-sustained deflagration wave. This critical size is somewhat smaller than previous estimates for RDX and for the closely related HMX. [161, 178, 181, 185] Next, the discussion will revolve around the transition to deflagration and the key molecular processes that enable it.

A detailed analysis of the 40 nm void simulations provides a description of the transition to deflagration with unprecedented detail that reveals three distinct stages. To illustrate this process, Figure 3.15 also shows maps of the molecular fractions of key species: RDX, main intermediates (NO_2 , NO , OH , $HONO$, $COOH$) and product molecules (N_2 , O_2 , CO_2 and H_2O). Figure 3.15 shows profiles of the same quantities as a function of position along the shock direction, averaged spatially over 3 nm along the center of the hot spot and across 0.3 ps.

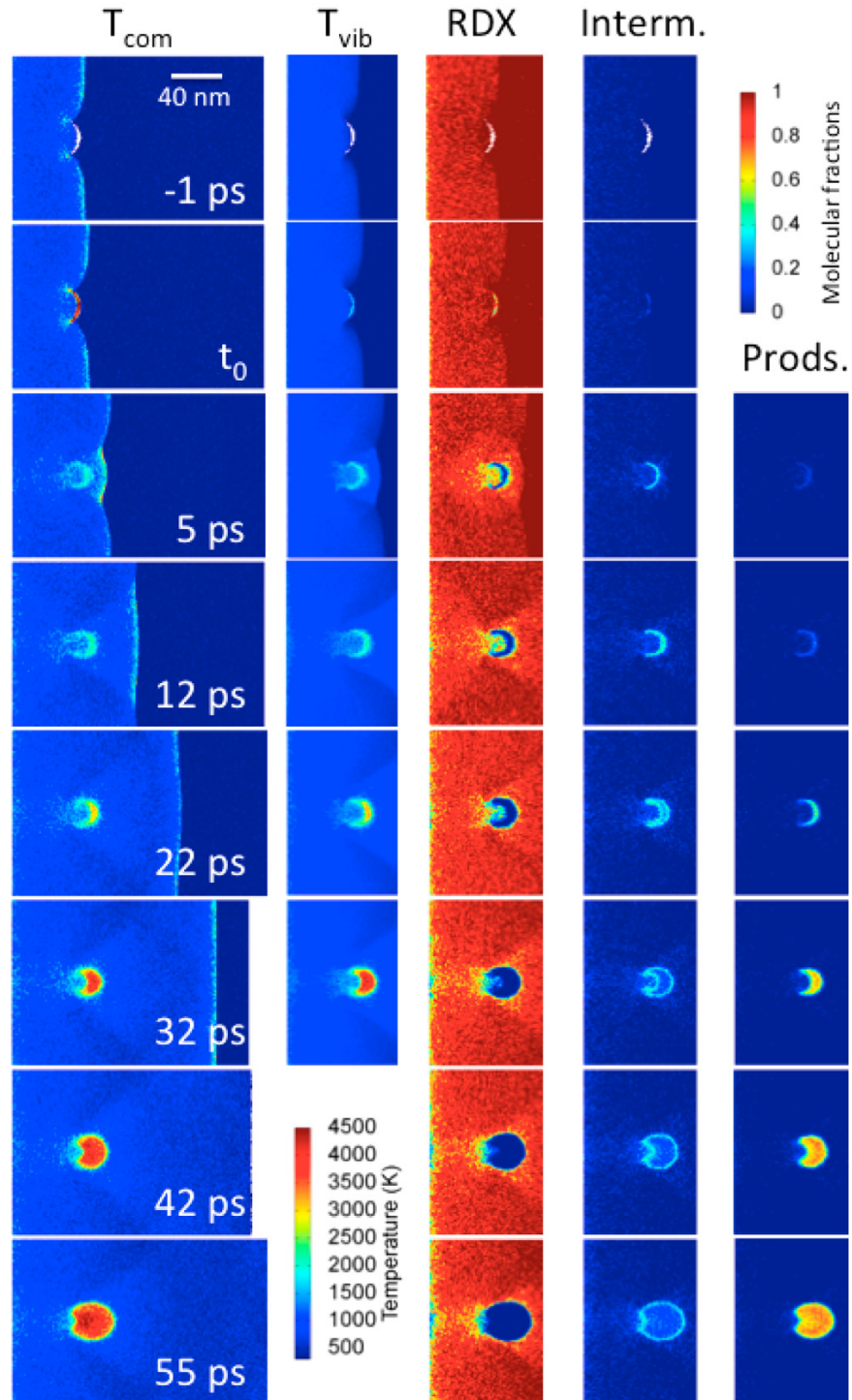


Figure 3.13. Maps of T_{CoM} and T_{Vib} , as well as molecular populations for RDX, intermediates and products at key stages in the shock to deflagration transition. t_0 corresponds to $t = 17.3ps$ after impact with the piston.

The first of the three stages lasts approximately 10 ps. During this period, the hot spot evolves from a very narrow crescent, generated by the molecular collisions during the pore collapse with a nonequilibrium temperature distribution ($T_{CoM} = 4000\text{K}$, $T_{Vib} = 1500\text{ K}$), to a broader crescent (5 nm at the broadest point) and more equilibrated temperature ($T_{CoM} = T_{Vib} = 2000\text{K}$) at 5 ps. This early evolution is captured in Figure 3.16 from panel A) to C), which highlights which molecular species are present during these early reactions. Surprisingly, this stage involves significant chemical reactions that traverse the entire multistep reaction path of RDX: its decomposition, a significant formation of intermediates, and the initial formation of products. The initial decomposition steps in secondary explosives such as RDX are endothermic and they tend to quench the hot spot. These reactions suppressed the growth of the 10 and 20nm pores enough to quench the overall reaction. Rarefaction waves and thermal conduction have the same effect, as they lower and disperse the temperature. However, the exothermic formation of products has the opposite effect, and their unexpectedly fast appearance helps maintain the hot spot temperature. As will be shown below, the reactions that follow the void collapse occur much faster than under thermal decomposition conditions. Thus, it can be concluded that this fast formation of product species is due to a combination of nonequilibrium (more on quantifying this in the subsequent discussion) and mechanochemical processes caused by the dynamical loading, [193,194] and this plays a nontrivial role in the development of the deflagration wave.

During the second stage of the reaction process (between approximately 10 and 25 ps after pore collapse), the material is in local thermal equilibrium and the formation of product species accelerates significantly. Two distinct reaction fronts form, one that propagates forward and sideways into the crystalline RDX surrounding the original pore structure, and one that travels more rapidly backward into the amorphous material pushed into the pore. The formation of final product species is accompanied by a rapid rise in temperature from approximately 2000 to 4000 K. At the end of the second stage, the core of the hot spot is close to fully reacted, and it has

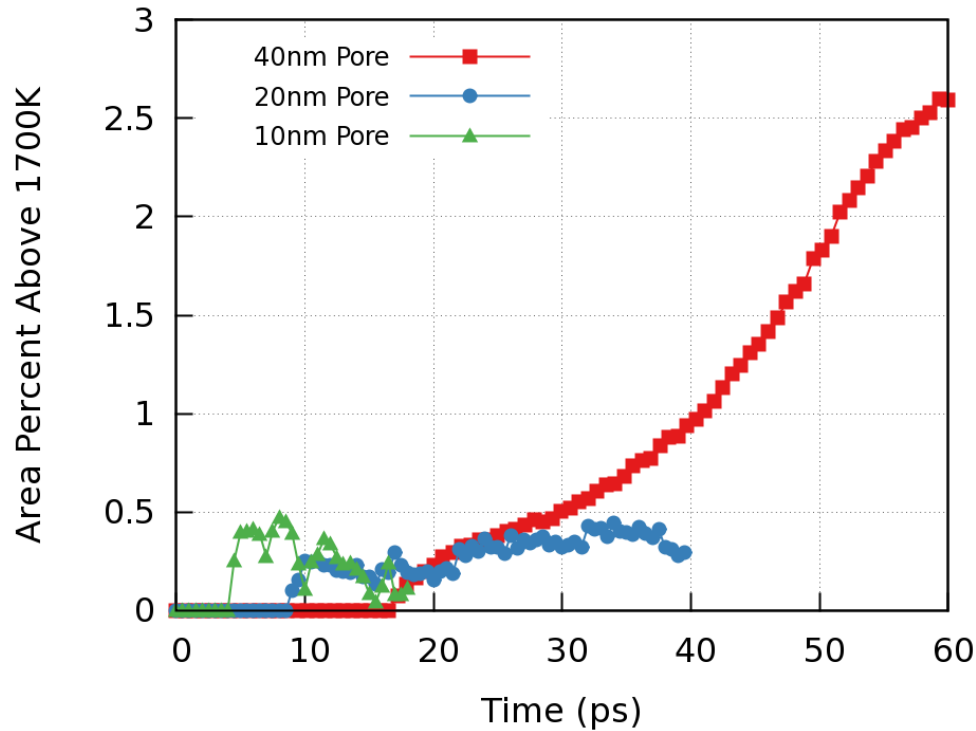


Figure 3.14. Area percent of material above a preset ignition temperature of 1700K for all pore sizes studied. Note the quenching of voids smaller than 40 nm. Raw simulation time is used here rather than the shifted reference as used in Figure 3.13

achieved a steady-state temperature close to 4000 K. This corresponds to times $t_0 + 12$ and $t_0 + 22$ ps in Figures 3.13 and Figure 3.15 B). The deflagration fronts show a well-defined structure of RDX/intermediates/products with a reaction zone width of about 5 nm, which is significantly smaller than those considered previously. [162, 180, 181] Also note that there are further, slower reactions continuing subsequent to this initial process, but a substantial amount of energy is released in this remarkably thin front.

The third stage involves the continued propagation of these narrow deflagration fronts at speeds of 250 m/s. The hot spot evolves from a crescent into a circular shape through slightly faster growth backward into the reshocked material occupying the formerly vacant pore space (see Figure 3.16 D). The faster rate can be attributed to the material being at a somewhat higher temperature, its structure being non-

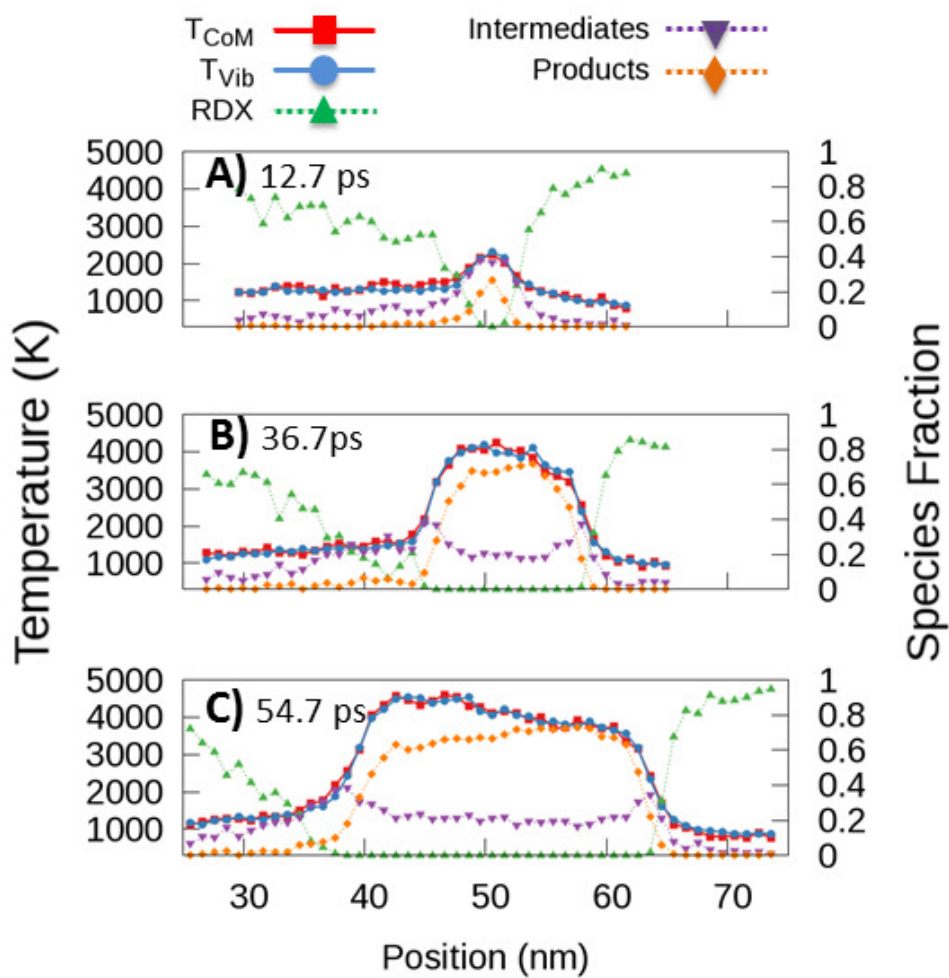


Figure 3.15. Profiles of T_{CoM} and T_{Vib} (left axis), and molecular populations of RDX, intermediates and products (right axes) at key stages in the shock to deflagration transition. Time is measured from void collapse (17.3 ps after impact)

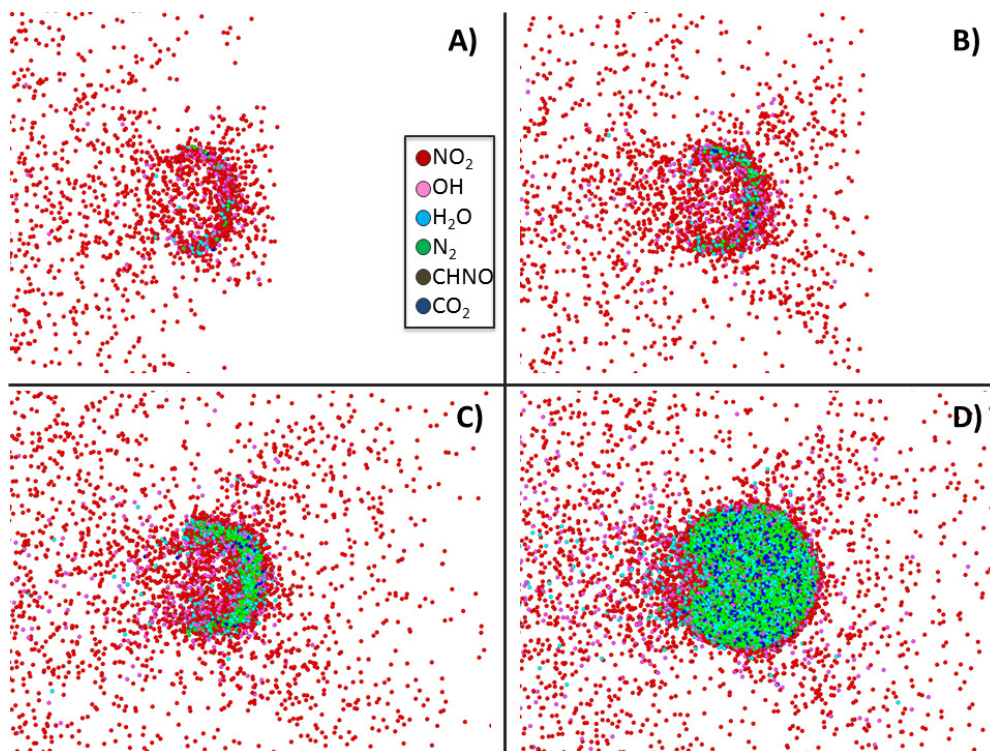


Figure 3.16. Example time snapshots of the intermediate and product molecules formed after the collapse of a 40nm void in RDX. The narrow reaction front that forms includes molecules from the entire reaction path of RDX decomposition.

crystalline, and may also be partially sensitized from partial decomposition of the RDX (see Figure 3.15 C), D)). The deflagration fronts propagate at near steady-state conditions in the simulated time here. These deflagration velocities are comparable to those measured for HMX under similar conditions (140 m/s) and are much faster than rates predicted from continuum models (7 m/s). [181,195]

To obtain additional insight regarding the conditions that make a hot spot critical, the details of the chemical reactions after the collapse of the 40 and 20 nm voids are studied. Internal and molecular temperatures of the RDX molecules right before they decompose are analyzed (averaged over 0.1 ps before they are last identified as a molecule), as are those of the intermediates and products during the first 0.1 ps of their existence. Figure 3.17 shows the time evolution of these temperatures

following the collapse of the 20 nm void (a) and the 40 nm one (b). In both cases, one can observe the initial RDX decomposition ($t < 10ps$) occurring away from local equilibrium, and for later times the internal temperatures are just below 1,500 K for the 20 nm case and just above 1,500 K for the 40 nm case. What is clearly different though, is that during the first few picoseconds after pore collapse, the intermediates for the 20 nm case are produced at a lower temperature ($\approx 1250K$), which is consistent with an endothermic reaction process. The products are produced at a somewhat higher temperature ($\approx 1500K$), consistent with an exothermic process. Importantly, these temperatures remain constant in time. In contrast, for the 40 nm pore, the intermediates form at higher temperatures (1750 K), and the products at a markedly increased temperature (2000 K). This indicates that there are sufficiently prompt exothermic reactions to elevate the local temperature, which then rapidly increases as the deflagration wave develops (10-30 ps). The temperature distribution between reactants, intermediates and products at late times (greater than 50 ps), coupled with the spatial distribution noted above, is analogous to flame structure profiles, [187,196–198] but happening over significantly smaller scales due to the high pressure/density. It is important to note that maintaining a critical temperature over a region of the material, against thermal conduction away from the hot spot and endothermic reactions, for a sufficiently long time is consistent with the standard hot spot models. [161,181,182] Lastly, these simulations indicate that the fast generation of exothermic products contributes to the criticality of nanoscale hot spots and, as will be shown next, so does its dynamical origin. The next key question is whether hot spot size and thermodynamic conditions alone are sufficient to determine its criticality. Thus, the temporal evolution of the hot spot formed by the collapse of the 40 nm pore with a family of artificial, thermally activated hot spots at equivalent thermodynamic conditions and sizes are compared. The artificial hot spots are created within a single crystal of α -RDX, measuring 40 nm by 3.6 nm by 40 nm, which has been precompressed and heated to shock conditions (11 GPa and 500 K). In all of the artificially seeded hot spots, a core temperature of 2000 K was assigned by

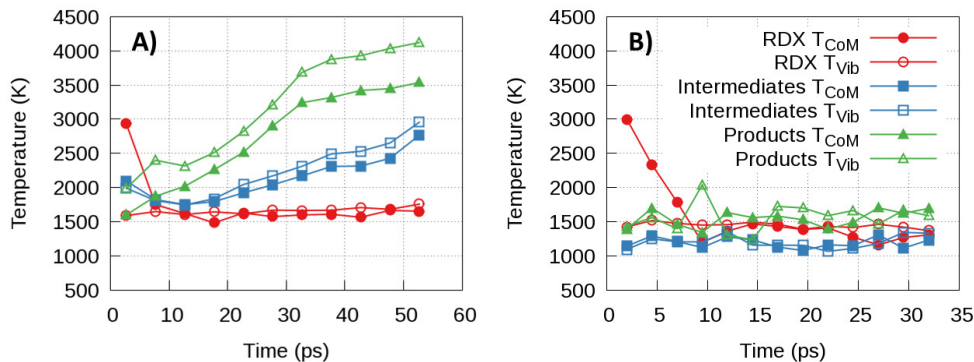


Figure 3.17. T_{CoM} and T_{Vib} of RDX molecules at the time of their decomposition, and those of intermediates and products at the time of their formation: (a) 20 nm void; (b) 40 nm void.

heating the region to that value in 2 ps, to match the heating rate experienced by the dynamically compressed material. These regions are then held for an additional 2.0 ps at $T = 2000\text{K}$ before completely removing the thermostat to ensure the hot spot evolves from the intended temperature. Parts B)-D) of Figure 3.18 show temperature maps of the initial configurations of all the artificial hot spots; for comparison, the hot spot formed after the collapse of the 40 nm pore at time $t = t_0 + 5\text{ps}$ is shown in Figure 3.18 A). The crescent shaped hot spot, Figure 3.18 B), matches the dynamical one in area. A broader crescent is used only for computational convenience; the area of RDX above 1900 K is equivalent at 30nm^2 between it and the shocked loaded sample. The circular hot spots are larger in area than the dynamic one. The hot spot in Figure 3.18 C) has a circular cross-section 10 nm in diameter, and the one in Figure 3.18 D) includes a 10 nm diameter region at 2000 K, surrounded by a region at 1000K with outer diameter of 20 nm. Figure 3.18 also shows temperature maps for each hot spot at a later time ($t_0 + 50\text{ps}$).

Parts A)-D) of Figure 3.19 compare the molecular population evolution for all cases (insets display the initial 10ps of chemistry, respectively). Quite surprisingly, the crescent-shaped artificial hot spot that matches the dynamic hot spot in size, Figure 3.18 B), does not become critical; while some reactions are observed, Figure

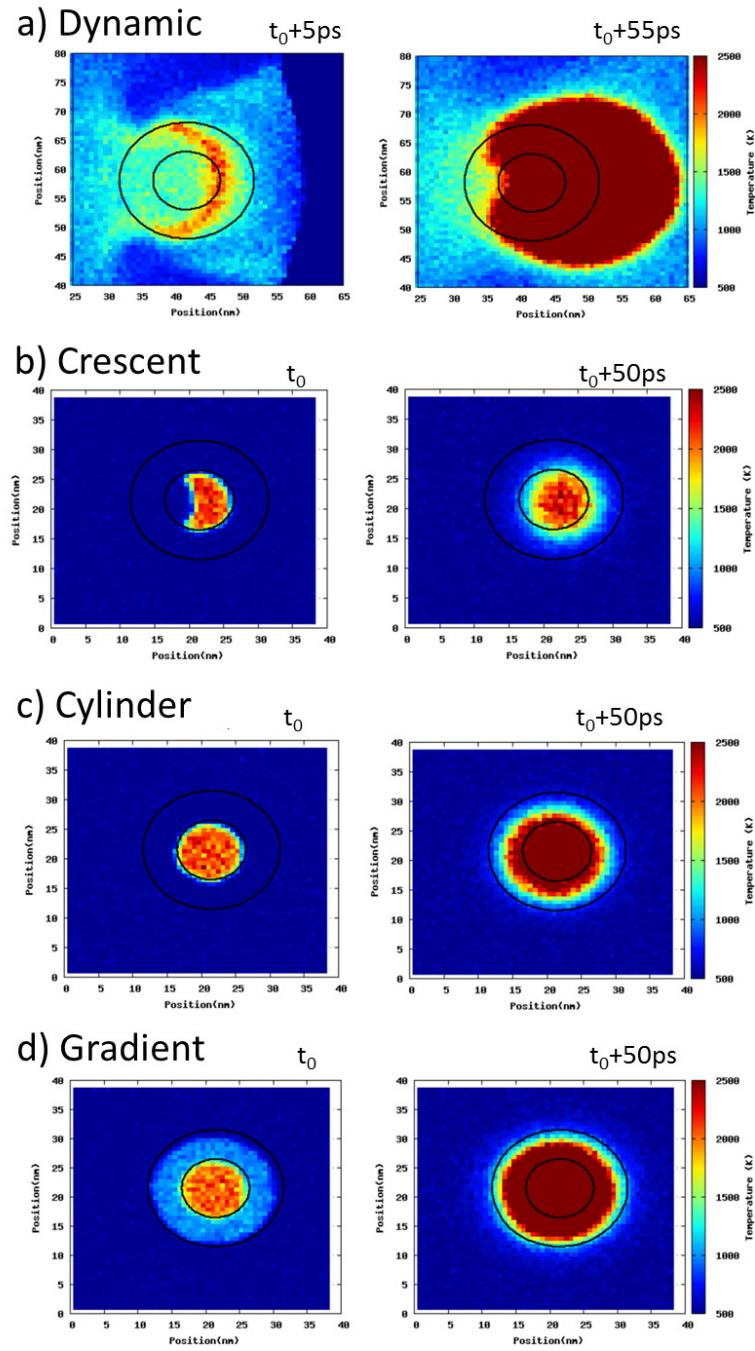


Figure 3.18. Initial and final states of the (a) dynamic hot spot formed following pore collapse, (b) crescent shaped thermal hot spot initially at 2000 K, (c) cylindrically shaped hot spot heated to 2000 K, and (d) cylindrical hot spot with an inner disc heated to 2000 K and the outer ring heated to 1000K.

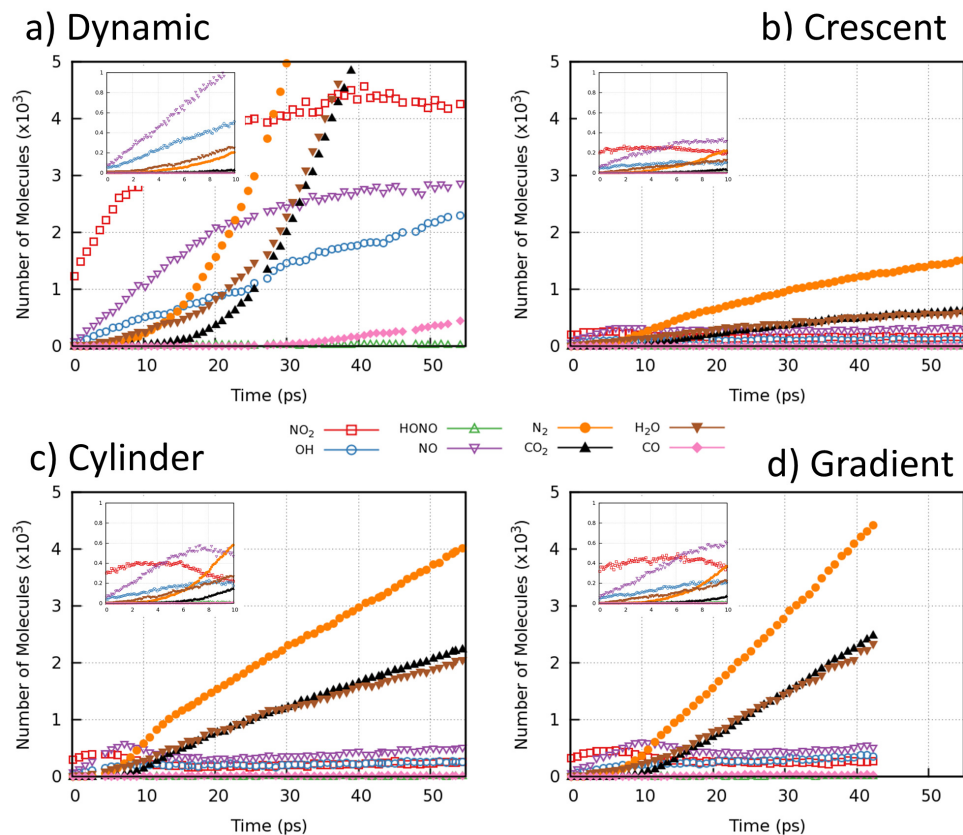


Figure 3.19. Chemistry evolution following shock and thermal initiation. Insets show an expanded view of events within the first 10 ps.

3.19 B, they are significantly slower than for the dynamical case, and the artificial hot spot quenches in 80 ps. The circular hot spots, larger in area than the dynamic one, do become critical, but at much later times. The temporal evolution of intermediate and final product species for the dynamic and thermally induced hot spots shown in Figure 3.19 provide insight into the differences. A dramatic production of intermediates (NO_2 , NO , OH) is observed during the first 10 ps of the dynamical hot spot (Figure 3.19 A), while these species remain relatively low in population over the same interval in the thermally activated cases (Figure 3.19B-D). Interestingly, in spite of being considerably larger than the dynamical one, their production of final exothermic products (N_2 , H_2O , CO_2) is considerably slower. In addition, the population of

the product species grows linearly in time, while the mechanically induced hotspot shows quadratic growth. These comparisons demonstrate that size and equilibrium thermodynamic state alone are not enough to characterize nanoscale hot spots that originate during dynamical loading. [182] The shock-induced pore collapse gives rise to very rapid reactions, accelerated by the mechanical concentration of energy, which play a key role in the criticality of nanoscale hot spots, and which should be accounted for in mesoscale models.

3.4.3 Conclusions

As with any theoretical predictions, it is important to establish model confidence for the problem at hand; this is particularly true for reactive MD simulations such as those presented here, where chaotic dynamics could easily amplify the effects of minor inaccuracies in the potential that are universally present. A comparison of these MD predictions against experiments and experimentally tuned models lends credence to this approach. Tarver *et al.* [161] developed models for the critical hot spot conditions in HMX and TATB based on the analysis of cookoff experiments. These pioneering kinetic models are still considered to be appropriate. [180] For a 100 nm diameter hot spot in HMX (the smallest size shown in their figures), they determined a critical temperature of 1200K that would cause that hot spot to develop into a runaway reaction within approximately 5 ns. From a simple extrapolation of those results down to a 10 nm diameter hot spot, an estimate of a critical temperature of 1600 K would develop into a runaway reaction in 50 ps. The MD predictions on display here show a 10 nm diameter hot spot in RDX at the higher temperature of 2000K does not show signs of a runaway reaction at 50 ps; thus, one can infer that the kinetics in the ReaxFF simulations are somewhat slower than those in Tarvers model. This is consistent with expectations, as RDX is known to have very similar, though slightly slower, kinetics than HMX. [196–198] It is important to stress that the key result of this work is a more mechanistic understanding of hot spot formation,

characterization of the transition to deflagration, and the importance of dynamical loading in their criticality.

Note that for larger voids, the compression of trapped gases provides additional temperature spikes. [180,181,185,186] These simulations do not include trapped molecules; it is believed that, for the small pore sizes used here, the largest 40 nm void in a 3 nm thick (periodic) sample would contain only about 100 molecules at standard conditions, which would not affect the major conclusions of these simulations. Rather than remaining as a separate phase, one can expect those gas molecules to intermix with the rarefying RDX and absorb a minor amount of heat from the collision process.

Finally, it is worth recognizing similar simulations to these have recently been performed with PETN, [133,189] though a full analysis of the reaction processes has not yet appeared. PETN is a more mechanically sensitive material than RDX, and is on the borderline between what are considered primary and secondary explosives. That is, the mechanical breaking of bonds in PETN [133] is a more significant initiation process compared to the thermal disruption associated the hot spot model. Detailed comparisons between these current results, and additional planned studies on the much less sensitive TATB, would be highly significant for the further development of models for explosive initiation.

In conclusion, the first atomistic description of the transition to deflagration following the shock loading of an energetic material provides significant insight into the role of mechanochemical processes occurring at length and time scales that have hitherto been inaccessible either computationally or experimentally. While one must acknowledge that the results should not be considered to be quantitative because of the limited high pressure reaction data available for calibration, there are no glaring inconsistencies with available information. Consequently, it is concluded that the physical processes discovered in this study should be highly relevant. Most significantly, it was found that ultrafast chemical reactions occurring within the first 5 ps of the pore collapse provide a significant impetus to accelerate the reactions beyond what would be expected for a simple thermally activated cook-off process. The exact

role of the non-equilibrium reactions ($T_{CoM} \neq T_{Vib}$) is still in question because the dynamically formed hot spot involves the amorphization of RDX, as well as gradients in pressure and temperature due to the re-shock. All of these other dynamic conditions are hard to reproduce in the artificially formed hot spots, though progress is being made to seed hot spots in purely amorphous RDX. Initial data in these new experiments show that the amorphous material can transition to deflagration at lower hot spot temperatures than the crystalline equivalent. Additionally, it was found that a local deflagration wave with a surprisingly small width (5 nm) rapidly develops in about 30 ps. Consequently, the small hot spots studied here are not immediately quenched by divergence factors or endothermic reactions. These results show that nanoscale hot spots should play a larger role in the initiation of energetic materials than previously thought. Lastly, note that the effect of loading conditions on accelerated chemistry may be less critical in larger hot spots, where quenching due to thermal diffusivity is not as significant, or for more gradual compression processes resulting from more diffuse loading fronts.

CHAPTER 4. THERMAL RESPONSE TO ACOUSTIC ENERGY INPUT

In reference to the title of this thesis, the following chapter will be concerned with the localization of energy provided by an acoustic wave. While the previous chapter dealt with more academic problems concerning the detailed chemistry of an energetic material, the work in this chapter will aim to best mimic a realistic energetic material. To that end, the material studied here will not be completely homogeneous and will include the polymeric binder that is common to all explosives for safety concerns. This work will address the capability of sound waves to detect subsurface features in a realistic energetic material and the capability for its use in the detection of explosives. By carefully preparing unique microstructures and controlling the details of the external stimuli, an understanding of the heating mechanisms within the composite material has been developed. Because the main experimental design space has to do with the strength, frequency and polarization of the incoming sound waves, the simulations shown here will follow suit.

4.1 Introduction

Detection of controlled or home made explosives at a distance remains an unsolved problem due to low vapor pressures of the energetic material and dynamic environment conditions. [199] However, a small increase in temperature would yield orders of magnitude increase in vapor pressure, which enables many chemically specific detection methods. [200–204] The use of a weak mechanical insult such as an acoustic wave has been proposed recently due to several advantages relevant to stand-off detection. First, the attenuation of sound waves in solids occurs over a very long length scale, meaning subsurface features contribute strongly to the materials' response. Therefore, energetic material hidden behind shielding layers is still able

to couple to the penetrating sound wave, providing the observer with, hopefully, a detectable signal. This acoustic inspection of materials has already been proposed as a non-destructive means to detect flaws, such as pores or cracks in engineered parts. [205] Here, a local temperature rise is detected once the heat dissipates to the surface, and the subsequent radiation is collected with an IR camera. Ideally, the thermal signature can be detected closer to the source of the heat generation, because it would provide more information about the material. In the present application, the increased temperature could provide a stronger electromagnetic signal characteristic of the material being probed. Or, alternatively, if the heating is localized in the energetic material itself, the acoustic insult could initiate decomposition. This later case would only be sought after if the user can provide the acoustic stimuli at a safe operating distance, but the limitations of this aspect of detection are beyond the scope of this work. Some of the potential mechanisms of heat generation from an acoustic insult were collected and described by Renshaw [205]; these include contact friction, plastic deformation and, additionally, viscoelastic losses. Also, Suslick *et al.* and Reifsnider emphasized that interface delamination could be a potent means of heat generation in solids; the former authors showed this effect with energetic crystals with various surface coatings. [206,207] Loginov has shown that the acoustic heating of energetic material is strongly frequency dependent, with some driving frequencies capable of initiating a reaction in RDX or lead azide. [208] Studying similar polymeric bonded explosives (PBX) containing energetic compounds HMX or TATB, Sutherland and Kennedy [209] showed that, in the frequency range of 0.5 to 4MHz, the compliant binder would decompose more readily than the crystalline explosive. This study suggests that the acoustic heating of composite materials is heterogeneous, and that which component is coupled to the stimulus can be controlled. More recently, in a series of publications Mares *et al.* explored a large driving frequency window in order to determine which heating mechanisms were active for isolated energetic crystals embedded in a polymer medium [210,211]. They found that below 1MHz viscoelastic losses dominated, but above an approximate of 10MHz particle size effects increased

the viscoelastic losses due to particle-particle friction. These particle size effects can be estimated by using the characteristic size of each crystal and the effective sound speed of the composite medium; the ratio of these quantities defines an approximate structural resonance frequency. This, of course, assumes that the crystalline grains are mono-dispersed in size, but also that the interfaces between each component do not disrupt the transmission of the elastic wave. The details of the interfaces between each material in the PBX is important for the localization and conversion of the mechanical energy into thermal energy, and thus ultimately the detection of the explosive. In order to extend the work from Mares *et al.*, molecular dynamics simulations are used to predict which component of the composite will localize the energy from the mechanical insult as a function of the interface characteristics between either material in the PBX [210,211].

4.2 Acoustic Coupling To Heterogeneous Media

The simulations shown in this chapter are unique with respect to all the other work on display in this document because they do not use a reactive force field. Primarily, this is driven by the need to run much longer simulations than is reasonably achieved using ReaxFF. Chemical reactions are not expected here, because this chapter is concerned with the thermal response of a material, but where the temperature rise is not severe enough to cause bonds to break. Therefore an expensive bond order potential is not needed. There is a significant computational reduction in having predetermined bonds and static atomic charges; in fact, the cost per timestep for two systems of the same size may be an order of magnitude less for the nonreactive IAP. Furthermore, larger timesteps (1fs versus 0.1fs) can be afforded, since the dynamics of the charges on each atom are now fixed.

Here, a pair of nonreactive IAP are used to describe each component of a composite material, respectively. This composite material is composed of a crystalline energetic material and an amorphous polymer arranged in a laminate structure with triply periodic cell dimensions. The energetic material is described by the Smith and

Bharawaj potential, while the polymer is described with DREIDING [40], and each system has Coulomb and van der Waals energies calculated between them. [212,213] Special care has to be taken to integrate these two subsystems together, specifically because the details of the interface between them is the focus of the work here. When designing these simulation cells one must consider the relevant length scales for sound propagation, as well as thermal conduction in the sample. While the sample is coupled to the external stimulus, these two effects work against one another to localize energy. The structural resonance frequency, which should couple strongly to the sound wave, is determined by the sound speed and length (or equivalently the elastic moduli and density) of the material in the propagation direction. But, keep in mind that this is a MD simulation, and the goal is to study these vibrations over time, but a resonance period of microseconds is not feasible with the current supercomputers (again with the hardware/software determining the science). Luckily, the physics around acoustic heating should be preserved even if small structures and large frequencies are studied, because these two parameters scale linearly with one another. If one chooses, based on resource availability, a limit of a few nanoseconds of simulation time and the condition that at least one-hundred periods of the acoustic insult is sufficient, then this forces acoustic frequencies into the GHz range (a 100GHz wave has period of 10ps). Experimentally, the sound speed of the composite material is known to be around 2.5 km/s, which forces the simulation cell dimension along the axis of propagation to be at least a few tens of nanometers. [214] In order to simplify the problem a bit, the interface between the two materials will be made perpendicular to the wave direction, which allows for the other two dimensions to be shortened without loss to the accessible acoustic frequencies.

To study the mechanisms for acoustic heating and the role of interface characteristics of a generic PBX, a composite made of octahydro-1,3,5,7-tetranitro-1,3,5,7-tetrazocine (HMX) and polytetrafluoro-ethylene (PTFE or Teflon) was chosen. The HMX portion was generated by replicating a relaxed (300K, 1atm) unit cell 6 by 4 by 16 times, leaving the (001) surface exposed toward the Teflon slab. In order to create

the polymeric portion of the simulation cell, a specialized polymer structure builder was employed. This tool, from Haley *et al.*, is known as Polymer Modeler and is published free to use on nanoHUB.org [215]. A structure of 20 chains of length 1000 monomers each was built at low density initially, then taken to a density of $1.8 \frac{g}{cm^3}$ at 600K using constantly contracting boundary conditions in the directions orthogonal to the free surface over 200ps. Thus far, each subsystem of this composite material has been prepared independently, while leaving an open boundary in the intended wave propagation direction.

To explore the differences in observed heating rates from Mares *et al.*, two different interface types of HMX were prepared [210,211]. Rather than embedding two different materials that possess varying interface characteristics, this simulation effort can precisely control the microstructure of a single material. Here, the two interface types are either planar or diffuse. The former would result from cleaving a crystal and the latter would be the result of crystals that have been aged or damaged. The main benefit of a simulation approach here is that the role of interface characteristics can be isolated and studied for its role in acoustic heating of heterogeneous media. After each subsystem has been properly relaxed, the two materials are heated to a temperature above the glass transition temperature of Teflon (600K used here). They are then merged, leaving a gap such that the interfaces form naturally. The planar interface case was pressed together to a density of $1.8 \frac{g}{cm^3}$ over a time of 100ps without any further modification. In contrast, for the diffuse interface, the HMX molecules at a depth less than 2 nm from the interface were heated to a temperature of 900K, causing them to melt and expand into the free space between the crystalline and polymeric materials. A few example still images of this diffuse structure build process are shown in Figure 4.1, it is important to emphasize that none of the starting HMX molecules decompose during this process, since the force field is non-reactive.

After either interface has formed, the entire structure is allowed to relax in the NPT ensemble at one atmosphere of pressure, which results in a slight expansion in the interface normal direction of the Teflon layer. The external acoustic insult

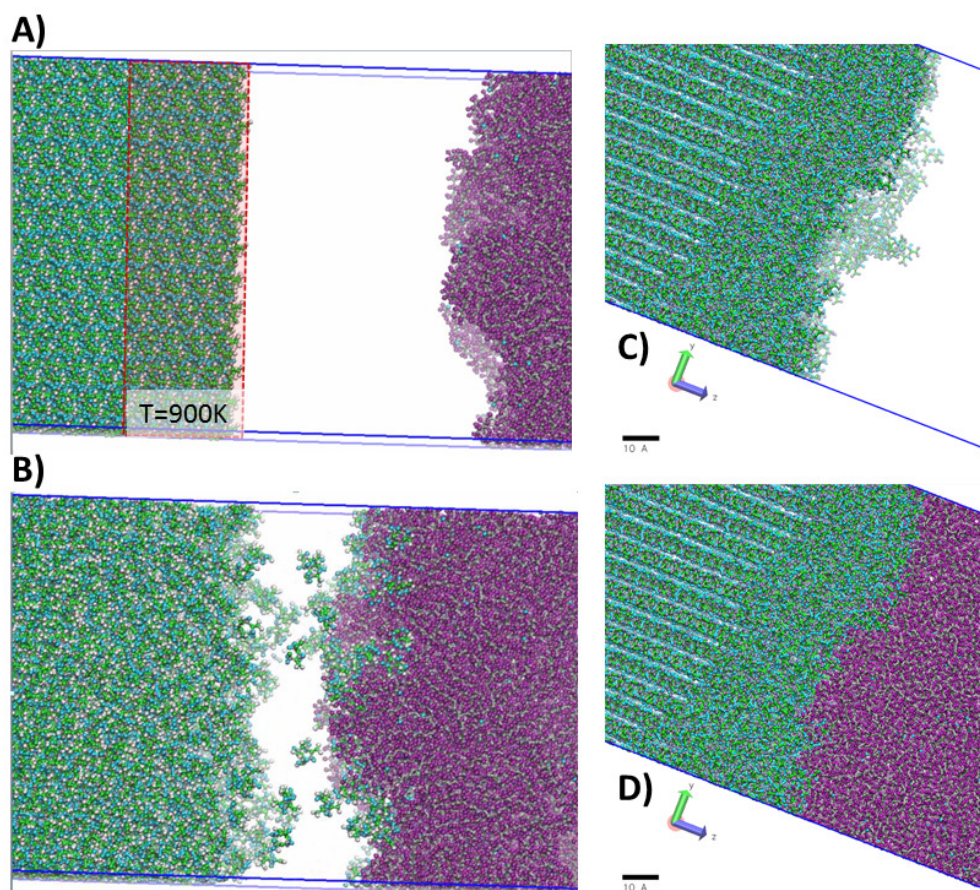


Figure 4.1. Example snapshots of the simulation cell as the PBX is formed. A) Initial structures with HMX to the left and Tefflon to the right. B) While the surface HMX is heated to 900K it vaporizes and forms an amorphous layer as the two systems are pressed together. C) Final structure with the Tefflon layer removed and D) with all components shown, scale bar is 1nm.

is provided to the simulation cell by periodically contracting and expanding the cell dimension, either as a longitudinal (compressive) or transverse (shear) wave. Both wave polarizations use the same amplitude of deformation (0.25nm or 0.012 strain) while the set of frequencies was slightly different; this is further discussed in the next section. Each simulation of an acoustic wave coupling to these microstructures is run in the microcanonical ensemble (NVE), so that any increase in the temperature or total energy is due to the presence of the external stimulus. Using the method outlined in Section 2.2, local properties will be calculated to identify which regions of the microstructure are absorbing and localizing energy from the acoustic insult.

4.2.1 Results and Discussion

After each of the structures have been relaxed, a simple tensile test was performed in order to determine the role of the interface characteristics on the overall mechanical behavior. To do so, a the direction perpendicular to the interface is elongated at a constant strain rate of $5 \times 10^8 s^{-1}$ while maintaining constant lattice dimensions in the perpendicular directions. This control over the lateral dimensions means that only the stress component in the tensile direction should be used, since the material is not allowed to contract proportional to its' individual Poisson ratio. The resulting stress-strain relationship for either interface type is shown in Figure 4.2, panels A) and B), along with representative images of the failure at a strain value of 0.4 in panels C) and D). For either interface, it was observed that the polymer layer would fail through cavitation prior to any interface delamination. This is likely the result of using short chains (low degree of polymerization), which would allow for individual chains to slide relative to one another in the absence of significant entanglement. Being a linear polymer with no side groups, much like polyethylene, Teflon is expected to exhibit little change in its mechanical behavior due to these entanglement effects. It is worth mentioning that atomistic simulations of polymers will always have problems with representing a true polymer with a high degree of polymerization (D_p) due to the excessive atom count needed to look at multiple inde-

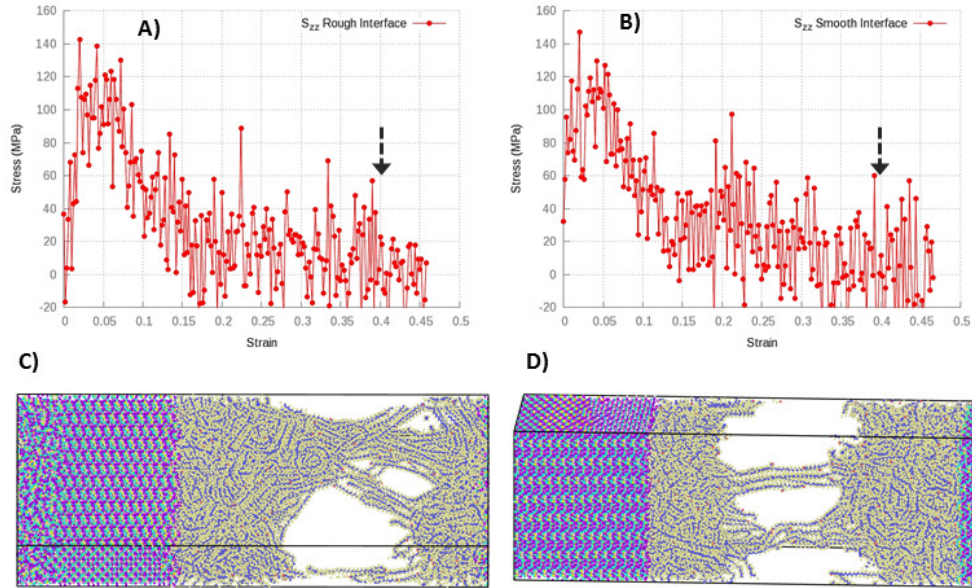


Figure 4.2. Stress-strain curves of tensile loading for the PBX with an A) Roughened or B) Planar Interface, arrows indicate when the snapshots shown in C) and D) are taken, respectively. Qualitatively, the interface properties did not affect the overall mechanical failure.

pendent chains of high D_p . This (qualitative) equality between either structure can be understood by comparing the total interaction energy density between the Teflon and HMX layers. Using the OVITO visualization software package [216], the surface area of the interface was calculated using a 0.35nm diameter probe (approx 1/2 the size of a single HMX molecule) resulting in areas of $198.1nm^2$ and $240.3nm^2$ for the planar and roughened interfaces, respectively. This resulted in total interaction energy densities of $16.3kcal/mol * nm^{-2}$ for the planar interface and $18.4kcal/mol * nm^{-2}$ for the roughened case. This slight change ($\approx 11\%$) in total interaction is likely washed away by the large strain rates that MD necessitates.

Turning now to the results of acoustic excitation of these PBX systems, the goal here is to resolve which heating modes are active, and how the details of the microstructure affect the absorption efficiency of this energy input. As was mentioned in the previous section, the frequency ranges of interest are those close to the structural resonances of either pure component, which of course is a sample size dependent

property. To that end, an attempt was made to distribute the test acoustic frequencies around the expected resonances. Classically, one would expect that the elastic structural resonance (breathing mode of the entire sample) is proportional to the bulk modulus and density ($\omega_{res}^2 = B/\rho$) or equivalently the sound speed and length along the propagation direction ($\omega_{res} = v_{sound}/L$). Since the two subsystems cannot move completely independently of one another with periodic boundary conditions applied, the simulation cell will have a pair of resonance frequencies expected, the symmetric and asymmetric combination of either pure resonance ($\omega_{res}^{total} = \frac{1}{\sqrt{2}}[\omega_{res}^{Teflon} \pm \omega_{res}^{HMX}]$). A transverse wave resonance will use the shear wave speed or the shear modulus in the calculation of these resonances, in contrast to the compressive waves that use the Bulk modulus and typical sound speed. The ratio of the bulk to shear moduli is expected to be approximately one-third, which means the transverse wave resonances are expected to be approx 57% lower than the longitudinal ones.

The set of observed heating rates for the longitudinal wave acoustic insults are shown in Figure 4.3, with the panels A) and B) displaying the rates for the planar and rough interfaces, respectively. Also, the low frequency resonances are shown in panels C) and D). In this range, the Teflon is absorbing most of the energy from the acoustic insult. In all of these plots, the series in red with boxed points represents the total heating rate of the simulation cell, which indicates which driving frequencies couple strongly to the insult. Since each driving frequency uses the same strain amplitude, the power of these insults is no longer constant. To correct for this, the heating rate is reported here as the temperature increase per period of oscillation. Interestingly, as a function of the insult frequency, different areas of the PBX are observed to localize the insult energy. At low frequencies, as shown in Figure 4.3 C) and D), the Teflon is observed to heat up quickly relative to the other components. Between the two observed resonances, the interface between either material localizes the insult energy, and subsequently is observed to heat up quickly. Beyond the high frequency resonances, the crystalline HMX is the predominate absorbing component. Comparing the two interface types, it was observed that the roughened interface

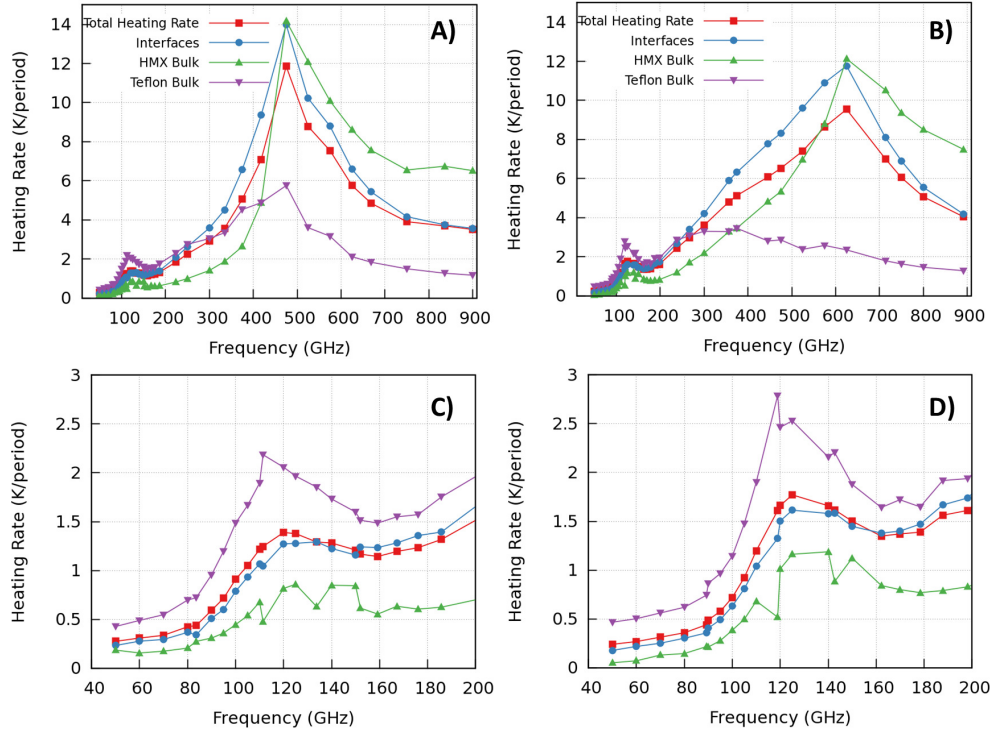


Figure 4.3. Observed heating rates of PBX structures subjected to a longitudinal polarized acoustic wave; the rate is normalized by the period of the oscillation to bias against increased energy deposition rates at high frequencies. The pair of plots shown in A) and C) correspond to the planar interface case while panels B) and D) are the observed heating rates, broken down by region in the sample, for the roughened interface. The the low frequency regime is shown in C) and D).

(Figure 4.3 B)) resulted in a weaker, but broader, high frequency resonance than the planar interface case. Conversely, the low frequency resonance for the roughened interface had an overall higher heating rate than the planar interface.

To better visualize the localization of energy from the acoustic insult, Figure 4.4 compares the local temperatures of each region (at an overall temperature of 400K) for either interface at a driving frequency of 375GHz. At this frequency, the peak temperatures at the planar interface are observed to be much higher than those of the

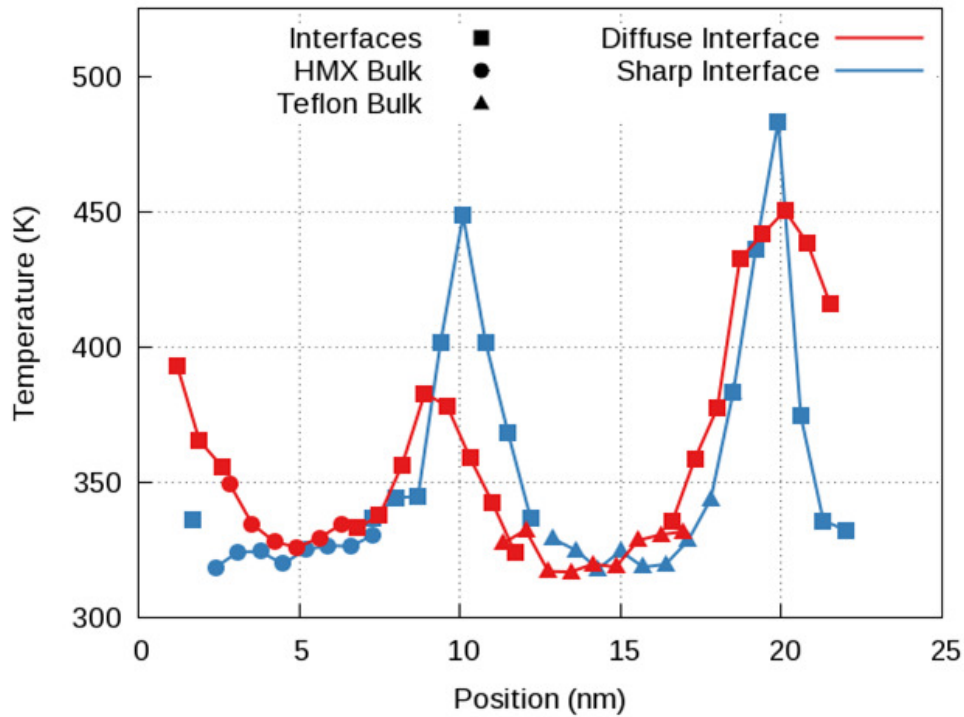


Figure 4.4. At a fixed overall temperature of 400K and driving frequency of 375GHz, the local temperatures vary based on which component is coupled to the acoustic insult. The diffuse (roughened) and sharp (planar) interfaces result in different widths of the localized energy, this is largely due to differences in thermal conductivity through these interfaces.

roughened interface. This temperature localization moves from one region to another as the frequency is changed, as indicated in Figure 4.3 A) and B).

In order to complement the longitudinal wave results above, acoustic waves of purely transverse polarization were also studied with the same PBX structures. When these elastic waves scatter inside the composite material, the angle of incidence between the propagation vector and interface normal will cause the wave to change polarizations. Therefore, understanding the interplay of elastic wave character and interface types is needed to predict the overall material response. These shear wave simulations are performed the same way as the compression waves, but now the simulation cell is deformed perpendicular to the interface normal; the strain

amplitude is still 0.25nm. Figure 4.5 collects the heating rates (per period) for each component of the PBX when a purely shear wave is simulated. Similar to the longitudinal waves, HMX is observed to couple strongly at high frequencies, while the polymer binder absorbs more efficiently at the lowest frequencies tested. However, only one clear resonance was observed per structure type, unlike the compressive waves that displayed a pair of resonant frequencies. The planar interface, in Figure 4.5 A) and C), shows a very narrow resonance coupling near 275GHz, as compared to the roughened interface PBX, which shows a broadband resonant absorption between 200 and 400GHz. For both structure types, there is little evidence of a low frequency resonant absorbing mode, but, consistent with the compressive waves, this regime is characterized by predominant Teflon absorption. In general, the purely shear waves localize less energy in the PBX than the compressive waves,. At peak coupling, the heating rates are approximately one-third of those observed in the longitudinal polarization. This is expected, because the small amplitude deformation yields little interface friction, which results when either component moves relative to one another, and is dominant for larger deformation insults. The results shown in Figure 4.5 and Figure 4.3 do well at capturing the global response of the PBX to the acoustic insult, but they lack the necessary detail to inform on how the material is coupling to the external stimuli. To aid in understanding this, one must look at the time evolution of the thermo-mechanical properties of the PBX. Earlier, it was discussed that the frequencies of interest are selected because they are close to the structural resonances of either pure component. To prove this is the case, the stress-strain histories for a few shear wave insults are plotted out in Figure 4.6 (planar interface) and Figure 4.7(roughened interface). Focusing on Figure 4.6, in panels A) ,C) and E) the density of points at each stress and strain value is shown with the color axis. Additionally, the temperature evolution(shown with the color axis) is included in panels B), D) and F) for the frequencies 145, 210 and 669GHz, respectively. The three frequencies shown represent cases where the driving frequency is one of the following: A),B) well below the observed resonance, C),D) close to the resonance mode or E),F) where the

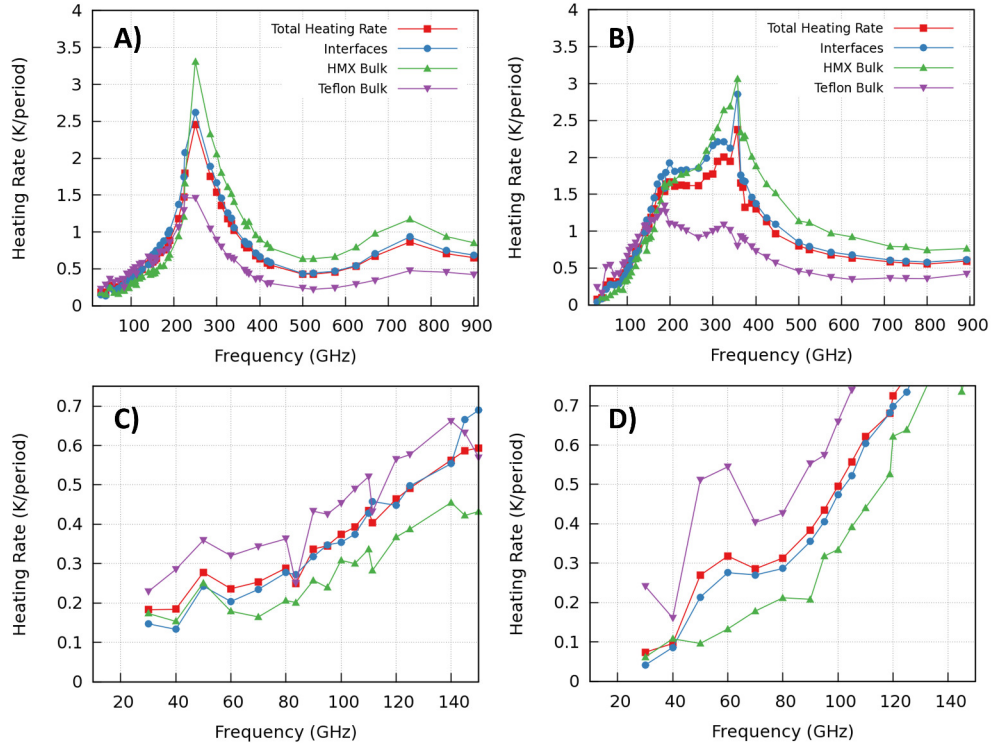


Figure 4.5. Observed heating rates of PBX structures subjected to a transverse polarized acoustic wave, this rate is normalized by the period of the oscillation to bias against increased energy deposition rates at high frequencies. The pair of plots shown in A) and C) correspond to the planar interface case while panels B) and D) are the observed heating rates, broken down by region in the sample, for the roughened interface. A close of up of the low frequency regime is shown in C) and D).

driving frequency is much greater than resonance coupling. Not only does the shape of the fatigue loop change as the material is cycled, a loop of greater area indicates more energy being dissipated by the PBX, but the line connecting the peak strain points changes sign as the driving frequency moves past the structural resonance. In other words, at driving frequencies lower than the structural resonance, the material response will be in phase with the direction of the applied strain (strain increasing, stress increasing), while above the resonance the material response is out of phase and can't 'keep up' with the applied strain (strain increasing, stress decreasing). From

panels B),D) and F) of Figure 4.6, it can be observed that the material response conforms quickly to the insult period and repeats the same path in stress and strain space within very few cycles (see initial points in purple). Interestingly, Figure 4.6 F) shows a slight shift in the fatigue loop at later times; this is attributed to the increased temperatures at these times.

Lastly, the thermo-mechanical histories for a collection of insult frequencies are shown in Figure 4.7 for a roughened interface and shear loading. Similar to the planar interfaces shown in Figure 4.6, the driving frequencies shown correspond to relative frequencies of far below (panels A) and B)), close proximity (panels C) and D)) and far above the structural resonance peak(panels E) and F)). Comparing the size of the fatigue loops shown here, it is clear to see that the shear waves impinging on an amorphous interface dissipate more of the acoustic insult energy relative to a pristine interface; this matches the results from Figure 4.3. What is unique to this interface type is that the observed phase switch between the acoustic wave and material response occurs at a frequency lower than the observed maxima in heating rate. Here, the last driving frequency with a positively correlated response (increasing strain, increasing stress) is 190GHz, shown in Figure 4.7 C). Between 190GHz and the structural resonance peak at 350GHz, the stress-strain maps show a mixed character of positive and negative correlation with the insult; often, the low temperature behavior has an opposite response as the high temperature one. Overall, this mixed mode coupling of the roughened interface leads to higher observed heating rates over a larger range of frequencies, although only in one direction relative to the absorption maxima, than in the PBX structures with planar interfaces.

4.2.2 Conclusions

Acoustic excitation of composite materials, or pure materials with defects, results in a localization of the mechanical energy into regions of elevated temperature. Depending on the frequency of the exciting mode, the mechanism of this local heating may be from viscoelastic, viscoplastic, interface friction, or interface delamination.

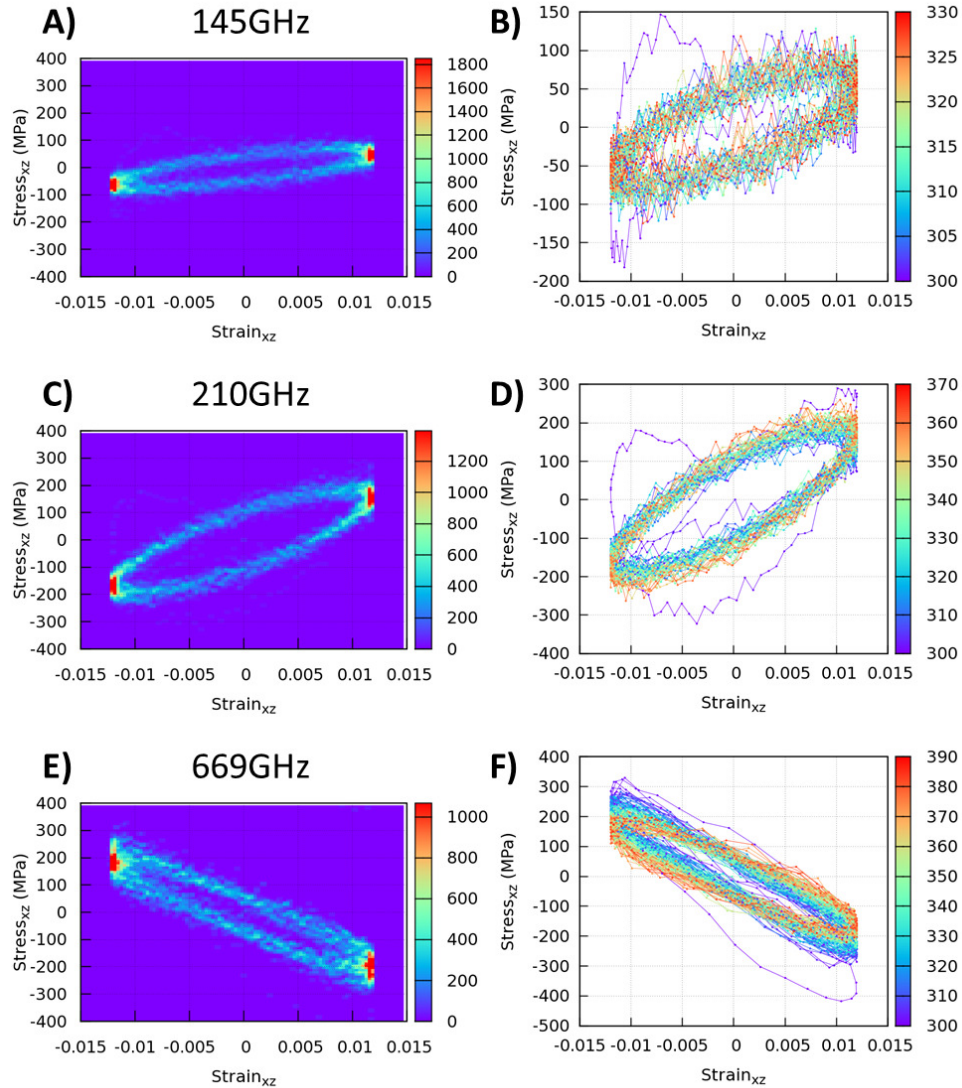


Figure 4.6. Stress-strain histories for PBX structures with a planar interface under shear polarized waves of various frequencies. The A), C) and E) panels show the density of points at each stress and strain value throughout the entire simulated time. The color axis in the right panels represents the overall temperature of the simulation cell. The frequencies shown here correspond to insults that are A), B) below the structural resonance, C), D) in close proximity to resonance and E), F) at frequencies much higher than resonance.

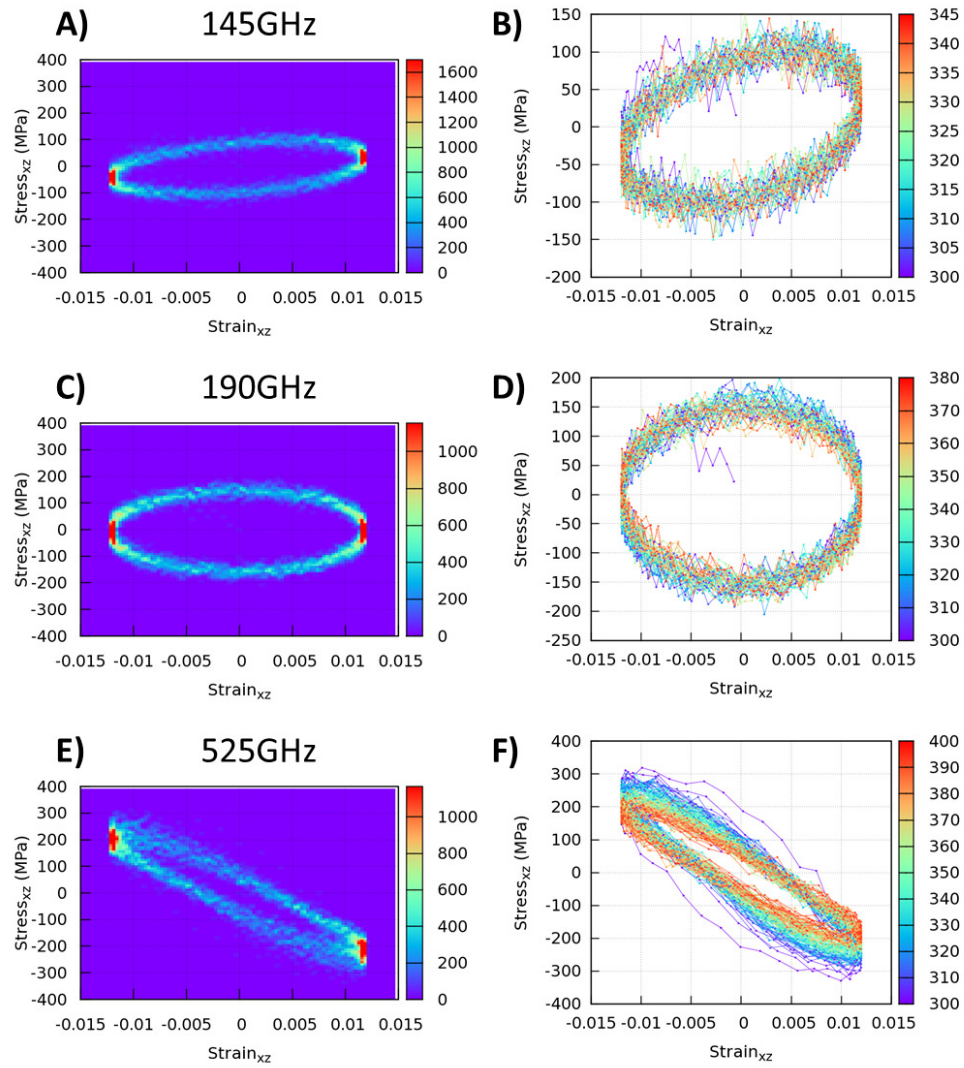


Figure 4.7. Stress-strain histories for PBX structures with a roughened interface under shear polarized wave of various frequencies. The A), C) and E) panels show the density of points at each stress and strain value throughout the entire simulated time. The color axis in the right panels represents the overall temperature of the simulation cell. The frequencies shown here correspond to insults that are A), B) below the structural resonance, C), D) in close proximity to resonance and E), F) at frequencies much higher than resonance.

In order to better understand the results from Mares *et. al.* [210, 211], a pair of PBX microstructures were constructed with contrasting interface characteristics: one with a pristine crystal interface pressed against the polymeric layer, the other with an amorphous boundary layer between either component. The former of these two structures can be thought of as an un-aged PBX, the latter being the result of significant thermal cycling that is common to aged PBX's. Understanding the mechanical response of aged explosives is critical for their safe and efficient use, and, in practice, the acoustic insults used here mimic their field use. By studying acoustic insults of either purely compressive or shear character, a basis for comparing the thermal response for either interface type was built. The simulations revealed that the aged PBXs are able to couple to acoustic insults with a range of frequencies around the predicted structural resonances, while the pristine samples only couple strongly to those that are narrowly tuned to the structural resonance mode. While two resonant modes are expected per wave polarization (symmetric or asymmetric combination of pure component resonances), only three total were observed, with the low frequency shear mode being under-resolved in this work. It is important to note that the absolute value of these resonant frequencies are system size dependent. The small sample sizes that MD necessitates resulted in these modes ranging from $\approx 100 - 650\text{GHz}$. A true PBX, will have a larger bandwidth of strongly absorbing modes due to the range of grain sizes of the molecular crystal, but these ranges will also depend on the age of the PBX as shown by the results in Figure 4.3 here. In order to use acoustic excitation as a means of detection and defeat of explosives, this insult frequency must be carefully chosen such that it will not strongly overheat the molecular crystal (for detection) or will purposely localize its energy into this material (for defeat).

CHAPTER 5. ELECTROMAGNETIC RESPONSE TO ENERGY INPUT

The most common means to characterize a materials' chemistry is through its interaction with light, more specifically what emitted light is characteristic to the material. However, not all wavelengths of light are useful for detecting and identifying molecular materials. Chemical specificity boils down to a limited subset of frequencies, ranging from phonons to electronic transitions; all others lack the ability to discern two materials of similar density. In the detection of energetic materials, there is a delicate balance between chemical specificity and the ability to penetrate shielding layers. In this chapter, a new mode of detection is explored by employing strong Tera-hertz waves to push a material far from equilibrium and use the characteristic frequency conversions of a material as the output signal.

5.1 Introduction

Despite the pressing need for remote sensing of energetic material worldwide, there still exists a gap in the current capability to the expected needs. Current airport personal threat detection technologies are capable of density contrast at a distance of under a meter; additional tests are required to determine chemical makeup. Experimental techniques such as Raman, FTIR, and NMR are all sensitive enough to probe compositional details, and subsequently have built up a significant library of observed spectra. [4,5,144,198,217,218] Unfortunately, these chemically specific tests cannot be done at a range of a few meters, which would be ideal for personal safety. Translating these technologies to the battlefield is even more challenging, where the environment is less controlled than either the lab or airport. As a last restriction on the detection capability, the source of excitation should not trigger any accidental chemical reactions due to the obvious danger that these energetic materials possess.

Minimally, the input energy that will yield the detectable signal should not ionize the material, and, for light pulses, this is not a well defined quantity due to local field enhancement effects. [203,204] Local field enhancements are expressed at acute edges of a crystal, where charge is localized in a conductor, but these effects are still present in the molecular crystals of interest here. [7,219] Terahertz spectroscopy has promise to surmount these challenges because it can penetrate dry materials, has standoff capability and is low power, which averts ionizing effects. [220,221] More importantly, new sources of controlled THz pulses have become available in recent years. [222] The THz range of frequencies are those that lie just above phonon modes and below the frequencies due to covalent bonds. They are usually attributed to large amplitude deformations of whole molecules. [220,223] Therefore, each unique molecular structure should be reflected in the THz range, and many reported spectra confirm this notion. However, the THz transition frequencies are smaller than typical operation temperature ($k_bT \approx \hbar\omega$), and the spectral lines in this frequency range are often broad and congested, blurring a true fingerprint of the material. Alternatively, non-linear signals in the THz range could offer a solution to this problem because only a subset of vibrations will be able to emit these non-linear frequencies. Therefore, the pair of native and non-linear spectra of a material should be able to provide a fingerprint that would alleviate temperature blurring.

5.2 Non-Linear Light-Matter Interactions

Non-linear light-matter interactions resulting from strong electromagnetic fields are well known [224], and can be generalized by expanding the electric polarizability

$$\mathbf{P} = \epsilon_0 \chi^{(1)} \cdot \mathbf{E} + \epsilon_0 \chi^{(2)} \cdot \mathbf{EE} + \epsilon_0 \chi^{(3)} \cdot \mathbf{EEE} + \dots \quad (5.1)$$

here $\chi^{(1)}$ is the linear susceptibility tensor, $\chi^{(i>1)}$ are the non-linear susceptibility tensors, and ϵ_0 is the permittivity of vacuum. Example non-linear signals include frequency mixing, Pockels and Kerr effects, and Raman scattering [8,225]. In addition, local field enhancements give rise to temperature hot spots in heterogeneous energetic

materials, which modify the optical properties by forcing atoms into anharmonic regions of the potential energy surface. This results in more non-linear effects. Trying to preferentially force a material into anharmonic regions of the PES will be the focus in this chapter, and capturing these effects in MD will be detailed below. Recently, Katz *et al.* [153] used reactive MD to explore Raman-like frequency conversion in the THz range, and focused on the time resolved emission of light in the same range. They found signals emitted at frequencies unique to the input wave, and, in addition, found them in cross-polarized directions. However, their study was limited in scope because a more realistic scenario for remote sensing would involve an EM wave impinging onto an air-explosive interface with the output signal gathered in the far field. In the work presented here, MD simulations are used to address the simplest interface in order to compute frequency-conversion tensors, absorption spectra and far field response for a pair of contrasting molecular crystals. Depending on the magnitude of the applied EM pulse, it can simply force the molecular system to make nonlinear excursions without inducing chemistry, or trigger decomposition of the energetic material leading to deflagration or even detonation [226]. Building off the results in Chapter 3.3, EM pulse strengths were chosen such that they would not induce chemical reactions, but would polarize the sample to result in non-negligible nonlinearities in the optical response. Here, a Gaussian pulse is used much like Katz *et al.* [153], shown in Equation 5.2, but the peak amplitude and width were adjusted given what was learned from prior work.

$$\mathbf{E}_{\text{in}}(\mathbf{x}, t) = \mathbf{e}_{\text{in}} E_{\text{in}} e^{i\mathbf{k}_{\text{in}} \cdot \mathbf{x}} e^{-(t-t_0)^2/2\sigma^2} \cos(\omega_{\text{in}} t), \quad (5.2)$$

where E_{in} is the amplitude of the wave, centered at t_0 , has a width σ , carrier frequency ω_{in} , \mathbf{k}_{in} is the input wave-vector ($k_{\text{in}} = |\mathbf{k}_{\text{in}}| = \omega_{\text{in}}/c$), and \mathbf{e}_{in} is the input polarization unit vector ($\mathbf{e}_{\text{in}} \cdot \mathbf{k}_{\text{in}} = 0$). An EM pulse such as this one will drive the atomic charges in the material according to the Lorentz force $\mathbf{F} = e\mathbf{E} + (\mathbf{v}/c) \times \mathbf{B}$. For the strong amplitudes used here, these charges explore the nonlinear regions of the energy landscape. For a single accelerated charge with a trajectory $\mathbf{r}(t')$, the far-field radiated electric field is given by $\mathbf{E}_{\text{rad}}(\mathbf{x}, t) = (e/c)[\mathbf{n} \times \mathbf{n} \times \dot{\boldsymbol{\beta}}/R]_{\text{ret}}$, where \mathbf{n} is a

unit vector in the direction of $\mathbf{R}(t') = \mathbf{x} - \mathbf{r}(t')$, $\dot{\boldsymbol{\beta}}(t') = \ddot{\mathbf{r}}(t')/c$ (a dot denotes the time derivative), and “ret” means that the quantity in the square brackets is to be evaluated at the retarded time given by $t' + R(t')/c = t$. A good approximation can be made that, since the observation point is assumed to be very far away, the unit vector \mathbf{n} is almost constant in time. The corresponding Fourier spectrum of these accelerated charges is given by:

$$\mathbf{E}_{\text{rad}}(\mathbf{x}, \omega) = \frac{e/c}{\sqrt{2\pi}} \int_{-\infty}^{\infty} dt' [\mathbf{n} \times \mathbf{n} \times \ddot{\mathbf{r}}(t')] \frac{e^{i\omega_{\text{in}}[t' - \mathbf{n} \cdot \mathbf{r}(t')/c]}}{R(t')}. \quad (5.3)$$

and for a discrete set of N accelerated charges like those contained in the simulation cell, one makes the replacement:

$$e[\mathbf{n} \times \mathbf{n} \times \ddot{\mathbf{r}}(t')] R^{-1}(t') e^{-i(\omega/c)\mathbf{n} \cdot \mathbf{r}(t')} \rightarrow \sum_{j=1}^N e_j [\mathbf{n}_j \times \mathbf{n}_j \times \ddot{\mathbf{r}}_j(t')] R_j^{-1}(t') e^{-i(\omega/c)\mathbf{n}_j \cdot \mathbf{r}_j(t')} \quad (5.4)$$

Again invoking a distant observation point, one can approximate $R_j(t') \approx R_0$ and $\mathbf{n}_j \approx \mathbf{n}$, where R_0 is the distance between the observation point \mathbf{x} and an origin of coordinates within the scattering volume, with the unit vector \mathbf{n} is along that direction. What is important for this study is that the acceleration of each charge $\ddot{\mathbf{r}}_j$ within the molecular crystal depends on the input electromagnetic field frequency ω_{in} . Indeed, most of the far-field radiation is emitted along the Rayleigh line, ($\omega = \omega_{\text{in}}$), but a small portion can be emitted at unique frequencies ($\omega \neq \omega_{\text{in}}$) due to non-linear light-matter interactions within the material. When the wavelength of light is much larger than the scatterer, a further simplification can be made. In this case of $(\omega/c)\mathbf{n}_j \cdot \mathbf{r}_j \ll 1$, one can take the leading order of the exponentials, i.e. $e^{-i(\omega/c)\mathbf{n}_j \cdot \mathbf{r}_j(t')} \approx 1$. This second approximation is justified, given that the THz radiation used here is impinging on a grain of an energetic material that is on the order of tens of nanometers.

From the input EM pulse, the material will polarize under this intense light generating dipole moments $\mathbf{p}_\alpha(t')$ at some atomic position \mathbf{r}_α . In Equation 5.4, these dipole moments correspond to a pair $(j, j')_\alpha$ of summation terms over j , such that $\mathbf{p}_\alpha(t') = |e_{j\alpha}|[\mathbf{r}_{j\alpha}(t') - \mathbf{r}_{j'\alpha}(t')]$. Therefore, the Fourier spectra (frequency rather than time representation) of these associated new dipole moments in the material becomes:

$$\mathbf{E}_{\text{rad}}(\mathbf{x}, \omega) = \frac{1}{\sqrt{2\pi}} \frac{1}{cR_0} \mathbf{n} \times \mathbf{n} \times \int_{-\infty}^{\infty} dt' e^{-i\omega t'} \sum_{\alpha} \ddot{\mathbf{p}}_{\alpha}(t'). \quad (5.5)$$

In the far-field, one can replace the individual dipole summations by the net dipole of the cell, $\mathbf{P} = \sum_{\alpha} \mathbf{p}_{\alpha}$, and the frequency spectra of its' second time derivative (charge acceleration moments) will be equivalent to the radiated EM field. There is one last approximation that goes with using classical MD, which is the back action of the radiated field on the sample is not captured. Although MD computes the dynamics of these dipole moments using a force field (see below), which includes long range electrostatics, the (assumed) weak interaction with these radiated field is neglected.

5.2.1 Simulation Details

With the classical description of absorption and frequency conversion provided in the previous section, Molecular Dynamics has been chosen as the simulation method. The hypothesis here is that anharmonicities in the PES give rise to frequency conversion that is characteristic of the material being probed. Therefore, a MD force field that is able to capture these delicate frequency conversion events is sought after. Commonly, harmonic bond terms are used to construct an IAP, but these harmonic chains of atoms cannot exchange energy (neglecting long range interactions) amongst themselves. These two conditions together make ReaxFF an ideal candidate for the IAP used, and several examples exist of its use to study molecular crystals under strong electric fields [78, 227, 228]. A reactive potential has to smoothly capture the transition from the reactant well to products; thus, is intrinsically anharmonic in nature (i.e. existence of a saddle point). It is important to note that this study is not concerned with inducing chemistry, as in Chapter 3, rather, the light pulse is intended to force short excursions into anharmonic regions of the PES. To ensure proper interaction between the external light source and the sample, a polarizable force field should be used. Dynamic polarization is captured in

ReaxFF through the charge equilibration scheme of Rappe and Goddard, with the atomic charges updated at each timestep ($\Delta t = 0.1fs$). [69] Both the ReaxFF IAP and charge updating scheme are deployed in LAMMPS, which is the simulation driver for all the work shown here. [35]

A pair of molecular crystals, pentaerythritol tetranitrate (PETN) and Ammonium Nitrate (AN) polymorph IV, are studied here to exemplify a benchmark test for threat detection capability using THz signals [5, 229]. PETN is a molecule with both oxidizer and fuel contained on a single chemical unit, while AN is an energetic cocrystal that forms a charge neutral lattice from a basis of charged molecular species, much like a ceramic material. Representative orthoscopic views of the two molecular crystals are displayed in 5.1 (a)-(d) [216]. Each simulation cell is generated by replicating a smaller cell that has been pre-relaxed to 50K and 1 atm of pressure in the isobaric-isothermal thermodynamic ensemble (NPT). For PETN, a total of 1008 molecules measuring $7.5 \times 7.8 \times 6.3nm^3$, and similarly for AN 729 molecule pairs measuring $4.7 \times 6.3 \times 4.8nm^3$, were used. As mentioned previously, the geometry of the simulation cell is set up to mimic a realistic configuration for far field detection. This is shown in Figure 5.1 (e). In this cell geometry, the Cartesian directions are chosen to align with the 100 directions, where the [100] (X-direction) and [010] (Y-direction) are periodic simulation cell directions. The last orthogonal direction is taken as the Poynting vector of the incoming light, [001], and has a free surface in order to mimic the experimental condition. Also, in this free surface direction, the crystal is finite in size on the order of ten nanometers which justifies the approximations in Equation 5.3 and 5.5. These crystallographic directions bear no particular importance for detection; another triplet of orthogonal directions equally could have been used.

As Figure 5.1 (a)-(d) shows, the molecular arrangements in either direction are unique, which gives an added variable of interest, which is the input light polarization. Now the emitted light is a function of both the carrier frequency (inside cosine term in Equation 5.2) and input polarization. To induce a strong polarization in the material

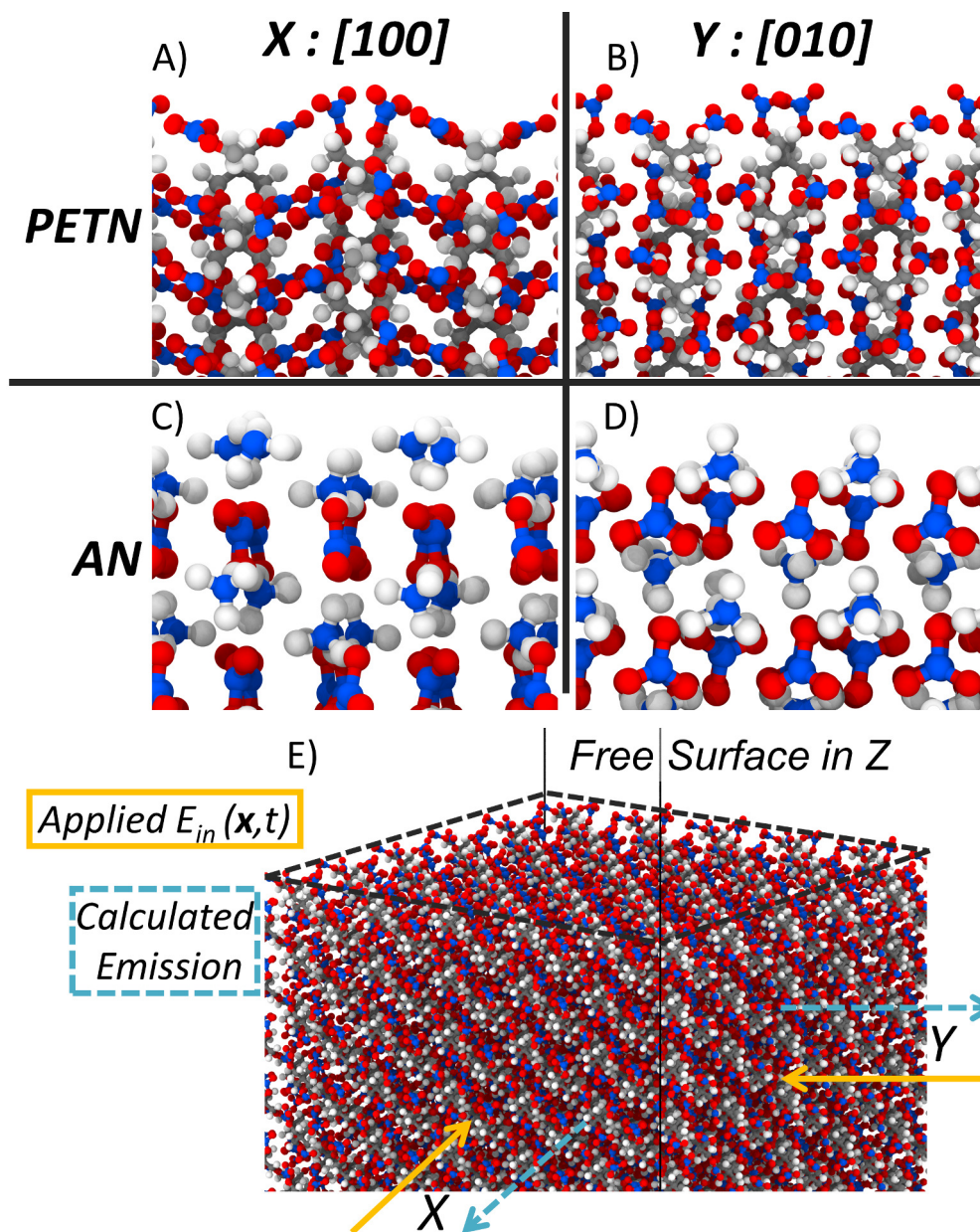


Figure 5.1. A), C) Representative orthoscopic views of the $[100]$ crystallographic direction for PETN and ammonium nitrate. Panels B), D) show the $[010]$ direction in either material, which exemplifies the unique molecule arrangement in either direction. E) Perspective view of the simulation domain showing how the free surface is created in MD, perpendicular to this free surface is the propagation direction of both applied and emitted fields. This simulation setup enables realistic absorption and emission polarizations within MD. Atom colors correspond to carbon (grey), hydrogen (white), oxygen (red) and nitrogen (blue).

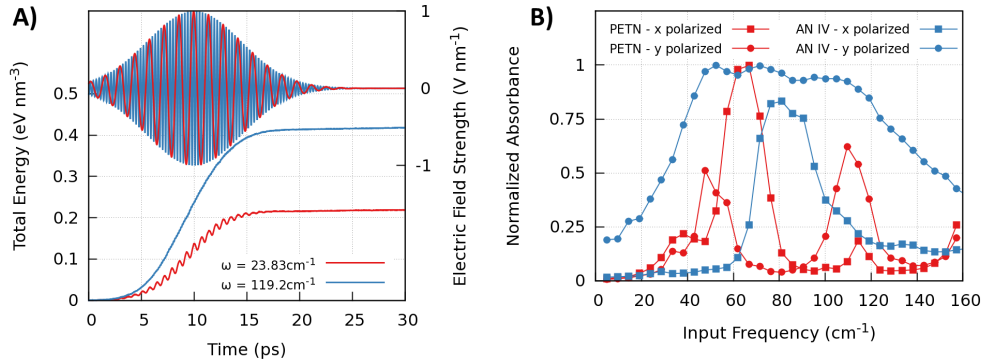


Figure 5.2. A) Two example Gaussian electric field pulses with different carrier frequencies applied in PETN. Absorption is measured as the difference between the total energy after and before the pulse is applied. B) Absorbance (normalized by the peak value for each polarization), as a function of the input carrier frequency and input polarization, for PETN (red) and AN IV (blue). The unique molecule geometry in each direction leads to polarization-dependent absorbance.

without decomposing the sample, a Gaussian shaped electric field pulse is used, as in Equation 5.2. It was determined that a pulse width of 20ps and peak intensity of $1\text{V}/\text{nm}$ to be sufficient to induce the necessary nonlinear effects for either material. Each simulation using this Gaussian pulse was run in the microcanonical ensemble such that any change in the total energy is due to this external stimuli. During this pulse, the dipole accelerations $\ddot{\mathbf{p}}_{\alpha}(\mathbf{t}')$ are recorded at 4fs intervals, which are used to calculate the net dipole moment in each Cartesian direction at each output time. This time series of net polarizations is used in Equation 5.5 to calculate the emission signals for each carrier frequency and polarization pairing. After the 20ps pulse, the external field is removed and the simulation remains in the microcanonical ensemble. This allows for accurate determination of the energy input. A pair of example simulations are shown in Figure 5.2 (a), where the initial structure ($t = 0\text{ps}$) is the relaxed PETN cell.

A volume normalized total energy is used here because the field is applied homogeneously (long wavelength approximation), therefore making the total energy

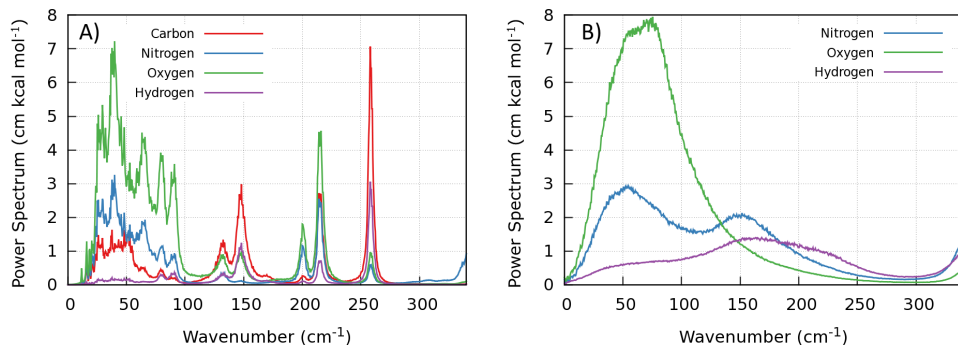


Figure 5.3. ReaxFF calculated power spectrum for A) PETN and B) AN at 50 K and 1 atm of pressure. These spectra aid in analyzing the radiated electric field signals shown in the Results section. The sum of all element contributions normalized by total kinetic energy yields the vibrational density of states.

absorbed dependent on the simulation cell size. The energy absorbed across all carrier frequencies, polarizations and materials tested is shown in Figure 5.2 (b) with the normalization coming from the strongest absorbing mode in either material, respectively. For reference, the strongest absorbing mode resulted in temperature changes of 165K and 360K for PETN and AN, respectively; neither final temperature is expected to initiate a chemical reaction. Each carrier frequency is approximately 5cm^{-1} apart over a range of $0\text{--}170\text{cm}^{-1}$, which was determined to be large enough frequency range to discern between these two materials. Interestingly, the unique molecule arrangements along crystallographic directions gives rise to a modified absorption of the incident light. To understand which modes are absorbing in this range, the vibrational density of states (Equation 2.6) is calculated, and is plotted for either material in Figure 5.3.

Most of these low frequency modes are dominated by oxygen motions. Specific examples of these include the nitro-wag mode in PETN ($\approx 40\text{cm}^{-1}$) and the ammonium umbrella mode in AN ($\approx 280\text{cm}^{-1}$). Conversely, while most of the AN modes contain some hydrogen character, the PETN modes in the same range show very little hydrogen contribution. These spectra, shown in Figure 5.3, provide a baseline for

what the frequency-conversion tensor may entail. While not all of these modes carry a dipole moment, it is possible that the strong electric field will polarize the sample and make for uniquely radiated signals. However, it is unexpected that new modes of vibration appear due to the lack of conformation or chemical change; rather, changes in emission intensity are expected.

5.2.2 Results and Discussion

In order to surmount the challenges of using THz spectroscopy for detection of explosives, it is the goal of this work to identify unique \mathbf{E}_{rad} traces for a subset of carrier frequencies. This section will present two-dimensional spectral maps of the emitted light intensity as a function of the input and emitted light frequencies. In order to correct for strongly absorbing modes, each emission spectrum will be normalized by the energy absorbed at that carrier frequency and polarization. Therefore, the color axis of Figures 5.4-5.6 represent the percent emission at the given input and emitted frequency pair. Since these materials are anisotropic, one should expect the emission to be sensitive to the polarization of the incident light. To study this anisotropy, the spectra will be displayed as a function of polarization direction, in order to confirm that frequency conversion of the incident light has taken place. Figure 5.4 displays the frequency conversion maps for all carrier frequencies and polarizations studied in PETN, where panels A) and B) have the emission polarization direction parallel to that of the input, and C) and D) are the converse. In the parallel directions, the strongest emission signal is the Rayleigh line where $\omega_{in} = \omega_{out}$, but there are other frequency converted signals that appear at higher frequencies than the input.

Most notably, there is a strong third harmonic that appears when the carrier frequency is one third that of a pre-existing mode in PETN, seen in Figure 5.3. The second harmonic emission is forbidden, since PETN (AN as well) possess an inversion symmetry. [219, 224] In addition, there are two modes at $\approx 170\text{cm}^{-1}$ and

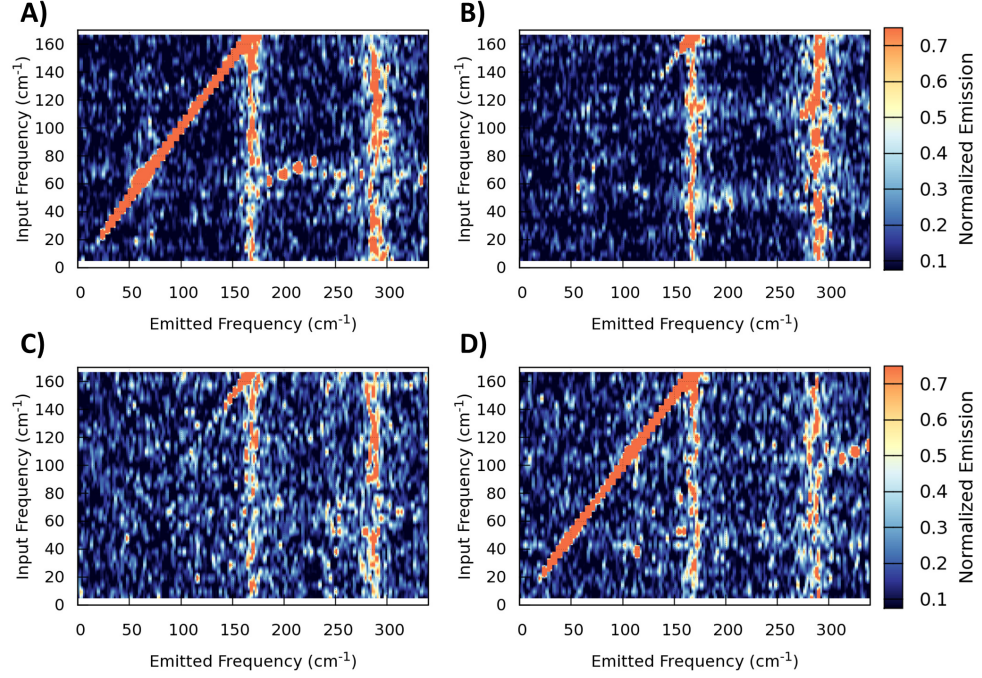


Figure 5.4. Emission signals from PETN along the $[100]$ (x direction) for electric field pulses applied in the A) $[100]$ and B) $[010]$ directions. Complementary emission signals, with pulses along the $[010]$ (y direction) for the C) $[100]$ and D) $[010]$ applied field directions in PETN. Where the emission signals are aligned with the pulse polarization, Rayleigh scattering dominates the observed emission. Perpendicular directions do show emission at unique frequencies different from the applied pulse, confirming the frequency conversion due to internal scattering.

$\approx 290\text{cm}^{-1}$ that light up for almost all carrier frequencies. These are phonon modes of the system [5], and can also be used to fingerprint these materials.

Orthogonal to the the applied field polarization, the emission signals are not as well defined, though certain islands of strong emission still exist. In fact, the existence of any emission signal in an orthogonal polarization confirms that the MD simulation is able to capture internal scattering of the material needed for frequency conversion. From Figure 5.4 B) and C), the Rayleigh emission is only observed for carrier frequencies greater than 125cm^{-1} , and the previously mentioned phonon modes have varying

intensity. These results are using a single pulse of light to calculate the emission, and thus contain significant noise. In a typical experimental setup, repeat pulses are used and should clear these results.

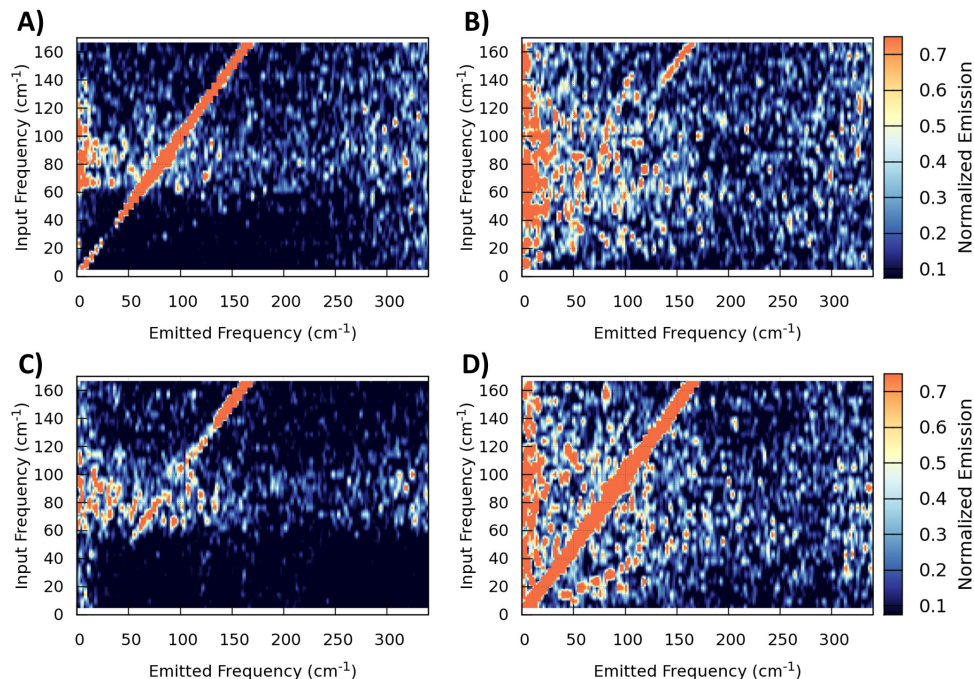


Figure 5.5. Emission signals from AN along the $[100]$ (x direction) for electric field pulses applied in the A) $[100]$ and B) $[010]$ directions. Complementary emission signals with pulses along the $[010]$ (y direction) for the C) $[100]$ and D) $[010]$ applied field directions in AN. Third harmonic emission is clearly seen for parallel emission directions to the applied field and is much weaker in orthogonal directions.

Turning now to the spectra of the energetic cocrystal AN, as shown in Figure 5.5, the conversion maps are distinct from those of PETN. Again, Rayleigh emission dominates the emission spectra in parallel emission directions, shown in panels A) and D). Meanwhile, the third harmonic emission is only weakly seen for a polarization in the X-direction, while incident light polarized in the Y-direction clearly yields a frequency conversion into the third harmonic frequencies below $\approx 125\text{cm}^{-1}$. In orthogonal polarizations, Figure 5.5 B) and C), a common Rayleigh emission at carrier

frequencies greater than 140cm^{-1} is observed, but these two output polarizations differ significantly in the features of the off-diagonal elements. Notably, in panel C) of Figure 5.5, there is only a nonlinear emission signal for carrier frequencies in the range of $60 - 110\text{cm}^{-1}$. Gathering each of these individual 2D spectra, one can predict the far field observed emission spectra. Showing each polarization separately confirms that the simulation method is capable of predicting frequency conversion within either material.

For the usual experimental case, where the input field is polarized but the detection is not polarization sensitive, it makes sense to perform an average over the X- and Y-polarizations for a given linearly polarized input field. These average emission spectra are displayed in Figure 5.6 A) and B) for PETN and 5.6 D) and E) for AN for the X- or Y-polarizations. Going one step further, if the incident light is unpolarized and the far field detector is not polarization sensitive, the averaging should be done over all 2D spectra shown previously. This total emission signal is shown in Figure 5.6 C) for PETN and Figure 5.6 F) for AN. Focusing just on the total emission results, these energetic materials need to be distinguished by their off-diagonal components, because each displays a strong Rayleigh emission.

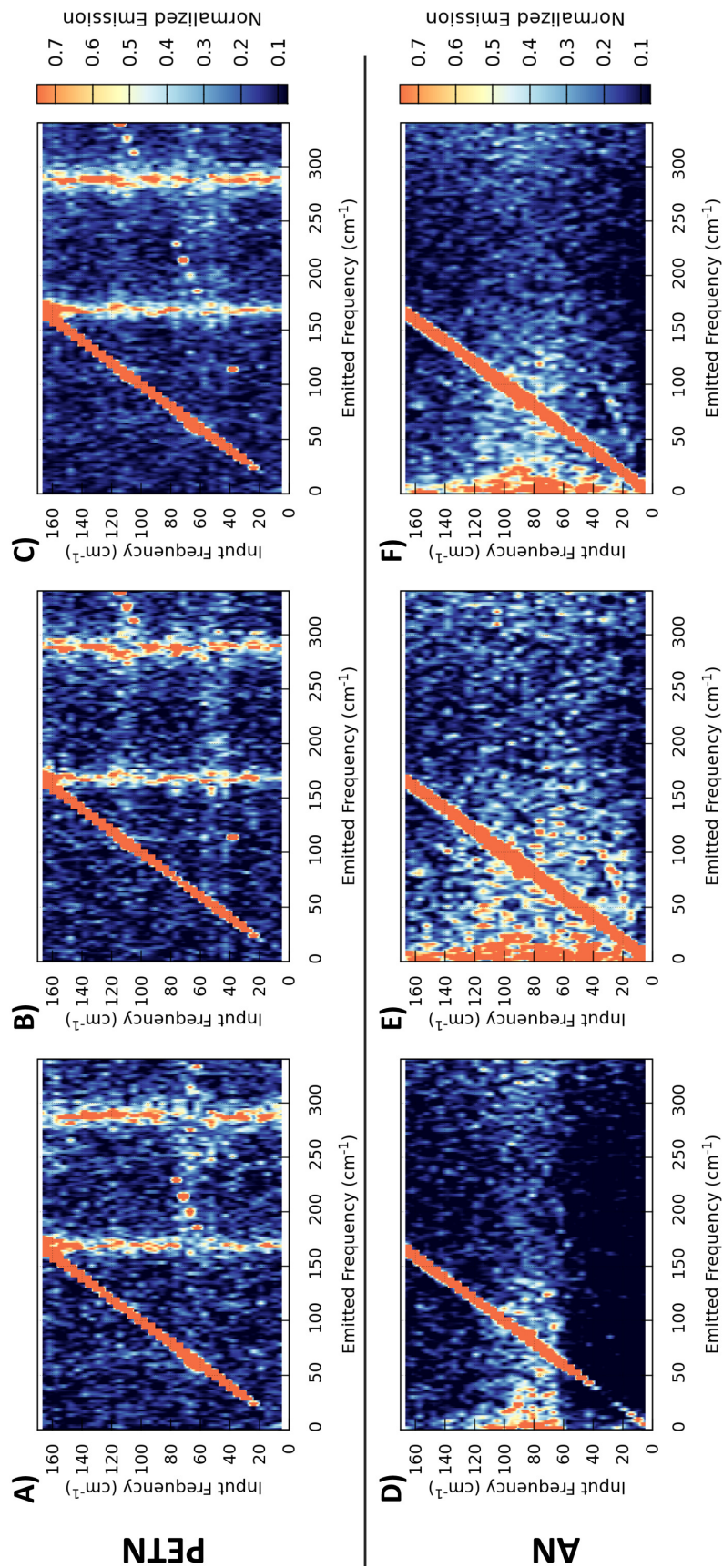


Figure 5.6. Average emission signals for all output polarizations for impulses applied in the [100] direction for A) PETN and D) AN, along with field pulses in the orthogonal, [010] direction in panels B) and E). Total emission signals for all absorption and exit polarizations for C) PETN and F) AN.

For PETN, a handful of third-harmonic frequencies show up clearly, all of which are above 100cm^{-1} . Reiterating the observation earlier, these unique nonlinear signals are the result of the third harmonic of the input wave coinciding, or in close proximity, with a peak in the vibrational spectra shown in Figure 5.3. On the other hand, a weak third-harmonic generation below 100cm^{-1} and unique nonlinear features occurring in the low-frequency region below 25cm^{-1} for input frequencies between 40 and 120cm^{-1} were seen for AN. These low-frequency nonlinear signals are inferred to be molecular rotations or multimolecular modes of AN that are activated due to strong absorption in the [010] polarized light; see Figure 5.1 D). Differences between the unpolarized frequency-conversion maps could provide signatures that an uninformed observer could use to distinguish between these two materials.

5.2.3 Conclusions

By leveraging molecular dynamics simulations and extensions of classical electrodynamics, predictions of nonlinear THz emission due to vibrational scattering in a pair of molecular crystals has been achieved. Extensions to prior work were made by constraining the simulation geometries and polarizations of the external electric field. These predictions are easily extended to the experimentally relevant far-field measurement. In addition, by using reactive MD simulations, approximations due to harmonic absorption or emission, as well as normal mode descriptions of the molecular vibrations, have been avoided. The use of ReaxFF versus, say, a non-reactive potential fit for use on the same materials [212,213], provides a more realistic description of absorption. As was seen from Section 3.3, the initial localization of energy on the target mode causes a local (frequency space) temperature spike. Now, high temperature anharmonicities that belong to the target mode act to distribute energy to other vibrations in the system. It is this chain of events that is suspected to cause the frequency conversion, but this is altogether absent when a non-reactive IAP is used. There are no temperature dependent portions of the non-reactive IAP that modify the harmonic nature of the bonds (again neglecting the weak long-range

portions of the potential); in a sense, all cross talk between vibrations is severely suppressed. While the use of any force field is an approximation of the actual physics of the problem, it does, however, allow for tractable simulations that provide useful and rapid 2D-spectra predictions. Two dimensional spectra of PETN and ammonium nitrate polymorph IV were displayed here that differ significantly in the THz frequency range due to changes in the location and intensity of third-harmonic emission of the input light, as well as other nonlinear frequency emissions. The emitted light is dramatically different in both polarization and frequency from the incident light pulse, which provides a potential for a THz detection technique with chemical specificity. Experimental challenges still exist to generate the electric field strengths that were used here, but realistically a weaker pulse could be used if it is set up for a repeated measurement. A pulse duration of 20ps is easily achievable with current technologies, with repeat rates of tens of thousands per second possible as well. [230, 231] In effect, if high quality crystals of PETN or AN are obtained, these predictions could be experimentally validated in a short amount of time. Another key feature of these predictions is their extension into other modeling and simulation tools. As was mentioned before, this simulation cell is an idealized case of light-matter interactions, and local field enhancements due to crystal geometry are neglected. These microstructural effects can be captured in finite element tools [13]. By expanding the electric permeability to include a tensor input of these frequency conversion maps, a greater insight into the far field emission signals can be achieved.

There are several avenues for improvement on this proof of concept work, with the primary concern being the clarity of the resultant signal that will be used to detect a material. The first of these is just to include more polarizations along different crystallographic directions. Adding these new conversion tensors to the averaged spectra, shown in Figure 5.6 C) and F), would make for a better prediction of the far field emission seen by an experiment. One set of information that would not require significant change in simulation setup is to measure the conversion efficiency of some of these third harmonic modes. Here, the emitted signal of interest would

be quantified relative to the Rayleigh emission as a function of the strength of the incident pulse. This result would narrow the number of emission signals that need to be tracked by experimentalists, and provides a more accurate fingerprint for each material. Also, with increasing pulse intensities, one can imagine using the resultant chemistry from the THz pulse as an additional means for standoff detection. However, there would be a necessary trade off of the specificity of the predicted nonlinear signals for chemical species detection due to the high-temperature broadening of these low-frequency modes of interest. The pulse intensity dependence, as well as further study of the orientation dependence of nonlinear signals in these anisotropic energetic materials, will be a subject of further study.

Deciding which of these nonlinear signals should be tracked in order to distinguish between materials would be made easier if a library of these 2D spectra are already available. Even with a limited subset of polarization directions, this study shows that preferential input of energy into THz modes can provide information to distinguish between the chemistries of AN and PETN. The true advantage of this method is that these predictions can be made simply by knowing the initial crystal structure of the energetic material and having a force field that provides a reasonable description of the vibrations. Therefore, a library of 2D THz spectra can be assembled with limited input by the users, provided all of the materials can be described by the same reactive force field. Although a standing library of predicted spectra would be ideal for this detection scheme, a stronger insight into the mechanisms of frequency conversion would constitute a significant advancement. The strongest signals observed here were due to well-known frequency mixing and higher harmonics that obey the symmetry of the crystal. Of future interest are the small islands of frequency conversion that appear in these maps; these are the anharmonicity of the target vibration. Understanding the types of vibrations that give rise to strong anharmonic emission of light would help dissect the conversion maps highlighted here. The challenge is individually representing a vibration without losing the necessary overlap between modes to give rise to frequency conversion. One possible method

was developed by Strachan [126]; it is based on the pairwise autocorrelations between atoms. In this paper, though, the solution to the eigenvalue equation necessitates that each mode (row in the covariance matrix) is orthogonal. It may be possible to compare the covariance matrix itself (prior to diagonalization) calculated at ambient conditions to one that was collected during the light pulses used here. The difference between these two situations may provide information to the overlap between anharmonic modes. However, this method has not been tested and is more of a conjecture than a planned route to solve the problem of predicting intermolecular vibrational energy transfer.

CHAPTER 6. SUMMARY

Although each chapter prior had a section dedicated to the results and discussion respectively, it is important to think of each chapter of this thesis as a subset of a larger topic as defined by the document title. Therefore, the conclusions in a thematic sense are discussed here and in effect offer an answer to the candid question of ‘*so what?*’ In this last chapter, albeit a short one, a handful of future directions of the research are also laid out. Because, although the author has spent significant time and effort on the work here, it is my belief that a detailed research discussion should never close the topic, rather open avenues of further study. It would be a strange case to write this document and not feel as though it is an incomplete collection of work.

The backdrop to all the work here was the enabling technology of high performance computing, without which the insight gained here would not have been possible. Although the experiments performed here were stuck in the virtual lab, each set of simulations was designed such that it best mimicked an experiment that could be done in a physical lab. While each of the calculated responses (chemical, thermal or electromagnetic) can also be accessed in the laboratory, the detail provided from the simulation work here aids in understanding and predicting the mechanisms responsible for these processes. Importantly, some of the methods and procedures used in this work are new to the field, and can (should) be used to expand our understanding of these problems at the atomic scale.

Starting with the work on non-statistical chemistry, I would argue that the minor approximations inherent to the the simulation method and choice of forcefield are outweighed by the number of new material systems that can be studied. The method outlined previously identifies anomalies in reaction behavior by comparing reactivity between equilibrium and non-equilibrium states of the material; there were

no caveats for which types of molecules would work within this scheme. Although the rates are approximate, the VER and chemical reactions are taken care of without ad hoc rules added to the simulation, leaving the door open to study any other molecules within this (or any other) ReaxFF force field. The observed change in reactivity to an intra-molecular localization of energy between the unimolecularly reacting PETN versus a bimolecular NM reaction should guide and narrow the future work in this avenue. The focus should remain on condensed phase systems, because there is little experimental evidence of non-statistical reactions in solids, and the computational approach could steer future work there. Even though multimolecular reactions are more common in solids (which were shown to have no change to the nonequilibrium reactions here), a continued effort should be made to identify cases where vibrational insults alter the kinetics relative to thermal insults. Rather than continuing with the same materials, a new set of molecules that exhibit a low activation energy (10-15 kcal/mol) should be sought after. This low barrier reaction would increase the possibility for reaction while $T_{mode} > T_{bulk}$, and enable the identification of key vibrations for the reaction progress. Ideally, a simple material system can be found that has competing reaction paths, and the use of a nonequilibrium state will favor one over the other.

It was mentioned in earlier chapters that the sizes of the molecules used here prohibited the use of phase trajectory mapping, but if few degrees of freedom are active (unimolecular case) this technique may be possible. The De Leon and Berne model of an isomerization reaction is a well studied example of efficient trajectory mapping that shows rich physics of both regular and chaotic behavior. What would be interesting is using the work of Reeve *et al.* [232] to identify the functional forms that yield chaotic (statistical reactions) or regular (non-RRKM) trajectories. Due to the low computational cost of this model form, a liquid or solid of these small molecules can be studied. By making small modifications to the interatomic potential, one can study what molecule geometries give rise to statistical or nonstatistical reactions. Also, the vibrational insults like those used in Chapter 3.3 can be employed to study

the changes in phase space trajectories on this small molecule; hopefully, they would shed light on the validity of the schematics laid out by Bunker and Hase. All together, these continued efforts would aid in understand how to externally control the dynamics of molecules, which as mentioned earlier has a wide range of applications.

Extensions of the shock to detonation transition work have the best possibility to enable fruitful multi-scale modeling efforts. Rather than running expensive shock induced pore collapse to study the initiation of solid explosives, it makes more sense to focus efforts on the artificial hot spot work. The data (initiation thresholds, burn rates, density changes, *etc.*) collected from these simulations can be translated into hydrodynamic codes (CHEETAH is one example code) that solve for material properties at the macroscopic scale. The method for testing these hot spots is robust with respect to what material is tested, and in the future this should include other HEs that are of interest to the national labs here in the U.S.; TATB and Hexanitrostilbene are prime candidates. At a more fundamental level, more work needs to be done to identify the role of non-equilibrium chemistry during shock loading. Where this work left off, there are hanging questions regarding the role of crystallinity and pressure gradients with respect to the non-equilibrium chemistry. These effects need to be studied using artificial hot spots before one can intentionally create a non-equilibrium hot spot to study its effect. To do so, a special type of thermostat needs to be programmed into LAMMPS that will only control the CoM velocities of molecules and will subtract energy from intramolecular vibrations, sort of like a Mueller-Plathe method for a single molecule. One should expect that the ignition threshold would change for systems that have $T_{CoM} \neq T_{Vib}$, especially for materials that have preferred multimolecular reactions.

There is plenty of work left to do in the thermal response of composite materials, primarily because it is the most recent endeavor of any of the chapters here. While the role of the surface characteristics has been studied in detail, there is still the approximation of using a quasi two dimensional system to study what is, in reality, a full microstructural effect. This would mean looking into shape factors on the spatial

localization of acoustic insults, which necessitates a change in how the simulation cells are built. Mares and coworkers [211] suspected this was the cause of differences in heating rate between otherwise equivalent embedded Ammonium Perchlorate crystals. Fully embedded HMX crystals in a Teflon matrix have been built either as a spherical nanoparticle or as a faceted octahedron (all (110) faces) in order to study this effect. These resultant structures are much larger than their 2D cousins, and would require more computational resources to evaluate this shape effect. However, due to time restraints, there were no simulations of acoustic excitation done with these geometries. What is also interesting in this system is the idea of phonon localization in the crystalline phase (Kapitza resistance), which would give rise to a material-specific heating mechanism. A detailed study of this was not undertaken here due to the unique simulation geometries that would be required. Here, the length of either phase should be many wavelengths of the phonons that are to be scattered at the interface in order to ‘watch’ a phonon be selectively transmitted or reflected. This has been studied in parallel systems within MD [233], but not with the aim of detection and defeat of explosives, which is an interesting angle on this known phenomena. A normal mode approach would be useful in order to initialize a traveling phonon in the crystal, and a simple measure of how much the temperature of the polymer increases would suffice to measure the transmission efficiency.

The THz frequency range offers a unique opportunity for spectroscopists to detect energetic materials, but is plagued by weak signals that oftentimes are intermixed with those of water. However, the non-linear emission that results from a strong input polarization was shown here to be a possible route to create a chemically specific signal that can be detected. While insightful, the scope of the work here was limited to just two input polarizations per material, which does not fully reproduce experimental conditions. The frequency conversion maps were still granulated, even when averaging over all input polarizations. A simple solution to this is to generate more unique signals by aligning the input light to more crystallographic directions. Clarifying which non-linear signals should be expected would make the experimental task

of differentiating between material chemistries much simpler, and finalizing a procedure, or threshold intensity, would enable high throughput screening of materials in order to generate a library of non-linear THz spectra. In order to best predict the experimental spectra, additional simulations are needed to measure the conversion efficiency of the non-linear signals. Here, the new frequency signals are compared to the the Rayleigh intensity as a function of the intensity of the input light. These results will help experimental efforts dial in the intensity of the THz pulses that should be used. In short, the most fruitful extensions of this particular work, in the authors opinion, will be to simplify the experimental task of THz detection.

Over the last few decades, simulation methods have solidified themselves as a viable technique in material science. Their applications have proved to be extremely diverse as well. This work stretched the uses of a single simulation method in MD in order to address how a single class of materials respond at extremely small length and time scales. What these MD simulations afforded was the ability to correlate the thermal, chemical and electromagnetic response to the means of energy input into the system. Most importantly, the work collected here showed, in multiple examples, that the material response will change from what is predicted thermodynamically while the system relaxes from its initial non-equilibrium state. The chemical response examples, in particular, show very promising results, where this non-equilibrium state can be controlled and indeed change the reactivity of the sample. Altogether, the predictions made here support or enable new experiments aimed at developing new detection and defeat technologies for hazardous energetic materials.

LIST OF REFERENCES

LIST OF REFERENCES

- [1] Ahmed H. Zewail. Femtochemistry: Atomic-Scale Dynamics of the Chemical Bond . *The Journal of Physical Chemistry A*, 104(24):5660–5694, jun 2000.
- [2] D H Semmes, J S Baskin, and a H Zewail. Picosecond real-time studies of mode-specific vibrational predissociation. *Journal of Chemical Physics*, 92(6):3359–3376, 1990.
- [3] Dana D. Dlott. New developments in the physical chemistry of shock compression. *Annual review of physical chemistry*, 62:575–597, jan 2011.
- [4] D D Dlott, S Hambir, and J Franken. The new wave in shock waves. *Journal of Physical Chemistry B*, 102(12):2121–2130, 1998.
- [5] Shawn D. McGrane, Jeffrey Barber, and Jason Quenneville. Anharmonic vibrational properties of explosives from temperature-dependent Raman. *Journal of Physical Chemistry A*, 109(44):9919–9927, 2005.
- [6] M. Greenfield, Y. Q. Guo, and E. R. Bernstein. Ultrafast photodissociation dynamics of HMX and RDX from their excited electronic states via femtosecond laser pump-probe techniques. *Chemical Physics Letters*, 430(4-6):277–281, 2006.
- [7] Kathryn E. Brown, Shawn D. McGrane, Cynthia a. Bolme, and David S. Moore. Ultrafast Chemical Reactions in Shocked Nitromethane Probed with Dynamic Ellipsometry and Transient Absorption Spectroscopy. *The journal of physical chemistry. A*, 118(14):2559–2567, 2014.
- [8] L D Landau, E M Lifshitz, and L P Pitaevskii. *Electrodynamics of Continuous Media*. Pergamon Press Ltd., Elmsford, New York, 8th edition, 1984.
- [9] Stanley P Marsh. *LASL shock Hugoniot data*, volume 5. Univ of California Press, 1980.
- [10] Stefano Curtarolo, Wahyu Setyawan, Shidong Wang, Junkai Xue, Kesong Yang, Richard H Taylor, Lance J Nelson, Gus LW Hart, Stefano Sanvito, Marco Buongiorno-Nardelli, et al. Aflowlib. org: A distributed materials properties repository from high-throughput ab initio calculations. *Computational Materials Science*, 58:227–235, 2012.
- [11] Dimitri Gidaspow. *Multiphase flow and fluidization: continuum and kinetic theory descriptions*. Academic press, 1994.
- [12] Hong-jun HU, Ming-bo YANG, Jing Luo, Chun-huan WANG, and Kang Chen. Application of the software procast in the casting of solidification simulation [j]. *Materials Science and Technology*, 3:019, 2006.

- [13] Comsol. *COMSOL Multiphysics: Version 3.3*. Comsol, 2006.
- [14] Olgierd Cecil Zienkiewicz, Robert Leroy Taylor, Olgierd Cecil Zienkiewicz, and Robert Lee Taylor. *The finite element method*, volume 3. McGraw-hill London, 1977.
- [15] Anubhav Jain, Shyue Ping Ong, Geoffroy Hautier, Wei Chen, William Davidson Richards, Stephen Dacek, Shreyas Cholia, Dan Gunter, David Skinner, Gerbrand Ceder, et al. Commentary: The materials project: A materials genome approach to accelerating materials innovation. *Apl Materials*, 1(1):011002, 2013.
- [16] Ashley White. The materials genome initiative: One year on. *MRS Bulletin*, 37(08):715–716, 2012.
- [17] John Bohannon. Whos afraid of peer review. 2013.
- [18] Ellad B Tadmor, Ryan S Elliott, Simon R Phillpot, and Susan B Sinnott. Nsf cyberinfrastructures: A new paradigm for advancing materials simulation. *Current Opinion in Solid State and Materials Science*, 17(6):298–304, 2013.
- [19] Ellad B Tadmor, RS Elliott, JP Sethna, RE Miller, and CA Becker. Knowledgebase of interatomic models (kim), 2011.
- [20] CA Becker. Nist interatomic potentials repository project.
- [21] Gerhard Klimeck, Michael McLennan, Sean P Brophy, George B Adams III, and Mark S Lundstrom. nanohub. org: Advancing education and research in nanotechnology. *Computing in Science & Engineering*, 10(5):17–23, 2008.
- [22] David P Anderson, Jeff Cobb, Eric Korpela, Matt Lebofsky, and Dan Werthimer. Seti@ home: an experiment in public-resource computing. *Communications of the ACM*, 45(11):56–61, 2002.
- [23] Jack J Dongarra, Hans W Meuer, and Erich Strohmaier. Top500 supercomputer sites, 1994.
- [24] G Kresse. Comput. matter sci. 6, 15 (1996);(d) kresse, g., and furthmuller. *Phys. Rev. B*, 54:11–169, 1996.
- [25] GERALD LIPPERT, MICHELE PARRINELLO, and JURG HUTTER. A hybrid gaussian and plane wave density functional scheme. *Molecular Physics*, 92(3):477–488, 1997.
- [26] Paolo Giannozzi, Stefano Baroni, Nicola Bonini, Matteo Calandra, Roberto Car, Carlo Cavazzoni, Davide Ceresoli, Guido L Chiarotti, Matteo Cococcioni, Ismaila Dabo, et al. Quantum espresso: a modular and open-source software project for quantum simulations of materials. *Journal of Physics: Condensed Matter*, 21(39):395502, 2009.
- [27] Peter J Feibelman. Force and total-energy calculations for a spatially compact adsorbate on an extended, metallic crystal surface. *Physical Review B*, 35(6):2626, 1987.

- [28] J Lepinoux and LP Kubin. The dynamic organization of dislocation structures: a simulation. *Scripta metallurgica*, 21(6):833–838, 1987.
- [29] Thomas JR Hughes. *The finite element method: linear static and dynamic finite element analysis*. Courier Corporation, 2012.
- [30] Giuseppe Milano and Florian Müller-Plathe. Mapping atomistic simulations to mesoscopic models: A systematic coarse-graining procedure for vinyl polymer chains. *The Journal of Physical Chemistry B*, 109(39):18609–18619, 2005.
- [31] David Jacqmin. Calculation of two-phase navier–stokes flows using phase-field modeling. *Journal of Computational Physics*, 155(1):96–127, 1999.
- [32] MBBJM Tuckerman, Bruce J Berne, and Glenn J Martyna. Reversible multiple time scale molecular dynamics. *The Journal of chemical physics*, 97(3):1990–2001, 1992.
- [33] Glenn J Martyna, Michael L Klein, and Mark Tuckerman. Nosé–hoover chains: the canonical ensemble via continuous dynamics. *The Journal of chemical physics*, 97(4):2635–2643, 1992.
- [34] Danny Perez, Blas P Uberuaga, Yunsic Shim, Jacques G Amar, and Arthur F Voter. Accelerated molecular dynamics methods: introduction and recent developments. *Annual Reports in computational chemistry*, 5:79–98, 2009.
- [35] Steve Plimpton. Fast Parallel Algorithms for Short-Range Molecular Dynamics. *Journal of Computational Physics*, 117(1):1–19, mar 1995.
- [36] Christopher D Snow, Linlin Qiu, Deguo Du, Feng Gai, Stephen J Hagen, and Vijay S Pande. Trp zipper folding kinetics by molecular dynamics and temperature-jump spectroscopy. *Proceedings of the National Academy of Sciences*, 101(12):4077–4082, 2004.
- [37] Martin Karplus and J Andrew McCammon. Molecular dynamics simulations of biomolecules. *Nature Structural & Molecular Biology*, 9(9):646–652, 2002.
- [38] Alexander D Mackerell and Niles K Banavali. All-atom empirical force field for nucleic acids: Ii. application to molecular dynamics simulations of dna and rna in solution. *Journal of Computational Chemistry*, 21(2):105–120, 2000.
- [39] Seung Soon Jang, Yun Hee Jang, Yong-Hoon Kim, William A Goddard, Amar H Flood, Bo W Laursen, Hsian-Rong Tseng, J Fraser Stoddart, Jan O Jeppesen, Jang Wook Choi, et al. Structures and properties of self-assembled monolayers of bistable [2] rotaxanes on au (111) surfaces from molecular dynamics simulations validated with experiment. *Journal of the American Chemical Society*, 127(5):1563–1575, 2005.
- [40] Stephen L Mayo, Barry D Olafson, and William A. Goddard. DREIDING: a generic force field for molecular simulations. *The Journal of Physical Chemistry*, 94(26):8897–8909, dec 1990.

- [41] Donald W Brenner, Olga A Shenderova, Judith A Harrison, Steven J Stuart, Boris Ni, and Susan B Sinnott. A second-generation reactive empirical bond order (rebo) potential energy expression for hydrocarbons. *Journal of Physics: Condensed Matter*, 14(4):783, 2002.
- [42] Thomas R. Mattsson, J. Matthew D Lane, Kyle R. Cochrane, Michael P. Desjarlais, Aidan P. Thompson, Flint Pierce, and Gary S. Grest. First-principles and classical molecular dynamics simulation of shocked polymers. *Physical Review B*, 81(5):054103, feb 2010.
- [43] Christopher G Mayne, Jan Saam, Klaus Schulten, Emad Tajkhorshid, and James C Gumbart. Rapid parameterization of small molecules using the force field toolkit. *Journal of computational chemistry*, 34(32):2757–2770, 2013.
- [44] MW Finnis and JE Sinclair. A simple empirical n-body potential for transition metals. *Philosophical Magazine A*, 50(1):45–55, 1984.
- [45] Murray S Daw, Stephen M Foiles, and Michael I Baskes. The embedded-atom method: a review of theory and applications. *Materials Science Reports*, 9(7):251–310, 1993.
- [46] Julius T. Su and William a. Goddard. Excited electron dynamics modeling of warm dense matter. *Physical Review Letters*, 99(18):2–5, 2007.
- [47] Christian R Trott, Simon D Hammond, and Aidan P Thompson. SNAP : Strong Scaling High Fidelity Molecular Dynamics Simulations on Leadership-Class Computing Platforms. pages 19–34, 2014.
- [48] A.P. Thompson, L.P. Swiler, C.R. Trott, S.M. Foiles, and G.J. Tucker. Spectral neighbor analysis method for automated generation of quantum-accurate interatomic potentials. *Journal of Computational Physics*, 285:316–330, 2015.
- [49] Albert P. Bartók, Mike C. Payne, Risi Kondor, and Gábor Csányi. Gaussian approximation potentials: The accuracy of quantum mechanics, without the electrons. *Physical Review Letters*, 104(April):1–4, 2010.
- [50] Mads R So, Arthur F Voter, et al. Temperature-accelerated dynamics for simulation of infrequent events. *The Journal of Chemical Physics*, 112(21):9599–9606, 2000.
- [51] Ole Krogh Andersen and Ove Jepsen. Explicit, first-principles tight-binding theory. *Physical Review Letters*, 53(27):2571, 1984.
- [52] MJ Cawkwell and Anders MN Niklasson. Energy conserving, linear scaling born-oppenheimer molecular dynamics. *The Journal of chemical physics*, 137(13):134105, 2012.
- [53] Adri C T Van Duin, Siddharth Dasgupta, Francois Lorant, and William A. Goddard. ReaxFF: A reactive force field for hydrocarbons. *Journal of Physical Chemistry A*, 105(41):9396–9409, oct 2001.

- [54] T. P. Senftle, S. Hong, M M Islam, S. B. Kylasaf, Y. Zheng, Y. K. Shin, C. Junkermeier, R. Engel-Herbert, M. J. Janik, H. M. Aktulga, T. Verstraelen, A. Grama, Adri C. T. van Duin, and Adri C T van Duin. The ReaxFF Reactive Force-field: Development, Applications, and Future Directions. *npj Computational Materials*, accepted(November 2015), 2016.
- [55] J. Tersoff. New empirical approach for the structure and energy of covalent systems. *Physical Review B*, 37(12):6991–7000, apr 1988.
- [56] T C Germann and B L Holian. Molecular Dynamics Simulations of Detonation in Defective Explosive Crystals. . . . *Detonation . . .*, 2002.
- [57] Shi, Donald W. Brenner, Yunfeng Shi, Donald W. Brenner, and North Carolina. Jetting and Detonation Initiation in Shock Induced Collapse of Nanometer-Scale Voids. *The Journal of Physical Chemistry C*, 112(16):6263–6270, apr 2008.
- [58] Yunfeng Shi and Donald W. Brenner. Molecular simulation of the influence of interface faceting on the shock sensitivity of a model plastic bonded explosive. *The journal of physical chemistry. B*, 112(47):14898–14904, nov 2008.
- [59] Donald W Brenner, DH Robertson, ML Elert, and CT White. Detonations at nanometer resolution using molecular dynamics. *Physical review letters*, 70(14):2174, 1993.
- [60] Frank H Stillinger and Thomas A Weber. Computer simulation of local order in condensed phases of silicon. *Physical review B*, 31(8):5262, 1985.
- [61] Frank H Stillinger and Thomas A Weber. Hidden structure in liquids. *Physical Review A*, 25(2):978, 1982.
- [62] Steven J Stuart, Alan B Tutein, and Judith A Harrison. A reactive potential for hydrocarbons with intermolecular interactions. *The Journal of chemical physics*, 112(14):6472–6486, 2000.
- [63] S. J. Zhou. Large-Scale Molecular Dynamics Simulations of Dislocation Intersection in Copper. *Science*, 279(5356):1525–1527, mar 1998.
- [64] Guy Dimonte, G. Terrones, F. J. Cherne, T. C. Germann, V. Dupont, K. Kadau, W. T. Buttler, D. M. Oro, C. Morris, and D. L. Preston. Use of the Richtmyer-Meshkov Instability to Infer Yield Stress at High-Energy Densities. *Physical Review Letters*, 107(26):264502, dec 2011.
- [65] TIMOTHY C. GERMANN and KAI KADAU. TRILLION-ATOM MOLECULAR DYNAMICS BECOMES A REALITY. *International Journal of Modern Physics C*, 19(09):1315–1319, sep 2008.
- [66] S. Davis Herring, Timothy C. Germann, and Niels Grønbech-Jensen. Effects of void size, density, and arrangement on deflagration and detonation sensitivity of a reactive empirical bond order high explosive. *Physical Review B*, 82(21):214108, dec 2010.

- [67] S. B. Kylasa, H. M. Aktulga, and A. Y. Grama. PuReMD-GPU: A reactive molecular dynamics simulation package for GPUs. *Journal of Computational Physics*, 272:343–359, 2014.
- [68] Sudhir B Kylasa. PG-PuReMD : A Parallel-GPU Reactive Molecular Dynamics Package. pages 1–9.
- [69] Anthony K. Rappe and William A. Goddard. Charge equilibration for molecular dynamics simulations. *The Journal of Physical Chemistry*, 95(8):3358–3363, apr 1991.
- [70] Nicolas Onofrio, David Guzman, and Alejandro Strachan. Atomic origin of ultrafast resistance switching in nanoscale electrometallization cells. *Nature materials*, 14(4):440–446, 2015.
- [71] Kimberly Chenoweth, Adri C T van Duin, and William A Goddard. ReaxFF reactive force field for molecular dynamics simulations of hydrocarbon oxidation. TL - 112. *The journal of physical chemistry. A*, 112 VN -(5):1040–1053, feb 2008.
- [72] Kevin D Nielson, Adri CT van Duin, Jonas Oxgaard, Wei-Qiao Deng, and William A Goddard. Development of the reaxff reactive force field for describing transition metal catalyzed reactions, with application to the initial stages of the catalytic formation of carbon nanotubes. *The Journal of Physical Chemistry A*, 109(3):493–499, 2005.
- [73] David A Newsome, Debasis Sengupta, Hosein Foroutan, Michael F Russo, and Adri C T van Duin. Oxidation of Silicon Carbide by O₂ and H₂O: A ReaxFF Reactive Molecular Dynamics Study, Part I. *The Journal of Physical Chemistry C*, 116(30):16111–16121, 2012.
- [74] Obaidur Rahaman, Adri CT van Duin, William A Goddard III, and Douglas J Doren. Development of a reaxff reactive force field for glycine and application to solvent effect and tautomerization. *The Journal of Physical Chemistry B*, 115(2):249–261, 2010.
- [75] You Han, Dandan Jiang, Jinli Zhang, Wei Li, Zhongxue Gan, and Junjie Gu. Development, applications and challenges of ReaxFF reactive force field in molecular simulations. *Frontiers of Chemical Science and Engineering*, pages 1–23, 2015.
- [76] Chen Bai, Lianchi Liu, and Huai Sun. Molecular dynamics simulations of methanol to olefin reactions in hzsm-5 zeolite using a reaxff force field. *The Journal of Physical Chemistry C*, 116(12):7029–7039, 2012.
- [77] Alejandro Strachan, Adri C. T. van Duin, Debashis Chakraborty, Siddharth Dasgupta, and William A Goddard. Shock Waves in High-Energy Materials: The Initial Chemical Events in Nitramine RDX. *Physical Review Letters*, 91(9):098301, aug 2003.
- [78] Mitchell a. Wood, Mathew J. Cherukara, Edward M. Kober, and Alejandro Strachan. Ultrafast Chemistry under Nonequilibrium Conditions and the Shock to Deflagration Transition at the Nanoscale. *Journal of Physical Chemistry C*, 119(38):22008–22015, sep 2015.

- [79] Yumi Park, Hasan Metin Atkulga, Ananth Grama, and Alejandro Strachan. Strain relaxation in si/ge/si nanoscale bars from molecular dynamics simulations. *Journal of Applied Physics*, 106(3):034304, 2009.
- [80] Nathan L Anderson, Ravi Pramod Vedula, Peter A Schultz, Renee M Van Ginhoven, and Alejandro Strachan. Defect level distributions and atomic relaxations induced by charge trapping in amorphous silica. *Applied Physics Letters*, 100(17):172908, 2012.
- [81] Steven J. Plimpton and Aidan P. Thompson. Computational aspects of many-body potentials. *MRS Bulletin*, 37(05):513–521, may 2012.
- [82] R. G. Kraus, S. T. Stewart, D. C. Swift, C. a. Bolme, R. F. Smith, S. Hamel, B. D. Hammel, D. K. Spaulding, D. G. Hicks, J. H. Eggert, and G. W. Collins. Shock vaporization of silica and the thermodynamics of planetary impact events. *Journal of Geophysical Research*, 117(E9):E09009, sep 2012.
- [83] M Millot, N Dubrovinskaia, A Černok, and S Blaha. Shock compression of stishovite and melting of silica at planetary interior conditions. *Science*, 2015.
- [84] Atanu Bhattacharya, Yuanqing Guo, and Elliot R. Bernstein. Nonadiabatic reaction of energetic molecules. *Accounts of Chemical Research*, 43(12):1476–1485, 2010.
- [85] Graham A Worth and Lorenz S Cederbaum. BEYOND BORN - OPPENHEIMER : Molecular Dynamics Through a Conical Intersection. *Annu Rev. Phys. Chem.*, 55:127–158, 2004.
- [86] Michal Ben-Nun, Jason Quenneville, and Todd J. Martínez. Ab Initio Multiple Spawning: Photochemistry from First Principles Quantum Molecular Dynamics. *The Journal of Physical Chemistry A*, 104(22):5161–5175, 2000.
- [87] Brad S. Veldkamp, Xinle Liu, Michael R. Wasielewski, Joseph E. Subotnik, and Mark a. Ratner. Molecular Excited States: Accurate Calculation of Relative Energies and Electronic Coupling Between Charge Transfer and Non-Charge Transfer States. *The Journal of Physical Chemistry A*, 119(2):253–262, 2015.
- [88] Salih Al-Jabour and Monika Leibscher. Effects of Molecular Symmetry on Quantum Reaction Dynamics: Novel Aspects of Photoinduced Nonadiabatic Dynamics. *The Journal of Physical Chemistry A*, 119(2):271–280, 2015.
- [89] M. M. Kuklja. On the initiation of chemical reactions by electronic excitations in molecular solids. *Applied Physics A: Materials Science and Processing*, 76(3):359–366, 2003.
- [90] Changes in Rdx Under Vibration. *Most*, 33(5):598–604, 1998.
- [91] Evgeniĭ Lifshits? *Statistical Physics: Theory of the Condensed State*.

- [92] Luzheng Zhang, SV V Zybin, Adri C.T. T van Duin, Siddharth Dasgupta, W. A. Goddard, and Edward M. Kober. Carbon cluster formation during thermal decomposition of octahydro-1, 3, 5, 7-tetranitro-1, 3, 5, 7-tetrazocine and 1, 3, 5-triamino-2, 4, 6-trinitrobenzene high explosives from reaxFF reactive molecular dynamics simulations. *The Journal of Physical Chemistry A*, 113:10619–10640, 2009.
- [93] Olexandr Isayev, Leonid Gorb, Mo Qasim, and Jerzy Leszczynski. Ab initio molecular dynamics study on the initial chemical events in nitramines: thermal decomposition of CL-20. *The journal of physical chemistry. B*, 112(35):11005–11013, 2008.
- [94] M Riad Manaa and Laurence E Fried. The reactivity of energetic materials under high pressure and temperature. *Advances in Quantum Chemistry*, 69:221–252, 2014.
- [95] Jaroslav Nešetřil, Eva Milková, and Helena Nešetřilová. On minimum spanning tree problem translation of both the 1926 papers, comments, history. *Discrete Mathematics*, 233(1):3–36, 2001.
- [96] B. Boulard, J. Kieffer, C.C. Phifer, and C.a. Angell. Vibrational spectra in fluoride crystals and glasses at normal and high pressures by computer simulation. *Journal of Non-Crystalline Solids*, 140:350–358, jan 1992.
- [97] Peter H. Berens, Donald H. J. Mackay, Gary M. White, and Kent R. Wilson. Thermodynamics and quantum corrections from molecular dynamics for liquid water. *Journal of Chemical Physics*, 79(5):2375, 1983.
- [98] Hua Guo and Bin Jiang. The sudden vector projection model for reactivity: Mode specificity and bond selectivity made simple. *Accounts of Chemical Research*, 47(12):3679–3685, 2014.
- [99] David W Chandler. A search for mode-selective chemistry: The unimolecular dissociation of t-butyl hydroperoxide induced by vibrational overtone excitation. *The Journal of Chemical Physics*, 77(9):4447, 1982.
- [100] D H Semmes, J S Baskin, and a H Zewail. Direct observation of a mode-selective (Non-RRKM) van der Waals reaction by picosecond photofragment spectroscopy. *J.Am.Chem.Soc.*, 109(1):4104–4106, 1987.
- [101] Bin Jiang, Minghui Yang, Daiqian Xie, and Hua Guo. Quantum dynamics of polyatomic dissociative chemisorption on transition metal surfaces: mode specificity and bond selectivity. *Chem. Soc. Rev.*, pages 20–23, 2015.
- [102] Li Chen, Hirokazu Ueta, Régis Bisson, and Rainer D. Beck. Vibrationally bond-selected chemisorption of methane isotopologues on Pt(111) studied by reflection absorption infrared spectroscopy. *Faraday Discussions*, 157(111):285, 2012.
- [103] F Fleming Crim. State- and Bond-Selected Unimolecular Reactions. *Science*, 249(4975):1387–1392, sep 1990.
- [104] Eric W Diau, Jennifer L Herek, Zee Hwan Kim, and Ahmed H Zewail. Concept of Nonergodic Molecules. *Science*, 279(February):847–851, 1998.

- [105] Mitchell A. Wood and Alejandro Strachan. Nonequilibrium Reaction Kinetics in Molecular Solids. *The Journal of Physical Chemistry C*, 120(1):542–552, jan 2016.
- [106] Gregory S. Ezra, Holger Waalkens, and Stephen Wiggins. Microcanonical rates, gap times, and phase space dividing surfaces. *Journal of Chemical Physics*, 130(16), 2009.
- [107] D. J. Wales. Perspective: Insight into reaction coordinates and dynamics from the potential energy landscape. *The Journal of Chemical Physics*, 142(13):130901, apr 2015.
- [108] P Morten Hundt, Bin Jiang, Maarten E van Reijzen, Hua Guo, and Rainer D Beck. Vibrationally promoted dissociation of water on Ni(111). *Science (New York, N.Y.)*, 344(6183):504–7, 2014.
- [109] Veronica Vaida. Spectroscopy of Photoreactive Systems: Implications for Atmospheric Chemistry . *The Journal of Physical Chemistry A*, 113(1):5–18, jan 2009.
- [110] Don Bunker and F. A. Wright, Karin R., Hase, William L., Houle. Exit Channel Coupling Effects in the Unimolecular Decomposition of Triatomics. 83(8):933–936, 1979.
- [111] Don L. Bunker. On non-RRKM unimolecular kinetics: Molecules in general, and CH₃NC in particular. *The Journal of Chemical Physics*, 59(9):4621, 1973.
- [112] Itamar Procaccia, Shaul Mukamel, and John Ross. On the theory of unimolecular reactions: Application of mean first passage time to reaction rates. *The Journal of Chemical Physics*, 68(7):3244, 1978.
- [113] Sarbani Patra and Srihari Keshavamurthy. Classical-quantum correspondence in a model for conformational dynamics: Connecting phase space reactive islands with rare events sampling. *Chemical Physics Letters*, 634:1–10, 2015.
- [114] Keith J Laidler and M Christine King. The Development of Transition-State Theory. *Journal of Physical Chemistry*, 87(15):2657–2664, 1983.
- [115] Pankaj Kumar Yadav and Srihari Keshavamurthy. Breaking of a bond: when is it statistical? *Faraday Discuss.*, 177:21–32, 2015.
- [116] Oscar K. Rice and H. C. Ramsperger. Theories of Unimolecular Gas Reactions At Low Pressures. *The Journal of the American Chemical Society*, 53(3):1929–1932, 1931.
- [117] R a Marcus. Unimolecular Dissociations and Free Radical Recombination Reactions. *The Journal of Chemical Physics*, 20(3):359, 1952.
- [118] Louis Stevenson Kassel. Studies in Homogeneous Gas Reactions. I. *Journal of Physical Chemistry*, 32(2):225–242, 1928.

- [119] Rudolph a Marcus. Theory of mass-independent fractionation of isotopes, phase space accessibility, and a role of isotopic symmetry. *Proceedings of the National Academy of Sciences of the United States of America*, 110(44):1213080110—, 2013.
- [120] Brian C Dian, Asier Longarte, and Timothy S Zwier. Conformational dynamics in a dipeptide after single-mode vibrational excitation. *Science (New York, N.Y.)*, 296(5577):2369–2373, 2002.
- [121] T Baer and A R Potts. Non-statistical chemical reactions: The isomerization over low barriers in methyl and ethyl cyclohexanones. *J. Phys. Chem. A*, 104(42):9397–9402, 2000.
- [122] Paranjothy Manikandan and Srihari Keshavamurthy. Dynamical traps lead to the slowing down of intramolecular vibrational energy flow. *Proceedings of the National Academy of Sciences*, 111(40):14354–14359, 2014.
- [123] Leonid a Bunimovich. Relative volume of KolmogorovArnoldMoser tori and uniform distribution, stickiness and nonstickiness in Hamiltonian systems. *Non-linearity*, 21(2):T13–T17, feb 2008.
- [124] Stavros C. Farantos, Reinhard Schinke, Hua Guo, and Marc Joyeux. Energy localization in molecules, bifurcation phenomena, and their spectroscopic signatures: the global view. *Chemical Reviews*, 109(9):4248–4271, 2009.
- [125] John C Polanyi. Accounts of chemical research. *Accounts of Chemical Research*, 5(5):161–168, 1972.
- [126] Alejandro Strachan. Normal modes and frequencies from covariances in molecular dynamics or monte carlo simulations. *Journal of Chemical Physics*, 120(1):1–4, 2004.
- [127] Graeme Henkelman, Blas P. Uberuaga, and Hannes Jonsson. A climbing image nudged elastic band method for finding saddle points and minimum energy paths. *The Journal of Chemical Physics*, 113(22):9901, 2000.
- [128] Lee-Ping Wang, Robert Treiman McGibbon, Vijay S. Pande, and Todd J. Martínez. Automated Discovery and Refinement of Reactive Molecular Dynamics Pathways. *Journal of Chemical Theory and Computation*, page acs.jctc.5b00830, 2015.
- [129] Mitchell a. Wood, Adri C. T. van Duin, Alejandro Strachan, van Duin, Adri C.T., Alejandro Strachan, Adri C. T. van Duin, and Alejandro Strachan. Coupled thermal and electromagnetic induced decomposition in the molecular explosive ??hMX; A reactive molecular dynamics study. *Journal of Physical Chemistry A*, 118(5):885–895, feb 2014.
- [130] Andrei Piryatinski, Sergei Tretiak, Thomas D. Sewell, and Shawn D. McGrane. Vibrational spectroscopy of polyatomic materials: Semiempirical calculations of anharmonic couplings and infrared and Raman linewidths in naphthalene and PETN crystals. *Physical Review B - Condensed Matter and Materials Physics*, 75(21):1–9, 2007.

- [131] Brandt C Pein, Yuxiao Sun, and Dana D Dlott. Controlling Vibrational Energy Flow in Liquid Alkylbenzenes. *The Journal of Physical Chemistry B*, 117(37):10898–10904, sep 2013.
- [132] Brandt C. Pein, Yuxiao Sun, and Dana D. Dlott. Unidirectional vibrational energy flow in nitrobenzene. *Journal of Physical Chemistry A*, 117(29):6066–6072, 2013.
- [133] Tzu-Ray Ray Shan, Ryan R. Wixom, Ann E. Mattsson, and Aidan P. Thompson. Atomistic simulation of orientation dependence in shock-induced initiation of pentaerythritol tetranitrate. *The journal of physical chemistry. B*, 117(3):928–936, jan 2013.
- [134] Alejandro Strachan and Brad Lee Holian. Energy Exchange between Mesoparticles and Their Internal Degrees of Freedom. *Physical Review Letters*, 94(1):14301, jan 2005.
- [135] Tingting Zhou, Sergey V. Zybin, Yi Liu, Fenglei Huang, and William A. Goddard. Anisotropic shock sensitivity for β -octahydro-1,3,5,7-tetranitro-1,3,5,7-tetrazocine energetic material under compressive-shear loading from ReaxFF-lg reactive dynamics simulations. *Journal of Applied Physics*, 111(12):124904, 2012.
- [136] Naomi Rom, Barak Hirshberg, Yehuda Zeiri, David Furman, Sergey V. Zybin, William A. Goddard, and Ronnie Kosloff. First-Principles-Based Reaction Kinetics for Decomposition of Hot, Dense Liquid TNT from ReaxFF Multi-scale Reactive Dynamics Simulations. *The Journal of Physical Chemistry C*, 117(41):21043–21054, oct 2013.
- [137] Naomi Rom, Sergey V. Zybin, Adri C. T. van Duin, William A Goddard, Yehuda Zeiri, Gil Katz, and Ronnie Kosloff. Density-Dependent Liquid Nitromethane Decomposition: Molecular Dynamics Simulations Based on ReaxFF. *The Journal of Physical Chemistry A*, 115(36):10181–10202, sep 2011.
- [138] David Furman, Ronnie Kosloff, Faina Dubnikova, Sergey V. Zybin, William A. Goddard, Naomi Rom, Barak Hirshberg, and Yehuda Zeiri. Decomposition of condensed phase energetic materials: Interplay between uni- and bimolecular mechanisms. *Journal of the American Chemical Society*, 136(11):4192–4200, mar 2014.
- [139] Si Ping Han, Adri C T van Duin, William A. Goddard, and Alejandro Strachan. Thermal decomposition of condensed-phase nitromethane from molecular dynamics from reaxff reactive dynamics. *Journal of Physical Chemistry B*, 115(20):6534–6540, 2011.
- [140] Fidel Castro-Marciano and Adri C.T. T van Duin. Comparison of thermal and catalytic cracking of 1-heptene from ReaxFF reactive molecular dynamics simulations. *Combustion and Flame*, 160(4):766–775, apr 2013.
- [141] J. P. Elder. The general applicability of the Kissinger equation in thermal analysis. *Journal of Thermal Analysis*, 30(3):657–669, 1985.
- [142] T. Ozawa. Kinetics of non-isothermal crystallization. *Polymer*, 12(3):150–158, mar 1971.

- [143] S Appalakondaiah, G Vaitheeswaran, and S Lebegue. A DFT study on structural, vibrational properties, and quasiparticle band structure of solid nitromethane. *Journal of Chemical Physics*, 138(18):184705, 2013.
- [144] Michael Pravica, Martin Galley, Eunja Kim, Philippe Weck, and Zhenxian Liu. A far- and mid-infrared study of HMX (octahydro-1,3,5,7-tetranitro-1,3,5,7-tetrazocine) under high pressure. *Chemical Physics Letters*, 500(1-3):28–34, 2010.
- [145] Yuri a. Gruzdkov and Yogendra M. Gupta. Vibrational properties and structure of pentaerythritol tetranitrate. *Journal of Physical Chemistry A*, 105(25):6197–6202, 2001.
- [146] Onise Sharia and Maija M. Kuklja. Ab initio kinetics of gas phase decomposition reactions. *Journal of Physical Chemistry A*, 114(48):12656–12661, 2010.
- [147] D. G. Truhlar and B. C. Garrett. Variational transition state theory. *Acc. Chem. Res.*, 235(24):440–448, 1980.
- [148] Craig M. Tarver and Tri D. Tran. Thermal decomposition models for HMX-based plastic bonded explosives. *Combustion and Flame*, 137(1-2):50–62, 2004.
- [149] Onise Sharia and Maija M Kuklja. Rapid materials degradation induced by surfaces and voids: ab initio modeling of β -octatetramethylene [corrected] tetranitramine. *Journal of the American Chemical Society*, 134(28):11815–11820, jul 2012.
- [150] Jimmie C Oxley, a. B. Kooh, R. Szekeres, and W. Zheng. Mechanisms of Nitramine Thermolysis. *The Journal of Physical Chemistry*, 98(28):7004–8, 1994.
- [151] Roman V. Tsyshevsky, Onise Sharia, and Maija M. Kuklja. Thermal decomposition mechanisms of nitroesters: Ab initio modeling of pentaerythritol tetranitrate. *Journal of Physical Chemistry C*, 117(35):18144–18153, 2013.
- [152] Sergey V. Zybin, William A. Goddard, Peng Xu, Adri C T Van Duin, and Aidan P. Thompson. Physical mechanism of anisotropic sensitivity in pentaerythritol tetranitrate from compressive-shear reaction dynamics simulations. *Applied Physics Letters*, 96(8):126–129, 2010.
- [153] G. Katz, S. Zybin, W. a. Goddard, Y. Zeiri, and R. Kosloff. Direct MD Simulations of Terahertz Absorption and 2D Spectroscopy Applied to Explosive Crystals. *The Journal of Physical Chemistry Letters*, 5(5):772–776, mar 2014.
- [154] D.R. Hardesty. An investigation of the shock initiation of liquid nitromethane. *Combustion and Flame*, 27:229–251, aug 1976.
- [155] Normand C Blais, Ray Engelke, and Stephen a Sheffield. Mass Spectroscopic Study of the Chemical Reaction Zone in Detonating Liquid Nitromethane. *J. Phys. Chem. A*, 101(44):8285–95, 1997.

- [156] Henry. Eyring. THE ENERGY OF ACTIVATION FOR BIMOLECULAR REACTIONS INVOLVING HYDROGEN AND THE HALOGENS, ACCORDING TO THE QUANTUM MECHANICS. *Journal of the American Chemical Society*, 53(7):2537–2549, jul 1931.
- [157] Roger C. Baetzold and David J. Wilson. Classical Unimolecular Rate Theory. III. Effect of Initial Conditions on Lifetime Distributions. *The Journal of Chemical Physics*, 43(12):4299, 1965.
- [158] Kai Kadau, Timothy C Germann, Peter S Lomdahl, and Brad Lee Holian. Microscopic View of Structural Phase Transitions Induced by Shock Waves. *Science*, 296(5573):1681–1684, may 2002.
- [159] Christine J Wu, Laurence E Fried, Lin H Yang, Nir Goldman, and Sorin Bastea. Catalytic behaviour of dense hot water. *Nature chemistry*, 1(1):57–62, apr 2009.
- [160] M D Knudson, M P Desjarlais, and D H Dolan. Shock-Wave Exploration of the High-Pressure Phases of Carbon. *Science (New York, N.Y.)*, 322(5909):1822–1825, dec 2008.
- [161] C.M. M Tarver, Steven K Chidester, Albert L Nichols III, A. L. Nichols III, Albert L Nichols III, and A. L. Nichols III. Critical conditions for impact-and shock-induced hot spots in solid explosives. *Journal of Physical Chemistry*, 100:5794–5799, 1996.
- [162] Evan J Reed, M Riad Manaa, Laurence E Fried, Kurt R Glaesemann, and J D Joannopoulos. A transient semimetallic layer in detonating nitromethane. *Nature Physics*, 4(1):72–76, dec 2007.
- [163] R W Armstrong and W L Elban. Materials science and technology aspects of energetic (explosive) materials. *Materials Science and Technology*, 22(4):381, 2006.
- [164] S. M. Walley, J. E. Field, and M. W. Greenaway. Crystal sensitivities of energetic materials. *Materials Science and Technology*, 22(4):402–413, 2006.
- [165] M Mareschal, S McNamara, and J B Maillet. Non-equilibrium molecular dynamics simulations: Techniques and applications. *AIP CONFERENCE . . .*, 2001.
- [166] Anaïs Hervouët, Nicolas Desbiens, Emeric Enteric Bourasseau, and Jean-Bernard Bernard Maillet. Microscopic Approaches to Liquid Nitromethane Detonation Properties. *The Journal of Physical Chemistry B*, 112(16):5070–5078, apr 2008.
- [167] C T White, S B Sinnott, J W Mintmire, D W Brenner, and D. H. Robertson. Chemistry and Phase Transitions from Hypervelocity Impacts. *International Journal of Quantum Chemistry*, 52(S28):129–137, feb 1994.
- [168] Frank Philip Bowden and Abraham David Yoffe. *Initiation and growth of explosion in liquids and solids*. CUP Archive, 1952.

- [169] B M Rice, W Mattson, J Grosh, and S F Trevino. Molecular-dynamics study of detonation. I. A comparison with hydrodynamic predictions. *Physical Review E*, 1996.
- [170] Betsy M Rice, William Mattson, and Samuel F Trevino. Molecular-dynamics investigation of the desensitization of detonable material. *Physical Review E*, 57(5):5106–5111, 1998.
- [171] Timothy C. Germann, Brad Lee Holian, Peter S. Lomdahl, and Ramon Ravelo. Orientation Dependence in Molecular Dynamics Simulations of Shocked Single Crystals. *Physical Review Letters*, 84(23):5351–5354, jun 2000.
- [172] Luzheng Zhang, Sergey V. Zybin, Adri C. T. Van Duin, William A. Goddard, Adri C T Van Duin, William A. Goddard, Adri C. T. Van Duin, William A. Goddard, Adri C T Van Duin, and William A. Goddard. Modeling High Rate Impact Sensitivity of Perfect RDX and HMX Crystals by ReaxFF Reactive Dynamics. *Journal of Energetic Materials*, 28(sup1):92–127, 2010.
- [173] Yao Long and Jun Chen. Systematic Study of the Reaction Kinetics for HMX. *The Journal of Physical Chemistry A*, 119(18):150427094542006, may 2015.
- [174] Qi An, Sergey V. Zybin, William A. Goddard, Andres Jaramillo-Botero, Mario Blanco, and Sheng-Nian Nian Luo. Elucidation of the dynamics for hot-spot initiation at nonuniform interfaces of highly shocked materials. *Physical Review B*, 84(22):220101, dec 2011.
- [175] Qi An, William A. Goddard, Sergey V. Zybin, Andres Jaramillo-Botero, Tingting Zhou, William A Goddard Iii, Sergey V. Zybin, and Andres Jaramillo-Botero. Highly shocked polymer bonded explosives at a nonplanar interface: Hot-spot formation leading to detonation. *Journal of Physical Chemistry C*, 117(50):26551–26561, 2013.
- [176] J. N. Johnson, P. K. Tang, and C. A. Forest. Shock-wave initiation of heterogeneous reactive solids. *Journal of Applied Physics*, 57(9):4323–4334, 1985.
- [177] B. L. Wescott, D. Scott Stewart, and W. C. Davis. Equation of state and reaction rate for condensed-phase explosives. *Journal of Applied Physics*, 98(5):53514, 2005.
- [178] E. L. Lee and C. M. Tarver. Phenomenological model of shock initiation in heterogeneous explosives. *Physics of Fluids*, 23(12):2362, 1980.
- [179] Eugenio Jaramillo, Thomas D. Sewell, and Alejandro Strachan. Atomic-level view of inelastic deformation in a shock loaded molecular crystal. *Physical Review B - Condensed Matter and Materials Physics*, 76(6):1–6, aug 2007.
- [180] G. Levesque, P. Vitello, and W. M. Howard. Hot-spot contributions in shocked high explosives from mesoscale ignition models. *Journal of Applied Physics*, 113(23):233513, 2013.
- [181] Ralph Menikoff. On Beyond the Standard Model for High Explosives: Challenges {&} Obstacles To Surmount. *AIP Conference Proceedings*, 18(2009):18–25, 2009.

- [182] Charles L. Mader. Initiation of Detonation by the Interaction of Shocks with Density Discontinuities. *Physics of Fluids*, 8(10):1811, 1965.
- [183] N. K. Bourne and A. M. Milne. The temperature of a shock-collapsed cavity. *Proceedings of the Royal Society A: Mathematical, Physical and Engineering Sciences*, 459(2036):1851–1861, 2003.
- [184] R Menikoff. Hot spot formation from shock reflections. *Shock Waves*, pages 141–148, 2011.
- [185] Nathan R Barton, Nicholas W Winter, and John E Reaugh. Defect evolution and pore collapse in crystalline energetic materials. *Modelling and Simulation in Materials Science and Engineering*, 17(3):035003, apr 2009.
- [186] F. M. Najjar, W. M. Howard, L. E. Fried, M. R. Manaa, A. Nichols, and G. Levesque. Computational study of 3-D hot-spot initiation in shocked insensitive high-explosive. *AIP Conference Proceedings*, 1426(2012):255–258, 2012.
- [187] William R Anderson and Clint B Conner. Comparison of gas-phase mechanisms applied to RDX combustion model. *Proceedings of the Combustion Institute*, 32(2):2123–2130, 2009.
- [188] Luzheng Zhang, Adri C T Van Duin, Sergey V. Zybin, and William A. Goddard. Thermal decomposition of hydrazines from reactive dynamics using the reaxff reactive force field. *Journal of Physical Chemistry B*, 113(31):10770–10778, 2009.
- [189] Tzu-Ray Shan, Adri C T van Duin, and Aidan P Thompson. Development of a ReaxFF reactive force field for ammonium nitrate and application to shock compression and thermal decomposition. *The journal of physical chemistry. A*, 118(8):1469–1478, feb 2014.
- [190] Tzu-Ray Shan, Ryan Wixom, and Aidan P. Thompson. Micron-scale Reactive Atomistic Simulations of Void Collapse and Hot spot Growth in Pentaerythritol Tetranitrate. *15th International Detonation Symposium Proceedings*, 2015.
- [191] Daniel E. Hooks, Kyle J. Ramos, a. Richard Martinez, and A. Richard Martinez. Elastic-plastic shock wave profiles in oriented single crystals of cyclotrimethylene trinitramine (RDX) at 2.25 GPa. *Journal of Applied Physics*, 100(2):24908, 2006.
- [192] Zhong Ding and S.M. M Gracewski. The behaviour of a gas cavity impacted by a weak or strong shock wave. *Journal of Fluid Mechanics*, 309(1996):183–209, 1996.
- [193] A. Landerville, I. I. Oleynik, M. A. Kozhushner, and C. T. White. First-principles reactive molecular dynamics of chemistry in detonating energetic materials. *AIP Conference Proceedings*, 955:447–450, 2007.
- [194] Ken-ichi Ichi Nomura, Rajiv K. Kalia, Aiichiro Nakano, and Priya Vashishta. Reactive nanojets: Nanostructure-enhanced chemical reactions in a defected energetic crystal. *Applied Physics Letters*, 91(18):183109, 2007.

- [195] A P Esposito, D L Farber, J E Reaugh, and Joseph M Zaug. Reaction propagation rates in HMX at high pressure. *Propellants, Explosives, Pyrotechnics*, 28(2):83–88, 2003.
- [196] Yeong-Cherng Liao and Vigor Yang. Analysis of RDX monopropellant combustion with two-phase subsurface reactions. *Journal of Propulsion and Power*, 11(4):729–739, 1995.
- [197] Anatoli Zenin. HMX and RDX: Combustion mechanism and influence on modern double-base propellant combustion. *J. Propul. Power*, 11(4):752–758, 1995.
- [198] Richard A. Yetter, Frederick L. Dryer, M. T. Allen, and J. L. Gatto. Development of Gas-Phase Reaction Mechanisms for Nitramine Combustion. *Journal of Propulsion and Power*, 11(4):683–697, 1995.
- [199] D. S. Moore. Instrumentation for trace detection of high explosives. *Review of Scientific Instruments*, 75(8):2499–2512, 2004.
- [200] Jorge Serrano, Javier Moros, Carlos Sánchez, Jorge Macías, and J. Javier Laserna. Advanced recognition of explosives in traces on polymer surfaces using LIBS and supervised learning classifiers. *Analytica Chimica Acta*, 806:107–116, 2014.
- [201] Javier Moros and Javier Laserna. New Raman{Å}Laser-Induced Breakdown Spectroscopy Identity Sensing Platform. pages 6275–6285, 2011.
- [202] Jimmie C. Oxley, James L. Smith, Joseph E. Brady IV, and Austin C. Brown. Characterization and analysis of tetranitrate esters. *Propellants, Explosives, Pyrotechnics*, 37(1):24–39, 2012.
- [203] Kathryn E. Brown, Margo T. Greenfield, Shawn D. McGrane, and David S. Moore. Advances in explosives analysis???part I: animal, chemical, ion, and mechanical methods. *Analytical and Bioanalytical Chemistry*, pages 35–47, 2015.
- [204] Kathryn E. Brown, Margo T. Greenfield, Shawn D. McGrane, and David S. Moore. Advances in explosives analysis???part II: photon and neutron methods. *Analytical and Bioanalytical Chemistry*, pages 49–65, 2015.
- [205] Jeremy Renshaw, John C. Chen, Stephen D. Holland, and R. Bruce Thompson. The sources of heat generation in vibrothermography. *NDT and E International*, 44(8):736–739, 2011.
- [206] Kenneth S Suslick and David J Flannigan. Inside a collapsing bubble: sonoluminescence and the conditions during cavitation. *Annual review of physical chemistry*, 59(December):659–683, 2008.
- [207] Sizhu You, Ming-wei Chen, Dana D Dlott, and Kenneth S Suslick. Ultrasonic hammer produces hot spots in solids. *Nat Commun*, 6:6581, 2015.
- [208] A.G Fallis. No Title No Title. *Journal of Chemical Information and Modeling*, 53(9):1689–1699, 2013.
- [209] Herbert J. Sutherland and James E. Kennedy. Acoustic characterization of two unreacted explosives. *Journal of Applied Physics*, 46(6):2439–2444, 1975.

- [210] J. O. Mares, J. K. Miller, N. D. Sharp, D. S. Moore, D. E. Adams, L. J. Groven, J. F. Rhoads, and S. F. Son. Thermal and mechanical response of PBX 9501 under contact excitation. *Journal of Applied Physics*, 113(8), 2013.
- [211] J. O. Mares, J. K. Miller, I. E. Gunduz, J. F. Rhoads, and S. F. Son. Heat generation in an elastic binder system with embedded discrete energetic particles due to high-frequency, periodic mechanical excitation. *Journal of Applied Physics*, 116(20), 2014.
- [212] G D Smith and R K Bharadwaj. Quantum Chemistry Based Force Field for Simulations of HMX. *J Phys Chem B*, 103(18):3570–3575, 1999.
- [213] Dmitry Bedrov, Chakravarthy Ayyagari, Grant D. Smith, Thomas D. Sewell, Ralph Menikoff, and Joseph M. Zaug. Molecular dynamics simulations of HMX crystal polymorphs using a flexible molecule force field. *Journal of Computer-Aided Materials Design*, 8(2-3):77–85, 2001.
- [214] Jerry J Dick, A Richard Martinez, and Robert S Hixson. Plane impact response of pbx 9501 and its components below 2 gpa. Technical report, Los Alamos National Lab., NM (United States), 1998.
- [215] Benjamin P Haley, Nate Wilson, Chunyu Li, Andrea Arguelles, Eugenio Jaramillo, and Alejandro Strachan. Polymer modeler, Aug 2016.
- [216] Alexander Stukowski. Visualization and analysis of atomistic simulation data with OVITOthe Open Visualization Tool. *Modelling and Simulation in Materials Science and Engineering*, 18(1):015012, 2009.
- [217] R. a. Isbell and M. Q. Brewster. Optical Properties of Energetic Materials: RDX, HMX, AP, NC/NG, and HTPB. *Propellants, Explosives, Pyrotechnics*, 23(4):218–224, 1998.
- [218] S Chen, W a Tolbert, and D D Dlott. Direct Measurement of Ultrafast Multiphonon up-Pumping in High Explosives. *Journal of Physical Chemistry*, 98(32):7759–7766, 1994.
- [219] G. T. Boyd, Th Rasing, J. R R Leite, and Y. R. Shen. Local-field enhancement on rough surfaces of metals, semimetals, and semiconductors with the use of optical second-harmonic generation. *Physical Review B*, 30(2):519–526, 1984.
- [220] Michael C. Kemp. Explosives Detection by Terahertz SpectroscopyA Bridge Too Far? *IEEE Transactions on Terahertz Science and Technology*, 1(1):282–292, 2011.
- [221] Lucia M. Lepodise, Joseph Horvat, and R. a. Lewis. Terahertz Spectroscopy of 2,4-Dinitrotoluene over a Wide Temperature Range (7245 K). *The Journal of Physical Chemistry A*, 119(2):263–270, 2015.
- [222] Zhao Chen, Xibin Zhou, Christopher A. Werley, and Keith A. Nelson. Generation of high power tunable multicycle terahertz pulses. *Applied Physics Letters*, 99(7):2009–2012, 2011.

- [223] Xiaojian Fu, Hongya Wu, Xiaoqing Xi, and Ji Zhou. Molecular rotation-vibration dynamics of low-symmetric hydrate crystal in the terahertz region. *Journal of Physical Chemistry A*, 118(2):333–338, 2014.
- [224] Robert W. Boyd. *Nonlinear Optics*. Academic Press, San Diego, 3rd edition, 1992.
- [225] J. D. Jackson. Classical Electrodynamics, 3rd ed. *American Journal of Physics*, 67(9):841, 1999.
- [226] David Steven Moore. Method and apparatus for detecting explosives, 2011.
- [227] Erik Cornelis Neyts, Adri C T van Duin, and Annemie Bogaerts. Insights in the Plasma-Assisted Growth of Carbon Nanotubes through Atomic Scale Simulations: Effect of Electric Field. *Journal of the American Chemical Society*, 134(2):1256–1260, jan 2012.
- [228] Huiran Li, Dahua Ren, and Xinlu Cheng. The theoretical investigation of the β -cristobalite structure under the effect of electric field. *Computational Materials Science*, 96:306–311, jan 2015.
- [229] James R Holden and Charles W Dickinson. Crystal Structures of Three Solid Solution Phases of Ammonium Nitrate and Potassium Nitrate. *J. Phys. Chem.*, 79(3):249–256, 1975.
- [230] Yanqiang Yang, Zhaoyong Sun, Shufeng Wang, Selezione a. Hambir, Hyunung Yu, and Dana D. Dlott. Ultrafast spectroscopy of laser-initiated nanoenergetic materials. *MRS Proceedings*, 800:4485–4493, 2003.
- [231] Dana D Dlott. Vibrational energy redistribution in polyatomic liquids : 3D infrared Raman spectroscopy. *Chemical Physics*, 266:149–166, 2001.
- [232] Samuel Reeve and Alejandro Strachan. Error correction in multi-fidelity molecular dynamics simulations using functional derivatives. pages 1–27.
- [233] Hyunseong Shin, Seunghwa Yang, Seongmin Chang, Suyoung Yu, and Maenghyo Cho. Multiscale homogenization modeling for thermal transport properties of polymer nanocomposites with Kapitza thermal resistance. *Polymer*, 54(5):1543–1554, 2013.

APPENDICES

Appendix A: Code Description

There are a number of analysis tools that have been written to perform or accelerate different parts of the work shown in this document, a description of how they work and how to operate them will be discussed here. Most of the code that was produced was written in FORTRAN, primarily because it has a very fast runtime and therefore is ideal for processing large data files. However, some Python codes also exist because they can be adapted and re-run on the fly without waiting to recompile, which is ideal if the analysis technique is collecting results over multiple simulations. The BASH scripts that are used for convenience won't be covered here, these are usually specific to their use and are hard to translate onto the next user. These are extremely useful in practice because the slowest portion of computational work is the human element, so anything that will make your job easier is worth learning how to do.

Local Properties:

Regardless of how fast a particular code is per calculation, the easiest way to reach the end result faster is to cut out unnecessary computation. For large simulations, this means making your code 'short-sighted' and neglect atom interactions beyond some distance. As an example, one could tell an MD code to calculate the van Der Waals force on every atom pair, regardless of distance. This would result in many terms being exactly zero, which we could have done without calculating because they do not affect the end result. The same idea is true when looking for covalent bonds in a molecular material, there are no realistic bonds beyond some cutoff distance.

The first code of interest is named `Local_Bonds.py` which is a python code that will find nearby bonds for each atom solely from the distance between them. The heavy lifting of this code is done when a large simulation cell is partitioned into smaller cells, but the size of the cell is critical because if it is too small there is significant noise in the local measurement. Here a bin size is chosen such that the average number of atoms in each smaller cell is around 50, but this can be smaller when only recognizing bonds. However, this atom count is critical when calculating local temperatures or pressures, some time should be spent to determine a balance between run times and accuracy of the result when this code is employed.

There are a few hard-coded portions of this code which need to be highlighted. This code expects separate LAMMPS dump file that are distinguished by a frame number (i.e. `GoodData.###.dump`), this frame number is used during the execution of the code and the file path is set in line 54. The frame number is also used in the execution of the code, by typing `'python Local_Bonds.py 100'` where the last number is the frame that will be processed. From here it is easy to see that a BASH script to incrementally change the frame number in the execute line will take care of repeat submission. Inside this code there are other hard coded objects that need to change if it is to properly find bonds. First, on line 48, the number of atoms (`n=###`) needs to be set depending on the system of interest. Next, the table of bond distances needs

to adjusted through the variable `rdict` on line 57. Here each index corresponds to a pair of atom types in the MD simulation, entry '23' : '1.8' means that atom type 2 bonds to 3 with a distance less than 1.8 Angstroms. Beyond these small changes, the code will partition the whole simulation cell into parts and only look for bonds with atoms in its own bin, or those immediately around it.

The output of this code will be a table of length of the number of atoms in the system called `mols.###.dump` where the frame number matches that from the code execution line. This table read as follows; AtomID AtomType NumberOfBonds BondedAtom_1 BondedAtom_2 *etc.*, which is the same as the `fix reax/bonds` command in LAMMPS. A list of bonded atoms can be useful when attempting to detect changes in chemical makeup, but is dependent on the problem at hand. In the next section, a code was developed that will use this bond information to reduce a simulation cell into molecule populations, among other things.

A similar code as `Local_Bonds.py` will calculate a handful of local thermodynamic quantities based on per atom quantities in the LAMMPS data files, this code is called `Local_Thermo.py`. Currently, the expected input is a LAMMPS dump file with positions and velocities and it will output the local temperature (after the center of mass velocity of the grid volume is subtracted) and the density. If per atom forces are included in the dump file, then local stress components can be calculated just use the `Local_ThermoStr.py`. Output from either one of these local average scripts will be stored in three different files, `###ps.noavg`, `###ps.avg`, and `correctedv.###.dump`. The first contains all of the local averages in the plane of interest (default is X-Z), the second has the first dimension averaged out so it is just the average local property along Z, the last is a corrected dump file which has the velocities modified such that there is no center of mass motion of the cell. Again, setting up a BASH script to process a large number of dump files is ideal, depending on the number of atoms this script will complete within a minute for a system of one-hundred thousand atoms. It is also good practice when running a large number of these analysis scripts to keep them off the front end nodes by using a job submission file.

Molecule Recognition

Primarily in use throughout Chapter 3, the ability to analyze a simulation in terms of molecular species rather than just atoms reveals a new set of data that provides new insight. The local properties section describes a method to cheaply recognize which atoms are bonded to one another, the obvious next step is to group these atoms into clusters to get molecular level properties. A FORTRAN code has been developed to recognize which molecular species are present, report their center of mass positions (trivial), their T_{CoM} and T_{Vib} . The necessary inputs are then a table of which atoms are bonded to one another, and the positions and velocities of all the atoms. Currently, in `MoleculeRec_wTemps.f` these files are hard coded as 'MolRec.dat' and 'Positions.dat' respectively, these were kept as dummy file names to avoid re-compiling the code when a new file was to be read in. Since FORTRAN is the equivalent to Latin in spoken language, it has to be compiled into an executable

before it can be used, to do so load your favorite Intel compiler and type ‘ifort -O3 MoleculeRec.wTemps.f -o Compiled.fort’. The name of the executable or its extension type doesn’t matter, it is good practice to attach a date to the compiled version for bookkeeping. To run the code in a UNIX environment, just type ./Compiled.fort, the best way to do this is make a symbolic link to the code via the ln command.

Initially, this code will store a single frames worth of connectivity, positions and velocities into sorted arrays based on the atom identification number. In order to save compute cost, a minimum spanning tree algorithm is used in order to only recognize a bonded pair of atoms once. The algorithm works as follows;

- 1) Find an atom that has not been recognized in any other cluster (a boolean array stores each atoms status here) and add it and its’ bonded atoms to a list, lets call this the first branch of atoms.
- 2) Take the bonded atoms if the first branch and add any *unique* atom IDs to the aforementioned list.
- 3) Keeping track of the number of unique atom IDs that are added to the list for this particular molecule, repeat until no more unique atoms are found.
- 4) Store the number of atoms in the cluster that was just completed, this will be stored in a separate array that will aid in looking up clusters in the future.

Up to this point, the execution times are very quick, even on large atom counts. What takes a significant amount of compute time is counting the population of unique molecules types, this is a type step process that involves reducing each molecule by unique composition (topology doesn’t matter now, which would be viable addition to this code). After molecules are tagged by composition, a loop over the total number of molecules is launched which compares if the current molecule has been recognized already. If true, add one to the population, if false, create a new instance into the list of unique molecules and set its population to one. The current state of the code skips much of this hard work by just looking for a set of molecules that have been deemed interesting for combustion of energetic materials. Also inside of this loop over molecules is the calculations of per molecule quantities such as position, velocity and temperature. This is easy to do once the atom IDs are known for each cluster, it becomes a lookup tag from the data stored when reading ‘Positions.dat’. Equations 2.4 and 2.5 are used to get temperatures per molecule, along with positions and velocities of molecules, a new, more compact, dump file is created in the .xyz format style. This new dump file is called COM_Molecules.xyz, and will be overwritten every frame unless there is a modification made to the code. Since these dump files can be quite large, having the default version of the code spit out thousands of these files seemed dangerous and was set up to overwrite itself. However, this new dump file can be rendered in any visualization program and make nice images of the simulation cell where the ‘atoms’ that are plotted now are whole molecules, see Figure ??.

There are three main outputs for this code, Output_MST.dat, Common_Mols.dat and FormatUncommon_Mols.dat. Output_MST.dat is a raw output of what molecules were recognized by the minimum spanning tree algorithm, this is useful as a first pass to determine what molecules are common to the chemical conversion that is hap-

pening in your simulation. The next two files are tabulated molecule populations of common and uncommon, which is to say they occur frequently but not in high number, with each row being a new frame that was analyzed. Feel free to change up the default species that are added to the latter two molecule population files, just go into the massive IF block at the bottom of the code and adjust the composition that it is looking for. Alternatively, while the clusters are being formed, add if statements that will count the number of bonds between interesting species, i.e counting the number of bonded carbon-nitrogen with time.

Spectroscopic Characterization

This last section of code will discuss how to generate spectroscopic data from and MD trajectory, Figure 4.3 is an example of what the output will look like. Unlike Raman or FTIR as it is performed in the lab, MD does not need to scatter a probe light source to sample the vibrations within a material. Simply, all of the vibrations that a material posses are wrapped up in the velocity history of all the atoms and a Fourier transform will reveal what the frequency of each of these characteristic vibrations are. Most importantly, this calculation is applicable to any material, even if the MD is being done on coarse grained systems with reduced forces. Also, unlike DFT, this measurement can be made at any temperature and does not use a normal mode approximation to determine vibrational frequencies. For systems that are evolving close to transition states, where some vibrations are highly anharmonic, this method will capture the shifting and broadening of modes as the material begins to decompose, this is not possible from a normal mode approach. So then, how does the code work? The computational method used in this code, called ‘VibDoS_Calc.f’, becomes very costly for large atoms counts greater than 10,000, but it gives very clean results otherwise. To compile, load up Intel compilers again and type ‘ifort -O3 -L -llapack -lblas -mcmmodel medium -shared-intel VibDoS_Calc.f -o Compiled.fort’, the extra bits here allow for a greater allocation of static memory and attach LAPACK libraries. Now to run: `./Compiled.fort < in.lammps`

This code works by reading through your LAMMPS input file (in.lammps) to identify where the starting data is stored (finds read_data and dump commands) and gathers the units, masses, dump file name, dump frequency, and which column the velocity data is stored. Personally, I just use a dummy LAMMPS input file so that I know this code is reading the correct data just in case there are multiple read_data or dump commands. Unlike the local analysis scripts, this code expects a single LAMMPS dump file for the entire trajectory. The main loop of this code will step through each atom in the system and read the corresponding time series of velocities, which are then Fourier transformed, see Equation 2.6. Herein lies why the code becomes time consuming when a large number of atoms are supplied, this code will perform a Fourier transform for every atom in the system. The benefits are twofold, the shapes of the vibrational peaks are better resolved since a larger number of spectra are calculated and then averaged. Secondly, this costly method means that vibrational properties can be broken down by which elements are contributing to each vibration,

see Figure 4.3. The total vibrational spectra is just an average over each atom's individual spectra, but we can selectively chose which atoms we average this total spectra over, the obvious choice is to divide the spectra by element types. Therefore, the output from this code will be a set of files called 'Vib_FFT_NM.atomtype#.out' with the number representing the atom type. The total vibrational spectrum will be outputted simply as 'Vib_FFT_NM.out' and will contain three columns which are Frequency(ps^{-1}), Frequency(cm^{-1}), Kinetic Energy Density. The integral of the last column (if done correctly) will be equal to the total kinetic energy of the system. If you are interested in calculating this quantity for a large number of atoms, it is best to pre-calculate the autocorrelation function of the velocities and then take just one Fourier transform of this. For more information of why this is true, I would suggest looking into the WienerKhinchin theorem.

The second code for this section will take advantage of this equivalence stated in the WienerKhinchin theorem, but will now look at which vibrations are infrared active. This code is 'IR_andNormalModes.f' and is compiled and run in the same fashion of the previous code. Here, the code is evaluating what is described in Equation 2.8 by reading through a continuous LAMMPS trajectory and collecting the charges and velocities of each atom. The output, 'IR_FFT_Modes.out' looks very similar to the full vibrational spectra with the last column now being the infrared intensity at that particular frequency. This intensity measure does not carry units, and can be normalized for plotting convenience. Currently, the second half of this code is turned off by the 'STOP' command on line 390. The second portion of this code is intended to calculate the normal modes of vibration using the method outlined by Strachan in his 2004 paper entitled 'Normal modes and frequencies from covariances in molecular dynamics or Monte Carlo simulations'. Unfortunately, this method is very computationally costly since it has to diagonalize large matrices in order to generate the normal modes of oscillation. It does create some nice trajectories that just have one vibrational mode expressed on the system, so thats nice. Use this portion of the code at your own risk, I did not spend much time debugging and making it full proof for any input material.

Appendix B: Published Work

At the time this thesis has been completed, here are all of the journal versions of the published work that have resulted from my graduate work. Some of this work is not discussed in this thesis, and is included here for completeness.

Reprinted (adapted) with permission from “Coupled Thermal and Electromagnetic Induced Decomposition in the Molecular Explosive HMX; A Reactive Molecular Dynamics Study” M. A. Wood, A. C. van Duin and A. Strachan, *Journal of Physical Chemistry A*, 2014, 118 (5). DOI: 10.1021/jp406248m. Copyright 2014 American Chemical Society.

Reprinted (adapted) with permission from Computation of the Density Matrix in Electronic Structure Theory in Parallel on Multiple Graphics Processing Units M. J. Cawkwell, M. A. Wood, A. M. N. Niklasson and S. M. Mniszewski, *Journal of Chemical Theory and Computation*, 2014, 10 (12). DOI: 10.1021/ct500822. Copyright 2014 American Chemical Society.

Reprinted (adapted) with permission from Ultra-fast Chemistry under Non-equilibrium Conditions and the Shock to Deflagration Transition at the Nanoscale M. A. Wood, M. J. Cherukara, E. M. Kober and A. Strachan, *Journal of Physical Chemistry C*, 2015 DOI: 10.1021/acs.jpcc.5b05362. Copyright 2015 American Chemical Society.

Reprinted (adapted) with permission from Nonlinear Electromagnetic Interactions in Energetic Materials M. A. Wood, D. A. R. Dalvit and D. S. Moore, *Physical Review Applied*, 2016 DOI: 10.1103/PhysRevApplied.5.014004. Copyright 2015 with License Number 3838280604060. American Physical Society.

Reprinted (adapted) with permission from Ultra-fast Chemistry under Non-equilibrium Conditions and the Shock to Deflagration Transition at the Nanoscale M. A. Wood, M. J. Cherukara, E. M. Kober and A. Strachan, *Journal of Physical Chemistry C*, 2015 DOI: 10.1021/acs.jpcc.5b05362. Copyright 2016 American Chemical Society.

Coupled Thermal and Electromagnetic Induced Decomposition in the Molecular Explosive α -HMX; A Reactive Molecular Dynamics Study

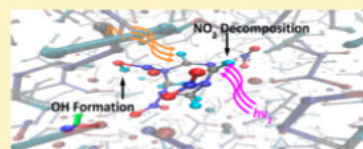
Mitchell A. Wood,[†] Adri C. T. van Duin,[‡] and Alejandro Strachan^{*,†}

[†]School of Materials Engineering and Birk Nanotechnology Center, Purdue University, West Lafayette, Indiana 47907, United States

[‡]Department of Mechanical and Nuclear Engineering, Pennsylvania State University, University Park, Pennsylvania 16801, United States

Supporting Information

ABSTRACT: We use molecular dynamics simulations with the reactive potential ReaxFF to investigate the initial reactions and subsequent decomposition in the high-energy-density material α -HMX excited thermally and via electric fields at various frequencies. We focus on the role of insult type and strength on the energy increase for initial decomposition and onset of exothermic chemistry. We find both of these energies increase with the increasing rate of energy input and plateau as the processes become athermal for high loading rates. We also find that the energy increase required for exothermic reactions and, to a lesser extent, that for initial chemical reactions depend on the insult type. Decomposition can be induced with relatively weak insults if the appropriate modes are targeted but increasing anharmonicities during heating lead to fast energy transfer and equilibration between modes that limit the effect of loading type.



1. INTRODUCTION

The ability of high-energy-density (HED) materials to transfer energy between their various inter- and intramolecular modes of vibration and to localize energy in so-called hot spots plays a key role in the initiation of chemical reactions in these materials. Understanding energy transfer and localization mechanisms is, thus, critical to develop predictive models for their performance and safety. Energy localization not only can happen spatially but also can happen in frequency space as loading at extremely high rates can lead to nonequilibrium conditions with some modes having more than their (equilibrium) share of the total kinetic energy. For example, the translational energy in shockwaves couples predominantly to low-frequency modes, and this energy needs to be up-pumped to localized, high-frequency modes that can lead to bond-breaking.^{1–7} Understanding vibrational properties of HED materials, their coupling to electromagnetic fields and energy localization/transfer mechanisms can also contribute to methods for their detection.^{8–10} In this paper we use atomistic simulations to characterize the amount of energy required to initiate the decomposition and to reach the onset of exothermic chemistry of the nitramine HMX excited by a variety of insults that couple to different vibrational modes and with different strengths.

Energy localization in hotspots is responsible for the initiation of detonation in HED materials and is often responsible for accidental explosion. A wealth of experimental^{10–19} and theoretical^{1–4,20–28} work has been focused on identifying and quantifying the role of defects in the generation of hot spots within a shocked material. As mentioned above, energy localization not only occurs spatially but also occurs in frequency space.^{10,29–33} This frequency localization and energy

transfer have been studied extensively by, among others, Dlott, Moore, and McGrane with advanced spectroscopic techniques on a number of liquid^{15,31,34–37} and solid phase materials.^{30,38–40} In addition, the works of Coffey and others have proposed energy-transfer models that have extended the theoretical understanding of initiation in these complex materials.^{41–43}

Anharmonic contributions to inter- and intramolecular vibrations in molecular materials allow for energy transfer between modes and, therefore, are important to understanding the kinetics of an excited material. The extremely fast time scales for vibron–vibron relaxation, in the 10^{-8} to 10^{-12} s range, make their experimental investigation challenging.^{6,29} Dlott and co-workers measured vibron decay times of stimulated CH-stretch modes in a number of aryl–halide liquids⁴⁴ and found that relaxation times for these high-frequency modes is dependent on the density of modes in the 1000–1600 cm^{-1} range that control the decay paths down to phonon modes. Similarly, studies by McGrane and co-workers measured the lifetimes and broadening times for a large number of vibron modes in a number of energetic materials.^{45,46} These results show that excited modes in HMX exhibit dephasing times ranging from 40 ps for low-frequency modes (less than 400 cm^{-1}), 20 ps in the 800–1200 cm^{-1} range, and less than 5 ps in nearly all other modes. In contrast, other materials, such as PETN and naphthalene, show dephasing times greater than 40 ps for their entire vibron frequency ranges (1–3200 cm^{-1}).⁴⁵ In addition to the work described so far, laser-driven shock experiments show great potential toward a highly repeatable and time-sensitive

Received: June 25, 2013

Revised: December 8, 2013

Published: January 8, 2014



ACS Publications

© 2014 American Chemical Society

885

dx.doi.org/10.1021/jp406248m | J. Phys. Chem. A 2014, 118, 885–895

approach for observing phonon up-pumping in a wide range of energetic and nonenergetic materials.^{34,40,47,48}

In this paper we use reactive molecular dynamics (MD) simulations to characterize how chemical reactions in HMX depend on the intensity and character (e.g., the vibrational modes it couples to) of the stimulus. We study systems subjected to various heating rates and electric fields with sinusoidal time dependence of various frequencies and strengths. We find that, for fast loading rates, chemical reactions can be initiated with relatively weak insults when the stimulus couples to appropriately chosen modes. The paper is organized as follows. Section 2 provides simulation details, and section 3 shows calculations on the vibrational and infrared spectrum. Section 4 focuses on our results of HMX decomposition by direct and electric field heating and their discussion. Section 5 addresses the role of insult type on decomposition kinetics, and section 6 correlates these results to frequency-resolved energy absorption and transfer. Section 7 studies the initial chemical reactions and their dependence on insult type. Finally, conclusions are drawn in section 8.

2. SIMULATION DETAILS

A. Molecular Dynamics Simulations. We use molecular dynamics with the reactive force field ReaxFF that has been extensively used to describe HED materials.^{1,2,49–53} The ReaxFF parametrization used is based on the original nitramines force field^{1,2} and includes bond dissociation curves for all viable C/O/N/H single, double, and triple bonds, angle distortions for all viable C/O/N/H angular combinations, dihedral barriers, and charge distributions. Furthermore, for a number of nitramine HED materials (RDX, HMX, and PETN) full dissociation pathways, including reaction barriers, were used in the ReaxFF parameter determination. This training set was obtained from DFT calculations at the B3LYP/6-311G** and 6-31G** levels.² Charge equilibration parameters are obtained to reproduce partial atomic charges obtained from DFT using Mulliken populations. The original ReaxFF nitramine description² was nontransferable with other ReaxFF parameter sets as it did not share general or atom parameters. To remediate this, we integrated the nitramine training set with the C/H/O combustion training set, as described by Chenoweth et al.⁵⁴ For HMX, the current parameter set leads to a NO₂ dissociation energy of 41.3 kcal/mol, which is in good agreement with the DFT result (39.8 kcal/mol). The ReaxFF parameter set used in this work predicts the HONO dissociation pathway to be mildly exothermic (−9.1 kcal/mol), whereas the concerted ring-opening is more exothermic (−19.0 kcal/mol), but this latter reaction has a very substantial barrier and as such is an unlikely initiation HMX initiation pathway.

The parameters used here are fully transferable with the “combustion” ReaxFF development branch, which contains a wide number of elements,^{55–58} enabling straightforward extension to, for example, metal additives. The parameter file is included in the Supporting Information.

During the MD simulations, partial atomic charges are obtained self-consistently at every time step with a conjugate gradient (CG) method with tolerance set to one part per million.⁵⁹ All simulations are carried out with the LAMMPS code⁶⁰ using a time step of 0.1 fs to integrate the equations of motion; this is sufficiently small to guarantee good energy conservation.

Direct thermal decomposition studies are performed via continuous heating using a Nose–Hoover thermostat with a coupling constant of 100 fs under isochoric conditions. After the

systems reach 2000 K, we follow their subsequent decomposition using constant energy and volume simulations (NVE ensemble). Constant volume simulations are appropriate due to the fast heating rates in our studies.

The electric-field induced decomposition studies are performed entirely using NVE simulations. A field of the desired amplitude and frequency is applied to the simulation cell. The power density is computed as $\rho = (\epsilon\epsilon_0\pi/2)E^2\omega$, where E is the amplitude of the field, ω is the frequency, and ϵ is the dielectric constant of HMX. These simulations are also followed by adiabatic simulations (turning the external field off) once the temperature reaches 2000 K. The field strengths were chosen such that the resulting heating rates led to decomposition time scales achievable with MD simulations and so are the rates chosen for direct heating. As a result, large electric fields are applied: from 5.6 to 35.6×10^8 V/m. For each target frequency, the amplitude of the field is adjusted to ensure a constant value for the calculated power density. Experimental setups used to study the laser damage on high explosives from Moore⁴⁰ used a 3 W laser confined to a spot size of approximately 200 μm on each side, which leads to power densities about one-thousand times smaller than those used in our studies. In these experiments temperature increases on the order of a few hundred Kelvin were observed over 100 s, far exceeding the time scales achievable with MD simulations. Spectroscopy techniques that measure laser-induced decomposition products use much higher pulse energies,^{61,62} which can reach into the megawatt power range. These powers, if confined to a volume of 20 μm^3 would approximately match the lowest power density used in this study.

Simulating the coupling of a material with an electromagnetic field, a quantum mechanical process, via classical MD simulations necessarily leads to an approximate description. As in the quantum case, within classical mechanics the energy in the electric field is primarily absorbed by modes of the corresponding frequency and only if the mode has an associated dipole moment. Unlike the real case, our classical system absorbs energy continuously, as opposed to doing so in a quantized manner. The fact that vibrational degrees of freedom can have any amount of energy, as opposed to being quantized to values $\hbar\omega(1/2 + n)$ (within the harmonic approximation), leads to an overestimation of the specific heat within classical mechanics. We note that the use of the reactive force field ReaxFF leads to an explicit description of anharmonicities in the potential energy surfaces. In addition, we ignore possible field-induced electronic excitations; as with all classical reactive MD simulations, we assume the electrons remain in their ground state throughout the process. Thus, processes such as dielectric breakdown are beyond the capability of the current MD simulations. Despite these approximations, our simulations provide interesting insight into how the manner in which energy is inputted into a reactive molecular crystal affects its response.

B. Systems of Interest. The α phase of HMX exhibits an orthorhombic unit cell containing eight molecules. An input structure with $2 \times 1 \times 4$ α -HMX unit cells resulting in 64 molecules (1792 atoms) is used in our simulations. Periodic boundary conditions are imposed along all directions leading to a defect-free perfect single crystal.

C. Simulation Analysis. Particularly important for this study is the spectral analysis of our samples. The power spectrum measures the kinetic energy density as a function of frequency and is obtained from the Fourier transformation of time-dependent atomic velocities.⁶³

$$P(\omega) = \frac{\beta\tau}{N} \sum_{j=1}^N m_j \sum_{n=0}^{N-1} v_j(n\Delta t) e^{-i2\pi n\omega\Delta t} \quad (1)$$

where $v_j(t)$ are the atomic velocities at time t , β is defined as $(k_B T)^{-1}$ with T being the temperature, τ is the sampling period, m_j is the mass of atom j , Δt is the sampling rate, and N is the number of frames to be analyzed. Our implementation uses a fast Fourier transform to solve eq 1. The vibrational density of states can be obtained by dividing eq 1 by $1/2k_B T$ under thermal equilibrium conditions, where every vibrational mode should have $1/2k_B T$ of kinetic energy. A subset of these vibrations is infrared (IR) active, and this can be determined by tracking the dipole moments over time. We compute the IR spectra from the Fourier transform of the time derivative of the total dipole moment in the simulation as shown in eq 2, where \dot{M} is defined as $\dot{M}(i) = \sum_{j=1}^N q_j(i) v_j(i)$, with $q_j(i)$ and $v_j(i)$ representing the charge and velocity of atom j at sampling frame i , respectively.⁶⁴

$$I(\omega) = \frac{2\pi\omega}{3\hbar c n} (1 - e^{-\beta\hbar\omega}) \sum_{n=0}^{N-1} e^{-i2\pi n\omega\Delta t} \left[\frac{1}{M-j} \sum_{i=1}^{M-j} \dot{M}(i) \cdot \dot{M}(i+j) \right] \quad (2)$$

3. VIBRATIONAL DENSITY OF STATES AND IR SPECTRA

Figure 1 shows the calculated vibrational and infrared spectra for α -HMX under ambient conditions. We used a 50-ps-long MD trajectory with a sampling rate of 3 fs, yielding a spectral window of 0–5000 cm^{-1} (0–150 THz) with a frequency resolution of 1.36 cm^{-1} for the vibrational spectrum and 2.72 cm^{-1} for the IR spectrum. To obtain good statistics in the autocorrelation function calculation, we compute it up to a time corresponding to half of the total simulation time. The dashed vertical bars in Figure 1b divide the spectra into frequency regions that will be used in section 5B.

The ReaxFF IR spectrum is in good overall agreement with experiments even though the potential was not tuned for vibrational accuracy. We observe a slight blue shift in the spectra; for example, the carbon–hydrogen symmetric and asymmetric stretch modes are known experimentally⁶⁵ to lie around 2950 cm^{-1} whereas we calculate them out as far as 3250 cm^{-1} . However, the relative peak positions and contributing elements agree with previous experimental and theoretical studies.^{65,66} Normal mode enumeration⁶⁷ was not undertaken in this study, though a comparable nonreactive force field⁶⁸ that was parametrized for vibrational accuracy was used for direct comparison of the power spectrum shown in Figure 1a.

4. THERMAL AND ELECTRIC FIELD INDUCED DECOMPOSITION AND REACTION

A. Thermal-Induced Decomposition. In the thermal-induced decomposition simulations we heat an α -HMX sample to 2000 K with a thermostat and at zero pressure, after which adiabatic simulations (NVE ensemble) are performed to follow the subsequent reactions. The heating rates were chosen to span both those observed experimentally for high explosives under critical shock loading (10–25 K/ps) and those that have been observed under laser driven shock experiments at high powers (50 K/ps and above).^{23,36,69}

Figure 2 shows the results of these direct heated cases with rates in the range 10–100 K/ps. The simulations of the reaction kinetics of HMX under constant heating rates are used as a baseline for the laser heated cases. The potential energy per molecule uses the perfect crystal as a reference ($-2571.492 \text{ kcal/mol molecule}^{-1}$)

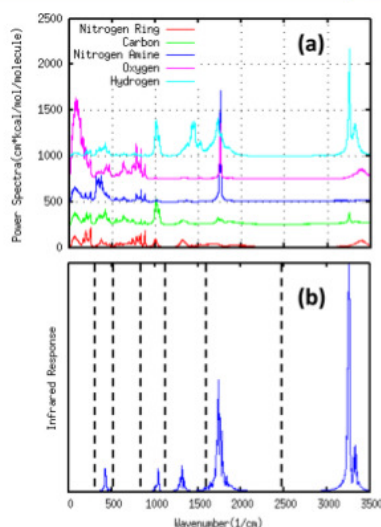


Figure 1. (a) Calculated vibrational spectrum of α -HMX at 300 K from molecular dynamics with the ReaxFF interatomic potential. Peak contributions by element type are offset vertically for clarity. (b) Infrared spectrum of α -HMX at 300 K calculated from the same trajectory used in the top panel.

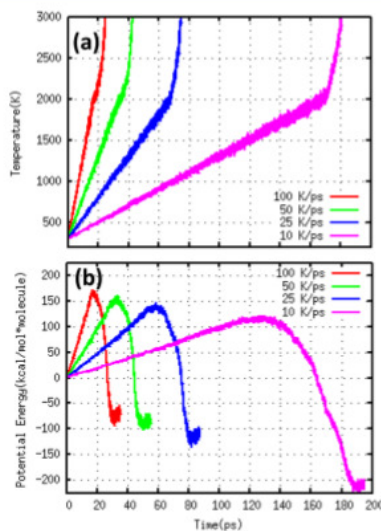


Figure 2. (a) Temperature of α -HMX over time in the canonical (NVT) ensemble while being ramped at various rates from 300 to 2000 K, after which simulation is run in the microcanonical ensemble (NVE). (b) Potential energy of the same system in the top panel. Values are zeroed on the initial configuration of the crystal at 300 K.

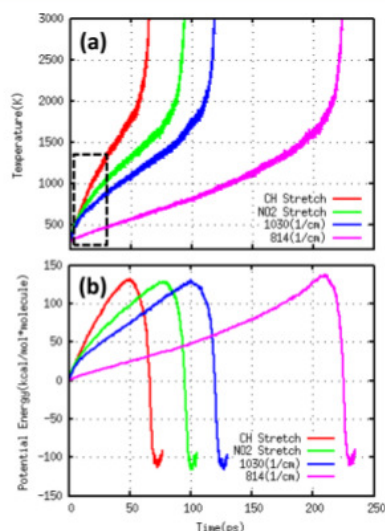


Figure 3. (a) Temperature of α -HMX over time in the microcanonical (NVE) ensemble under laser insult at varying frequencies for $1.604 \mu\text{W}/\text{nm}^2$. (b) Potential energy of the same system in the top panel. Values are zeroed on the initial configuration of the crystal at 300 K.

at room temperature and ambient pressure. As an additional validation of both the reactive potential and the simulation method for direct heating, we performed a Kissinger analysis of the potential energy and temperature evolution from these simulations.^{73,77} We used the temperature corresponding to the onset of exothermic reactions and preset heating rates in a Kissinger plot to extract an activation energy of 23,529 kcal/mol; see Figure S1 in the Supporting Information. This value is comparable to the activation energy of 35 kcal/mol extracted by Henson and collaborators from a wide range of experiments⁷⁸ and those in prior MD studies² of RDX, a HED nitramine similar HMX.

The increase in the rate of heating after the thermostated stage, Figure 2a, is due to the exothermic reactions of HMX;

this can be observed in the decrease in potential energy seen in Figure 2b. We observe the beginning of exothermic reactions during the heating stage but its onset depends on the heating rate. Increasing the heating rates leads to larger potential energies before exothermic reactions start decreasing the potential energy. In other words, fast heating rates lead to higher potential energy before exothermic reactions. Note that higher potential energies are achieved in the reacted material for the faster heating rates because the thermostat needs to add more energy to take the system to 2000 K; for slower rates, the exothermic reactions contribute more to the heating up to 2000 K. This is an artifact of our simulation setup.

B. Electric Field-Induced Decomposition. We chose four frequencies to study the response of α -HMX to electromagnetic radiation; these frequencies are chosen on the basis of the spectral analysis in section 3. Three frequencies are selected to couple with IR-active moments: 3254 cm^{-1} (97.62 THz, CH stretch), 1765 cm^{-1} (52.95 THz, NO₂ stretch), and 1030 cm^{-1} (30.9 THz). The fourth frequency, 814 cm^{-1} (24.42 THz), corresponds to a low-frequency mode with no significant IR activity. Due to the capability of the atomic charges to redistribute, it is possible to have a mode without an IR moment to couple with an electric field, as long as the external field can cause some amount of polarization in the material.

In the simulations represented in Figure 3 electric fields with a power density of $1.604 \mu\text{W}/\text{nm}^2$ at the various frequencies are applied to the samples. Figure 3a shows the time evolution of the temperature and Figure 3b of potential energy. As in the thermal-induced decomposition studies, the insult is turned off once the samples reach a temperature of 2000 K and the subsequent dynamics is described with constant energy MD. Our simulations show different regimes of energy absorption leading to different heating rates.

We are interested in understanding the energy transfer from the electric field to the sample, and Figure 4a shows the temperature evolution during the initial stages. These results indicate a two-stage heating process: (i) At short time scales, fields that couple to an IR mode of the material lead to rapid heating. As will become apparent in section 5B, during this stage the material is away from thermal equilibrium and we will denote this process nonequilibrium heating. (ii) The second stage is marked by a decrease in the heating rate (see the change in slopes in Figure 4a); this stage will be called steady-state heating. The decrease in the coupling is due to the target modes (and the vibrational peaks in general) becoming broader

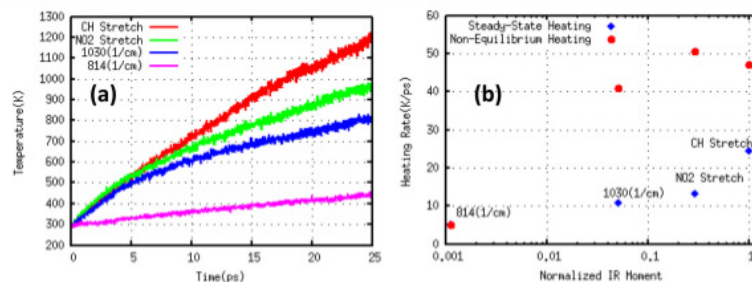


Figure 4. (a) Enhanced version of the temperature vs time plot shown in Figure 3a (dashed box). (b) Heating rates observed from α -HMX under laser insult targeting various vibrational modes at $1.604 \mu\text{W}/\text{nm}^2$. The IR moments on the horizontal axis were calculated at 300 K and zero pressure.

with increasing temperature. Broadening of peaks leads to weaker coupling with the harmonic electric field and the steady-state heating rates show less dependence on frequency than the initial rates. Note that the simulation corresponding to 814 cm^{-1} (where there is no IR active mode) exhibits only stage two. To identify how much these modes broaden and shift with increasing temperature, the vibrational density of states (vDOS) is plotted in Figure 5 for α -HMX for temperatures in the range

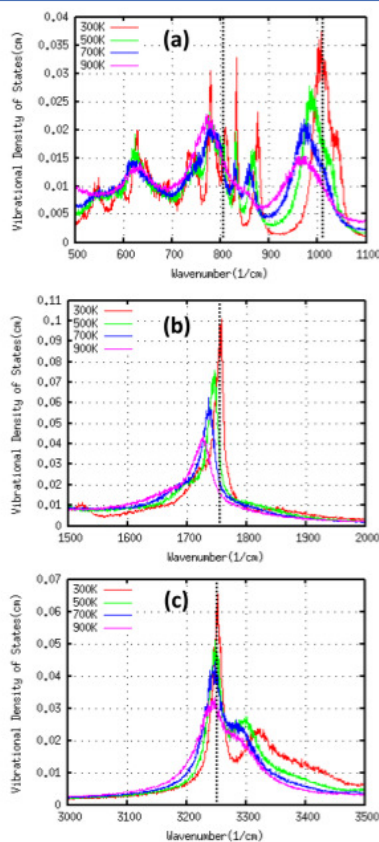


Figure 5. Vibrational density of states for α -HMX for a range of temperatures around the transition between nonequilibrium and steady-state heating. To keep all series on the same ordinate scale, the density of states is used rather than the power spectrum as in Figure 1a. Dashed lines indicate the frequencies used for electric-field driven simulations.

300–900 K. In each panel of Figure 5, a dashed line marks the frequency of the electric field. Comparing the vibrational peak positions to the excitation frequency, we see how the red shifts affect the efficient absorption from the electric field insult. In no case is the shift in frequency enough to negate coupling with the field. The closest to this extreme case is the NO_2 stretch mode,

which shifts by approximately 30 cm^{-1} from 300 to 900 K but is still observed to maintain strong coupling at high temperatures, as seen from Figure 3a.

The results in Figures 4 and 5 provide a qualitative verification of our simulations coupling electric fields and reactive MD simulations. We find the expected correlation between heating rate and oscillator strength of the target mode. In addition, the effects of the anharmonic coupling between modes and its temperature dependence can be seen. Of interest for the reactive model is how these anharmonic couplings preferentially heat the material and how this electromagnetic insult will differ from direct heating.

5. ROLE OF INSULT TYPE AND MAGNITUDE ON CHEMICAL KINETICS AND ENERGETICS

The simulations described in section 4 were expanded upon and carried out for six direct heating rates ranging from 5 to 200 K/ps and five power densities ranging from 1.604 to $16.04\text{ }\mu\text{W}/\text{nm}^2$. Simulations for each of the four target modes outlined previously were carried out for all five laser power densities, giving us an equally wide scope of heating rates from the electromagnetic insult as the direct heating simulations. We now focus on the analysis of the role of insult type and rate of energy increase on chemical reactions.

A. Initial Decomposition. To characterize the effect of insult type and magnitude on the initial chemical decomposition, we track the time evolution of the number of HMX molecules. Figure 6a shows the decrease in the number of HMX molecules as decomposition occurs. As will be discussed below, the initial reactions involve NO_2 loss followed closely by OH, HONO, and H_2O formation. This sequence of molecules, however, is liable to be altered with high-power-density insults, as will be shown in section 7. To set a standard across all simulations, we define the time for initial decomposition as that when the population of HMX molecules is reduced to three-fourths of its original value. We are interested in the amount of energy in the material when initial decomposition is achieved for the various insults. Thus, we define the energy increase for initial chemistry ($\Delta\epsilon_{\text{init}}$) as the increase in potential energy from the initial, ground-state energy (at $T = 300\text{ K}$), to the one corresponding to the time where one-fourth of the initial HMX molecules have decomposed. Figure 6b shows $\Delta\epsilon_{\text{init}}$ as a function of heating rate for the various cases studied. The values of $\Delta\epsilon_{\text{init}}$ were averaged over ten independent simulations for each electric field strength and frequency combination. Our MD results indicate that the amount of energy required for initial decomposition depends strongly on insult type and the rate at which energy is inputted into the HED material. Regardless of insult character, we find that higher rates of energy input lead to higher values of $\Delta\epsilon_{\text{init}}$; these changes in rate can almost double the $\Delta\epsilon_{\text{init}}$. This is somewhat expected, as fast coupling tends to overshoot thermally activated processes. For fast enough heating, the process is assumed to become athermal wherein the $\Delta\epsilon_{\text{init}}$ plateaus at a maximum value. This limiting $\Delta\epsilon_{\text{init}}$ of approximately 150 kcal/mol per HMX molecule can be compared with the energy associated with NO_2 dissociation $\sim 41\text{ kcal/mol}$ in the gas phase and the activation energy of 23.529 kcal/mol calculated from the Kissinger analysis in section 4.

More interesting is the observation that the energy required to induce decomposition is strongly dependent on insult type. Figure 6b shows that electromagnetic coupling to high-frequency modes responsible for the initial chemical reactions

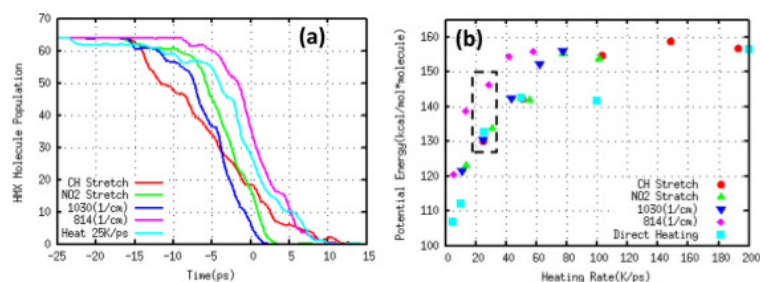


Figure 6. (a) HMX population for insult strengths resulting in a heating rate near 25 K/ps. The simulations for these population curves have their corresponding points bound by a dashed box in Figure 6b. The time scale has a reference ($t = 0$) to the onset of exothermic chemistry. (b) Potential energy change from the perfect crystal value for one-quarter decomposition of HMX molecules as a function of heating rate for all insult types, obtained from an ensemble average over ten independent simulations.

leads to decomposition with $\Delta\epsilon_{\text{int}}$ approximately the same as directly heated samples. On the other hand, if the electromagnetic field couples to low-frequency modes decomposition requires significantly more energy (greater change in potential energy). This effect is most notable in the range of heating rates between 20 and 60 K/ps where a collection of field driven samples at 814 cm^{-1} show significantly higher $\Delta\epsilon_{\text{int}}$ than the directly heated samples.

Interestingly, we find that the population of HMX molecules remaining at the onset of exothermic chemistry depends strongly on the insult type (Figure 6a). Note that the time axis in the figure is referenced to the time corresponding to the onset of exothermicity for each condition (each time is determined with an accuracy of approximately 1 ps across ten simulations). Targeting high-frequency modes results in smaller HMX populations at the time exothermicity is first observed. Strong electromagnetic fields can result in additional changes in initial chemistry as will be shown in section 7.

B. Exothermic Reactions. We now turn our attention to whether the insult type has an effect on the onset of exothermic chemistry. The maximum in potential energy (Figures 2 and 3) defines an energy increase for the onset exothermic chemistry ($\Delta\epsilon_{\text{exo}}$). Figure 7 shows $\Delta\epsilon_{\text{exo}}$ as a function of heating rate for all insults studied (electric fields at different frequencies and temperatures). The energy increase is measured from the

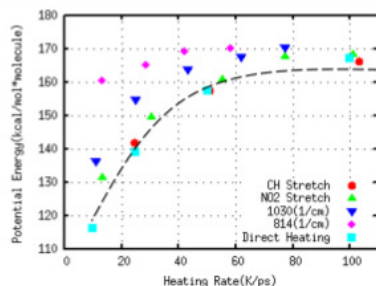


Figure 7. Maximum potential energy achieved as the system is heated plotted against the strength of the insult. Values are not absolute, but energy input is above the common starting structure at 300 K.

ground state of the crystal, and a dashed line fitted to the direct heating simulation results is included to guide the eye. As with the initial chemical reactions, $\Delta\epsilon_{\text{exo}}$ increases with increasing heating rate. The $\Delta\epsilon_{\text{exo}}$ for direct heating is similar to those associated with electromagnetic insults targeted at modes that can initiate chemical reactions, but with a thermostat each vibration is given the same amount of energy.

When the low-frequency, IR-inactive mode at 814 cm^{-1} is targeted, more energy input is required to trigger the initial endothermic reactions. This result indicates that energy transfer from such low-frequency modes to higher frequency ones responsible for chemical reactions remains weak even after the initial chemical decomposition occurs. It is interesting to note that the rate limiting step in shock-induced detonation is the up-pumping of energy from low-frequency phonons to high-frequency vibrons; our results indicate that under such conditions the effective internal energy increase for exothermic chemistry may be quite a bit higher than the one associated with thermal initiation.

6. FREQUENCY-RESOLVED ENERGY INPUT AND TRANSFER

Thus far, our results have shown that the manner in which energy is inputted into an energetic material affects the onset of decomposition and exothermic reactions. To understand these observed trends, we now focus on the spectral energy content in the material as a function of insult frequency. Figure 8 shows the kinetic energy content in the frequency regions marked in Figure 1b as a function of time for the four different target modes at a power density of 1.604 $\mu\text{W}/\text{nm}^3$. Spectra were calculated using a 10 ps sampling window with frames every 3 fs for both laser and direct heated samples. The spectra are then broken down into seven distinct, sequential, frequency ranges that are then integrated over to give the amount of kinetic energy contained in that particular region of frequencies. These values of kinetic energy will continuously increase with time as long as the insult is present, but the amount and rates at which they change will differ depending on the insult type. For direct comparison, we normalize each frequency region by the amount of kinetic energy observed in a comparable direct heated case. This corrects for peaks that broaden or shift across the preset regions as the temperature is increased. As closely as possible, given the discrete sampling window, we match the heating rate and temperature of the electric field driven

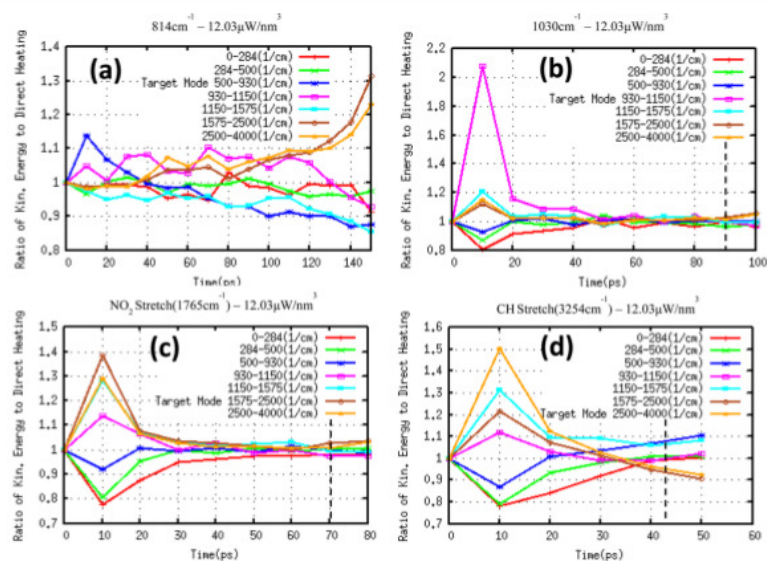


Figure 8. Energy localization plots for the four laser targeted modes of α -HMX at a power density of $27.86 \mu\text{W}$ ($1.604 \mu\text{W}/\text{nm}^2$). (a) Insult targeting the mode at 814 cm^{-1} . (b) Insult targeting the mode at 1030 cm^{-1} . (c) Insult targeting the NO_2 Stretch mode. (d) Insult targeting the CH stretch mode. The vertical axis for all four plots is the integrand of the laser heated vibrational spectra normalized by a comparable heating rate and temperature of a direct heated sample. A value of unity refers to equal energy distribution seen from direct heating.

simulations to a calculated spectra from a directly heated sample. For example, if the observed heating rate in an electric field heated study is 14 K/ps with a temperature around 1000 K we will choose from the appropriate 10 ps window of the 10 K/ps directly heated sample that is closest to this temperature. This process also allows us to correct for the initial high heating rates observed with laser heated samples. Once these spectra are paired, each integrating region is normalized, yielding values close to unity. Therefore, in this analysis, a value of unity is an energy distribution from the field driven samples that matches that of direct heating and can be considered as an equilibrium state of the system.

With the exception of Figure 8a, each plot in Figure 8 is terminated when the potential energy maxima have been reached (that is at the beginning of overall exothermic reaction) and the vertical dashed lines indicate the $1/4$ decomposition mark. Figure 8 also shows that each of the four electric fields will initially preferentially heat up modes close to its target mode. In the first 10 ps , there are noticeable differences in the magnitude of energy localization at the target mode that varies from a 15% change in energy in the 814 cm^{-1} target mode up to 210% increase over direct heating as seen in the target mode at 1030 cm^{-1} . In the two highest frequency target modes, NO_2 (Figure 8c) and CH stretch (Figure 8d), the localization of energy in the target mode is also accompanied by other modes of lower frequency being excited. This suggests significant coupling between these sets of molecular modes. In all cases except the one corresponding to 814 cm^{-1} , there is an initial excitation and successive relaxation through modes in the range of $1150\text{--}1575 \text{ cm}^{-1}$ (light blue series in Figure 8a–d);

this range of frequencies is dominated by contributions from hydrogen, carbon and nitrogen on the ring of HMX. This observation suggests that these modes are responsible for the coupling of high-frequency modes to the lower frequency, molecular deformation modes. It is also worth noticing in Figure 8a that the energy distribution becomes less uniform at later times. We attribute this to the loss of high-frequency modes in the directly heated spectrum used to normalize these results due to chemical reactions. Thus, the lack of chemical events in the system excited at 814 cm^{-1} at the same temperature as a directly heated sample results in the apparent increase of energy stored in these high-frequency modes. This result further supports our claim that there are inefficient energy-transfer mechanisms from low- to high-frequency vibrons, in agreement with previous work on vibron relaxation and multiphonon up pumping.^{41,42}

The intramolecular vibrational energy-transfer rates in HMX have been observed to be much faster than in other HE materials.⁴⁶ This rapid energy transfer between molecular modes and subsequently to the phonon bath brings the material into equilibrium with the insult on very short time scales. As a result, low-power-density insults cannot heat the material up to decomposition temperatures in the time scales of vibrational energy transfer. However, the decomposition kinetics can be altered if higher power density fields are used, as will be shown in section 7.

7. ROLE OF INSULT TYPE AND ENERGY INCREASE RATE ON CHEMICAL REACTIONS

We now focus our attention to whether the insult type affects the initial chemical reactions. Using the results discussed in

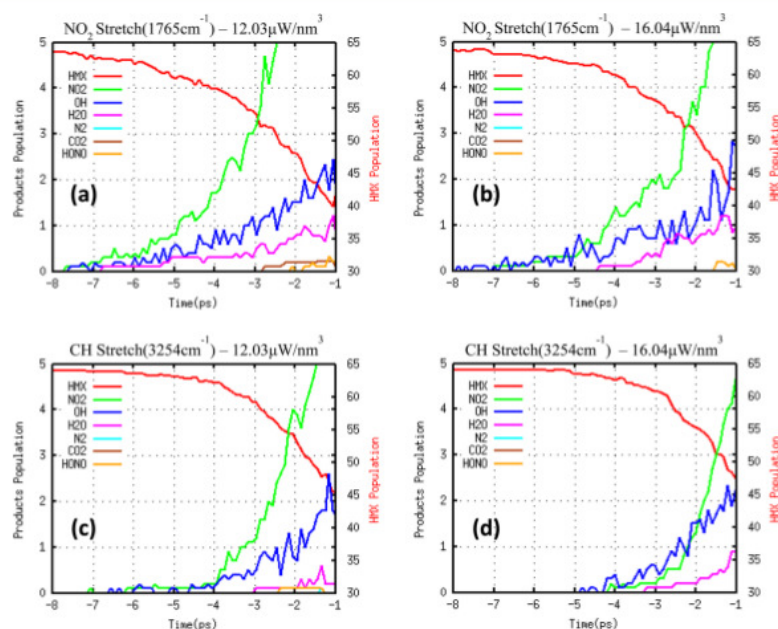


Figure 9. Changes in initial chemistry observed with high-power-density fields targeting the NO_2 and CH stretch modes, respectively. Time scales are set such that at zero the potential energy of the system is at its maximum (exotherm onset). Two laser powers are shown for each target mode to show the switch from NO_2 to OH and H_2O formation. Fractional values of molecule populations are allowed because each plot has the molecule populations averaged over ten independent simulations to reduce noise.

Figure 8 as a guide, we now move to much higher power density electric fields and study the resulting molecules formed from this nonequilibrium energy distribution of energy among the vibrons in α -HMX. Figure 9a–d shows the time evolution of the population of small products and intermediate molecules as well as HMX during electric field heating. The time in these plots is measured from the beginning of exothermic reaction (maximum in potential energy). Consistent with previous atomistic studies^{26,50,70} we identify NO_2 and OH, in that order, as the first molecules to form from both low-power-density field driven samples and directly heated samples. This is also in agreement with experimental observations.^{71,72} Example molecule population analyses for a pair of directly heated α -HMX samples are given in the Supporting Information, Figures S2(a,b) and S3(a,b). Changes in the initial steps of decomposition in α -HMX under electric field insult are shown in Figure 9. In Figure 9, (a) and (b) correspond to fields with frequency matching the NO_2 stretch mode whereas (c) and (d) show the results from targeting the CH stretch mode.

To display the initial chemical events clearly, the HMX populations over time are displayed on the right y-axis and the populations of the product molecules are displayed on the left. Each plot in Figure 9 has the data averaged over ten independent runs, thus allowing for fractional values of the molecule population. Figure 9a,b shows that the HMX population has dropped by about half from its starting value at the exotherm onset with NO_2 , OH, and H_2O molecules being

formed in that order for both power densities shown. Despite the fluctuations intrinsic to atomistic simulations our results show that targeting the NO_2 modes with high-strength fields favors the early formation of NO_2 molecules and at a larger time interval between the initial decomposition and the onset of exothermic reactions as compared to the CH stretch excitation. Conversely, at the highest power densities tested matching the CH stretch frequency we see an earlier onset of the OH population rise, along with the reversal of the first two chemical species identified during decomposition. This can be seen in Figure 9c,d where the rise of OH and H_2O are seen earlier, and even before, the rise of NO_2 molecules.

8. DISCUSSION AND CONCLUSIONS

In summary, we performed extensive MD simulations of decomposition of the HED material HMX with the reactive potential ReaxFF. We induce decomposition either with electric fields (of various frequencies) or via direct heating. We characterized the energy input into the material as a function of frequency for the various electric fields and found nonequilibrium conditions and a two-stage process when IR-active modes are targeted. Furthermore, the simulations show that the character and strength of the insult affects the energy increase required for initial chemistry and for the onset of exothermic chemical reactions. Furthermore, for high-strength fields the initial chemical reactions are affected by the selected target mode. We find that fields with frequencies matching

high-frequency modes can lead to decomposition with significantly less overall energy input in regards to similar field-driven samples at lower frequencies.

These results displaying changes in the initial chemical events that depend on the character of the insult are very reminiscent of work done by Bunker and Hase^{74,75} into the non-RRKM reaction kinetics of gas phase molecules. RRKM behavior implies that prior to reaction the material will explore all available states, including those leading to the reaction, and achieve local equilibrium. Figures 8 and 9 indicate that high-strength electric fields can lead to a nonequilibrium distribution of energy among vibron modes and can, in turn, result in non-RRKM behavior.^{74–76} Additional work connecting nonequilibrium reactive MD simulations with non-RRKM behavior would, in our view, contribute to a deeper understanding of nonequilibrium chemical reactions in the condensed phase and improve the interpretation of the simulations. The results presented in this paper contribute to a deeper understanding of chemical reactions in high-energy-density materials and can lead to a more detailed understanding of detonation and accidental initiation. Additional work into the mechanisms and time scales for energy localization and the role of defects as well as extending these studies to other materials would be critical to develop a complete picture of chemical initiation in HED materials.

■ ASSOCIATED CONTENT

■ Supporting Information

Kissinger plot for simulations heated using a Nose–Hoover thermostat. Graphics of decomposition time for products. ReaxFF parameter set used in this work. This information is available free of charge via the Internet at <http://pubs.acs.org>.

■ AUTHOR INFORMATION

Corresponding Author

*A. Strachan: e-mail, Strachan@purdue.edu.

Notes

The authors declare no competing financial interest.

■ REFERENCES

- (1) Strachan, A.; van Duin, A. C. T.; Chakraborty, D.; Dasgupta, S.; Goddard, W. A. Shock waves in high-energy materials: The Initial Chemical Events in Nitramine RDX. *Phys. Rev. Lett.* **2003**, *91*, 4.
- (2) Strachan, A.; Kober, E. M.; van Duin, A. C. T.; Oxgaard, J.; Goddard, W. A. Thermal Decomposition of RDX From Reactive Molecular Dynamics. *J. Chem. Phys.* **2005**, *122*, 05402.
- (3) Holian, B. L.; Germann, T. C.; Maillet, J. B.; White, C. T. Atomistic Mechanism for Hot Spot Initiation. *Phys. Rev. Lett.* **2002**, *89*, 4.
- (4) Jaramillo, E.; Sewell, T. D.; Strachan, A. Atomic-Level View of Inelastic Deformation in a Shock Loaded Molecular Crystal. *Phys. Rev. B* **2007**, *76*, 6.
- (5) An, Q.; Zybin, S. V.; Goddard, W. A.; Jaramillo-Botero, A.; Blanco, M.; Luo, S. N. Elucidation of the Dynamics for Hot-Spot Initiation at Nonuniform Interfaces of Highly Shocked Materials. *Phys. Rev. B* **2011**, *84*, 5.
- (6) Chen, S.; Tolbert, W. A.; Dlott, D. D. Direct Measurement of Ultrafast Multiphonon Up-Pumping in High Explosives. *J. Phys. Chem.* **1994**, *98*, 7759–7766.
- (7) Tolmakoﬀ, A.; Fayer, M. D.; Dlott, D. D. Chemical-Reaction Initiation and Hot-Spot Formation in Shocked Energetic Molecular Materials. *J. Phys. Chem.* **1993**, *97*, 1901–1913.
- (8) Ye, S.; Tonokura, K.; Koshi, M. Vibron Dynamics in RDX, beta-HMX and Tetryl Crystals. *Chem. Phys.* **2003**, *293* (1), 1–8.
- (9) Fried, L. E.; Ruggiero, A. J. Energy-Transfer Rates in Primary, Secondary, and Insensitive Explosives. *J. Phys. Chem.* **1994**, *98*, 9786–9791.
- (10) Hong, X. Y.; Chen, S.; Dlott, D. D. Ultrafast Mode-Specific Intermolecular Vibrational-Energy Transfer To Liquid Nitromethane. *J. Phys. Chem.* **1995**, *99*, 9102–9109.
- (11) Dlott, D. D. Thinking Big (and Small) About Energetic Materials. *Mater. Sci. Technol.* **2006**, *22*, 463–473.
- (12) Kuklja, M. M. On The Initiation Of Chemical Reactions By Electronic Excitations In Molecular Solids. *Appl. Phys. A: Mater. Sci. Process.* **2003**, *76*, 359–366.
- (13) Ahmad, S. R.; Russell, D. A. Laser Ignition of Pyrotechnics - Effects of Wavelength, Composition and Confinement. *Propellants Explosives Pyrotechnics* **2005**, *30*, 131–139.
- (14) Ahmad, S. R.; Russell, D. A. Studies into Laser Ignition of Confined Pyrotechnics. *Propellants Explosives Pyrotechnics* **2008**, *33*, 396–402.
- (15) Seong, N.-H.; Fang, Y.; Dlott, D. D. Vibrational Energy Dynamics of Normal and Deuterated Liquid Benzene. *J. Phys. Chem. A* **2009**, *113*, 1445–1452.
- (16) Shigeto, S.; Pang, Y.; Fang, Y.; Dlott, D. D. Vibrational Relaxation of Normal and Deuterated Liquid Nitromethane. *J. Phys. Chem. B* **2008**, *112*, 232–241.
- (17) Yu, H.; Hambir, S. A.; Dlott, D. D. Ultrafast Dynamics Of Nanotechnology Energetic Materials. In *Multifunctional Energetic Materials*; Thadhani, N. N.; Armstrong, R. W.; Gash, A. E.; Wilson, W. H., Eds.; MRS Symposium Proceedings; MRS: Warrendale, PA, 2006; Vol. 896, pp 71–79.
- (18) Armstrong, R. W.; Ammon, H. L.; Elban, W. L.; Tsai, D. H. Investigation Of Hot Spot Characteristics In Energetic Crystals. *Thermochim. Acta* **2002**, *384*, 303–313.
- (19) Mares, J. O.; Miller, J. K.; Sharp, N. D.; Moore, D. S.; Adams, D. E.; Groven, L. J.; Rhoads, J. F.; Son, S. F. Thermal and Mechanical Response of PBX 9501 Under Contact Excitation. *J. Appl. Phys.* **2013**, *113*, 084904.
- (20) Xiao, J.; Zhao, L.; Zhu, W.; Chen, J.; Ji, G.; Zhao, F.; Wu, Q.; Xiao, H. Molecular Dynamics Study on the Relationships of Modeling, Structural and Energy Properties With Sensitivity For RDX-Based PBXs. *Science China-Chemistry* **2012**, *55*, 2587–2594.
- (21) Xiao, J. J.; Wang, W. R.; Chen, J.; Ji, G. F.; Zhu, W.; Xiao, H. M. Study on Structure, Sensitivity and Mechanical Properties of HMX and HMX-Based PBXs With Molecular Dynamics Simulation. *Comput. Theor. Chem.* **2012**, *999*, 21–27.
- (22) Xiao, J. J.; Li, S. Y.; Chen, J.; Ji, G. F.; Zhu, W.; Zhao, F.; Wu, Q.; Xiao, H. M. Molecular Dynamics Study on the Correlation Between Structure and Sensitivity For Defective RDX Crystals and Their PBXs. *J. Mol. Model.* **2013**, *19*, 803–809.
- (23) Dlott, D. D.; Hambir, S.; Franken, J. The New Wave in Shock Waves. *J. Phys. Chem. B* **1998**, *102*, 2121–2130.
- (24) Kuklja, M. M.; Rashkeev, S. N. Modeling Defect-Induced Phenomena. *Static Compression of Energetic Materials* **2008**, 291–326.
- (25) Rice, B. M.; Sorescu, D. C.; Kabadi, V.; Agrawal, P. M.; Thompson, D. L. Molecular Simulations of Dynamic Processes of Solid Explosives. *Transformational Science and Technology for the Current and Future Force* **2006**, 42.
- (26) Zhou, T.-T.; Huang, F.-L. Effects of Defects on Thermal Decomposition of HMX via ReaxFF Molecular Dynamics Simulations. *J. Phys. Chem. B* **2011**, *115*, 278–287.
- (27) Cawkwell, M. J.; Sewell, T. D.; Zheng, L.; Thompson, D. L. Shock-Induced Shear Bands in an Energetic Molecular Crystal: Application of Shock-Front Absorbing Boundary Conditions to Molecular Dynamics Simulations. *Phys. Rev. B* **2008**, *78*, 014107.
- (28) Menikoff, R.; Sewell, T. D. Constituent Properties of HMX Needed for Mesoscale Simulations. *Combust. Theor. Model.* **2002**, *6*, 103–125.
- (29) Chen, S.; Hong, X. Y.; Hill, J. R.; Dlott, D. D. Ultrafast Energy-Transfer in High Explosives - Vibrational Cooling. *J. Phys. Chem.* **1995**, *99*, 4525–4530.

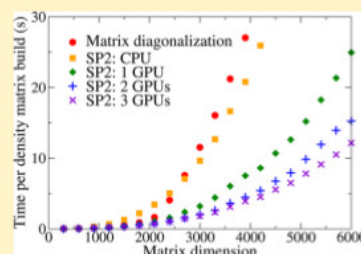
- (30) Deak, J. C.; Iwaki, L. K.; Dlott, D. D. Vibrational Energy Redistribution in Polyatomic Liquids: Ultrafast IR-Raman Spectroscopy of Acetonitrile. *J. Phys. Chem. A* **1998**, *102*, 8193–8201.
- (31) Dlott, D. D. Vibrational Energy Redistribution in Polyatomic Liquids: 3D Infrared-Raman Spectroscopy. *Chem. Phys.* **2001**, *266*, 149–166.
- (32) Kim, H.; Dlott, D. D. Molecular-Dynamics Simulation Of Nanoscale Thermal Conduction And Vibrational Cooling In A Crystalline Naphthalene Cluster. *J. Chem. Phys.* **1991**, *94*, 8203–8209.
- (33) Aluker, E. D.; Krechetov, A. G.; Mitrofanov, A. Y.; Zverev, A. S.; Kuklja, M. M. Understanding Limits of the Thermal Mechanism of Laser Initiation of Energetic Materials. *J. Phys. Chem. C* **2012**, *116*, 24482–24486.
- (34) Dang, N. C.; Bolme, C. A.; Moore, D. S.; McGrane, S. D. Shock Induced Chemistry in Liquids Studied With Ultrafast Dynamic Ellipsometry and Visible Transient Absorption Spectroscopy. *J. Phys. Chem. A* **2012**, *116*, 10301–10309.
- (35) Carter, J. A.; Wang, Z.; Lagutchev, A.; Fang, Y.; Seong, N.-H.; Cahill, D. G.; Dlott, D. D. Ultrafast Shock Wave Coherent Dissociation and Spectroscopy Of Materials. APS-SCCM, Waikoloa, HI, Jun 24–29, 2007.
- (36) Conner, R. W.; Dlott, D. D. Time-Resolved Spectroscopy of Initiation and Ignition of Flash-Heated Nanoparticle Energetic Materials. *J. Phys. Chem. C* **2012**, *116*, 14737–14747.
- (37) Iwaki, L. K.; Dlott, D. D. Three-dimensional Spectroscopy of Vibrational Energy Relaxation in Liquid Methanol. *J. Phys. Chem. A* **2000**, *104*, 9101–9112.
- (38) Moore, D. S.; Schmidt, S. C. Vibrational Spectroscopy Of Materials Under Extreme-Pressure And Temperature. *J. Mol. Struct.* **1995**, *347*, 101–111.
- (39) Hare, D. E.; Franken, J.; Dlott, D. D. A New Method For Studying Picosecond Dynamics Of Shocked Solids - Application To Crystalline Energetic Materials. *Chem. Phys. Lett.* **1995**, *244*, 224–230.
- (40) McGrane, S. D.; Moore, D. S. Continuous Wave Laser Irradiation of Explosives. *Propellants Explosives Pyrotechnics* **2011**, *36*, 327–334.
- (41) McNesby, K. L.; Coffey, C. S. Spectroscopic Determination of Impact Sensitivities of Explosives. *J. Phys. Chem. B* **1997**, *101*, 3097–3104.
- (42) Coffey, C. S.; Sharma, J. Plastic Deformation, Energy Dissipation, and Initiation of Crystalline Explosives. *Phys. Rev. B* **1999**, *60*, 9365–9371.
- (43) Namkung, J.; Coffey, C. S. Plastic Deformation Rate and Initiation Of Crystalline Explosives. APS-SCCM, Atlanta, GA, 2002; pp 1003–1006.
- (44) Pein, B. C.; Seong, N.-H.; Dlott, D. D. Vibrational Energy Relaxation of Liquid Aryl-Halides X-C₆H₅ (X = F, Cl, Br, I). *J. Phys. Chem. A* **2010**, *114*, 10500–10507.
- (45) McGrane, S. D.; Shreve, A. P. Temperature-Dependent Raman Spectra of Trinitrotrinitrobenzene: Anharmonic Mode Couplings in an Energetic Material. *J. Chem. Phys.* **2003**, *119*, 5834–5841.
- (46) McGrane, S. D.; Barber, J.; Quenneville, J. Anharmonic Vibrational Properties of Explosives from Temperature-Dependent Raman. *J. Phys. Chem. A* **2005**, *109*, 9919–9927.
- (47) Brown, K. E.; Shaw, W. L.; Zheng, X.; Dlott, D. D. Simplified Laser-Driven Flyer Plates for Shock Compression Science. *Rev. Sci. Instrum.* **2012**, *83*, 103901.
- (48) Brown, K. E.; Fu, Y.; Shaw, W. L.; Dlott, D. D. Time-Resolved Emission of Dye Probes in a Shock-Compressed Polymer. *J. Appl. Phys.* **2012**, *112*, 103508.
- (49) Zhang, L. Z.; van Duin, A. C. T.; Zybin, S. V.; Goddard, W. A. Thermal Decomposition of Hydrazines from Reactive Dynamics Using the ReaxFF Reactive Force Field. *J. Phys. Chem. B* **2009**, *113*, 10770–10778.
- (50) Zhang, L. Z.; Zybin, S. V.; van Duin, A. C. T.; Dasgupta, S.; Goddard, W. A.; Kober, E. M. Carbon Cluster Formation during Thermal Decomposition of Octahydro-1,3,5,7-tetranitro-1,3,5,7-tetrazocine and 1,3,5-Triamino-2,4,6-trinitrobenzene High Explosives from ReaxFF Reactive Molecular Dynamics Simulations. *J. Phys. Chem. A* **2009**, *113*, 10619–10640.
- (51) Zhang, L.; Zybin, S. V.; van Duin, A. C. T.; Goddard, W. A. Modeling High Rate Impact Sensitivity of Perfect RDX and HMX Crystals by ReaxFF Reactive Dynamics. *Journal of Energetic Materials* **2010**, *28*, 92–127.
- (52) Rom, N.; Zybin, S. V.; van Duin, A. C. T.; Goddard, W. A.; Zeiri, Y.; Katz, G.; Kosloff, R. Density-Dependent Liquid Nitromethane Decomposition: Molecular Dynamics Simulations Based on ReaxFF. *J. Phys. Chem. A* **2011**, *115*, 10181–10202.
- (53) Zybin, S. V.; Goddard, W. A.; Xu, P.; van Duin, A. C. T.; Thompson, A. P. Physical Mechanism of Anisotropic Sensitivity in Pentaerythritol Tetranitrate From Compressive-Shear Reaction Dynamics Simulations. *Appl. Phys. Lett.* **2010**, *96*, 081918.
- (54) Chenoweth, K.; van Duin, A. C. T.; Goddard, W. A. ReaxFF Reactive Force Field for Molecular Dynamics Simulations of Hydrocarbon Oxidation. *J. Phys. Chem. A* **2008**, *112*, 1040–1053.
- (55) Castro-Marciano, F.; van Duin, A. C. T. Comparison of Thermal and Catalytic Cracking of 1-heptene From ReaxFF Reactive Molecular Dynamics Simulations. *Combust. Flame* **2013**, *160*, 766–775.
- (56) Neyts, E. C.; Khalilov, U.; Pourtois, G.; van Duin, A. C. T. Hyperthermal Oxygen Interacting with Silicon Surfaces: Adsorption, Implantation, and Damage Creation. *J. Phys. Chem. C* **2011**, *115*, 4818–4823.
- (57) Salmon, E.; van Duin, A. C. T.; Loran, F.; Marquaire, P. M.; Goddard, W. A. Thermal Decomposition Process in Algaenan of *Botryococcus Braunii* Race L Part 2: Molecular Dynamics Simulations Using The Reaxff Reactive Force Field. *Org. Geochem.* **2009**, *40*, 416–427.
- (58) Chenoweth, K.; van Duin, A. C. T.; Dasgupta, S.; Goddard, W. A. Initiation Mechanisms and Kinetics of Pyrolysis and Combustion of JP-10 Hydrocarbon Jet Fuel. *J. Phys. Chem. A* **2009**, *113*, 1740–1746.
- (59) Rappe, A. K.; Goddard, W. A. Charge Equilibration for Molecular-Dynamics Simulations. *J. Phys. Chem.* **1991**, *95*, 3358–3363.
- (60) Plimpton, S. Fast Parallel Algorithms For Short-Range Molecular-Dynamics. *J. Comput. Phys.* **1995**, *117*, 1–19.
- (61) De Lucia, F. C.; Harmon, R. S.; McNesby, K. L.; Winkel, R. J.; Miziolek, A. W. Laser-induced Breakdown Spectroscopy Analysis of Energetic Materials. *Appl. Opt.* **2003**, *42*, 6148–6152.
- (62) Waterbury, R. D.; Pal, A.; Killinger, D. K.; Rose, J.; Dottery, E. L.; Ontai, G. Standoff LIBS Measurements of Energetic Materials Using a 266nm Excitation Laser. 9th Annual Conference for Chemical, Biological, Radiological, Nuclear, and Explosives (CBRNE) Sensing, Orlando, FL, Mar 18–20, 2008.
- (63) Berens, P. H.; Mackay, D. H. J.; White, G. M.; Wilson, K. R. Thermodynamics and Quantum Corrections From Molecular-Dynamics for Liquid Water. *J. Chem. Phys.* **1983**, *79*, 2375–2389.
- (64) Boulard, B.; Kieffer, J.; Phifer, C. C.; Angell, C. A. Vibrational Spectra In Fluoride-Crystals And Glasses At Normal And High-Pressures By Computer-Simulation. *J. Non-Cryst. Solids* **1992**, *140*, 350–358.
- (65) Brand, H. V.; Rabie, R. L.; Funk, D. J.; Diaz-Acosta, I.; Pulay, P.; Lippert, T. K. Theoretical and Experimental Study of the Vibrational Spectra of the alpha, beta, and delta Phases of Octahydro-1,3,5,7-tetranitro-1,3,5,7-tetrazocine (HMX). *J. Phys. Chem. B* **2002**, *106*, 10594–10604.
- (66) Zhu, W.; Xiao, J.; Ji, G.; Zhao, F.; Xiao, H. First-principles Study of the Four Polymorphs of Crystalline Octahydro-1,3,5,7-tetranitro-1,3,5,7-tetrazocine. *J. Phys. Chem. B* **2007**, *111*, 12715–12722.
- (67) Pravica, M.; Galley, M.; Kim, E.; Weck, P.; Liu, Z. A Far- and Mid-Infrared Study of HMX (octahydro-1,3,5,7-tetranitro-1,3,5,7-tetrazocine) Under High Pressure. *Chem. Phys. Lett.* **2010**, *S00*, 28–34.
- (68) Smith, G. D.; Bharadwaj, R. K. Quantum Chemistry Based Force Field for Simulations of HMX. *J. Phys. Chem. B* **1999**, *103*, 3570–3575.
- (69) Yang, Y. Q.; Sun, Z. Y.; Wang, S. F.; Dlott, D. D. Fast Spectroscopy of Laser-Initiated Nanoenergetic Materials. *J. Phys. Chem. B* **2003**, *107*, 4485–4493.

- (70) Chakraborty, D.; Muller, R. P.; Dasgupta, S.; Goddard, W. A. A Detailed Model for the Decomposition of Nitramines: RDX and HMX. *J. Comput.-Aided Mater. Des.* **2002**, *8*, 203–212.
- (71) Adams, G. F.; Shaw, R. W. Chemical-Reactions in Energetic Materials. *Annu. Rev. Phys. Chem.* **1992**, *43*, 311–340.
- (72) Behrens, R.; Bulusu, S. Thermal-Decomposition of Energetic Materials 0.2. Deuterium-Isotope Effects and Isotopic Scrambling in Condensed-Phase Decomposition of Octahydro-1,3,5,7-Tetranitro-1,3,5,7-Tetrazocine. *J. Phys. Chem.* **1991**, *95*, 5838–5845.
- (73) Orava, J.; Greer, A. L.; Gholipour, B.; Hewak, D. W.; Smith, C. E. Characterization of Supercooled Liquid Ge₂Sb₂Te₅ and its Crystallization by Ultrafast-Heating Calorimetry. *Nat. Mater.* **2012**, *11*, 279–283.
- (74) Bunker, D. L.; Hase, W. L. Non-RRKM Unimolecular Kinetics - Molecules in General, and CH₃NC in Particular. *J. Chem. Phys.* **1973**, *59*, 4621–4632.
- (75) Bunker, D. L.; Wright, K. R.; Hase, W. L.; Houle, F. A. Exit-Channel Coupling Effects in the Unimolecular Decomposition Of Triatomics. *J. Phys. Chem.* **1979**, *83* (8), 933–936.
- (76) Viswanathan, R.; Raff, L. M.; Thompson, D. L. Monte-Carlo Transition-State Theory - CH₄-CH₃+H, SiH₄-SiH₃+H. *J. Chem. Phys.* **1984**, *81*, 828–832.
- (77) Kissinger, H. E. Variation of Peak Temperature With Heating Rate in Differential Thermal Analysis. *J. Res. Natl. Bur. Std.* **1956**, *57*, 217–221.
- (78) Henson, B. F.; Asay, B. W.; Smilowitz, L. B.; Dickson, P. M. Ignition chemistry in HMX from thermal explosion to detonation. APS-SCCM, Atlanta, GA, Jun 24–29, 2001; American Institute of Physics: Atlanta, GA, 2001; pp 1069–1072.

Computation of the Density Matrix in Electronic Structure Theory in Parallel on Multiple Graphics Processing Units

M. J. Cawkwell,^{*,†} M. A. Wood,^{†,‡} Anders M. N. Niklasson,[†] and S. M. Mniszewski[‡][†]Theoretical Division and [‡]Computer, Computational, and Statistical Sciences Division, Los Alamos National Laboratory, Los Alamos, New Mexico 87545, United States[‡]School of Materials Engineering, Purdue University, 701 West Stadium Avenue, West Lafayette, Indiana 47907, United States

ABSTRACT: The algorithm developed in Cawkwell, M. J. et al. *J. Chem. Theory Comput.* **2012**, *8*, 4094 for the computation of the density matrix in electronic structure theory on a graphics processing unit (GPU) using the second-order spectral projection (SP2) method [Niklasson, A. M. N. *Phys. Rev. B* **2002**, *66*, 155115] has been efficiently parallelized over multiple GPUs on a single compute node. The parallel implementation provides significant speed-ups with respect to the single GPU version with no loss of accuracy. The performance and accuracy of the parallel GPU-based algorithm is compared with the performance of the SP2 algorithm and traditional matrix diagonalization methods on a multicore central processing unit (CPU).



1. INTRODUCTION

The calculation of the density matrix, \mathbf{P} , from the Kohn–Sham Hamiltonian, Fockian, or a semiempirical Hamiltonian in electronic structure theory is often a significant burden on overall computational performance, especially for large systems.^{1–3} The density matrix has traditionally been computed from the eigenvalues and eigenvectors of the Hamiltonian or Fockian. While algorithms based on matrix diagonalization can be applied to metals and insulators equally well and provide a straightforward route to the introduction of a finite electronic temperature, their complexity leads to an undesirable cubic scaling, $O(N^3)$, of the computation time on the number of atoms, N . Alternatives to matrix diagonalization have been developed that lead to $O(N)$ performance if matrix sparsity is present and utilized.^{3–6} The second-order spectral projection (SP2) method,⁷ which is based on a recursive expansion of the Fermi-operator in a series of generalized matrix–matrix multiplications, is one such method. While we have demonstrated fast, low-prefactor $O(N)$ applications of the SP2 algorithm in both static and molecular dynamics simulations,⁴ its performance in limit of $O(N^3)$ dense matrix algebra was also found to be better than that of traditional $O(N^3)$ algorithms.⁸

The performance of the SP2 algorithm is controlled by the cost of the $O(N^3)$ generalized matrix–matrix multiplication, $\mathbf{C} \leftarrow \alpha\mathbf{AB} + \beta\mathbf{C}$, where \mathbf{A} , \mathbf{B} , and \mathbf{C} are matrices, and α and β are scalars. Highly optimized implementations of the BLAS level 3 DGEMM subroutine^{9,10} are available for performing generalized matrix–matrix multiplications on multicore central processing units (CPUs) and many-core general purpose graphics processing units (GPUs).¹¹ We demonstrated that CPU and GPU implementations of the SP2 algorithm can

outperform algorithms based on matrix diagonalization (with highly optimized diagonalization subroutines).⁸ At the same time, the errors in the density matrices computed using the SP2 algorithm were as small or smaller than those measured in density matrices computed via diagonalization. The GPU-implementation provided by far the best performance, even in double precision arithmetic, owing to the very high floating point operation rates (FLOPs) and memory bandwidth available on these devices with respect to contemporary multicore CPUs.

Our original GPU implementation of the SP2 algorithm used the cuBLAS¹² DGEMM on a Fermi-architecture Nvidia GPU.⁸ We obtained the best overall performance by porting the entire SP2 algorithm to the GPU to avoid the transfer of large arrays between the GPU and CPU at each step in the recursive expansion. Nevertheless, we found that the data transfer constitutes only a small fraction of the total compute time such that very good performance gains could be obtained with the simplest algorithm where each call to the DGEMM subroutine on the CPU is replaced by a call to the cuBLAS version on the GPU.

Compute nodes on parallel supercomputers and high-end desktop workstations can accept multiple general purpose GPUs. Hence, we have parallelized our GPU implementation of the SP2 algorithm such that the expensive generalized matrix–matrix multiplication is partitioned between multiple GPUs. The new algorithm is based on a simple blocking algorithm for the generalized matrix–matrix multiplication that still uses the highly efficient cuBLAS DGEMM as the underlying multi-

Received: September 10, 2014

Published: October 31, 2014

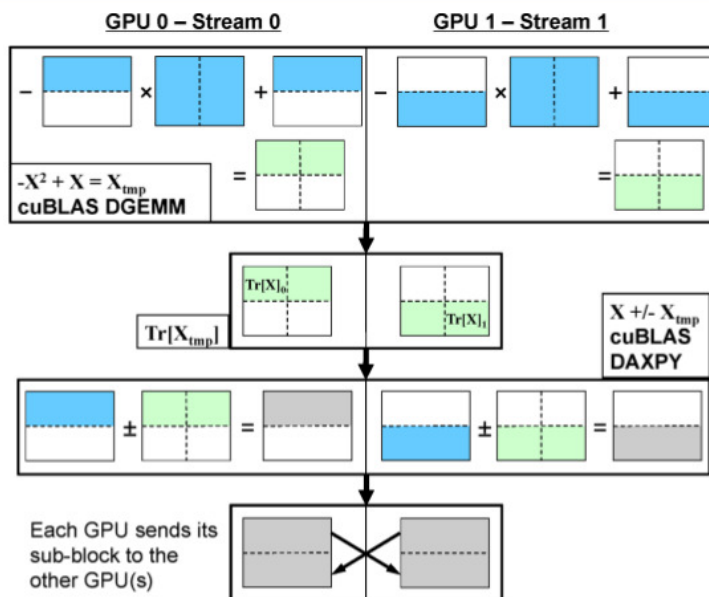


Figure 1. Schematic illustration of the parallel GPU implementation of the SP2 algorithm.

plication kernel. Although nowhere near as computationally expensive as the generalized matrix–matrix multiplication, we also compute matrix traces and matrix–matrix additions using the cuBLAS DAXPY subroutine at the sub-block level across the GPUs. This approach minimizes data transfer between the devices. We found that execution on one GPU gave the best performance for density matrices of dimensions less than about 900×900 . Running the algorithm in parallel on two GPUs gives the best performance for density matrices greater than 900×900 up to about 2000×2000 . For density matrices greater than approximately 2000×2000 , parallel execution on three GPUs was optimal. We again found that the SP2 algorithm on both GPUs and CPUs generated density matrices with errors as small or smaller than when matrix diagonalization is applied.

In the next Section we provide a brief overview of the SP2 algorithm. Our simple blocking algorithm for the parallelization of the generalized matrix–matrix multiplication across multiple GPUs on a single compute node is described in Section 4. Timings and errors analyses from the CPU and parallel GPU implementations of the SP2 algorithm and traditional matrix diagonalization are provided in Section 5, followed by conclusions in Section 6.

2. SECOND-ORDER SPECTRAL PROJECTION METHOD

At zero electronic temperature, the Fermi–Dirac distribution becomes equivalent to the Heaviside step function, $\theta[x]$, with the step formed at the chemical potential, μ .¹³ The density matrix can then be written using the matrix form of the Heaviside step function as

$$\mathbf{P} = \theta[\mu\mathbf{I} - \mathbf{H}] \quad (1)$$

where \mathbf{I} is the identity matrix, and \mathbf{H} is the Hamiltonian matrix obtained from density functional theory, Hartree–Fock theory, or a semiempirical method. The SP2 algorithm⁷ is based on a recursive expansion of eq 1

$$\theta[\mu\mathbf{I} - \mathbf{H}] = \lim_{j \rightarrow \infty} f_j \{f_{j-1} \{ \dots f_0 \{ \mathbf{X}_0 \} \dots \} \} \quad (2)$$

where

$$\mathbf{X}_0 = \frac{e_{\max}\mathbf{I} - \mathbf{H}}{e_{\max} - e_{\min}} \quad (3)$$

and e_{\max} and e_{\min} are estimates for the maximum and minimum eigenvalues of the Hamiltonian, respectively. In practice, estimates for e_{\max} and e_{\min} can be obtained very efficiently through the Gershgorin circle theorem.¹⁴

At convergence, the trace of the density matrix is equal to the number of occupied states or equivalently

$$2\text{Tr}[\mathbf{P}] = N_e \quad (4)$$

where $\text{Tr}[\mathbf{x}]$ denotes the trace of matrix \mathbf{x} , and N_e is the total number of electrons. The recursive expansion in eq 2 uses the following projection polynomials that guarantee that eq 4 is satisfied at convergence

$$f_j[\mathbf{X}_j] = \begin{cases} \mathbf{X}_j^2 & \text{if } |2\text{Tr}[\mathbf{X}_j] - 2\text{Tr}[-\mathbf{X}_j^2 + \mathbf{X}_j] - N_e| \\ & \leq |2\text{Tr}[\mathbf{X}_j] + 2\text{Tr}[-\mathbf{X}_j^2 + \mathbf{X}_j] - N_e| \\ 2\mathbf{X}_j - \mathbf{X}_j^2 & \text{otherwise} \end{cases} \quad (5)$$

The application of the projection polynomials in eq 5 pushes the unoccupied and occupied states to 0 and 1, respectively, depending on target occupation of the density matrix. The projection polynomial at each iteration is selected to give the best occupancy in the next iteration.⁸ Both of the projection polynomials take the form of a generalized matrix–matrix multiplication. Prior knowledge of the chemical potential is not required, and the number of recursive iterations scales as $\ln(1/\Delta\epsilon)$, where $\Delta\epsilon$ is the difference in energy between the highest occupied and lowest unoccupied molecular orbitals, or HOMO–LUMO gap.⁷ Hence, the SP2 algorithm is efficient only when applied to insulators.

2.1. Convergence Criteria. The recursive expansion in eq 2 is terminated when we detect that further iterations will not improve the idempotency of the density matrix, that is $\mathbf{P}^2 = \mathbf{P}$. This condition can be identified very reliably using

$$|\text{Tr}[\mathbf{X}_{i-1}] - \text{Tr}[\mathbf{X}_{i-2}]| \leq |\text{Tr}[\mathbf{X}_{i+1}] - \text{Tr}[\mathbf{X}_i]| \quad (6)$$

Although a number of alternative termination criteria exist, eq 6 was employed in the implementations of the SP2 algorithm discussed in this work.

3. ALGORITHMS FOR CENTRAL PROCESSING UNITS

3.1. Matrix Diagonalization. Optimized LAPACK and BLAS algorithms were used to the greatest possible extent in the calculation of the density matrix. The Hamiltonian matrix is diagonalized using the LAPACK routine DSYEV. Better performance can be achieved by using the divide-and-conquer version of the algorithm, DSYEVD, but we have found this to be unreliable on occasion. The outer products between the eigenvectors of the occupied states are computed using the BLAS subroutine DGER. Replacing our own OpenMP-threaded code with the DGER subroutine for computing the outer products led to significant improvements in performance with respect to our previous results presented in ref 8.

3.2. SP2 Method. Pseudocode for the CPU implementation of the SP2 algorithm is given in Algorithm 1. The timings we report in Section 5 include the computation of ϵ_{max} and ϵ_{min} .

4. IMPLEMENTATION OF THE SP2 ALGORITHM FOR MULTIPLE GRAPHICS PROCESSING UNITS

Our parallel GPU implementation of the SP2 algorithm is based on Algorithm 3 from ref 8. This algorithm gave the best overall performance on one GPU as it minimizes data transfer between the CPU and GPU. The Hamiltonian matrix, ϵ_{max} , ϵ_{min} , and N_e are passed to each GPU at the start of the algorithm, and the converged density matrix is returned to the CPU upon completion. Only a single float, $\text{Tr}[-\mathbf{X}_i^2 + \mathbf{X}_i]$, is sent to the CPU at each step in the recursive expansion in order to select which projection polynomial to apply in the subsequent step. As illustrated in Figure 1, the workload was partitioned between the multiple GPUs using CUDA streams.

We employed the simplest possible blocking scheme to partition the generalized matrix–matrix multiplication across N_{GPU} GPUs. This is illustrated schematically in Figure 1. The dimensions of the sub-blocks are kept as large as possible since GPUs yield better FLOP rates for larger problems,^{8,15} that is, it is best to keep the GPUs fully occupied. Generalized matrix–matrix multiplications are performed on each GPU between the sub-block assigned to that device with each of the N_{GPU} sub-blocks of the whole array using the cuBLAS DGEMM. The sub-blocks do not need to be copied to or from temporary

Algorithm 1 Pseudo code for the CPU implementation of the SP2 algorithm

```

Estimate  $\epsilon_{\text{max}}$  and  $\epsilon_{\text{min}}$ 
 $\mathbf{X} \leftarrow (\epsilon_{\text{max}}\mathbf{I} - \mathbf{H})/(\epsilon_{\text{max}} - \epsilon_{\text{min}})$ 
 $\text{TraceX} \leftarrow \text{Tr}[\mathbf{X}]$ 
BreakLoop  $\leftarrow$  0
 $i \leftarrow$  0
while BreakLoop = 0 do
   $i \leftarrow i + 1$ 
   $\mathbf{X}_{\text{tmp}} \leftarrow \mathbf{X}$ 
   $\mathbf{X}_{\text{tmp}} \leftarrow -\mathbf{X}^2 + \mathbf{X}_{\text{tmp}} / * \text{DGEMM} *$ 
   $\text{TraceXtmp} \leftarrow \text{Tr}[\mathbf{X}_{\text{tmp}}]$ 
  if  $|2\text{TraceX} - 2\text{TraceXtmp} - N_e| > |2\text{TraceX} + 2\text{TraceXtmp} - N_e|$  then
     $\mathbf{X} \leftarrow \mathbf{X} + \mathbf{X}_{\text{tmp}}$ 
     $\text{TraceX} \leftarrow \text{TraceX} + \text{TraceXtmp}$ 
  else
     $\mathbf{X} \leftarrow \mathbf{X} - \mathbf{X}_{\text{tmp}}$ 
     $\text{TraceX} \leftarrow \text{TraceX} - \text{TraceXtmp}$ 
  end if
  IdemErri  $\leftarrow |\text{TraceXtmp}|$ 
  if IdemErri-2  $\leq$  IdemErri and  $i > i_{\text{min}}$  then
    BreakLoop  $\leftarrow$  1
  end if
end while
 $\mathbf{P} \leftarrow \mathbf{X}$ 

```

working arrays to perform the DGEMM since the indices for the first elements of the sub-blocks in the input and output arrays as well as their dimensions can be passed to the cuBLAS DGEMM directly.

The subsequent steps of the SP2 algorithm do not require the N_{GPU} sub-blocks of the \mathbf{X}_{tmp} to be reassembled. As depicted in Figure 1, we compute the trace of \mathbf{X}_{tmp} in parallel across the GPUs. The partial traces are summed across the GPUs and sent to the CPU. The application of the projection polynomial, $\mathbf{X}_{i+1} = \mathbf{X}_i \pm \mathbf{X}_{\text{tmp}}$, can also be performed in parallel across the GPUs on each of the distributed sub-blocks. Finally, each GPU sends its sub-block of \mathbf{X}_{i+1} to the other GPUs so that every device has a copy of the whole array at the start of the next iteration. The recursive expansion is terminated when the inequality in eq 6 is satisfied after which one GPU returns the density matrix to the CPU.

4.1. Padding Arrays on the GPU. Padding the dimensions of the arrays passed to the cuBLAS DGEMM can significantly improve the performance of the calculation.^{8,15} The optimal padding for the arrays depends on the array dimensions, whether single or double precision arithmetic is used, and appears to be dependent on the model of the GPU. For Nvidia C2090 GPUs we found that the best performance is obtained if the dimensions of the arrays in the serial algorithm are integer multiples of 16. The $M \times M$ arrays are allocated with dimensions $M_{\text{pad}} \times M_{\text{pad}}$ on the GPU where

$$M_{\text{pad}} = 16N_{\text{GPU}} \left(\left\lceil \frac{M-1}{16N_{\text{GPU}}} \right\rceil + 1 \right) \quad (7)$$

where $\lceil x \rceil$ denotes the closest integer with value $\leq x$. By increasing the dimensions of the arrays in increments of $16N_{\text{GPU}}$, we ensure that both dimensions of the sub-blocks in the parallel GPU implementation are also integer multiples of 16. We have also assessed the effect of padding arrays on the GPU such that M_{pad} is the smallest value that allows the workload to be partitioned equally between the N_{GPU} devices, that is

$$M_{\text{pad}} = N_{\text{GPU}} \left(\left\lceil \frac{M-1}{N_{\text{GPU}}} \right\rceil + 1 \right) \quad (8)$$

The effect the padding schemes in eqs 7 and 8 have on the wall clock time for the generalized matrix–matrix multiplication on

one, two, and three GPUs is depicted in Figures 2(a), (b), and (c), respectively. The timings reported in Figure 2 are an

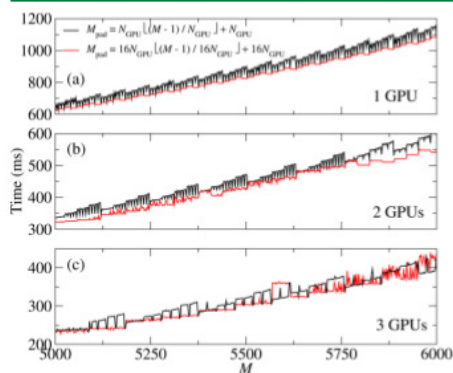


Figure 2. Effect of array padding on the wall clock time per generalized matrix-matrix multiplication. (a) 1 GPU, (b) 2 GPUs, and (c) 3 GPUs.

average of ten generalized matrix-matrix multiplications for each M . Figures 2(a) and (b) show clear improvements in the wall time per generalized matrix-matrix multiplication on one and two GPUs using the padding scheme in eq 7. Figure 2(c) indicates that the padding scheme in eq 7 generally improves the wall time per generalized matrix-matrix multiplication although the simpler padding scheme in eq 8 that only ensures load balancing can occasionally lead to better performance.

5. ANALYSIS OF PERFORMANCE AND ERRORS

5.1. Test Systems. The performance and accuracy of the three algorithms, (i) matrix diagonalization on a CPU, (ii) the SP2 algorithm on a multicore CPU, (iii) and the parallel GPU implementation of the SP2 algorithm, were assessed with Hamiltonian matrices computed using self-consistent charge transfer tight binding theory (SC-TB), also known as density functional tight binding theory.^{4,16–18} The Hamiltonian in SC-TB theory is a sum of a Slater-Koster tight binding Hamiltonian and an electrostatic potential arising from Mulliken partial charges centered on each atom. Since the Hamiltonian depends on Mulliken partial charges that are derived from the density matrix, the SC-TB equations are solved self-consistently.

Our test systems comprised boxes of 50 to 1000 water molecules at normal liquid density under periodic boundary conditions. Each oxygen atom was described by one s and 3 p orbitals, while each hydrogen atom had one s orbital. The systems from which timings were computed were snapshots from molecular dynamics simulations run at a temperature of 300 K. Since the radial distribution function, $g(R)$, for water obtained from our SC-TB parametrization corresponds well to experimental measurements,¹⁹ as depicted in Figure 3, our test systems present a real-world challenge to the three algorithms. The HOMO–LUMO gap of liquid water from our SC-TB model is about $\Delta\epsilon = 5.54$ eV. This value lies within the spectrum of those obtained from other methods.²⁰

5.2. Timings. Timings for the matrix diagonalization and CPU implementation of the SP2 algorithm were gathered on

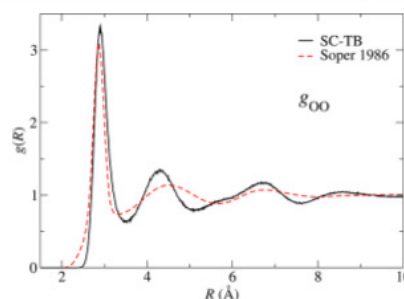


Figure 3. O–O radial distribution function for liquid water at a temperature of 300 K from a SC-TB molecular dynamics simulation and experiment.¹⁹

one node of the Moonlight cluster at Los Alamos National Laboratory. Each node of Moonlight is comprised of two eight-core 2.6 GHz Intel Xeon E5-2670 CPUs. The CPU code was compiled with the pgf90 compiler version 13.7 with the -fast optimization flag and the threaded ACML implementation of the LAPACK and BLAS libraries. All calculations were performed using 16 OpenMP threads. The timings for the parallel GPU algorithm, which include all data transfers between devices, were gathered on one node of the Carter supercomputer at Purdue University. Each node contained three Nvidia C2090 GPUs, and our CUDA code was compiled using the compilers and CuBLAS library distributed with the Nvidia toolkit version 5.5. A threadblock size of 1024 was used for all GPU calculations. We used two different machines to obtain timings only because the performance of the CPU-based algorithms was better on Moonlight than Carter. Similarly, Moonlight has only two Nvidia M2090 GPUs per node rather than the three available on Carter.

The time per density matrix build as a function of the matrix dimension, M , is presented on linear and logarithmic scales in Figures 4 and 5, respectively. Figure 4 shows clearly that the performance of the SP2 algorithm on a multicore CPU can exceed that of traditional matrix diagonalization even in the limit of $O(M^3)$ dense matrix algebra. The superior performance of the CuBLAS DGEMM on general purpose GPUs leads to

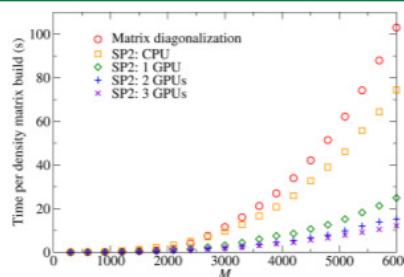


Figure 4. Time per $M \times M$ density matrix build via matrix diagonalization and the CPU and parallel GPU implementations of the SP2 algorithm.

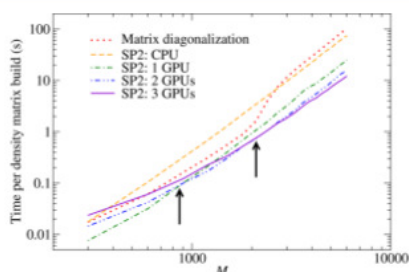


Figure 5. Time per $M \times M$ density matrix build via matrix diagonalization and the CPU and parallel GPU implementations of the SP2 algorithm on logarithmic axes. The arrows denote the matrix dimensions for which the timings for execution on one and two GPUs and two and three GPUs are approximately equal.

very significant improvements in the computational time required for each density matrix build if the problem size is large. For the 1000 water molecule test system we find that executing the SP2 algorithm in parallel on 3 GPUs yields a $\times 6.2$ speed-up with respect to the multicore CPU implementation and a $\times 8.6$ speed-up with respect to matrix diagonalization.

Figure 5 is informative since it depicts clearly how the performance of each algorithm depends on the dimensions of the matrices. For instance, matrix diagonalization is faster than the SP2 method on the CPU up to a matrix dimension of about $M = 2650$. However, owing to the better scaling of the DGEMM with respect to the more complex DSYEV matrix diagonalization subroutine, the SP2 method is fastest for the largest systems. Surprisingly, Figure 5 reveals that the performance of the GPU implementation of the SP2 method is superior to both matrix diagonalization and the CPU implementation of the SP2 algorithm for all problem sizes. Hence, the outstanding performance of the CuBLAS DGEMM even for the relatively small 50 molecule test case more than compensates for overhead arising from data transfers between the CPU and GPU.

Comparing the performance of the GPU implementation on one, two, and three GPUs reveals that one GPU is fastest for matrices smaller than about 900×900 , two GPUs are fastest for intermediate problem sizes from 900×900 to about 2000×2000 , whereafter execution on 3 GPUs provides the smallest wall clock time per density matrix build. The dependence of the wall clock time on the number of GPUs arises both from the communication overheads and the strong dependence of the available FLOPs to populate the available GPUs and allow multithreading to keep the cores busy. By parallelizing a small calculation across multiple GPUs each GPU becomes relatively inefficient and underutilized. Therefore, there exists a trade-off between the performance gains that can be achieved through parallelization and the inefficiencies that derive from giving each GPU a smaller task.

5.3. Analysis of Errors. While Figures 4 and 5 show that the SP2 algorithm enables a significant reduction in the wall clock time per density matrix build with respect to matrix diagonalization, it is important to know whether this comes at the expense of a loss of accuracy. As in ref 8 we have estimated

the errors in the density matrices using measures of the idempotency

$$\epsilon_{\text{idem}} = \|\mathbf{P}^2 - \mathbf{P}\|_2 \quad (9)$$

where $\|X\|_2$ denotes the spectral norm of matrix X , and the commutation between the density matrix and Hamiltonian

$$\epsilon_{\text{comm}} = \|\mathbf{H}, \mathbf{P}\|_2 \quad (10)$$

Both ϵ_{idem} and ϵ_{comm} equal zero if \mathbf{P} is exact.

The errors in the commutation between the $M \times M$ Hamiltonian and density matrices, ϵ_{comm} (eq 10), are presented in Figure 6. The values of ϵ_{comm} for density matrices computed

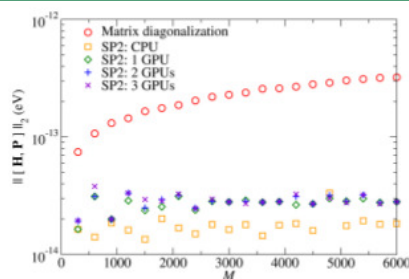


Figure 6. Error in the commutation between the Hamiltonian and density matrices computed using matrix diagonalization and the CPU and parallel GPU implementations of the SP2 method.

via matrix diagonalization are about 1 order of magnitude larger than for those computed using the SP2 method. Furthermore, the matrix diagonalization algorithm leads to errors that increase with system size, whereas for the SP2 method the errors do not depend on M . We attribute the dependence of the commutation errors obtained from the diagonalization-based algorithm on the matrix dimension to a tolerance in the LAPACK DSYEV subroutine on the orthogonality of the eigenvectors. The commutation error for the density matrices computed using the CPU implementation of the SP2 algorithm is smaller than those obtained via the parallel GPU implementation by a factor of about 1.5. The magnitude of the errors arising from the parallel GPU implementation does not depend on the number of GPUs.

The idempotency errors, ϵ_{idem} (eq 9), for the water test systems are presented in Figure 7. Again we observe that the errors in the density matrices obtained using the CPU or parallel GPU implementations of the SP2 method are generally smaller than those obtained via matrix diagonalization, albeit with slightly greater scatter. The scatter in the idempotency errors derived from the SP2 algorithm could not be reduced by increasing the minimum number of iterations of eq 5 during the computation of \mathbf{P} . Hence, we attribute the scatter in ϵ_{idem} to the somewhat stochastic nature of the systems of liquid water used in the calculations that were taken from snapshots from molecular dynamics simulations. The idempotency errors reported in ref 8 did not exhibit any scatter and were computed from idealized, fully relaxed geometries rather than from molecular dynamics snapshots. As with ϵ_{comm} , the idempotency errors measured in the density matrices computed by matrix diagonalization increase with system size, whereas the errors measured in the density matrices computed using the

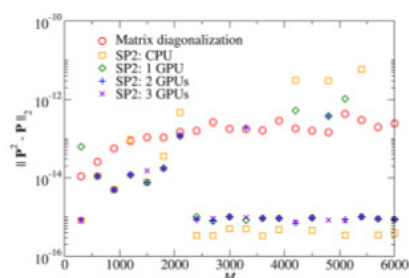


Figure 7. Idempotency error, ϵ_{idem} for the $M \times M$ density matrices computed using matrix diagonalization and the CPU and parallel GPU implementations of the SP2 algorithm.

SP2 method do not exhibit any systematic dependence on M . Taking Figures 6 and 7 together, it is evident that one does not have to compromise accuracy for performance when adopting the SP2 method.

6. CONCLUSIONS

The SP2 method for computing the density matrix in electronic structure theory at zero electronic temperature was originally envisioned for use with linear scaling solvers. The performance of the method in the $O(N^3)$ limit in dense matrix algebra can clearly exceed that of traditional algorithms based on matrix diagonalization. The outstanding performance of the SP2 method can be attributed to the highly optimized implementations of the level 3 BLAS DGEMM generalized matrix–matrix multiplication subroutines that are available for both CPUs and general purpose GPUs.

Compute nodes containing multiple GPUs are nowadays neither uncommon nor prohibitively expensive. We have developed a simple and effective blocking scheme to parallelize the DGEMM, matrix trace, and DAXPY vector–vector addition operations across multiple GPUs on a single compute node. Our parallel GPU implementations of the SP2 algorithm yield significant speed-ups with respect to execution on a single GPU for large problems and are almost $\times 9$ faster than matrix diagonalization on a contemporary multicore CPU. Owing to overheads arising from data transfer between the CPU and GPU(s) and the dependence of the FLOP rate on problem size seen on GPUs, the best performance for small systems ($M < 900$) is achieved by running on one GPU. Intermediate sized problems with $900 < M < 2000$ run fastest on two GPUs, and problems with $M > 2000$ run fastest on three GPUs.

The SP2 method yields density matrices with errors that are as small or smaller than those obtained by matrix diagonalization. Hence, the application of the SP2 algorithm in electronic structure calculations can provide both significant improvements in wall clock time and accuracy, provided the system has a gap at the chemical potential.

AUTHOR INFORMATION

Corresponding Author

*E-mail: cawkwell@lanl.gov.

Notes

The authors declare no competing financial interest.

ACKNOWLEDGMENTS

We thank Ed Sanville, Nick Bock, Kyle Spafford, and Jeffrey Vetter for their contributions and valuable discussions. This work was supported by the Laboratory Directed Research and Development program of Los Alamos National Laboratory. Computing resources were provided in part by the Los Alamos National Laboratory Institutional Computing Program, which is supported by the U.S. Department of Energy National Nuclear Security Administration.

REFERENCES

- (1) Goedecker, S. *Rev. Mod. Phys.* **1999**, *71*, 1085–1123.
- (2) Finnis, M. *Interatomic Forces in Condensed Matter*; Oxford University Press: 2003.
- (3) Bowler, D. R.; Miyazaki, T. *Rep. Prog. Phys.* **2012**, *75*, 036503.
- (4) Cawkwell, M. J.; Niklasson, A. M. N. *J. Chem. Phys.* **2012**, *137*, 134105.
- (5) Millam, J. M.; Scuseria, G. E. *J. Chem. Phys.* **1997**, *106*, 5569–5577.
- (6) Daniels, A. D.; Scuseria, G. E. *J. Chem. Phys.* **1999**, *110*, 1321–1328.
- (7) Niklasson, A. M. N. *Phys. Rev. B* **2002**, *66*, 155115.
- (8) Cawkwell, M. J.; Sanville, E. J.; Mnuszewski, S. M.; Niklasson, A. M. N. *J. Chem. Theory Comput.* **2012**, *8*, 4094.
- (9) <http://www.netlib.org/blas> (accessed Oct 11, 2014).
- (10) Dongarra, J.; Du Croz, J.; Hammarling, S.; Duff, I. *ACM Trans. Math. Software* **1990**, *16*, 1–17.
- (11) Leang, S. S.; Rendell, A. P.; Gordon, M. S. *J. Chem. Theory Comput.* **2014**, *10*, 908.
- (12) <http://docs.nvidia.com/cuda/cublas> (accessed Oct 11, 2014).
- (13) McWeeny, R. *Proc. R. Soc. London, Ser. A* **1956**, *235*, 496.
- (14) Golub, G.; van Loan, C. F. *Matrix Computations*; Johns Hopkins University Press: Baltimore, 1996; p 200.
- (15) Song, F.; Tomov, S.; Dongarra, J. *Efficient Support for Matrix Computations on Heterogeneous Multi-core and Multi-GPU Architectures*; University of Tennessee Computer Science Technical Report UT-CS-11-668; 2011.
- (16) Finnis, M. W.; Paxton, A. T.; Methfessel, M.; van Schilfgarde, M. *Phys. Rev. Lett.* **1998**, *81*, 5149.
- (17) Elstner, M.; Porezag, D.; Jungnickel, G.; Elsner, J.; Haugk, M.; Frauenheim, T.; Suhai, S.; Seifert, G. *Phys. Rev. B* **1998**, *58*, 7260.
- (18) Frauenheim, T.; Seifert, G.; Elstner, M.; Hajnal, Z.; Jungnickel, G.; Porezag, D.; Suhai, S.; Scholz, R. *Phys. Status Solidi B* **2000**, *217*, 41.
- (19) Soper, A. K.; Phillips, M. G. *Chem. Phys.* **1986**, *107*, 47.
- (20) Cabral do Couto, P.; Estácio, S. G.; Costa Cabral, B. J. *J. Chem. Phys.* **2005**, *123*, 054510.

Ultrafast Chemistry under Nonequilibrium Conditions and the Shock to Deflagration Transition at the Nanoscale

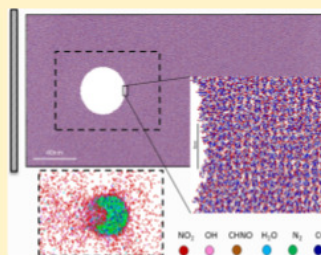
Mitchell A. Wood,^{†,‡,§} Mathew J. Cherukara,^{†,‡,§} Edward M. Kober,^{*,‡} and Alejandro Strachan^{*,†}

[†]School of Materials Engineering and Birk Nanotechnology Center, Purdue University, West Lafayette, Indiana 47907, United States

[‡]Theoretical Division, Los Alamos National Laboratory, Los Alamos, New Mexico 87545, United States

[§]Supporting Information

ABSTRACT: We use molecular dynamics simulations to describe the chemical reactions following shock-induced collapse of cylindrical pores in the high-energy density material RDX. For shocks with particle velocities of 2 km/s we find that the collapse of a 40 nm diameter pore leads to a deflagration wave. Molecular collisions during the collapse lead to ultrafast, multistep chemical reactions that occur under nonequilibrium conditions. Exothermic products formed during these first few picoseconds prevent the nanoscale hotspot from quenching. Within 30 ps, a local deflagration wave develops; it propagates at 0.25 km/s and consists of an ultrathin reaction zone of only ~5 nm, thus involving large temperature and composition gradients. Contrary to the assumptions in current models, a static thermal hotspot matching the dynamical one in size and thermodynamic conditions fails to produce a deflagration wave indicating the importance of nonequilibrium loading in the criticality of nanoscale hot spots. These results provide insight into the initiation of reactive decomposition.



1. INTRODUCTION

The chemical and structural response of materials subjected to dynamical mechanical loads has long been an area of intense activity and resulted in important contributions to materials science,¹ chemistry,² and astrophysics.³ In the case of energetic materials, shock-induced deflagration and detonation provide unique opportunities to study the interplay between thermo-mechanical and chemical processes under extreme conditions of temperature and pressure.⁴ Invariably, shock initiation requires the localization of mechanical energy into so-called "hot spots" that nucleate self-propagating reaction fronts.⁵ Several fundamental mechanisms could contribute to the conversion of the initial mechanical energy into chemical reaction, ranging from direct mechanical disruption of bonds to thermal activation following the transfer of energy from lattice phonons to molecular vibrations (up-pumping).^{6–8} In addition, within some of the pressure and temperature ranges of interest, the formation of plasma and metallized states is plausible, further complicating the definition of chemical mechanisms.⁹ Given the extremely short time scales (pico to nanoseconds), spatial scales down to the submicron regime, and extreme conditions of temperature and pressure associated with these processes, it has proven to be experimentally challenging to unravel the different contributions to the overall process of initiation.⁴ Early reactive MD simulations showed the potential for the technique to investigate hot spots¹⁸ and recent large-scale simulations demonstrate that capturing the transition to detonation is becoming possible on real energetic materials with current computational capabilities.^{32,39} Yet, despite

significant progress, the central problem of how dynamical mechanical loads initiate sustained chemical reactions has not been fully elucidated. The nonequilibrium reactive molecular dynamics (MD) simulations presented here provide the first detailed atomic picture of the shock to deflagration transition in a solid high-energy material.

We focus on hot spots originating from the shock-induced collapse of voids within the secondary energetic material RDX. Such defects are presumed to be the dominant initiation sites in this class of materials and most initiation models include some *ad hoc* representation of their physical response.^{10–12} Continuum models have been used to analyze the hot spot initiation process, but these necessarily make assumptions regarding reaction kinetics, local equilibration and materials properties that are not well-known under the conditions of interest.^{8,13–16,37,40–42} Additionally, continuum simulations are limited in their resolution by the underlying computational mesh (with cell dimensions typically ranging from a micro to 10 nm) and, in the case of nanoscale hot spots, by the validity of continuum descriptions when properties change significantly over few nanometers. MD simulations provide, naturally, atomic resolution and the pertinent question is then whether they can access a sufficiently large spatial and temporal regime for analysis. As shown below, our MD simulations capture, for the first time, the transition to deflagration following the formation of a hot spot in a realistic material with

Received: June 4, 2015

Published: June 13, 2015



ACS Publications

© 2015 American Chemical Society

22008

DOI: 10.1021/acs.jpc.5b05362
J. Phys. Chem. C 2015, 119, 22008–22015

subdetonation conditions with no other approximation than those inherent in the interatomic potential used. We find that multistep chemical reactions, including the formation of exothermic products, occur in time scales shorter than previously thought and contribute to the development of a deflagration wave characterized by an extremely thin chemical reaction front. We also find that dynamical loading plays a key role in the prompt transition to deflagration.

The remainder of this paper is organized as follows, section 2 describes the simulation and computational details, section 3 discusses the formation of the dynamical hotspot following pore collapse, and section 4 describes the subsequent development of a deflagration wave for the largest pore size studied. In section 5, we draw comparisons between the dynamical hotspot and artificially created thermal hotspots. Finally in section 6, we discuss our inferences and the impact of this manuscript.

2. SIMULATION DETAILS

2.1. RDX Samples. In order to characterize the role of pores on the initiation of energetic materials, we simulated supported shock loading of a series of RDX samples with pores of various sizes ranging from 10 to 40 nm in diameter. The initial structures for the simulations consist of a perfect crystal of α -RDX with the exception of a single cylindrical pore of variable size. Figure 1 shows the initial structure of the largest

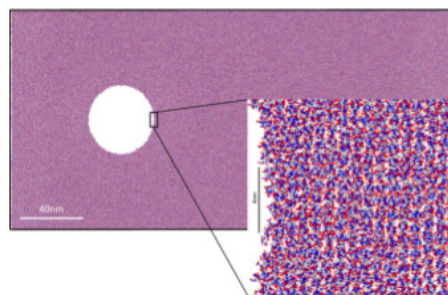


Figure 1. Initial structure for the largest sample of RDX studied with a pore of diameter 40 nm. The shock is directed from left to right along the [001] crystal direction with the pore axis aligned with the [010] direction.

system studied, with a pore 40 nm in diameter and obtained by replicating an α -RDX unit cell (8 molecules) 84 times along the x [100] direction, 3 along the y (the axial direction of the pore), and 204 times along the z (the shock direction, [001] crystal direction). The total length of the largest simulation along the shock direction is 243.1 nm and its width is 120.6 nm where the cylindrical pore of 40 nm in diameter is centered 60 nm from the impact surface. The structure was relaxed via energy minimization and equilibrated at 300 K under isobaric, isothermal conditions for 5 ps followed by isochoric, isothermal conditions for 10 ps. We similarly built samples with 20 and 10 nm pore diameters with linear dimensions along x and z scaled by the pore diameter. That is, the sample with the 20 nm pore was created by replicating the unit cell 42, 3, and 102 times, while the 10 nm pore was created by unit cell replications of 21

$\times 3 \times 51$. In these smaller samples, the pores are centered at 30 and 15 nm from the sample edge, respectively.

2.2. Reactive Interatomic Potential. All simulations were performed using the LAMMPS package¹⁷ with atomic interactions described by the ReaxFF force field.¹⁸ The parametrization used¹⁹ has been trained to describe numerous unimolecular and multimolecular reactions. Specifically, the force field used here merges the nitramines force field from ref 29 with the combustion branch of ReaxFF³⁰ using training data that captures numerous unimolecular and multimolecular reactions for RDX. Self-consistent partial atomic charges are updated at every time step (0.1 fs) using a conjugate gradient method with a tolerance of 1×10^{-6} , which has been shown to properly describe chemical reactions at extreme conditions.¹⁹ ReaxFF's accuracy to describe mechano-chemistry in nitramines, including combustion of RDX, has been established in several prior publications^{7,20–22} as well as shock induced chemistry in the energetic nitroester, PETN.^{31,32} We further validated the force field against more accurate quantum mechanics-based simulations of the decomposition of HMX (RDX's analogue eight-membered ring nitramine). Our results show good overall agreement with the density functional tight binding (DFTB) as described in the [Supporting Information](#).^{6,22,23} While these tests indicate the appropriateness of ReaxFF for the problem at hand, uncertainties in the description of atomic interactions are inescapable for such complex systems. As discussed below, comparison of the evolution of the dynamically formed hot spot with an artificial one show that the main conclusions of the paper are robust with respect to such uncertainties.

2.3. Nonequilibrium Shock, Artificial Thermal Hot Spots, and Simulation Analysis. To establish a supported shock wave, all atoms are assigned at time zero an additional velocity over their thermal ones toward an infinitely massive piston, modeled here as a momentum mirror. The shock is then modeled using constant energy MD (NVE ensemble). A particle velocity of 2 km/s (leading to a pressure of approximately 11 GPa) was chosen because it leads to insignificant chemistry in a defect-free sample (at least on the subps time scales of accessible to MD) and the effects of pore collapse can be isolated. For the chosen particle velocity the shock front is sharp (about 4 nm thickness) and the material is plastically overdriven,³³ i.e. plastic deformation occurs immediately following the shock front.

To characterize spatial variations in thermodynamic properties and chemical structure during the formation of the hot spot and its subsequent reactions we use a $7 \text{ \AA} \times 7 \text{ \AA}$ grid on the x – z plane. Local temperatures are obtained after subtracting the translational center of mass (CoM) velocity for each grid cell. It is well-known that shockwaves drive materials away from local equilibrium and it is useful to define two local temperatures: one associated with the velocity of the molecular centers of mass (T_{CoM}) and a vibrational one associated with the intramolecular degrees of freedom measured from their molecular center of mass T_{vib} ; see [Supporting Information](#) for additional details on the calculation of local temperatures. Molecular species were identified using a minimum spanning tree algorithm based on pairwise-distance cutoffs obtained from the equilibrium structure. Comparisons to ReaxFF calculated bond order based cluster recognition are contained in the [Supporting Information](#).

To simulate purely thermal hot spots equivalent to those formed under pore collapse, we create several hot spots that

match the dynamical one in thermodynamic conditions and with similar shapes and sizes using a thermostat only in select regions of the sample. These hotspots are created within a simulation cell that is preheated to 500 K and precompressed to 11 GPa. These conditions are chosen to match the bulk conditions of the shocked, unreacted, and defect free regions of the crystal. Temperatures in the hot spot are ramped from 500 to 2000 K in 2.0 ps (same as the shock rise time), and then subsequently held at 2000 K for 2.0 ps, while keeping the rest of the sample at 500 K. Afterward the thermostats are removed, and the evolution of chemistry is followed under NVE conditions. Several different geometries and sizes of these artificially formed thermal hot spots were studied, as discussed in section 5.2.

3. DYNAMICAL HOT SPOT FORMATION

The interaction of the shockwave with the cylindrical pores of different sizes results in similar processes and leads to the formation of hot spots in all cases. Local temperature maps of T_{CoM} and T_{vib} at various times (Figure 2) provide insight into

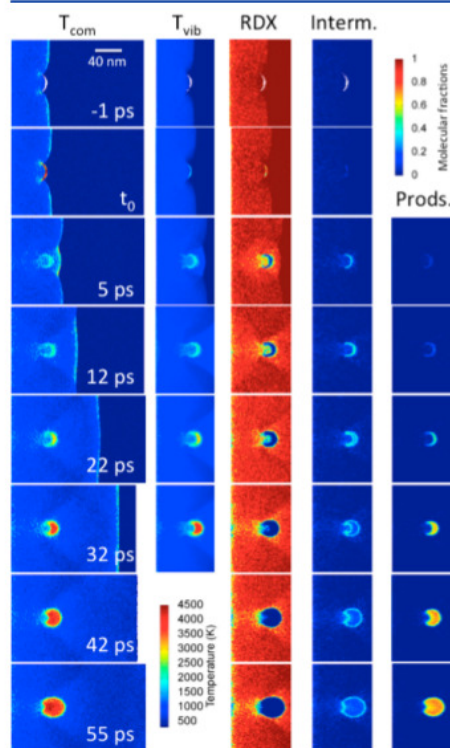


Figure 2. Maps of T_{com} and T_{vib} as well as molecular populations for RDX, intermediates and products at key stages in the shock to deflagration transition. t_0 corresponds to $t = 17.3$ ps after impact. (Also see supplementary movies SMI-SMS).

the void collapse process and subsequent chemistry. Time will be measured from the point when the ejecta impact the downstream surface of the void (t_0 in the second row of Figure 2). As the shock hits the upstream section of the void, a rarefaction wave is created while the ejecta expands freely into the vacuum and undergoes slight cooling. The material entering the pore near the periphery heats up due to friction; see temperature maps at $t = t_0 - 1$ ps. The impact of ejected material against the far wall of the pore leads to a significant spike in the local temperatures giving rise to a crescent-shaped hot spot; see temperature maps at t_0 in Figure 2. Note that the initial hot spot is far away from local equilibrium, with molecular CoM degrees of freedom (which couple strongly with the translational energy in the shock) exhibiting a significantly higher temperature than the intramolecular modes. This impact generates a forward directed shock that starts out stronger than the initial, planar shock; though its strength diminishes with time because of its divergent flow. The collision also generates a backward-directed shock wave that recompresses and heats the material that has flowed into the void; see times 5 and 12 ps in Figure 2.

The hot spots for all pore sizes are characterized by significantly higher temperatures than the homogeneously shocked material and give rise to accelerated chemical reactions. Locally, the initial temperature is somewhat independent of pore size (~ 1500 K), but the volume of high temperature material increases with void size. Figure 3 shows

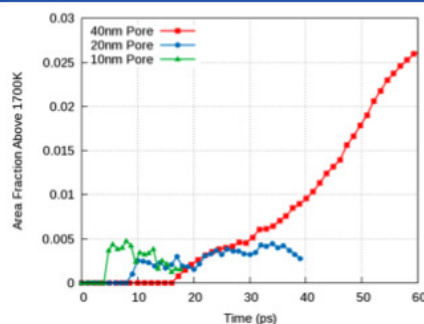


Figure 3. Area fraction of material above a preset ignition temperature of 1700 K for all pore sizes studied, note the quenching of voids smaller than 40 nm.

the time evolution of the spatial extent of the dynamically formed hotspots for different pore sizes by tracking the amount of material in the simulation cell above 1700 K. In all cases studied, there is an initial sudden rise in the hot spot area due to the collision of the ejected material with the downstream wall of the pore. The overall behavior described thus far is fairly consistent with current understanding of hot spot formation from continuum modeling and experiments.^{14,16,24,25,37,40–42} An important distinction is the initial temperature spike and local nonequilibrium state at short times, which continuum models suppress through limited resolution, artificial viscosity and equilibrated equations of state. Following pore collapse, thermal conduction away from the hot spot and the initial endothermic quench the hot spots for the smaller pores with 10 and 20 nm diameters, as shown in Figure 3. The

remarkable result of the simulations is that the 40 nm pore results in a rapid, self-sustained deflagration wave. This critical size is somewhat smaller than previous estimates for RDX and for the closely related HMX.^{6,12,15,41} Section 4 discusses the transition to deflagration and the key molecular processes that enable it.

4. SHOCK TO DEFLAGRATION TRANSITION

A detailed analysis of the 40 nm void simulations provides a description of the transition to deflagration with unprecedented detail that reveals three distinct stages. To illustrate this process Figure 2 also shows maps of the molecular fractions of key species: RDX, main intermediates (NO_2 , NO , OH , HONO , COOH) and product molecules (N_2 , O_2 , CO_2 and H_2O). Figure 4 shows profiles of the same quantities as a function of position along the shock direction averaged spatially over 3 nm along the center of the hot spot and across 0.3 ps.

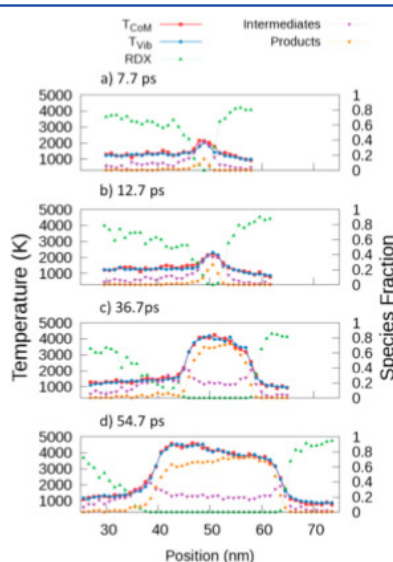


Figure 4. Profiles of T_{COM} and T_{VIB} (left axis), and molecular populations of RDX, intermediates and products (right axes) at key stages in the shock to deflagration transition. Time is measured from void collapse (17.3 ps after impact) (also see Supporting Information, Movie SM6).

The first of the three stages lasts approximately 10 ps. During this period the hot spot evolves from a very narrow crescent generated by the molecular collisions during the pore collapse with a nonequilibrium temperature distribution ($T_{\text{COM}} \sim 4000$ K, $T_{\text{VIB}} \sim 1500$ K), to a broader crescent (~ 5 nm at the broadest point) and more equilibrated temperature ($T_{\text{COM}} \approx T_{\text{VIB}} \sim 2000$ K) at 5 ps. Surprisingly, this stage involves significant chemical reactions that traverse the entire multistep reaction path of RDX: its decomposition, a significant formation of intermediates, and the initial formation of products. The initial decomposition steps in secondary

explosives such as RDX are endothermic and they tend to quench the hot spot. Rarefaction waves and thermal conduction have the same effect as they lower and disperse the temperature. However, the exothermic formation of products has the opposite effect and their unexpectedly fast appearance helps maintain the hot spot temperature. As will be shown below, the reactions that follow the void collapse occur much faster than under thermal decomposition conditions. Thus, we conclude that this fast formation of product species is due to a combination of nonequilibrium and mechanochemical processes caused by the dynamical loading,^{26,27} and this plays a nontrivial role in the development of the deflagration wave.

During the second stage of the reaction process (between approximately 10 and 25 ps after pore collapse) the material is in local thermal equilibrium and the formation of product species accelerates significantly. Two distinct reaction fronts form, one that propagates forward and sideways into the crystalline RDX surrounding the original pore structure, and one that travels more rapidly backward into the amorphous material pushed into the pore. The formation of final product species is accompanied by a rapid rise in temperature from ~ 2000 to ~ 4000 K. At the end of the second stage, the core of the hot spot is close to fully reacted and it has achieved a steady-state temperature ~ 4000 K. This corresponds to times $t_0 + 12$ and $t_0 + 22$ ps in Figures 2 and Figure 4b. The deflagration fronts show a well-defined structure of RDX/intermediates/products with a reaction zone width of ~ 5 nm, which is significantly smaller than those considered previously.^{9,14,15} We note that there are further slower reactions continuing subsequent to this initial process, but a substantial amount of energy is released in this remarkably thin front.

The third stage involves the continued propagation of these narrow deflagration fronts at speeds of ~ 250 m/s. The hot spot evolves from a crescent into a circular shape through slightly faster growth backward into the reshocked material occupying the formerly vacant pore space. The faster rate can be attributed to the material being at a somewhat higher temperature, its structure being noncrystalline, and may also be partially sensitized from partial decomposition of the RDX; see Figure 4c,d. The deflagration fronts propagate at near steady-state conditions. These deflagration velocities are comparable to those measured for HMX under similar conditions (~ 140 m/s) and are much faster than rates predicted from continuum models (~ 7 m/s).^{15,28}

5. HOT SPOT CRITICALITY

5.1. Exothermic Chemistry Prior to Thermal Equilibrium. To obtain additional insight regarding the conditions that make a hot spot critical, we studied the chemical reactions after the collapse of the 40 and 20 nm voids. We analyze the internal and molecular temperatures of the RDX molecules right before they decompose (averaged over 0.1 ps before they are last identified as a molecule) and those of the intermediates and products during the first 0.1 ps of their existence. Figure 5 shows the time evolution of these temperatures following the collapse of the 20 nm void (a) and the 40 nm one (b). In both cases, we observe the initial RDX decomposition ($t < 10$ ps) occurring away from local equilibrium, and for later times the internal temperatures are just below 1500 K for the 20 nm case and just above 1500 K for the 40 nm case. What is clearly different though, is that during the first few picoseconds after pore collapse, the intermediates for the 20 nm case are produced at a lower temperature (~ 1250 K), which is

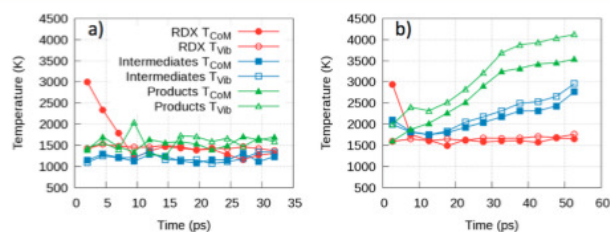


Figure 5. T_{com} and T_{vb} of RDX molecules at the time of their decomposition, and those of intermediates and products at the time of their formation: (a) 20 nm void; (b) 40 nm void.

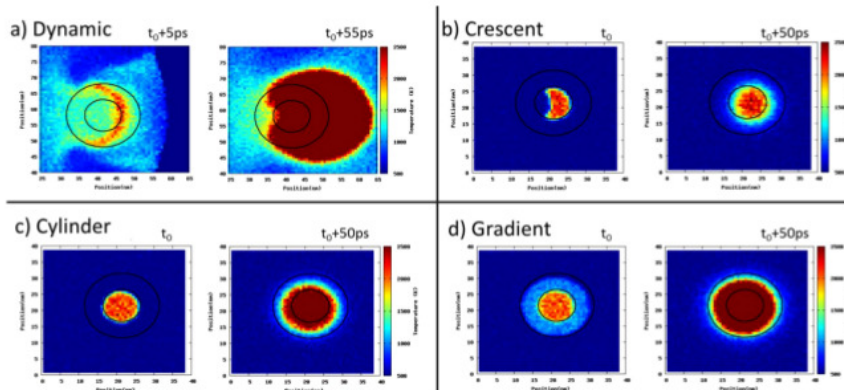


Figure 6. Initial and final states of the (a) dynamic hotspot formed following pore collapse, (b) crescent shaped thermal hotspot initially at 2000 K, (c) cylindrically shaped hotspot heated to 2000 K, and (d) cylindrical hotspot with an inner disc heated to 2000 K and the outer ring heated to 1000 K.

consistent with an endothermic reaction process. The products are produced at a somewhat higher temperature (~ 1500 K), consistent with an exothermic process. Importantly, these temperatures remain constant in time. In contrast, for the 40 nm pore, the intermediates form at higher temperatures (~ 1750 K), and the products at a markedly increased temperature (~ 2000 K). This indicates that there are sufficiently prompt exothermic reactions to elevate the local temperature, which then rapidly increases as the deflagration wave develops (10–30 ps). The temperature distribution between reactants, intermediates and products at late times (~ 50 ps), coupled with the spatial distribution noted above, is analogous to flame structure profiles,^{21,34–36} but happening over significantly smaller scales due to the high pressure/density. We note that the importance of maintaining a critical temperature over a region of the material against thermal conduction away from the hot spot and endothermic reactions for a sufficiently long time is consistent with the standard hot spot models.^{8,15,16} Importantly, our simulations indicate that the fast generation of exothermic products contribute to the criticality of nanoscale hot spots and, as will be shown next, so does its dynamical origin.

5.2. Comparison to Artificial, Thermal Hotspots. The next key question is whether hot spot size and thermodynamic

conditions alone are sufficient to determine its criticality. Thus, we compare the temporal evolution of the hot spot formed by the collapse of the 40 nm pore with a family of artificial, thermally activated hot spots at equivalent thermodynamic conditions and sizes. The artificial hot spots are created within a single crystal of α -RDX measuring $40 \text{ nm} \times 3.6 \text{ nm} \times 40 \text{ nm}$ that has been precompressed and heated to shock conditions (11 GPa and 500 K). In all of the artificially seeded hot spots we assigned a core temperature of 2000 K by heating the region to that value in 2 ps, to match the heating rate experienced by the dynamically compressed material, these regions are then held for an additional 2.0 ps at $T = 2000 \text{ K}$ before completely removing the thermostat to ensure the hot spot evolves from the intended temperature.

Parts b–d of Figure 6 show temperature maps of the initial configurations of all the artificial hot spots, for comparison the hot spot formed after the collapse of the 40 nm pore at time $t = t_0 + 5$ ps is shown in Figure 6a. The crescent shaped hot spot (Figure 6b) matches the dynamical one in area. A broader crescent is used only for computational convenience; the area of RDX above 1900 K is equivalent at 30 nm^2 between it and the shocked loaded sample. The circular hot spots are larger in area than the dynamical one. The hot spot in Figure 6c has a circular cross-section 10 nm in diameter and the one in Figure

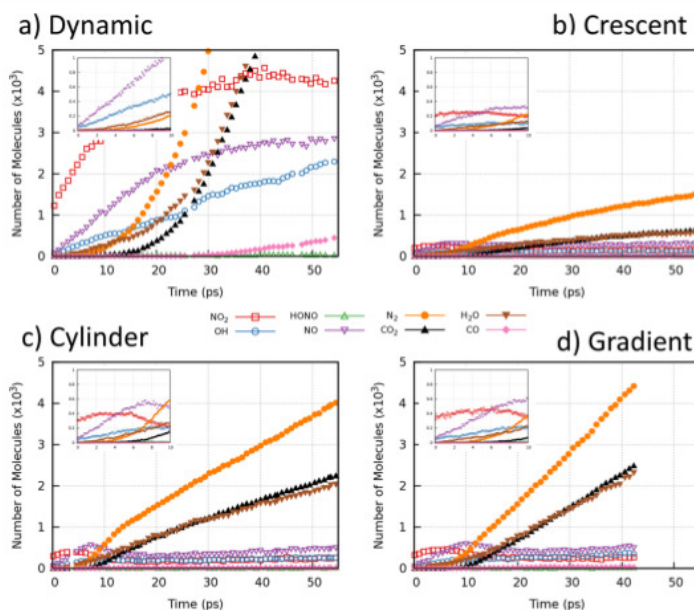


Figure 7. Chemistry evolution following shock and thermal initiation. Insets show an expanded view of events within the first 10 ps.

6d includes a 10 nm diameter region at 2000 K surrounded by a region at 1000 K with outer diameter of 20 nm. Figure 6 also shows temperature maps for each hot spot at a later time ($t_0 + 50$ ps).

Parts a–d of Figure 7 compare the molecular population evolution for all cases (insets display the initial chemistry respectively). Quite surprisingly, the crescent-shaped artificial hot spot that matches the dynamic hotspot in size, Figure 6b, does not become critical; while some reactions are observed, Figure 7b, they are significantly slower than for the dynamical case and the artificial hot spot quenches in 80 ps. The circular hotspots, larger in area than the dynamic one, do become critical but at much later times. The temporal evolution of intermediate and final product species for the dynamic and thermally induced hotspots shown in Figure 7 provide insight into the differences. We observe a dramatic production of intermediates (NO_2 , NO , OH) during the first 10 ps of the dynamical hot spot (Figure 7a) while these species remain relatively low in population over the same interval in the thermally activated cases (Figure 7b–d). Interestingly, in spite of being considerably larger than the dynamical one, their production of final exothermic products (N_2 , H_2O , CO_2) is considerably slower. In addition, the population of the product species grows linearly in time while the mechanically induced hotspot shows quadratic growth. These comparisons demonstrate that size and equilibrium thermodynamic state alone are not enough to characterize nanoscale hot spots that originate during dynamical loading.¹⁶ The shock-induced pore collapse gives rise to very rapid reactions, accelerated by the mechanical concentration of energy, that play a key role in the criticality of

nanoscale hot spots and which should be accounted for in mesoscale models.

6. DISCUSSION

As with any theoretical predictions, it is important to establish model confidence for the problem at hand; this is particularly true for reactive MD simulations such as those presented here where chaotic dynamics could easily amplify the effects of minor inaccuracies in the potential that are universally present. A comparison of our MD predictions against experiments and experimentally tuned models lends credence to our approach. Tarver et al.⁸ developed models for the critical hot spot conditions in HMX and TATB based on the analysis of cook-off experiments. These pioneering kinetic models are still considered to be appropriate.¹⁴ For a 100 nm diameter hot spot in HMX (the smallest size shown in their figures), they determined a critical temperature of 1200 K that would cause that hot spot to develop into a runaway reaction within approximately 5 ns. From a simple extrapolation of those results down to a 10 nm diameter hot spot, we estimate a critical temperature of 1600 K would develop into a runaway reaction at ~ 50 ps. Our MD predictions show a 10 nm diameter hot spot in RDX at the higher temperature of 2000 K does *not* show signs of a runaway reaction at 50 ps; thus we infer that the kinetics in our ReaxFF simulations are somewhat slower than those in Tarver's model. This is consistent with expectations as RDX is known to have very similar though slightly slower kinetics than HMX.^{34–36} This point is illustrated further in the [Supporting Information](#) where we show that the ReaxFF condensed phase chemical reaction rates compare well

to those determined by electronic structure methods. We stress that the key result of our paper is a more mechanistic understanding of hot spot formation, characterization of the transition to deflagration and the importance of dynamical loading in their criticality.

We note that for larger voids the compression of trapped gases provides additional temperature spikes.^{14,15,41,42} Our simulations do not include trapped molecules; we believe that this is justified for the small pore sizes since the largest 40 nm void in a 3 nm thick (periodic) sample would contain only ~100 molecules at standard conditions which would not affect the major conclusions of our simulations. Rather than remaining as a separate phase, we expect those gas molecules to intermix with the rarefying RDX and absorb a minor amount of heat from the collision process.

Finally, we note that similar simulations to these have recently been performed with PETN,^{25,32} though a full analysis of the reaction processes has not yet appeared. PETN is a more mechanically sensitive material than RDX, and is on the borderline between what are considered primary and secondary explosives. That is, the mechanical breaking of bonds in PETN¹¹ is a more significant initiation process compared to the thermal disruption associated the hot spot model. Detailed comparisons between these current results, and additional planned studies on the much less sensitive TATB, would be highly significant for the further development of models for explosive initiation.

7. CONCLUSION

In conclusion, the first atomistic description of the transition to deflagration following the shock loading of an energetic material provides significant insight into the role of mechanochemical processes occurring at length and time scales that have hitherto been inaccessible either computationally or experimentally. While we acknowledge that the results should not be considered to be quantitative because of the limited high pressure reaction data available for calibration, there are no glaring inconsistencies with available information. Consequently, we conclude that the physical processes discovered in this study should be highly relevant. Most significantly, we find that ultrafast chemical reactions occurring within the first 5 ps of the pore collapse provide a significant impetus to accelerate the reactions beyond what would be expected for a simple thermally activated cook-off process. We also find that a local deflagration wave with a surprisingly small width (~5 nm) rapidly develops in ~30 ps. Consequently, the small hot spots studied here are not immediately quenched by divergence factors. These results show that nanoscale hot spots should play a larger role in the initiation of energetic materials than previously thought. We note that effect of loading conditions on accelerated chemistry may be less critical in larger hot spots where quenching due to thermal diffusivity is not as significant, or for more gradual compression processes resulting from more diffuse loading fronts.

■ ASSOCIATED CONTENT

Supporting Information

Further details of the verification of this potential and identification of species, including movies. The Supporting Information is available free of charge on the ACS Publications website at DOI: 10.1021/acs.jpcc.5b05362.

■ AUTHOR INFORMATION

Corresponding Authors

*(E.M.K.) E-mail: emk@lanl.gov.

*(A.S.) E-mail: strachan@purdue.edu.

Author Contributions

[§]M.J.C. and M.A.W. contributed equally to this work; they performed and analyzed the simulations. All authors were equally involved with the design and interpretation of the simulations and writing of the paper.

Notes

The authors declare no competing financial interests.

■ ACKNOWLEDGMENTS

This research was primarily supported by the U.S. Office of Naval Research through Grant Number N00014-11-1-0466 and by the U.S. Defense Threat Reduction Agency, HDTRA1-10-1-0119 (Program Manager Suhithi Peiris). E.M.K. acknowledges funding support from the Institute for Materials Science and the ASC High Explosives modeling program at LANL. He also acknowledges Ralph Menikoff (LANL) for many useful conversations.

■ REFERENCES

- (1) Kadau, K.; Germann, T. C.; Lomdahl, P. S.; Holian, B. L. Microscopic view of structural phase transitions induced by shock waves. *Science* **2002**, *296*, 1681–4.
- (2) Wu, C.; Fried, L.; Yang, L.; Goldman, N.; Bastea, S. Catalytic behaviour of dense hot water. *Nat. Chem.* **2009**, *1*, 57–62.
- (3) Knudson, M.; Desjarlais, M.; Dolan, D. Shock-wave exploration of the high-pressure phases of carbon. *Science* **2008**, *322*, 1822–1825.
- (4) (a) Dlott, D. D. New developments in the physical chemistry of shock compression. *Annu. Rev. Phys. Chem.* **2011**, *62*, 575–97. (b) Armstrong, R. W.; Elban, W. L. Materials science and technology aspects of energetic (explosive) materials. *Mater. Sci. Technol.* **2006**, *22*, 381. (c) Walley, S. M.; Field, J. E.; Greenaway, M. W. Crystal sensitivities of energetic materials. *Mater. Sci. Technol.* **2006**, *22*, 402.
- (5) Cherukara, M. J.; Germann, T. C.; Kober, E. M.; Strachan, A. Shock Loading of Granular Ni/Al Composites. Part 1: Mechanics of Loading. *J. Phys. Chem. C* **2014**, *118*, 26377–26386.
- (6) Manaa, M. R.; Fried, L. E. The reactivity of energetic materials under high pressure and temperature. *Adv. Quantum Chem.* **2014**, *69*, 221–252.
- (7) Strachan, A.; van Duin, A. C. T.; Chakraborty, D.; Dasgupta, S.; Goddard, W. A. Shock Waves in High-Energy Materials: The Initial Chemical Events in Nitramine RDX. *Phys. Rev. Lett.* **2003**, *91*, 098301.
- (8) Tarver, C. M.; Chidester, S. K.; Nichols, A. L., III. Critical conditions for impact and shock-induced hot spots in solid explosives. *J. Phys. Chem.* **1996**, *100*, 5794–5799.
- (9) Reed, E. J.; Riad Manaa, M.; Fried, L. E.; Glaesemann, K. R.; Joannopoulos, J. D. A transient semimetallic layer in detonating nitromethane. *Nat. Phys.* **2007**, *4*, 72–76.
- (10) Johnson, J. N.; Tang, P. K.; Forest, C. A. Shock-wave initiation of heterogeneous reactive solids. *J. Appl. Phys.* **1985**, *57*, 4323.
- (11) Wescott, B. L.; Stewart, D. S.; Davis, W. C. Equation of state and reaction rate for condensed-phase explosives. *J. Appl. Phys.* **2005**, *98*, 053514.
- (12) Lee, E. L.; Tarver, C. M. Phenomenological model of shock initiation in heterogeneous explosives. *Phys. Fluids* **1980**, *23*, 2362.
- (13) Jaramillo, E.; Sewell, T. D.; Strachan, A. Atomic-level view of inelastic deformation in a shock loaded molecular crystal. *Phys. Rev. B* **2007**, *76*, 064112.
- (14) Levesque, G.; Vitello, P.; Howard, W. M. Hot-spot contributions in shocked high explosives from mesoscale ignition models. *J. Appl. Phys.* **2013**, *113*, 233513.

- (15) Menikoff, R. On Beyond the Standard Model for High Explosives: Challenges & Obstacles To Surmount. *AIP Conf. Proc.* **2009**, *18*, 18–25.
- (16) Mader, C. L. Initiation of Detonation by the Interaction of Shocks with Density Discontinuities. *Phys. Fluids* **1965**, *8*, 1811.
- (17) Plimpton, S. Fast Parallel Algorithms for Short-Range Molecular Dynamics. *J. Comput. Phys.* **1995**, *117*, 1–19.
- (18) Van Duin, A. C. T.; Dasgupta, S.; Lorant, F.; Goddard, W. A. ReaxFF: A Reactive Force Field for Hydrocarbons. *J. Phys. Chem. A* **2001**, *105*, 9396–9409.
- (19) Wood, M.; van Duin, A. C. T.; Strachan, A. Coupled Thermal and Electromagnetic Induced Decomposition in the Molecular Explosive α HMX; A Reactive Molecular Dynamics Study. *J. Phys. Chem. A* **2014**, *118*, 885.
- (20) Strachan, A.; Kober, E. M.; van Duin, A. C. T.; Oxgaard, J.; Goddard, W. A. Thermal decomposition of RDX from reactive molecular dynamics. *J. Chem. Phys.* **2005**, *122*, 54502.
- (21) Anderson, W. R.; Conner, C. B. Comparison of gas-phase mechanisms applied to RDX combustion model. *Proc. Combust. Inst.* **2009**, *32*, 2123–2130.
- (22) Zhang, L.; Zybin, S. V.; van Duin, A. C. T.; Dasgupta, S.; Goddard, W. A.; Kober, E. M. Carbon cluster formation during thermal decomposition of octahydro-1, 3, 5, 7-tetranitro-1, 3, 5, 7-tetrazocine and 1, 3, 5-triamino-2, 4, 6-trinitrobenzene high explosives from ReaxFF reactive molecular dynamics simulations. *J. Phys. Chem. A* **2009**, *113*, 10619–10640.
- (23) Manaa, M. R.; Fried, L. E.; Melius, C. F.; Elstner, M.; Frauenheim, T. Decomposition of HMX at Extreme Conditions: A Molecular Dynamics Simulation. *J. Phys. Chem. A* **2002**, *106*, 9024–9029.
- (24) Ding, Z.; Gracewski, S. The behaviour of a gas cavity impacted by a weak or strong shock wave. *J. Fluid Mech.* **1996**, *309*, 183–209.
- (25) Shan, T.; Thompson, A. P. Shock-induced hotspot formation and chemical reaction initiation in PETN containing a spherical void. *J. Phys. Conf. Ser.* **2014**, *172*, 012009.
- (26) Landerville, A.; Oleynik, I. I.; Kozhushner, M. A.; White, C. T. First-Principles Reactive Molecular Dynamics of Chemistry in Detonating Energetic Materials. *AIP Conf. Proc.* **2007**, *955*, 447–450.
- (27) Nomura, K. I.; et al. Dynamic Transition in the Structure of an Energetic Crystal during Chemical Reactions at Shock Front Prior to Detonation. *Phys. Rev. Lett.* **2007**, *99*, 148303.
- (28) Esposito, A.; Farber, D.; Reaugh, J. E.; Zaug, J. M. Reaction propagation rates in HMX at high pressure. *Propellants, Explos. Pyrotech.* **2003**, *28*, 83–88.
- (29) Strachan, A.; Kober, E. M.; van Duin, A. C. T.; Oxgaard, J.; Goddard, W. A. Thermal decomposition of RDX from reactive molecular dynamics. *J. Chem. Phys.* **2005**, *122*, 54502.
- (30) Chenoweth, K.; van Duin, A. C. T.; Goddard, W. A. ReaxFF reactive force field for molecular dynamics simulations of hydrocarbon oxidation. *J. Phys. Chem. A* **2008**, *112*, 1040–53.
- (31) Shan, T.; Wixom, R.; Mattsson, A.; Thompson, A. Atomistic simulation of orientation dependence in shock-induced initiation of pentaerythritol tetranitrate. *J. Phys. Chem. B* **2013**, *117*, 928–936.
- (32) Shan, T.; Wixom, R.; Thompson, A. Micron-scale reactive atomistic simulations of void collapse and hot spot growth in pentaerythritol tetranitrate. 15th International Detonation Symposium Proc., in press.
- (33) Hooks, D. E.; Ramos, K. J.; Martinez, A. R. Elastic-plastic shock wave profiles in oriented single crystals of cyclotrimethylene trinitramine (RDX) at 2.25 GPa. *J. Appl. Phys.* **2006**, *100*, 024908.
- (34) Liao, Y.-C.; Yang, V. Analysis of RDX Monopropellant Combustion with two-phase subsurface reactions. *J. Prop. Power* **1995**, *11*, 729.
- (35) Zenin, A. HMX and RDX: Combustion mechanism and influence on modern double-base propellant combustion. *J. Prop. Power* **1995**, *11*, 752.
- (36) Yetter, R. A.; Dryer, F. L.; Allen, M. T.; Gatto, J. L. Development of Gas-phase reaction mechanisms for nitramine combustion. *J. Prop. Power* **1995**, *11*, 683.
- (37) Bourne, N. K.; Milne, A. M. The temperature of a shock-collapse cavity. *Proc. R. Soc. London, A* **2003**, *459*, 1851.
- (38) van Duin, A. C. T.; Zybin, S.; Chenoweth, K.; Zhang, L.; Han, S.; Strachan, A.; Goddard, W. A. Reactive force fields based on quantum mechanics for applications to materials at extreme conditions. *AIP Conf. Proc.* **2006**, *845*, 581–584.
- (39) Plimpton, S.; Thompson, A. Computational aspects of many-body potentials. *Mater. Res. Soc. Bull.* **2012**, *37*, 513–521.
- (40) Menikoff, R.; Shaw, M. Modeling detonation waves in nitromethane. *Combust. Flame* **2011**, *158*, 2549–2558.
- (41) Barton, N.; Winter, N.; Reaugh, J. Defect evolution and pore collapse in crystalline energetic materials. *Modelling Simul. Mater. Sci. Eng.* **2009**, *17*, 035003.
- (42) Najjar, F.; Howard, W.; Fried, L.; Manaa, M.; Nichols, A., III; Levesque, G. Computational study of 3-D hot-spot initiation in shocked insensitive high-explosive. *AIP Conf. Proc.* **2012**, *1426*, 255–259.

Nonlinear Electromagnetic Interactions in Energetic Materials

M. A. Wood,^{1,2} D. A. R. Dalvit,² and D. S. Moore³

¹*School of Materials Engineering and Birck Nanotechnology Center, Purdue University, West Lafayette, Indiana 47907, USA*

²*Theoretical Division, MS B213, Los Alamos National Laboratory, Los Alamos, New Mexico 87545, USA*

³*Explosive Science and Shock Physics Division, MS P952, Los Alamos National Laboratory, Los Alamos, New Mexico 87545, USA*

(Received 5 October 2015; revised manuscript received 1 December 2015; published 12 January 2016)

We study the scattering of electromagnetic waves in anisotropic energetic materials. Nonlinear light-matter interactions in molecular crystals result in frequency-conversion and polarization changes. Applied electromagnetic fields of moderate intensity can induce these nonlinear effects without triggering chemical decomposition, offering a mechanism for the nonionizing identification of explosives. We use molecular-dynamics simulations to compute such two-dimensional THz spectra for planar slabs made of pentaerythritol tetranitrate and ammonium nitrate. We discuss third-harmonic generation and polarization-conversion processes in such materials. These observed far-field spectral features of the reflected or transmitted light may serve as an alternative tool for standoff explosive detection.

DOI: 10.1103/PhysRevApplied.5.014004

I. INTRODUCTION

Although remote sensing of energetic materials is a pressing current problem worldwide, there is a serious gap in the suite of technologies available to detect energetic materials, namely the use of nonionizing radiation for bulk explosive detection [1]. Terahertz spectroscopy has arisen as a promising tool for the remote sensing of explosives because it can penetrate dry materials, is nonionizing, is standoff capable, and, importantly, new sources of THz radiation are becoming available. Most previous studies of the interaction between THz radiation and explosives have concentrated on molecular fingerprinting of the spectral responses of typical explosives in the 0.1–3.0 THz region [2]. However, since the involved transition frequencies are much smaller than the working temperatures, the resulting spectral lines are broadened and congested, making the fingerprint assignment difficult.

Active nonlinear responses of explosives to electromagnetic radiation in the GHz-to-THz range offer an alternative potential route towards signatures for standoff detection. As is well known, strong electromagnetic (EM) fields modify the optical properties of matter, resulting in a nonlinear relation between the applied field and the electric polarizability [3], $\mathbf{P} = \epsilon_0 \chi^{(1)} \cdot \mathbf{E} + \epsilon_0 \chi^{(2)} \cdot \mathbf{E}\mathbf{E} + \epsilon_0 \chi^{(3)} \cdot \mathbf{E}\mathbf{E}\mathbf{E} + \dots$. Here, $\chi^{(1)}$ is the linear susceptibility tensor, $\chi^{(i>1)}$ are the nonlinear susceptibility tensors, and ϵ_0 is the permittivity of vacuum. A myriad of nonlinear effects are possible, including frequency mixing, Pockels and Kerr effects, and Raman scattering [4,5]. In addition, the electromagnetic heating of energetic materials, particularly heterogeneous ones, generates the appearance of “hot spots,” regions of concentration of electric fields, and, therefore, possibly enhanced nonlinear effects.

These hot spots also result in locally enhanced temperatures that modify the optical properties of the explosive material by forcing atoms and electrons to explore anharmonic regions of the energy landscape, resulting in further nonlinear effects.

Recently, Katz *et al.* [6] have employed molecular dynamics (MD) to simulate the two-dimensional spectroscopy of a few bulk explosive crystals under an applied THz linearly polarized electric field that is homogeneous throughout the bulk material. They found frequency-conversion Raman-like effects both in the co- and cross-polarized optical responses, which can serve as potential alternative fingerprints of explosives. A more realistic remote sensing scenario, though, would involve an EM wave impinging onto an air-explosive interface and the evaluation of the optical nonlinear signatures in the far field at a standoff distance from the energetic material. Here, we use a MD approach to simulate the simplest air-explosive planar interface, and compute absorption spectra, frequency-conversion tensors, and far-field response for various energetic materials, including pentaerythritol tetranitrate (PETN) and ammonium nitrate. Depending on the magnitude of the applied electromagnetic field, the incident pulse can simply force the molecular system to make nonlinear excursions without inducing chemistry (“tickling the dragon”), or trigger decomposition of the various high-explosive crystals leading to deflagration and detonation [7]. In the present study, we consider EM pulses strong enough to result in non-negligible nonlinearities in the optical response of the energetic materials, but not so strong as to induce chemical reactions.

II. FREQUENCY CONVERSION IN LIGHT-MATTER INTERACTIONS

A. Scattering of electromagnetic waves in molecular crystals

One of the most important processes in the propagation of electromagnetic waves in transparent media is scattering, in which small-intensity scattered waves are produced whose wave vectors, frequencies, and states of polarization are different from the incoming wave [4,5]. Scattering is the result of the change in the motion of the charges in the medium as a result of an incident electromagnetic field. In the following, we briefly review the classical theory of scattering. Let us consider a linearly polarized input plane-wave electromagnetic field of the form

$$\mathbf{E}_{\text{in}}(\mathbf{x}, t) = \mathbf{e}_{\text{in}} E_{\text{in}} e^{i\mathbf{k}_{\text{in}} \cdot \mathbf{x}} e^{-i(t-t_0)^2/2\sigma^2} \cos(\omega_{\text{in}} t), \quad (1)$$

where E_{in} is the amplitude of the wave, \mathbf{k}_{in} is the input wave vector ($k_{\text{in}} = |\mathbf{k}_{\text{in}}| = \omega_{\text{in}}/c$), and \mathbf{e}_{in} is the input polarization unit vector ($\mathbf{e}_{\text{in}} \cdot \mathbf{k}_{\text{in}} = 0$). The Gaussian pulse is centered at t_0 , has a width σ , and a carrier frequency ω_{in} . The field drives the charges in the molecular crystal according to the Lorentz force $\mathbf{F} = e\mathbf{E} + (\mathbf{v}/c) \times \mathbf{B}$, and for sufficiently strong amplitudes the charges explore the nonlinear regions of the energy landscape. For a single accelerated (nonrelativistic) charge following a trajectory $\mathbf{r}(t')$, the far-field radiated electric field is given by $\mathbf{E}_{\text{rad}}(\mathbf{x}, t) = (e/c)[\mathbf{n} \times \mathbf{n} \times \dot{\mathbf{p}}/R]_{\text{ret}}$, where \mathbf{n} is a unit vector in the direction of $\mathbf{R}(t') = \mathbf{x} - \mathbf{r}(t')$, $\dot{\mathbf{p}}(t') = \ddot{\mathbf{r}}(t')/c$ (the dot denotes time derivative), and “ret” means that the quantity in the square brackets is to be evaluated at the retarded time given by $t' + R(t')/c = t$. Note that since the observation point is assumed to be far away from the region of space where the acceleration takes place, the unit vector \mathbf{n} is almost constant in time. The corresponding Fourier spectrum is given by

$$\mathbf{E}_{\text{rad}}(\mathbf{x}, \omega) = \frac{e/c}{\sqrt{2\pi}} \int_{-\infty}^{\infty} dt' [\mathbf{n} \times \mathbf{n} \times \ddot{\mathbf{r}}(t')] \frac{e^{i\omega_{\text{in}}[t' - \mathbf{n} \cdot \mathbf{r}(t')/c]}}{R(t')}. \quad (2)$$

For a collection of N accelerated charges, one makes the replacement $e[\mathbf{n} \times \mathbf{n} \times \ddot{\mathbf{r}}(t')]R^{-1}(t')e^{-i\omega_{\text{in}}[t' - \mathbf{n} \cdot \mathbf{r}(t')/c]} \rightarrow \sum_{j=1}^N e_j[\mathbf{n}_j \times \mathbf{n}_j \times \ddot{\mathbf{r}}_j(t')]R_j^{-1}(t')e^{-i\omega_{\text{in}}[t' - \mathbf{n}_j \cdot \mathbf{r}_j(t')/c]}$. Furthermore, because the observation point is very far from the accelerated charges, one can approximate $R_j(t') \approx R_0$ and $\mathbf{n}_j \approx \mathbf{n}$, where R_0 is the distance between the observation point \mathbf{x} and an origin of coordinates within the scattering volume, and the unit vector \mathbf{n} is along that direction. Note that the acceleration of each charge $\ddot{\mathbf{r}}_j$ within the molecular crystal depends on the input electromagnetic field, and in particular is a function of the input frequency ω_{in} . Most of the far-field radiation is emitted at the same frequency as

the input one $\omega = \omega_{\text{in}}$ (Rayleigh scattering), but a small portion can be emitted at a frequency different from the incident one $\omega \neq \omega_{\text{in}}$ (Raman scattering) due to nonlinear light-matter interactions within the material. A further simplification takes place when the emitted (and also the incident) light have wavelengths $\lambda = 2\pi\omega/c$ much larger than the typical linear size of the scatterer. In this case $(\omega/c)\mathbf{n}_j \cdot \mathbf{r}_j \ll 1$, and one can replace the exponentials by unity, $e^{-i(\omega/c)\mathbf{n}_j \cdot \mathbf{r}_j(t')} \approx 1$; this corresponds to the leading order in a multipolar expansion. In the following, we will consider THz radiation impinging on energetic materials of a typical size on the order of tens of nanometers, for which this is an excellent approximation.

The input electromagnetic field polarizes the molecular crystal, and generates electric dipole moments $\mathbf{p}_a(t')$ at each atomic position \mathbf{r}_a . Each of these dipole moments corresponds to a pair $(j, j')_a$ of terms in the above summations over j , such that $\mathbf{p}_a(t') = |e_{ja}|[\mathbf{r}_{ja}(t') - \mathbf{r}_{j'a}(t')]$. We can then write the following expression for the far-field Fourier spectrum of the emitted light by the molecular crystal:

$$\mathbf{E}_{\text{rad}}(\mathbf{x}, \omega) = \frac{1}{\sqrt{2\pi}} \frac{1}{cR_0} \mathbf{n} \times \mathbf{n} \times \int_{-\infty}^{\infty} dt' e^{-i\omega t'} \sum_a \ddot{\mathbf{p}}_a(t'). \quad (3)$$

Therefore, the far-field frequency spectra can be obtained from the Fourier transform of the second time derivative of the full dipole moment of the system, $\mathbf{P} = \sum_a \mathbf{p}_a$.

It is worth mentioning that as each atom is polarized by the impinging electromagnetic field, the induced accelerated dipole produces secondary radiation that also acts as a field source for all other dipoles. The total local field on each dipole is then the sum of the external field plus all of these secondary fields, and the time evolution for the system of dipoles should be solved self-consistently. However, although MD computes the dynamics of the full system of dipoles self-consistently in terms of force fields (see below), it does not take into account the backaction of the secondary electromagnetic fields from the accelerated dipoles onto the dynamics of the dipoles themselves. In the following, we will assume that these secondary fields are much weaker than the incident one, and disregard local field corrections.

B. Molecular-dynamics methods

Given the classical description of absorption and far-field emission measurement from the previous section, we have opted to use MD simulations as the underlying simulation tool for dynamically calculating nonlinear scattering in molecular crystals. To ensure proper interaction with an externally applied electric field, a polarizable interatomic potential must be used. Reactive force field ReaxFF [8] is one such polarizable interatomic potential that is commonly used for energetic materials [9–11], and has been employed by several others to study the response of molecular crystals

to strong electric fields [12–15]. Dynamic polarization is captured by allowing the partial atomic charges to be updated at each time step ($\Delta t = 0.1$ fs) with a conjugate gradient method [16] to the local minima in electrostatic energy with a tolerance set to 10^{-6} . In addition, because the ReaxFF force field captures the reactive potential energy surface, it is intrinsically anharmonic at elevated temperatures as the system approaches transition states. It is important to note that the Gaussian electric field pulses simulated here are not sufficiently strong to initiate any chemical decomposition. However, these short electric field pulses push the system to explore anharmonic portions of the potential energy minima; this will be further discussed in Sec. III. All MD simulations are run using the LAMMPS [17] MD code with the force-field parametrization described in detail in Refs. [12,18,19].

Recently, Katz *et al.* used reactive MD to study THz emission in 1,3,5-trinitro-1,3,5-triazine and triacetone triperoxide and reported the first evidence that ReaxFF can be used to predict THz frequency-conversion processes [6]. In contrast to Katz *et al.*, who dealt with only an infinite (bulk) material, here we consider the more physical situation of an explosive slab surrounded by air. In this case of a finite-size structure (in the z direction), the use of Eqs. (2) and (3) for the far-field emission is justified. In our simulations, we will consider the faces of the slab (i.e., the free surfaces) to be orthogonal to one of the principal axes of the HE crystal (here arbitrarily chosen to be the [001] direction). Light impinges normal to the slab with polarization in the orthogonal [100] or [010] directions, and we observe emitted light in the z direction for both output polarizations. A schematic view of our simulation setup is shown in Fig. 1(e). We have selected a pair of materials, PETN and ammonium nitrate polymorph IV (AN IV), that exemplify a benchmark test for detection capability using THz signals [20,21]. PETN is a molecule with both oxidizer and fuel contained on a single chemical unit, while AN is an energetic cocrystal that forms a charge-neutral lattice from a basis of charged molecular species much like a ceramic material. Representative orthoscopic views of the two molecular crystals are displayed in Figs. 1(a)–1(d) [22].

The PETN simulation cell is generated by replicating the geometrically relaxed unit cell six times in each direction (1008 molecules, $7.5 \times 7.8 \times 6.3$ nm³) before removing the periodic boundary in [001] and relaxing in the isobaric-isothermal thermodynamic ensemble at 50 K and 1 atm of pressure. Similarly, the AN unit cell is replicated 12 times in each direction (729 molecule pairs, $4.7 \times 6.3 \times 4.8$ nm³) and relaxed using the same procedure. All simulations of an applied electric field are run in the microcanonical ensemble (constant number of particles and volume) so that any change in total energy is due to the material coupling with the electromagnetic impulses. Special care must be taken when choosing the peak intensity and duration of the

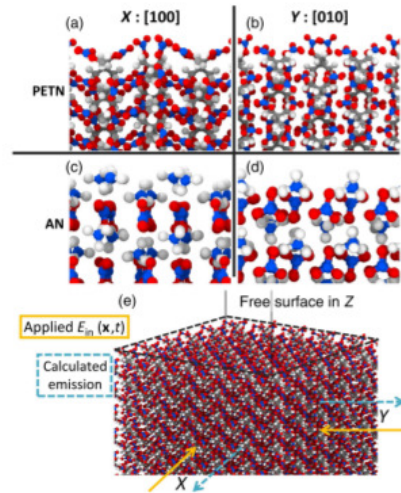


FIG. 1. (a),(c) Representative orthoscopic views of the [100] crystallographic direction for PETN and ammonium nitrate. Panels (b),(d) show the [010] direction in either material which exemplifies the unique molecule arrangement in either direction. (e) Perspective view of the simulation domain showing how the free surface is created in MD; perpendicular to this free surface is the propagation direction of both applied and emitted fields. This simulation setup enables realistic absorption and emission polarizations within MD. Atom colors correspond to carbon (gray), hydrogen (white), oxygen (red), and nitrogen (blue).

electric field pulse because the material needs to experience an impulse strong enough to sample anharmonic regions of the potential energy surface, but remain chemically unreacted. A Gaussian pulse of width 20 ps and a peak amplitude of 1 V/nm is determined to be sufficient to induce the nonlinear effects of interest. During this pulse duration, the dipole accelerations $\ddot{\mathbf{p}}_a(t')$ are outputted at 4-fs intervals, and are then used to calculate the emission spectra for each carrier frequency. At each output time, the net dipole acceleration (sum on all atoms) in each Cartesian direction of the system is recorded and it is this time series that is Fourier transformed, as in Eq. (3). These resultant spectra will be discussed in detail in the next section. After this 20-ps pulse, the electric field is removed and the microcanonical dynamics are continued, which allows for an accurate determination of the energy input. Figure 2(a) shows a pair of example electric field pulses applied to PETN along with the total energy change due to the material coupling with this pulse. A volume normalized total energy is used here because the field is applied homogeneously (long wavelength approximation), therefore making the total energy absorbed dependent on the simulation cell size.

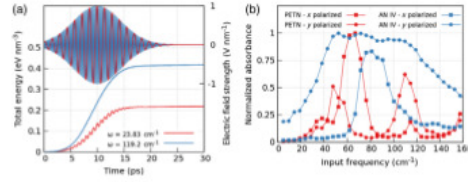


FIG. 2. (a) Two example Gaussian electric field pulses with different carrier frequencies applied in PETN. Absorption is measured as the difference between the total energy after and before the pulse is applied. (b) Absorbance (normalized by the peak value for each polarization), as a function of the input carrier frequency and input polarization, for PETN (red) and AN IV (blue). The unique molecule geometry in each direction leads to polarization-dependent absorbance.

As a function of carrier frequency and polarization, Fig. 2(b) shows the absorbance of either material normalized by the highest absorbing mode tested. Each carrier frequency is approximately 5 cm^{-1} apart, spanning the range of $0\text{--}170 \text{ cm}^{-1}$ in 35 steps. In these MD simulations the back interaction on the electric field from the material is not captured, but rather the pulse shape and intensities are fixed regardless of whether or not there is an absorbing mode present. The strongest absorbing mode resulted in a 165 K rise for PETN and 360 K for AN; neither final temperature is expected to initiate decomposition. Interestingly, each polarization of the incident field causes a unique absorption signal due to the asymmetry in the structure along these crystallographic directions, see Fig. 1. In this range of frequencies tested, most vibrations are either multimolecular modes or small-amplitude unimolecular deformation modes. Examples of these include the nitro-wag mode in PETN ($\approx 40 \text{ cm}^{-1}$) and the ammonium-umbrella mode in AN ($\approx 280 \text{ cm}^{-1}$). The collection of all predicted vibrations can be obtained by Fourier transforming the time series of atomic velocities [23]. This is known as the power spectrum, or kinetic energy per mode in the system,

$$S(\omega) = \frac{\tau}{M} \sum_{j=1}^M m_j \left| \sum_{n=0}^{M-1} \nu_j(n\Delta t) e^{-i2\pi\omega n\Delta t} \right|^2. \quad (4)$$

Here, ν_j and m_j are the atomic velocities and masses, respectively, at time t , τ is the sampling rate, and M is the number of discrete frames to be analyzed in the Fourier transform. An overall normalization by the total kinetic energy in Eq. (4) yields the vibrational density of states. The ReaxFF-predicted spectra (broken down by element type) for PETN and AN at 50 K are displayed in Fig. 3. At these low frequencies, PETN and AN exhibit mostly oxygen-dominated vibrations and very few modes in PETN below 300 cm^{-1} contain a significant contribution

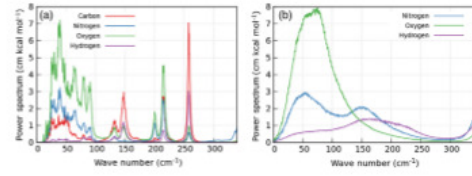


FIG. 3. ReaxFF-calculated power spectrum for (a) PETN and (b) AN at 50 K and 1 atm of pressure. These spectra aid in analyzing the radiated electric field signals shown in Sec. III. The sum of all element contributions normalized by total kinetic energy yields the vibrational density of states.

from hydrogen, while all vibrations in AN have some hydrogen character. While not all of these modes carry a dipole moment, it is possible that the strong electric field will polarize the sample and make for uniquely radiated signals. The spectra shown in Fig. 3 provide a baseline for what the frequency-conversion tensor may entail. While the input pulses are able to strongly polarize the samples, we do not expect that new modes of vibration will be observed due to the lack of conformation or chemical change.

III. RESULTS

In the previous discussion of frequency conversion, Eq. (2) is implicitly a function of the carrier frequency of the applied Gaussian pulse; it is the goal of this work to identify unique \mathbf{E}_{rad} traces for a range of THz carrier frequencies. For each polarization direction shown in

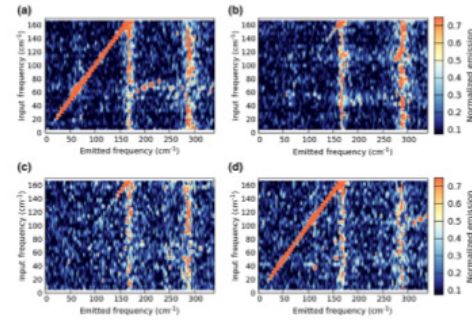


FIG. 4. Emission signals from PETN along the [100] (x direction) for electric field pulses applied in the (a) [100] and (b) [010] directions. Complementary emission signals with pulses along the [010] (y direction) for the (c) [100] and (d) [010] applied field directions in PETN. Where the emission signals are aligned with the pulse polarization, Rayleigh scattering dominates the observed emission. Perpendicular directions do show emission at unique frequencies different from the applied pulse, confirming the frequency conversion due to internal scattering.

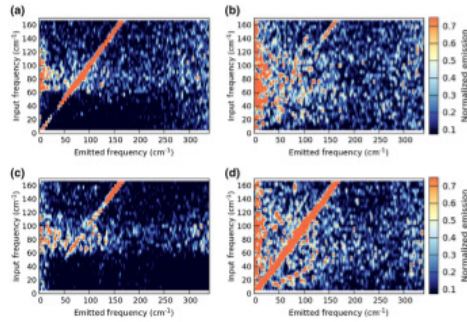


FIG. 5. Emission signals from AN along the $[100]$ (x direction) for electric field pulses applied in the (a) $[100]$ and (b) $[010]$ directions. Complementary emission signals with pulses along the $[010]$ (y direction) for the (c) $[100]$ and (d) $[010]$ applied field directions in AN. Third-harmonic emission is clearly seen for parallel emission directions to the applied field and is much weaker in orthogonal directions.

Fig. 1(e), two emission spectra are calculated from each simulation of a given carrier frequency. The collection of all emission spectra over the range of input frequencies results in a two-dimensional map of the frequency conversion for either material. These emission signals are normalized to the amount of energy absorbed for the given input frequency; the color axis in Figs. 4–6 represents the percent total emission at the given input and emitted frequency pair. Since the materials of this study are anisotropic, we expect polarization mixing even for the case of normal incidence.

The set of calculated frequency-conversion maps for PETN is contained in Fig. 4. Emission parallel to the

applied field, shown in panels (a) and (d) of Fig. 4, displays distinct Rayleigh emission above an input frequency of 20 cm^{-1} . In addition, the third-harmonic generation is clearly seen in Figs. 4(a) and 4(d), where the input frequency is one-third that of an existing mode in the material, see Fig. 3(a). The second harmonic is forbidden since PETN has inversion symmetry [3]. Orthogonal to the applied field polarization, the emitted signal is not as well defined as the parallel emission, though unique islands of frequency conversion can be identified. In panels (b) and (c) of Fig. 4, the Rayleigh emission is not uniformly seen for all carrier frequencies and varying emitted intensities are observed near 160 and 270 cm^{-1} across all input frequencies. These are phonon modes of the system [20] and add an additional fingerprint of the material tested.

The energetic cocrystal AN has a unique set of frequency-conversion maps, as shown in Fig. 5. Parallel to the applied field, the third-harmonic emission is only weakly seen for a field pulse applied in the x direction, Fig. 5(a), but is visible for all carrier frequencies tested here. Conversely, the parallel emission for a y -polarized field only results in a clear third-harmonic emission below 125 cm^{-1} . Orthogonal emission to the applied field, Figs. 5(b) and 5(c), has a common Rayleigh emission at input frequencies higher than 140 cm^{-1} but each polarization yields contrasting off-diagonal elements. Namely, the x -polarized pulse shows only nonlinear elements for input frequencies in the range of 60 – 110 cm^{-1} , where modes below 25 cm^{-1} or above 300 cm^{-1} become strongly emitting signals. Gathering each of these frequency-conversion tensors, one can predict the far-field observed emission spectra. The rationale behind showing all polarization components in Figs. 4 and 5 is to confirm that the

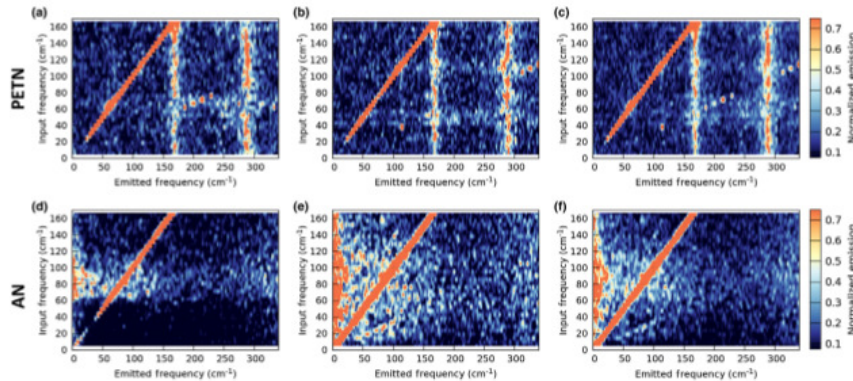


FIG. 6. Average emission signals for all output polarizations for impulses applied in the $[100]$ direction for (a) PETN and (d) AN along with field pulses in the orthogonal, $[010]$ direction in panels (b) and (e). Total emission signals for all absorption and exit polarizations for (c) PETN and (f) AN.

input light is being scattered within the crystal, resulting in both a polarization and frequency change.

For the usual experimental case where the input field is polarized but the detection is not polarization sensitive, it makes sense to perform an average over the x and y polarizations for a given linearly polarized input field. The frequency-conversion maps of these cases are shown in Figs. 6(a) and 6(b) for PETN and Figs. 6(d) and 6(e) for AN. Furthermore, in the case that the input field is unpolarized and the far-field detector is also not polarization sensitive, it makes sense to perform an average over the x and y input polarizations, and the x and y output polarizations. The results of this computation for PETN and AN are shown in Figs. 6(c) and 6(f), respectively. Focusing on the pair of spectra shown in Figs. 6(c) and 6(f), these energetic materials have to be distinguished by the off-diagonal portions of the emitted light because both show strong Rayleigh signals. For PETN, there are only a handful of third-harmonic frequencies that show up clearly and all of these are above 100 cm^{-1} . These unique nonlinear signals are the result of the third harmonic of the input wave coinciding or in close proximity with a peak in the vibrational spectra shown in Fig. 3(a). In contrast, AN shows only a weak third-harmonic generation below 100 cm^{-1} and unique nonlinear features occurring in the low-frequency region below 25 cm^{-1} for input frequencies between 40 and 120 cm^{-1} . These low-frequency nonlinear signals are inferred to be molecular rotations or multimolecular modes that are activated due to strong absorption in the $[010]$ polarized light. These unique features in the unpolarized frequency-conversion maps provide signatures that an uninformed observer could use to distinguish between these two materials.

IV. CONCLUSIONS

In this contribution we have leveraged molecular-dynamics simulations and extensions of classical electrodynamics to predict nonlinear THz emission due to vibrational scattering in a pair of molecular crystals. By constraining the simulation geometries and polarizations of the external electric, our predictions are easily extended to the experimentally relevant far-field measurement. In addition, by using reactive MD simulations we have avoided any approximations due to harmonic absorption or emission as well as normal mode descriptions of the molecular vibrations. While the use of a force field is an approximation of the actual physics of the problem, it does, however, allow for tractable simulations that provide useful and rapid 2D-spectra predictions. We have shown the 2D spectra of PETN and ammonium nitrate polymorph IV that differ significantly in the THz frequency range due to changes in the location and intensity of third-harmonic emission of the input light as well as other nonlinear frequency emissions. These output signals are dramatically different in both polarization and frequency from the input electric field pulse, which provides a potential for a THz

detection technique with chemical specificity. With increasing pulse intensities one can imagine using the resultant chemistry from the THz pulse as an additional means for standoff detection, but this is beyond the scope of this contribution. There would be a necessary tradeoff of the specificity of the predicted nonlinear signals for chemical-species detection due to the high-temperature broadening of these low-frequency modes of interest. The pulse-intensity dependence as well as further study of the orientation dependence of nonlinear signals in these anisotropic energetic materials will be a subject of further study.

ACKNOWLEDGMENTS

We would like to thank Wilton Kort-Kamp for discussions. M. A. W. recognizes partial support for this research by the U.S. Office of Naval Research through Grant No. N00014-11-0466. D. A. R. D. and D. S. M. gratefully acknowledge funding from the U.S. DOE through the LANL LDRD program.

- [1] K. E. Brown, M. T. Greenfield, S. D. McGrane, and D. S. Moore, Advances in explosives analysis—Part II: Photon and neutron methods, *Anal. Bioanal. Chem.* **407**, 1 (2015).
- [2] M. C. Kemp, Explosives detection by terahertz spectroscopy—A bridge too far?, *Terahertz Sci. Technol.* **1**, 282 (2011).
- [3] R. W. Boyd, *Nonlinear Optics*, 3rd ed. (Academic Press, San Diego, 1993).
- [4] L. D. Landau, E. M. Lifshitz, and L. P. Pitaevskii, *Electrodynamics of Continuous Media* (Pergamon Press, New York, 1984).
- [5] J. D. Jackson, *Classical Electrodynamics*, 3rd ed. (Wiley, New York, 1998).
- [6] G. Katz, S. Zybin, W. A. Goddard, Y. Zeiri, and R. Kosloff, Direct MD simulations of terahertz absorption and 2D spectroscopy applied to explosive crystals, *J. Phys. Chem. Lett.* **5**, 772 (2014).
- [7] D. S. Moore, Method and apparatus for detecting explosives, U.S. Patent No. 7,939,803, May 10, 2011.
- [8] A. C. T. van Duin, S. Dasgupta, F. Lorant, and W. A. Goddard, ReaxFF: A reactive force field for hydrocarbons, *J. Phys. Chem. A* **105**, 9396 (2001).
- [9] N. Rom, S. V. Zybin, A. C. T. van Duin, W. A. Goddard, Y. Zeiri, G. Katz, and R. Kosloff, Density-dependent liquid nitromethane decomposition: Molecular dynamics simulations based on ReaxFF, *J. Phys. Chem. A* **115**, 10181 (2011).
- [10] T. Zhou, S. V. Zybin, Y. Liu, F. Huang, and W. A. Goddard, Anisotropic shock sensitivity for β -octahydro-1,3,5,7-tetranitro-1,3,5,7-tetrazocine energetic material under compressive-shear loading from ReaxFF-Ig reactive dynamics simulations, *J. Appl. Phys.* **111**, 124904 (2012).
- [11] A. Strachan, A. C. T. van Duin, D. Chakraborty, S. Dasgupta, and W. A. Goddard, Shock Waves in High-Energy Materials: The Initial Chemical Events in Nitramine RDX, *Phys. Rev. Lett.* **91**, 098301 (2003).

- [12] M. A. Wood, A. C. T. van Duin, and A. Strachan, Coupled thermal and electromagnetic induced decomposition in the molecular explosive α HMX; A reactive molecular dynamics study, *J. Phys. Chem. A* **118**, 885 (2014).
- [13] E. C. Neyts, A. C. T. van Duin, and A. Bogaerts, Insights in the plasma-assisted growth of carbon nanotubes through atomic scale simulations: Effect of electric field, *J. Am. Chem. Soc.* **134**, 1256 (2012).
- [14] H. Li, D. Ren, and X. Cheng, The theoretical investigation of the β -crystalalite structure under the effect of electric field, *Comput. Mater. Sci.* **96**, 306 (2015).
- [15] See Supplemental Material at <http://link.aps.org/supplemental/10.1103/PhysRevApplied.5.014004> for the ReaxFF parametrization used in this work.
- [16] A. K. Rappe and W. A. Goddard, Charge equilibration for molecular dynamics simulations, *J. Phys. Chem.* **95**, 3358 (1991).
- [17] S. Plimpton, Fast parallel algorithms for short-range molecular dynamics, *J. Comput. Phys.* **117**, 1 (1995).
- [18] F. Castro-Marciano and A. C. T. van Duin, Combustion of an Illinois No. 6 coal char simulated using an atomistic char representation and the ReaxFF reactive force field, *Combust. Flame* **160**, 766 (2013).
- [19] M. A. Wood, M. J. Cherukara, E. M. Kober, and A. Strachan, Ultrafast chemistry under nonequilibrium conditions and the shock to deflagration transition at the nanoscale, *J. Phys. Chem. C* **119**, 22008 (2015).
- [20] S. D. McGrane, J. Barber, and J. Quenneville, Anharmonic vibrational properties of explosives from temperature-dependent Raman, *J. Phys. Chem. A* **109**, 9919 (2005).
- [21] J. R. Holden and C. W. Dickinson, Crystal structures of three solid solution phases of ammonium nitrate and potassium nitrate, *J. Phys. Chem.* **79**, 249 (1975).
- [22] A. Stukowski, Visualization and analysis of atomistic simulation data with OVITO—The open visualization tool, *Simul. Mater. Sci. Eng.* **18**, 015012 (2010).
- [23] P. H. Berens, D. H. J. Mackay, G. M. White, and K. R. Wilson, Thermodynamics and quantum corrections from molecular dynamics for liquid water, *J. Chem. Phys.* **79**, 2375 (1983).

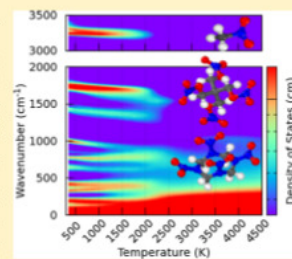
Nonequilibrium Reaction Kinetics in Molecular Solids

Mitchell A. Wood and Alejandro Strachan*

School of Materials Engineering and Birk Nanotechnology Center, Purdue University, West Lafayette, Indiana 47907, United States

Supporting Information

ABSTRACT: We explore the possibility of nonstatistical chemical reactions in condensed-phase energetic materials via reactive molecular dynamics (MD) simulations. We characterize the response of nitromethane [CH_3NO_2], HMX [cyclic $(\text{CH}_2\text{-NNO}_2)_4$], and PETN [$\text{C}-(\text{CH}_2\text{-ONO}_2)_4$] to different types of insults: electric fields of various frequencies and strengths and direct heating at various rates. We find that nonequilibrium states can be created for short time scales when energy input targets specific vibrations through the electric fields and that equilibration eventually occurs even while the insults remain present. Interestingly, for strong fields these relaxation time scales are comparable to those of the initial chemical decomposition of the molecules. NM decomposes predominantly via bimolecular reactions, and while insults targeting specific modes lead to strong nonequilibrium states, they do not affect the kinetics associated with decomposition. PETN decomposes via the unimolecular formation of NO_2 and, quite interestingly, exhibits faster initial decomposition and lower activation energy when excited by frequency-targeted electric fields. HMX, a larger cyclic molecule, exhibits faster internal relaxation time scales, and the degree of nonequilibrium achieved is smaller than in the other two materials. Therefore, its decomposition is rather independent of insult type and does not deviate from statistical behavior. These results provide insight into nonequilibrium or coherent initiation of chemistry in the condensed phase that would be of interest in fields ranging from catalysis to explosives.



1. INTRODUCTION

Despite decades of experimental^{1–6} and theoretical efforts,^{7–12} nonstatistical chemical reactions remain only partially understood, particularly in condensed-phase systems.^{13,14} This lack of fundamental understanding has practical implications and has hindered our ability to achieve mode-selective chemistry that would be attractive for a range of applications from direct initiation of energetics^{2,15} to catalysis.^{16–20} Statistical chemical reactions apply when the system can be considered to have achieved equilibrium before the transition state is reached; under such circumstances, unimolecular reactions can be described with the Rice–Ramsperger–Kassel–Marcus (RRKM)²¹ or RRK²² theories. Deviations from these theoretical predictions have been documented in theoretical and experimental studies^{1,5,6} for small molecules and clusters by Thompson et al.^{23,24} and very recently by Wales.²⁵ Striking manifestations of nonstatistical chemistry include mode-specific excitations affecting dissociation of chemisorbed methane,²⁶ water,²⁷ and their deuterated analogues²⁸ on transition metal surfaces as well as atmospheric photodissociation.²⁹

Multiple processes can lead to non-RRK behavior including: (i) anharmonicities in the potential energy surfaces³ (which by themselves do not indicate nonstatistical behavior); (ii) cases where energy is localized in a small number of modes at the time chemistry occurs—this requires inputting energy in a mode-specific way and intramolecular vibrational energy redistribution (IVR) rates being slow or comparable with those associated with chemistry;^{30–32} and (iii) systems with phase space exhibiting bottlenecks that keep them from reaching the transition state; an

example would be molecules that require a conformational change prior to bond scission.³ Most of the theoretical efforts dedicated to nonstatistical chemistry so far have focused on gas-phase reactions,^{21,22} and little is known about nonstatistical chemistry in the condensed phase; this second case is the focus of our paper.

Our study is enabled by the development of reactive interatomic potentials that provide a realistic description of complex chemical reactions in a computationally efficient way, enabling large-scale reactive simulations in condensed matter.^{33,34} Our prior work demonstrated that the mechanisms by which energy is inputted into the high-energy density material octahydro-1,3,5,7-tetranitro-1,3,5,7-tetrazocine (HMX) can affect its initial decomposition, hinting at nonstatistical behavior.³⁵ In this paper we study the decomposition of nitromethane (NM), HMX, and pentaerythritol tetranitrate (PETN) under a range of mode-specific energy insults and quantify the non-statistical degree of their decomposition.

To a first approximation, the solvation shell or crystal environment surrounding a reacting molecule in a condensed-phase system can be taken as an inert medium, resulting in only small modifications on the observed kinetics from the gas phase. However, in the molecular crystals studied here the local environment is not inert, and local reaction kinetics will certainly be affected by nearby endothermic or exothermic processes.

Received: October 7, 2015

Revised: November 17, 2015

Published: December 8, 2015

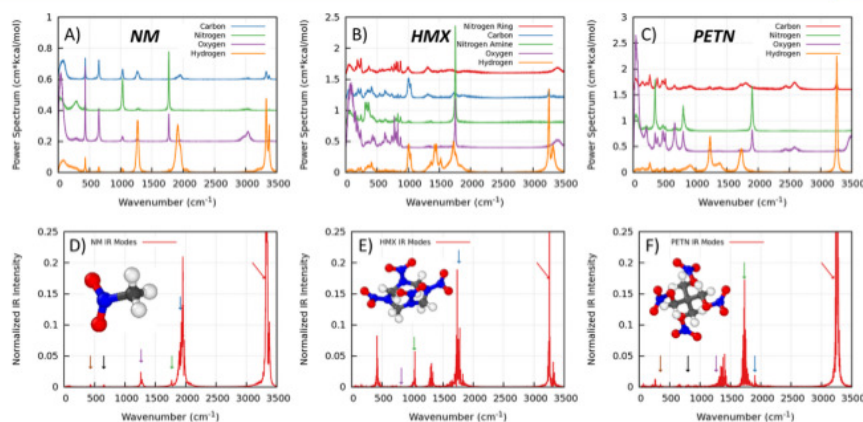


Figure 1. Calculated power spectrum per molecule from MD at 300 K and 1 atm for (A) nitromethane, (B) HMX, and (C) PETN from the Fourier transform of atomic velocities. The vertical offset is for visual clarity. Panels (D)–(F) contain the predicted infrared spectrum of the respective vertically aligned material with colored arrows indicating the frequency of vibrational insults used in this study. Atom colors correspond to carbon (gray), hydrogen (white), oxygen (red), and nitrogen (blue).

Therefore, we expect a nontrivial interplay between chemical activation from a thermal bath versus the local environment that leads to reactions in the condensed phase. Furthermore, short IVR time scales and strong intermolecular interactions in molecular crystals tend to negate nonstatistical chemistry.^{36–38} Thus, the main goal of this paper is to establish whether nonequilibrium states (unequal energy distribution among vibrations) can be constructed via frequency-localized insults for long enough time scales to affect chemistry. We use reactive molecular dynamics and apply constant excitation to a subset of intramolecular modes using external electric fields with frequency matched to a specific vibration. Reactions resulting from such insults are compared to those that maintain equilibrium conditions through constant coupling to a thermal bath.³⁹ Our results, supported by experimental work,^{32,40} show that nonequilibrium states can be created with these mode-specific insults, and for strong electric fields, these time scales are comparable to those of the initial chemical decomposition of the molecules.^{1,5} In all cases the appropriate choice of target vibration and insult strength can result in initial reactions under conditions where the temperature of the target modes exceeds that of the bulk, sometimes up to hundreds of degrees Kelvin. Differences drawn between the three materials, which we consider as model materials given the contrasting IVR and reaction time scales, aid in our understanding of (non)statistical reaction behavior, in particular for condensed-phase systems, and in the capability of externally controlled reactions.

The remainder of the paper is organized as follows: Section 2 and its subsections will discuss simulation details including the analysis tools that calculate the vibrational and chemical information. Section 3 will focus on how we compare vibrational spectra across insult types to identify where energy is being localized, and Section 4 will show the results for the kinetics of the resulting decomposition for all insult types and materials followed by a discussion and concluding remarks in Sections 5 and 6, respectively.

2. SIMULATION DETAILS

2.1. Materials and Force Field. We study the decomposition and reaction of various energetic materials using the reactive force field ReaxFF that has been successfully used to study the shock^{41–44} and thermal^{45–48} decomposition of such materials. The force field used here merges the training set from the combustion branch⁴⁹ with the nitramines force field⁴³ and has been parametrized against unimolecular as well as multi-molecular reactions that occur in the condensed phase.³⁴ The parameter set can be found in the Supporting Information. This is the same force field used in refs 34 and 40. All simulations were performed using the LAMMPS code.⁵⁰ Self-consistent partial atomic charges are updated at every time step (0.1 fs) using a conjugate gradient method with a tolerance of 1×10^{-6} , which has been shown to properly describe chemical reactions at extreme conditions.³⁵

To more effectively study the differences in reaction behavior as a function of insult type we chose to study three molecular high-energy density (HE) materials with different characteristics. The simplest of the three is NM (CH_3NO_2) which has been widely studied for its combustion, detonation, and vibrational properties using both experimental and computational approaches. The initial structure is a perfect crystal with 3D periodic boundary conditions obtained by replicating the orthorhombic crystal structure four times along *a*, four along *b*, and four along *c* resulting in 256 molecules. The secondary explosive HMX (cyclic $(\text{CH}_2\text{NNO}_2)_4$) is a nitramine that exhibits an alternating carbon–nitrogen ring. We start from the α -crystal structure and replicate the unit cell $2 \times 1 \times 4$ to obtain a simulation cell with 64 molecules. Lastly, we studied PETN ($\text{C}(\text{CH}_2\text{ONO}_2)_4$) which has different molecular geometry and chemistry than both NM and HMX but a similar initial reaction mechanism as HMX. Both the nitroester (PETN) and nitramine (HMX) initially decompose through the unimolecular NO_2 loss through N–O or N–N scission, respectively. PETN has a tetragonal crystal structure that we replicate $4 \times 4 \times 4$ times resulting in 128 molecules in the simulation cell.

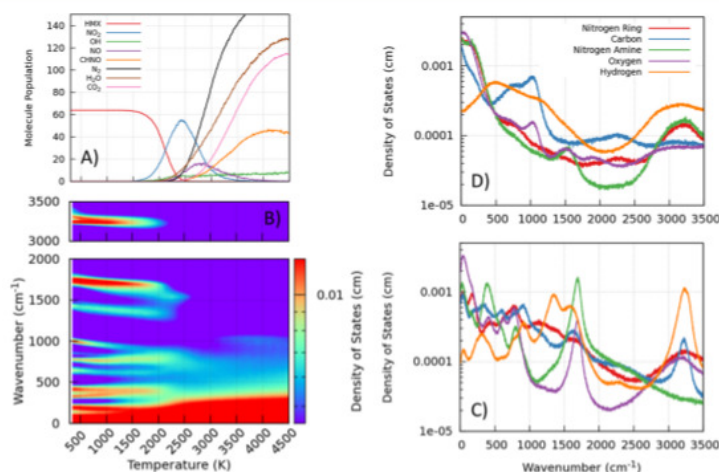


Figure 2. Typical simulation of HMX decomposition due to a constant heating of the system via a Nose–Hoover thermostat at a rate of 50 K/ps. Chemical species information in (A) and dynamic vibrational density of states in (B) share a common axis which is the temperature of the system. Panels (C) and (D) are per element spectra at 1750 and 3500 K, respectively, during the simulation.

Differences in the molecular structures of the three materials lead to different vibrational properties and inter- and intra-molecular energy relaxation characteristics. This can be seen in the top panels of Figure 1 where we show the vibrational power spectrum of the three systems computed from the Fourier transform of the atomic velocities.⁵¹ The infrared (IR) intensities extracted from the autocorrelation of the change in dipole moment⁵² are shown in the bottom panels, and these will be used to discuss the coupling of the vibrations to the electric field insults.

2.2. Simulation of Thermal- and Electromagnetic-Induced Reactions. In order to characterize the decomposition of the materials of interest under various conditions, a constant insult is applied throughout the simulation as either a sinusoidal electric field at various frequencies or a constant heating rate with a Nose–Hoover thermostat. This continuous input of energy is in contrast with our previous work which used a pulsed insult³⁵ and enables the study of the reacting systems in the presence of the insult. Also, since these systems are heated at known rates, traditional kinetics analysis techniques can be applied to the reacting system to extract activation energies and attempt frequencies;^{53,54} this will be further discussed in Section 4. We use electric field strengths in the range 0.01–1 V/nm which result in heating rates of the order 0.1–100 K/ps, sufficient to decompose the material on MD time scales. Several field frequencies were applied as described below to localize energy into various modes. For each insult type and strength we performed ten statistically independent simulations after a thermalization at 300 K for 20 ps. Each simulation had velocities initially assigned from a randomly seeded Maxwell–Boltzmann distribution, which decouples the trajectories from one another by the time the insult is applied. Since the Nose–Hoover thermostat scales all atomic velocities by the same number, the initial equipartition of energy per mode is held even when the system is constantly heated with this thermostat.

We selected a set of frequencies for the electric field insults for each material based on vibrational properties; these are indicated by arrows in the lower panels of Figure 1. For each driving frequency chosen, ten different field strengths were applied in order to properly address the effect of insult strength on the relaxation times and resultant chemistry.

Identification of vibrational modes can be performed using the per element power spectra shown in Figure 1 in conjunction with experimentally reported spectra. From these results and Appalakondaiah et al.⁵⁵ the NM target modes were assigned as follows: 3330 cm^{−1} (CH stretch), 1913 cm^{−1} (CH₂ angle bend + CH₃ deform), 1772 cm^{−1} (NO stretch), 1266 cm^{−1} (NCH deform + CN stretch), 651 cm^{−1} (CN stretch + NO₂ angle bend), and 433 cm^{−1} (NO₂ rock). Similarly, following Pravica et al.⁵⁶ for HMX: 3254 cm^{−1} (CH stretch), 1765 cm^{−1} (NO stretch), 1030 cm^{−1} (NN stretch + CH₂ rock), and 814 cm^{−1} (Ring twist + NO₂ angle bend). Lastly for PETN, following Gupta et al.⁵⁷ 3258 cm^{−1} (CH stretch), 1903 cm^{−1} (NO stretch), 1728 cm^{−1} (CH₂ angle bend), 1266 cm^{−1} (CH₂ wag + CO stretch + C₅ deform), 799 cm^{−1} (O–NO₂ umbrella), 348 cm^{−1} (O–NO₂ rock + C₅ deform). We note that while ReaxFF is not parametrized to reproduce the entire vibrational spectra of energetic materials it provides a reasonable description as compared with the ab initio predictions (see refs 54–56); this is because ReaxFF is parametrized to describe bond breaking, angle, and torsion bending curves. The largest discrepancies in vibrational frequencies are associated with high-frequency bond stretch modes such as the N–O and C–H modes that are common to all three materials. As will be discussed in Section 3 the exact peak positions do not affect the main results of our paper.

A simulation of such complexity necessarily involves approximations: the most significant ones are those associated with the description of atomic interactions using the ReaxFF force field, and the second is the use of classical mechanics (as

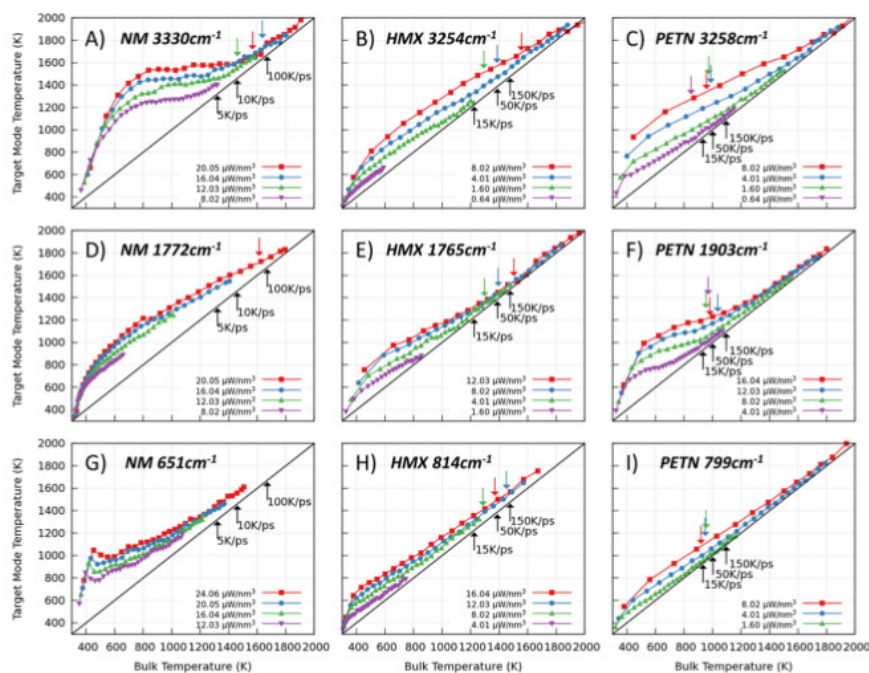


Figure 3. Two temperature plots of target mode temperature versus bulk temperature during an electric field in-sult as calculated in eq 1. Each data point is 1 ps apart. Panels (A)–(C) are the CH stretch modes in each material, respectively, (D)–(F) the NO stretch mode, and (G)–(I) are low-frequency intramolecular modes that are unique to each molecule's geometry. Color matched arrows indicate the first chemical reaction for each insult, and the equilibrium reactions are indicated in black. The nonequilibrium distribution of energy among vibrations is clearly seen as data points lying above the solid black equipartition line ($T_{\text{mode}} = T_{\text{bulk}}$).

opposed to quantum) to describe ionic dynamics. The implications of these approximations in our results are addressed in Section 5.

2.3. Simulation Analysis: Characterizing Thermodynamic and Chemical States. One of the main goals of the paper is to understand whether nonequilibrium states, i.e., when the energy is not equally distributed among the various inter- and intramolecular modes as dictated by equilibrium statistical mechanics, can exist for long enough to affect chemical reactions in the condensed phase. In order to quantify how energy is distributed in the system as a function of frequency we compute the power spectrum from atomic velocities. However, the short time scales involved in the loading and reaction of HEs requires high time resolution, which limits the spectral resolution. A typical calculation of the vibrational spectrum requires a trajectory of, at least, 10 ps in length for suitable resolution ($\sim 0.1 \text{ cm}^{-1}$), but this is impossible when dealing with processes that involve smaller time scales. To circumvent this, an equivalent trajectory is assembled for spectral analysis that is sampled from small time segments over many independent simulations. While this leads to smoother spectra it creates artifacts that need to be acknowledged. Velocity discontinuities at the times when trajectories are merged lead to unphysical high-frequency signals and a slight broadening of spectral features (see Supporting

Information Figure S2) in the frequency range of interest ($1\text{--}4000 \text{ cm}^{-1}$). For the work presented here, a trajectory window of 1 ps and velocity sampling rate of 4.7 fs give a resolvable frequency window of $33\text{--}3500 \text{ cm}^{-1}$, within which all three test materials have their full vibrational spectrum. A comparison of the power spectrum of HMX calculated by this assembled pseudotrajectory method to a single continuous trajectory is given in the Supporting Information (Figure S1). Lastly, this method proves extremely useful when calculating dynamic spectral changes of a material that has the overall energy changing with time. If all replicates from which a pseudotrajectory is assembled have a common reference time (presence of an insult), there is no added complication to the method outlined above.

Figure 2 illustrates a typical simulation of thermal decomposition of HMX for a heating rate of 50 K/ps. Figure 2(a) shows the population of HMX, key intermediate, and final product molecules as a function of temperature, and panel (b) shows the evolution of the vibrational DoS (obtained from normalizing the power spectrum) with temperature. We use ReaxFF bond orders to identify chemical bonds, and this connectivity information is subsequently analyzed with a cluster expansion algorithm to identify molecules. Figures 2(c) and (d) show the vibrational spectra broken down by element type at 1750 and 3500 K,

respectively. Figures 2(a) and (b) show that significant red-shifts and broadening of the HMX peaks occur before decomposition begins. At temperatures over 1500 K we observe peaks in the density of states disappearing, indicating chemical reactions. We note that the original NO stretch peaks ($\sim 1765\text{ cm}^{-1}$) in HMX persist longer than other high-frequency modes; this is due to the large number of NO and NO₂ moieties at early stages of the decomposition. At very high temperatures, where small product molecules are predominant, we see the appearance of a carbon–oxygen peak near 1000 cm^{-1} (Figure 2c) that correlates with the appearance of CO and CO₂ species (see Figure 2a). The large number of small and very mobile molecules explains the strong signal at low frequencies coming from intermolecular collisions. All together, the increased time resolution on the vibrational spectra and molecule recognition allows for greater insight into the decomposition and, as will be shown, how these processes can be altered by the means of energy input.

3. CREATING NONEQUILIBRIUM STATES

In order to quantify whether a nonequilibrium state is achieved in the samples excited by the electric fields, we compare their power spectra (i.e., kinetic energy density as a function of frequency) with those of thermally activated cases with comparable heating rates and at the same overall temperature. Specifically, we compute the relative kinetic energy associated with modes within frequency ranges of interest to that of the thermally loaded sample to quantify the degree of nonequilibrium. Consider the power spectra of the electromagnetic and thermally heated samples at the same overall kinetic energy. The relative energy content in the frequency ranges of interest describes differences in the partition of energy between the two systems. The temperature associated with modes in a given frequency range can be estimated assuming the thermally excited system remains in equilibrium and that both systems undergo similar chemical reactions as

$$T^*(\omega_1, \omega_2) = T_0 \frac{\int_{\omega_1}^{\omega_2} P_{\text{EM}}(\omega) d\omega}{\int_{\omega_1}^{\omega_2} P_{\text{th}}(\omega) d\omega} \quad (1)$$

where T_0 is the bulk temperature of the normalizing spectra; $P_{\text{th}}(\omega)$ is the power spectrum of the directly heated (equilibrium) sample; $P_{\text{EM}}(\omega)$ is the power spectrum in the presence of the electromagnetic insult; and ω_1 and ω_2 are the frequency ranges that capture sets of modes near the target frequency. The frequency ranges used for each material studied are given in Table S1 in the Supporting Information. The equilibrium spectra used to compute frequency resolved temperatures are chosen such that the instantaneous bulk temperature and heating rate match those observed with the electromagnetic insult. After the nonequilibrium spectra have been normalized, each group of modes can be assigned a temperature that aids in the analysis of the effect of direct vibration coupling with an external electric field.

Figure 3 shows the temperature associated with modes within frequency regions including the target mode versus bulk temperature (obtained from the overall kinetic energy in the simulation cell) of each material for a few target frequencies tested. The solid diagonal solid lines with slope one indicate equilibrium, i.e., the selected modes exhibiting the same temperature as the overall system; in other words, the solid lines indicate equipartition of energy. We observe that, in all cases, the frequency range containing the excited mode exhibits more than

its share of the kinetic energy; i.e., those modes are hotter than the rest. As expected, higher energy input rates lead to increased nonequilibrium. Interestingly, even though the insult is maintained throughout the simulations the systems eventually achieve equilibrium; each point on these plots is 1 ps apart, which gives a measure of the relaxation process in both time and temperature. This relaxation occurs because anharmonicities in the potential energy surface (PES) are sampled more predominantly as temperature increases (see peak broadening in Figure 2), leading to faster energy transfer between modes and weaker coupling with the external electric field.

The arrows matching the plot lines in color in Figure 3 mark the average times at which the first molecule is observed to decompose, while the solid black arrows indicate the first decomposition in the directly heated samples for comparable heating rates. Interestingly, we observe that often the time scales for equilibration are comparable to those associated with the initial chemistry; for some target modes in HMX and PETN decomposition occurs when the target modes are several hundreds of degrees Kelvin higher than the bulk temperature when the material begins to decompose. The vibrationally tuned insults are labeled by the energy density of the electric field. More details about this calculation and additional two temperature plots can be found in the Supporting Information.

The results in Figure 3 point to several possible scenarios regarding the possibility of nonstatistical decomposition. In the case of NM, while a significant degree of nonequilibrium is achieved in samples excited with the electric fields, the chemical reactions occur after equilibration has occurred. Actually it appears that the targeted insults may delay the reactions as compared to thermal excitation (color arrows indicate higher temperatures than the black ones). PETN also exhibits a significant degree of nonequilibrium, and contrary to NM, reactions occur at these elevated mode temperatures. Quite significantly, reactions in PETN under targeted insults occur at lower bulk temperatures than those in thermally excited samples. HMX exhibits the least degree of nonequilibrium, and except in the case of fields targeting CH vibrations, the reactions occur under essentially equilibrium conditions. Even in the high-frequency excitation case, reactions occur at temperatures comparable to the thermal cases indicating that the localized energy input does not significantly affect chemistry. Section 4 quantifies the effect of insult type and strength on chemistry.

4. ROLE OF INSULT TYPE AND STRENGTH ON CHEMISTRY

4.1. Reaction Kinetics. To quantify the kinetics associated with the insult-dependent reactions discussed in Section 3 we studied the decomposition rate as a function of temperature for all insult types and strengths. A first-order, thermally activated process would lead, within the harmonic approximation, to an exponential decomposition rate of the form

$$\dot{n}(t) = \frac{\dot{\alpha}(t)}{\alpha(t)} = \theta e^{-(\Delta G/kT)} \quad (2)$$

where the dot denotes time derivative; $\alpha(t)$ is the population of the HE molecules remaining at time t ; ΔG is the activation energy for decomposition; T is temperature; and k is Boltzmann's constant. The prefactor θ can be thought of as an attempt frequency; more accurately, within transition state theory, it is the ratio of the 3N vibrational frequencies of the reagents divided by the 3N – 1 positive vibrational frequencies at

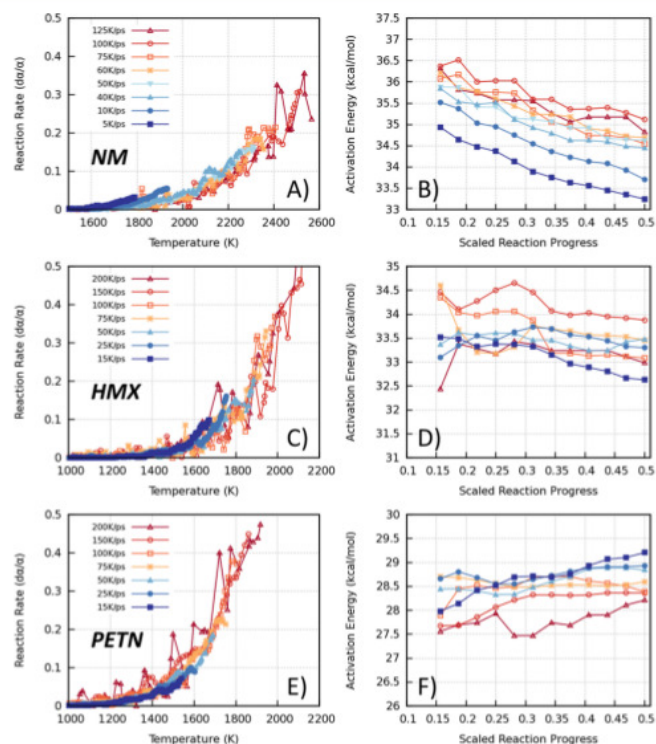


Figure 4. Observed reaction rates under equilibrium conditions for (A) NM, (C) HMX, and (E) PETN. Each data series is heated at a constant rate given the description in Section 2.2. Using the procedure outlined in Section 4.1 activation energies obtained from fitting eq 2 are plotted against the reaction progress for (B) NM, (D) HMX, and (F) PETN, respectively.

the transition state.^{58–60} The reactive MD simulations provide direct access to the quantities, α and $\dot{\alpha}$, in eq 2 (see left panels in Figure 4) and, thus, enable a direct comparison of the effect of insult type and chemistry on kinetics.

To isolate the role of insult type and strength on the activation barrier and to minimize correlations with the frequency prefactor we adopt a two-step process to fit eq 2 to the MD data. First we fit eq 2 to the collection of all thermal insult strengths for each material, NM, PETN, and HMX. The resulting frequency prefactor is taken as a constant for all other fitting procedures within the same material. For this global fitting procedure of the thermally induced decomposition, the reaction rate is fitted up to a value of $\alpha(t)/\alpha(t=0) = 0.5$, i.e., the initial decomposition of one-half of the starting HE. This is an important choice for condensed-phase reactions where the evolving molecular environment can affect chemical reactions. After this global two-parameter fit, which forces θ into a constant, the activation energy is, thus, the only free fit parameter, and we will use it to compare the kinetics across insult types and strengths. In addition, the fitting of the reaction rate is carried out up to different amounts of reaction progress (i.e., $\alpha(t)/\alpha(t=0)$) which provides information regarding changes in eq 2 as the evolving

environment of intermediate and final products can affect the decomposition of the remaining HE molecules.

4.1.1. Thermal Excitation. Left panels in Figure 4 show decomposition rates as a function of temperature for thermal excitation for various heating rates (high to low in red to blue), and the right panels show the extracted activation energies for the various heating rates as a function of the maximum reaction progress used in the exponential fits. In all these cases involving energy input with a thermostat, the effect of heating rate and reaction progress on activation energy is relatively weak. This is an important validation of our approach to extract kinetics parameters from reactive MD simulations. Still, within these weak dependencies some interesting trends can be observed. Both for HMX and NM we observe a slight increase in activation energy with increasing heating rate; this can be expected as faster heating might lead to overshooting of the transition state. Interestingly, PETN exhibits the reverse trend: the activation energy decreases slightly for faster heating rates. In addition, HMX and PETN show little to no effect of heating rate (about 1 kcal/mol in activation energy) on reaction progress which is consistent with a unimolecular reaction.^{61–64}

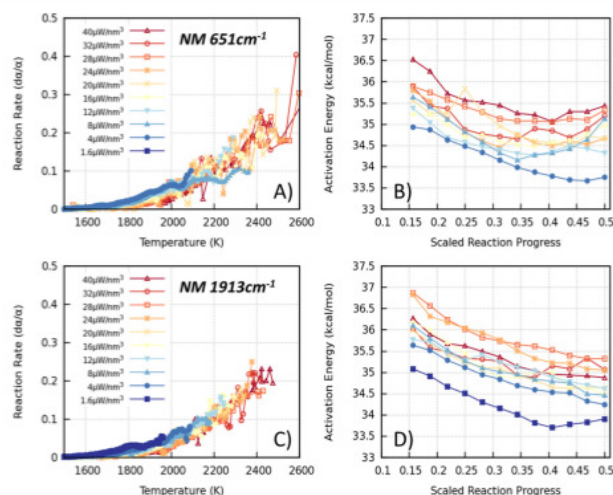


Figure 5. Nitromethane reaction rates obtained from simulations of electric field induced decomposition for the intramolecular modes at (A) 651 cm^{-1} and (C) 1913 cm^{-1} ; see section 2.2 for mode assignments. The fits to eq 2 yield the activation energies plotted in panels (B) for the mode at 651 cm^{-1} and (D) for the mode at 1913 cm^{-1} .

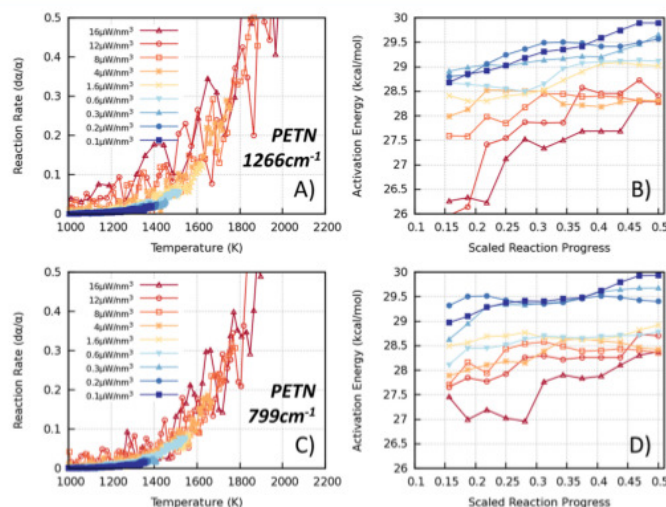


Figure 6. PETN reaction rates obtained from simulations of electric field induced decomposition for the intramolecular modes at (A) 1266 cm^{-1} and (C) 799 cm^{-1} (see section 2.2 for mode assignments). The fits to eq 2 yield the activation energies plotted in panels (B) for the mode at 1266 cm^{-1} and (D) the mode at 799 cm^{-1} . Both target modes show clear insult strength dependence as seen by lower activation energies at high insult strengths and early reaction progress.

4.1.2. Electromagnetic Insults. Figure 5 shows the observed reaction rates versus temperature and resulting activation energies as a function of extent of reaction for various insult strengths for two selected electric field frequencies coupled to

vibrations in NM. The resulting activation energies and their dependence on insult strength and extent of reaction are similar to those for the thermal decomposition in Figure 4. This is consistent with the observation in Section 3 that chemistry in

NM occurs after equilibration between the various degrees of freedom is achieved. Decomposition rates and activation barriers for HMX are included in the [Supporting Information](#) (Figures S9 and S11). As with NM, we do not find significant differences in the activation energies between frequency-targeted insults and thermal excitation. This is also consistent with the results in [Section 3](#) that show HMX to have the weakest degree of nonequilibrium kinetic energy distributions between vibrational modes out of the three materials.

Turning now to the reaction kinetics for PETN, [Figure 6](#) shows decomposition rates and the resulting activation energies for two field frequencies and a range of insult strengths. The results show striking differences with the prior cases. For both frequencies, stronger insults (faster heating rates) result in *reduced* effective activation energies; this can be confirmed from the left panels that clearly show faster decomposition for stronger insults (red). For both target modes shown in [Figure 6](#), the energy input rate not only leads to the opposite trend in activation energy with respect to NM and HMX but also its effect is more dramatic. This is consistent with the results in [Section 3](#), where reactions are seen earlier in the frequency-targeted insults in PETN and suppressed in NM. Furthermore, the data shown in [Figure 5\(A\)](#) and (C) show that the observed reaction rate is particularly low for early decomposition due to the strongest fields. Both frequencies show low activation energy for the early decomposition at high insult strengths that relax back to a value close to the thermal insults for higher decomposition degrees.

4.2. Reaction Progress. To provide a complementary picture of whether inputting energy of specific frequencies accelerates or hinders the initial chemistry we study the temperature at which one-third of the original molecules have decomposed. This is clearly a heating rate dependent quantity, thus [Figure 7](#) shows the temperature corresponding to one-third of the original molecules having decomposed as a function of heating rate for the various insult types. The simulations of electric field induced decomposition result in time-dependent heating rates due to modulations of coupling strength between the fields and the HE material (see [Supplemental Figure S13](#)). The reported heating rate in [Figure 7](#) is simply the linear approximation up to one-third decomposed: $(T_{1/3} - T_0)/\Delta t$.

The simulations exhibit very interesting trends of initial chemistry on molecular structure and insult. PETN was shown to exhibit nonstatistical decomposition for some electric field frequencies, and we find that for many of those cases 1/3 decomposition is achieved at lower temperatures than when heating with a thermostat (orange line). This is consistent with the reduced activation barrier shown in [Figure 6](#). In the case of NM, several vibrationally tuned energy inputs result in an apparent delay of initial reactions as compared to thermally excited cases and, consequently, require higher temperatures (and energy input) to reach one-third decomposition. HMX lies somewhere between these two cases; except for the 814 cm^{-1} field excitation that slows down reactions, the temperatures corresponding to one-third decomposition are rather insensitive to insult type. In NM and HMX, the temperatures at one-third decomposed are close to the onset of exothermic chemistry which means any delay in the initial reactions will lead to a large temperature difference in [Figure 7](#). This is exemplified in [Supplemental Figure S13](#) where insults applied to NM with heating rates close to 50 K/ps result in one-third decomposition temperatures of $2200\text{--}2300\text{ K}$ which neighbor a significant increase in heating rate. This late increase in heating rate has

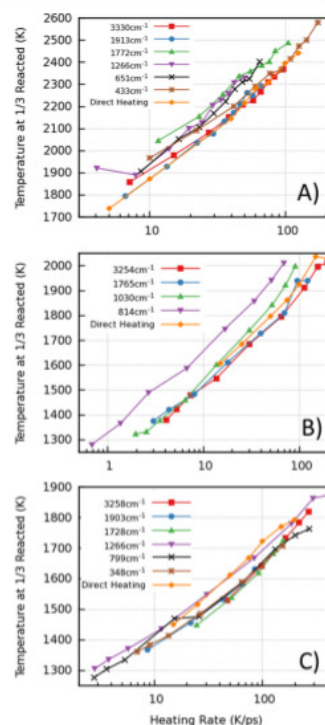


Figure 7. Observed bulk temperature at a fixed one-third decomposition for (A) NM, (B) HMX, and (C) PETN where each point is averaged over ten independent simulations at the same insult strength. Equilibrium decomposition is denoted by the direct heating data series in orange diamonds in all panels.

contributions from exothermic chemistry as well as additional coupling of the electric field with product molecules.

5. DISCUSSION

Understanding energy localization, transfer, and relaxation in condensed-phase materials and their effect on chemical reactions is a key step toward coherent control of chemistry with the potential to impact fields like catalysis, atmospheric chemistry, and energetic materials. For the energetic materials studied here, the interplay of vibrational energy relaxation and chemistry plays a significant role in the formation of a self-sustained deflagration wave.⁴¹ More generally, coherent initiation of high-energy density materials could lead to safer formulations and remote detection or neutralization of explosives.

Our simulations demonstrate that frequency-localized insults can affect the decomposition of certain HE materials with respect to thermal equilibrium reactions. More importantly, these effects can be explained based on the vibrational spectra and decomposition mechanism of the material. The sample sizes, however, prohibit a detailed phase trajectory mapping that might provide direct information about these nonequilibrium states

(nonergodic trajectories) and explain the origin of the change in activation barrier. Future work along these lines could provide a more quantitative understanding of how insult character and strength affect the exploration of phase space and match them with the various categories for non-RRKM behavior proposed by Bunker and Hase.^{7,8}

It is worth discussing at this point the two fundamental approximations made in our simulations and their impact on the results. First, the use of ReaxFF (or of any other method, including electronic structure ones) leads to an approximate description of the interactions between atoms. This affects the time scales for relaxation and equilibration processes and also kinetics and energetics associated with chemical reactions. ReaxFF has been extensively used to model energetic materials,^{43,65–67} and it is known to capture key aspects of the decomposition mechanisms of these materials and the overall reaction time scales. Its activation energies are in reasonable agreement with available experiments^{61,63,68,69} and electronic-structure-based calculations.^{59,62,64} The use of a model or approximate PES underlies all trajectory mapping or direct studies of non-RRKM chemical reactions;^{13,70} our simulation method is no different. More importantly, the main results in the current paper are drawn from differences in the response of the same model to various insults; in a way these results could be thought of as representing model materials as opposed to actual NM, PETN, and HMX. These model materials give us varying characteristics of preferred reaction path (uni- and multi-molecular) as well as IVR and reaction time scales.

A second fundamental approximation in our work is the use of classical (rather than quantum) mechanics to describe ions. Classical mechanics lacks energy quantification that affects how high-frequency modes (those where the quantum of energy $\hbar\omega$ is comparable to or larger than kT) exchange energy with an electromagnetic field and their relative distribution of energy. Rather, the classical description allows for a continuous absorption of energy from the electric field, and at low temperatures every mode shares $1/2kT$ of the total energy. Similarly, the classical description allows for anharmonic exchange of energy between modes continuously rather than in a quantized fashion. Despite these differences, both in quantum and classical mechanics, a field couples to modes with an associated electric dipole matching in frequency and equilibration occurs via anharmonicities in the PES. Thus, the classical description is able to describe energy localization and its equilibration as well as the general trends of relaxation time scales with temperature which are key to the present study.

6. CONCLUSIONS

We used molecular dynamics to study the effect of frequency-localized energy input on the excitation and decomposition of three energetic materials. NM, PETN, and HMX were chosen since they exhibit different vibrational spectra and decomposition mechanisms. Interestingly, these materials chemically react in time scales comparable with the intramolecular relaxation times. Despite the similarity of overlapping critical time scales the effect of energy input on chemistry showed disparate results. HMX exhibited the smallest degree of thermal nonequilibrium which we attribute to the higher density of intermediate frequency modes that help energy equilibration. Consequently, the insult type and strength had a negligible effect on chemistry. For nitromethane, whose decomposition is governed by multi-molecular reactions, the frequency-localized insults do not affect its decomposition kinetics even though a significant thermal

nonequilibrium is achieved. PETN, on the other hand, decomposes unimolecularly via the formation of NO_2 , and frequency-localized insults lead to nonstatistical decomposition with an observed reduction in activation energy. This work provides new insight into the possibility of coherent control of chemical reactions in energetic materials and in other fields.

■ ASSOCIATED CONTENT

Supporting Information

The Supporting Information is available free of charge on the ACS Publications website at DOI: 10.1021/acs.jpcc.5b09820.

Further details of the simulation setup and analysis tools used in this work along with additional reaction kinetics data (PDF)

Specific ReaxFF parametrization used (TXT)

■ AUTHOR INFORMATION

Corresponding Author

*E-mail: strachan@purdue.edu.

Notes

The authors declare no competing financial interest.

■ ACKNOWLEDGMENTS

The authors recognize funding support from the U.S. Office of Naval Research through grant N00014-11-1-0466.

■ REFERENCES

- (1) Diau, E. W.; Herek, J. L.; Kim, Z. H.; Zewail, A. H. Concept of Nonergodic Molecules. *Science* **1998**, *279*, 847–853.
- (2) Greenfield, M. T.; McGrane, S. D.; Scharff, R. J.; Moore, D. S.; et al. Towards Coherent Control Of Energetic Material Initiation. *AIP Conf. Proc.* **2009**, *339*, 339–342.
- (3) Forst, W. *Theory of Unimolecular Reactions*; Academic Press: New York City, 1973.
- (4) Douglas, J. Kinetics of the Thermal Cis-Trans Isomerization of Dideuteroethylene. *J. Chem. Phys.* **1955**, *23*, 315–324.
- (5) Semmes, D. H.; Baskin, J. S.; Zewail, A. H. Picosecond Real-Time Studies of Mode-Specific Vibrational Predissociation. *J. Chem. Phys.* **1990**, *92*, 3359–3376.
- (6) Semmes, D. H.; Baskin, J. S.; Zewail, A. H. Direct Observation of a Mode-Selective (Non-RRKM) van Der Waals Reaction by Picosecond Photofragment Spectroscopy. *J. Am. Chem. Soc.* **1987**, *109*, 4104–4106.
- (7) Bunker, D. L.; Hase, W. L. On Non-RRKM Unimolecular Kinetics: Molecules in General, and CH_3NC in Particular. *J. Chem. Phys.* **1973**, *59*, 4621–4632.
- (8) Bunker, D.; Wright, Karin, R.; Hase, William, L.; Houle, F. A. Exit Channel Coupling Effects in the Unimolecular Decomposition of Triatomics. *J. Phys. Chem.* **1979**, *83*, 933–936.
- (9) Thompson, D. L. Practical Methods for Calculating Rates of Unimolecular Reactions. *Int. Rev. Phys. Chem.* **1998**, *17*, 547–589.
- (10) Shalashilin, D. V.; Thompson, D. L.; Carlo, M. Intrinsic Non-RRK Behavior: Classical Trajectory, Statistical Theory, and Diffusional Theory Studies of a Unimolecular Reaction. *J. Chem. Phys.* **1996**, *105*, 1833–1845.
- (11) Procaccia, I.; Mukamel, S.; Ross, J. On the Theory of Unimolecular Reactions: Application of Mean First Passage Time to Reaction Rates. *J. Chem. Phys.* **1978**, *68*, 3244–3253.
- (12) Baetzel, R. C.; Wilson, D. J. Classical Unimolecular Rate Theory. III. Effect of Initial Conditions on Lifetime Distributions. *J. Chem. Phys.* **1965**, *43*, 4299–4303.
- (13) Yadav, P. K.; Keshavamurthy, S. Breaking of a Bond: When Is It Statistical? *Faraday Discuss.* **2015**, *177*, 21–32.
- (14) Manikandan, P.; Keshavamurthy, S. Dynamical Traps Lead to the Slowing down of Intramolecular Vibrational Energy Flow. *Proc. Natl. Acad. Sci. U. S. A.* **2014**, *111*, 14354–14359.

- (15) Bhattacharya, A.; Guo, Y.; Bernstein, E. R. Nonadiabatic Reaction of Energetic Molecules. *Acc. Chem. Res.* **2010**, *43*, 1476–1485.
- (16) Ko, A.-N.; Rabinovitch, B. S. Initial State Selection and Intramolecular Vibrational Relaxation in Reacting Polyatomic Molecules. Neopentylcyclobutane Precursor. *Chem. Phys.* **1978**, *30*, 361–374.
- (17) Chandler, D. W. A Search for Mode-Selective Chemistry: The Unimolecular Dissociation of T-Butyl Hydroperoxide Induced by Vibrational Overtone Excitation. *J. Chem. Phys.* **1982**, *77*, 4447–4458.
- (18) Simkovitch, R.; Gepshtein, R.; Huppert, D. Fast Photoinduced Reactions in the Condensed Phase Are Nonexponential. *J. Phys. Chem. A* **2015**, *119*, 1797–1812.
- (19) Thiele, E.; Goodmann, M.; Stone, J. Can Lasers Be Used To Break Chemical Bonds Selectively? *Opt. Eng.* **1980**, *19*, 191010–191015.
- (20) Jiang, B.; Yang, M.; Xie, D.; Guo, H. Quantum Dynamics of Polyatomic Dissociative Chemisorption on Transition Metal Surfaces: Mode Specificity and Bond Selectivity. *Chem. Soc. Rev.* **2015**, 20–23.
- (21) Marcus, R. A. Unimolecular Dissociations and Free Radical Recombination Reactions. *J. Chem. Phys.* **1952**, *20*, 359–364.
- (22) Rosenstock, H. M.; Wallenstein, M. B.; Wahrhaftig, A. L.; Eyring, H. Absolute Rate Theory For Isolated Systems And The Mass Spectra Of Polyatomic Molecules. *Proc. Natl. Acad. Sci. U. S. A.* **1952**, *38*, 667–678.
- (23) Viswanathan, R.; Raff, L. M.; Thompson, D. L. Monte Carlo Transition-State Theory: $\text{XH}_4 \rightarrow \text{XH}_3 + \text{H}$ ($\text{X} = \text{C}, \text{Si}$). *J. Chem. Phys.* **1984**, *81*, 828–832.
- (24) Wales, D. J. Insight into Reaction Coordinates and Dynamics from the Potential Energy Landscape. *J. Chem. Phys.* **2015**, *142*, 130901–130912.
- (25) Smith, R. R. Preference for Vibrational over Translational Energy in a Gas-Surface Reaction. *Science* **2004**, *304*, 992–995.
- (26) Hundt, P. M.; Jiang, B.; van Reijzen, M. E.; Guo, H.; Beck, R. D. Vibrationally Promoted Dissociation of Water on Ni(111). *Science* **2014**, *344*, 504–507.
- (27) Chen, L.; Ueta, H.; Bisson, R.; Beck, R. D. Vibrationally Bond-Selected Chemisorption of Methane Isotopologues on Pt(111) Studied by Reflection Absorption Infrared Spectroscopy. *Faraday Discuss.* **2012**, *157*, 285–295.
- (28) Vaida, V. Spectroscopy of Photoreactive Systems: Implications for Atmospheric Chemistry. *J. Phys. Chem. A* **2009**, *113*, 5–18.
- (29) Yang, Y.; Sun, Z.; Wang, S.; Hambir, S. A.; Yu, H.; Dlott, D. D. Ultrafast Spectroscopy of Laser-Initiated Nanoenergetic Materials. *MRS Online Proc. Libr.* **2003**, *800*, 4485–4493.
- (30) Chen, S.; Hong, X.; Hill, J. R.; Dlott, D. D. Ultrafast Energy Transfer in High Explosives: Vibrational Cooling. *J. Phys. Chem.* **1995**, *99*, 4525–4530.
- (31) Pein, B. C.; Sun, Y.; Dlott, D. D. Controlling Vibrational Energy Flow in Liquid Alkylbenzenes. *J. Phys. Chem. B* **2013**, *117*, 10898–10904.
- (32) Chenoweth, K.; van Duin, A. C. T.; Goddard, W. A. ReaxFF Reactive Force Field for Molecular Dynamics Simulations of Hydrocarbon Oxidation. *J. Phys. Chem. A* **2008**, *112*, 1040–1053.
- (33) van Duin, A. C. T.; Dasgupta, S.; Lorant, F.; Goddard, W. A. ReaxFF: A Reactive Force Field for Hydrocarbons. *J. Phys. Chem. A* **2001**, *105*, 9396–9409.
- (34) Wood, M. A.; van Duin, A. C. T.; Strachan, A. Coupled Thermal and Electromagnetic Induced Decomposition in the Molecular Explosive αHMX : A Reactive Molecular Dynamics Study. *J. Phys. Chem. A* **2014**, *118*, 885–895.
- (35) McGrane, S. D.; Barber, J.; Quenneville, J. Anharmonic Vibrational Properties of Explosives from Temperature-Dependent Raman. *J. Phys. Chem. A* **2005**, *109*, 9919–9927.
- (36) Piryatinski, A.; Tretiak, S.; Sewell, T. D.; McGrane, S. D. Vibrational Spectroscopy of Polyatomic Materials: Semiempirical Calculations of Anharmonic Couplings and Infrared and Raman Linewidths in Naphthalene and PETN Crystals. *Phys. Rev. B: Condens. Matter Mater. Phys.* **2007**, *75*, 1–9.
- (37) Brown, K. E.; McGrane, S. D.; Bolme, C. A.; Moore, D. S. Ultrafast Chemical Reactions in Shocked Nitromethane Probed with Dynamic Ellipsometry and Transient Absorption Spectroscopy. *J. Phys. Chem. A* **2014**, *118*, 2559–2567.
- (38) Pollak, E.; Talkner, P.; Berezhkovskii, A. M. A Theory for Nonisothermal Unimolecular Reaction Rates. *J. Chem. Phys.* **2001**, *107*, 3542–3549.
- (39) Pein, B. C.; Sun, Y.; Dlott, D. D. Unidirectional Vibrational Energy Flow in Nitrobenzene. *J. Phys. Chem. A* **2013**, *117*, 6066–6072.
- (40) Wood, M. A.; Cherukara, M. J.; Kober, E. M.; Strachan, A. Ultrafast Chemistry under Nonequilibrium Conditions and the Shock to Deflagration Transition at the Nanoscale. *J. Phys. Chem. C* **2015**, *119*, 22008–22015.
- (41) Shan, T.-R. R.; Wixom, R. R.; Mattsson, A. E.; Thompson, A. P. Atomistic Simulation of Orientation Dependence in Shock-Induced Initiation of Pentaerythritol Tetranitrate. *J. Phys. Chem. B* **2013**, *117*, 928–936.
- (42) Strachan, A.; Kober, E. M.; Van Duin, A. C. T.; Osgaard, J.; Goddard, W. A. Thermal Decomposition of RDX from Reactive Molecular Dynamics. *J. Chem. Phys.* **2005**, *122*, 6534–6540.
- (43) Zhou, T.; Zybin, S. V.; Liu, Y.; Huang, F.; Goddard, W. A. Anisotropic Shock Sensitivity for β -Octahydro-1,3,5,7-Tetranitro-1,3,5,7-Tetrazocine Energetic Material under Compressive-Shear Loading from ReaxFF-Lg Reactive Dynamics Simulations. *J. Appl. Phys.* **2012**, *111*, 124904–124911.
- (44) Rom, N.; Hirshberg, B.; Zeiri, Y.; Furman, D.; Zybin, S. V.; Goddard, W. A.; Kosloff, R. First-Principles-Based Reaction Kinetics for Decomposition of Hot, Dense Liquid TNT from ReaxFF Multiscale Reactive Dynamics Simulations. *J. Phys. Chem. C* **2013**, *117*, 21043–21054.
- (45) Rom, N.; Zybin, S. V.; van Duin, A. C. T.; Goddard, W. A.; Zeiri, Y.; Katz, G.; Kosloff, R. Density-Dependent Liquid Nitromethane Decomposition: Molecular Dynamics Simulations Based on ReaxFF. *J. Phys. Chem. A* **2011**, *115*, 10181–10202.
- (46) Furman, D.; Kosloff, R.; Dubnikova, F.; Zybin, S. V.; Goddard, W. A.; Rom, N.; Hirshberg, B.; Zeiri, Y. Decomposition of Condensed Phase Energetic Materials: Interplay between Uni- and Bimolecular Mechanisms. *J. Am. Chem. Soc.* **2014**, *136*, 4192–4200.
- (47) Han, S. P.; van Duin, A. C. T.; Goddard, W. A.; Strachan, A. Thermal Decomposition of Condensed-Phase Nitromethane from Molecular Dynamics from ReaxFF Reactive Dynamics. *J. Phys. Chem. B* **2011**, *115*, 6534–6540.
- (48) Castro-Marciano, F.; van Duin, A. C. T. Comparison of Thermal and Catalytic Cracking of 1-Heptene from ReaxFF Reactive Molecular Dynamics Simulations. *Combust. Flame* **2013**, *160*, 766–775.
- (49) Plimpton, S. Fast Parallel Algorithms for Short-Range Molecular Dynamics. *J. Comput. Phys.* **1995**, *117*, 1–19.
- (50) Berens, P. H.; Mackay, D. H. J.; White, G. M.; Wilson, K. R. Thermodynamics and Quantum Corrections from Molecular Dynamics for Liquid Water. *J. Chem. Phys.* **1983**, *79*, 2375–2389.
- (51) Boulard, B.; Kieffer, J.; Phifer, C. C.; Angell, C. A. Vibrational Spectra in Fluoride Crystals and Glasses at Normal and High Pressures by Computer Simulation. *J. Non-Cryst. Solids* **1992**, *140*, 350–358.
- (52) Elder, J. P. The General Applicability of the Kissinger Equation in Thermal Analysis. *J. Therm. Anal.* **1985**, *30*, 657–669.
- (53) Ozawa, T. Kinetics of Non-Isothermal Crystallization. *Polymer* **1971**, *12*, 150–158.
- (54) Appalakondaiah, S.; Vaitheeswaran, G.; Lebegue, S. A DFT Study on Structural, Vibrational Properties, and Quasiparticle Band Structure of Solid Nitromethane. *J. Chem. Phys.* **2013**, *138*, 184705–184710.
- (55) Pravica, M.; Galley, M.; Kim, E.; Weck, P.; Liu, Z. Far- and Mid-Infrared Study of HMX (octahydro-1,3,5,7-Tetranitro-1,3,5,7-Tetrazocine) under High Pressure. *Chem. Phys. Lett.* **2010**, *500*, 28–34.
- (56) Gruzdkov, Y. A.; Gupta, Y. M. Vibrational Properties and Structure of Pentaerythritol Tetranitrate. *J. Phys. Chem. A* **2001**, *105*, 6197–6202.
- (57) Laidler, K. J.; King, M. C. The Development of Transition-State Theory. *J. Phys. Chem.* **1983**, *87*, 2657–2664.

- (58) Shariya, O.; Kuklja, M. M. Ab Initio Kinetics of Gas Phase Decomposition Reactions. *J. Phys. Chem. A* **2010**, *114*, 12656–12661.
- (59) Truhlar, D. G.; Garrett, B. C. Variational Transition State Theory. *Acc. Chem. Res.* **1980**, *13*, 440–448.
- (60) Tarver, C. M.; Tran, T. D. Thermal Decomposition Models for HMX-Based Plastic Bonded Explosives. *Combust. Flame* **2004**, *137*, 50–62.
- (61) Shariya, O.; Kuklja, M. M. Rapid Materials Degradation Induced by Surfaces and Voids: Ab Initio Modeling of β -Octotetramethylene Tetranitramine. *J. Am. Chem. Soc.* **2012**, *134*, 11815–11820.
- (62) Oxley, J. C.; Kooh, A. B.; Szekeres, R.; Zheng, W. Mechanisms of Nitramine Thermolysis. *J. Phys. Chem.* **1994**, *98*, 7004–7008.
- (63) Tsyshevsky, R. V.; Shariya, O.; Kuklja, M. M. Thermal Decomposition Mechanisms of Nitroesters: Ab Initio Modeling of Pentaerythritol Tetranitrate. *J. Phys. Chem. C* **2013**, *117*, 18144–18153.
- (64) Strachan, A.; van Duin, A. C. T.; Chakraborty, D.; Dasgupta, S.; Goddard, W. A. Shock Waves in High-Energy Materials: The Initial Chemical Events in Nitramine RDX. *Phys. Rev. Lett.* **2003**, *91*, 098301–098304.
- (65) Zybin, S. V.; Goddard, W. A.; Xu, P.; van Duin, A. C. T.; Thompson, A. P. Physical Mechanism of Anisotropic Sensitivity in Pentaerythritol Tetranitrate from Compressive-Shear Reaction Dynamics Simulations. *Appl. Phys. Lett.* **2010**, *96*, 126–129.
- (66) Katz, G.; Zybin, S.; Goddard, W. A.; Zeiri, Y.; Kosloff, R. Direct MD Simulations of Terahertz Absorption and 2D Spectroscopy Applied to Explosive Crystals. *J. Phys. Chem. Lett.* **2014**, *5*, 772–776.
- (67) Hardesty, D. R. An Investigation of the Shock Initiation of Liquid Nitromethane. *Combust. Flame* **1976**, *27*, 229–251.
- (68) Blais, N. C.; Engelke, R.; Sheffield, S. A. Mass Spectroscopic Study of the Chemical Reaction Zone in Detonating Liquid Nitromethane. *J. Phys. Chem. A* **1997**, *101*, 8285–8295.
- (69) Bunimovich, L. A. Relative Volume of Kolmogorov–Arnold–Moser Tori and Uniform Distribution, Stickiness and Nonstickiness in Hamiltonian Systems. *Nonlinearity* **2008**, *21*, 13–17.
- (70) Eyring, H. The Energy Of Activation For Bimolecular Reactions Involving Hydrogen And The Halogens, According To The Quantum Mechanics. *J. Am. Chem. Soc.* **1931**, *53*, 2537–2549.

VITA

VITA

Mitchell Wood graduated with a Ph.D. from the Materials Engineering department at Purdue University in 2016 and was previously at Michigan State University where he obtained a B.S in Physics in 2011. At Purdue, his work was focused on using atomistic simulations to study materials at extremes of temperature, pressure and radiation and his research interests here are to understand the non-equilibrium physics that stem from these abnormal environments. In addition, he has developed several user-friendly, web-enabled simulation tools that have been deployed on the NSF supported cloud computing website, nanoHUB.org. Other efforts of his have been in collaboration with Los Alamos National Lab to develop efficient quantum molecular dynamics codes. He is an active member of the American Chemical Society, American Physical Society and Materials Research Society and has been recognized several times by these societies for research and presentation excellence. He has won awards for excellence in teaching Physics at Michigan State University, teaching Introductory Materials Engineering at Purdue as well as the Top Graduating Graduate Student Award from Purdue Materials Engineering in 2016. After leaving Purdue, he joined the Center of Computing Research at Sandia National Labs in Albuquerque, New Mexico as a postdoctoral fellow where he will be involved in the development of scalable simulation codes for high performance computing.